High speed flow measurement devices for gasoline fuel injectors

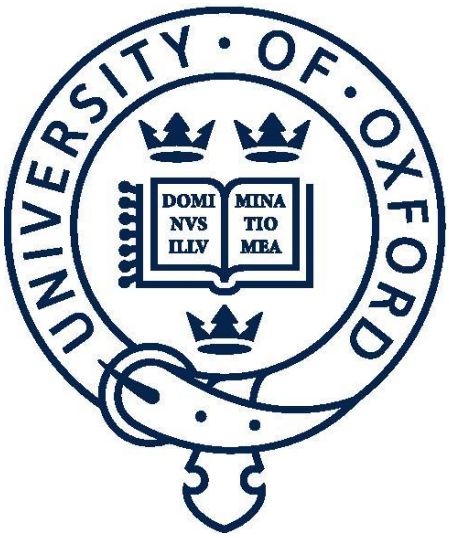

Maruthi Rochishnu N.V.L.N. Malladi

Exeter College

University of Oxford

A thesis submitted in partial fulfilment of the requirements for the degree of Doctor of Philosophy

Michaelmas Term 2021

Acknowledgements

This thesis would not have been possible without the support, advice, and inspiration of many people. I want to take this opportunity to thank the people without whom I would not have been able to complete this research endeavour.

I want to thank my supervisors, Professor Martin Davy and Professor Felix Leach, for this opportunity and the guidance to undertake this project at the University of Oxford.

I would like to express my gratitude to Engineering and Physical Sciences Research Council (EPSRC) and British Petroleum (BP) International Limited for their generous financial support.

I want to express my sincere thanks to Dr Martin Gold and Dr Richard Pearson from BP for their guidance and supervision, providing me with an industrial insight and the opportunity to present and discuss my findings.

I am grateful to Professor Richard Stone and Professor Ben Williams for their helpful advice and insights during my transfer and confirmation.

The Coriolis data collection and processing would not have been possible without the assistance of the Advanced Instrumentation Research Group (AIRG). I want to extend my special thanks to Dr Manus Henry for helping me understand the mechanics of the Coriolis and PRISM signal processing techniques and the observations made in the Coriolis data.

My thanks to Dr Joseph Camm for his help and advice regarding the gasoline rig setup and operation.

My thanks to Varun Shankar and Sam White for help with running the optical engine and the on-engine data acquisition.

Thanks to the workshop, maintenance, electronics, and IT teams at the Department of Engineering Science for helping me in designing and building components to run my experiments.

I would like to thank Professor Thomas Povey and Professor Steve Collins, my undergraduate tutors, for their advice and for inspiring me through the eight years I have spent being a student learning and researching at the University of Oxford.

I owe immeasurable thanks to Hannah Rana, Kharthik Chakravarthy and Priyav Shah – who became my closest friends – for *so many things* during the four years of this journey; including, but not limited to, being inspiring and wonderful people to share ideas and stories with, and being an infinite source of support. You helped make every day a fun and exciting experience.

I want to thank Mimi, Anya, Haengeun, Razia and all the other friends I made during my time at the University of Oxford for your support and friendship.

I am greatly indebted to my mother, Padmavathi, my father, Vidyadhar, and my sister, Maanasa, for their love, care, tolerance, and unwavering support during my academic endeavours. Finally, thank you, Sailusha, for your patience with me during the thesis writing – I am looking forward to our many future adventures together.

Abstract

Internal combustion engines (ICEs) are currently widely used in the transport sector, and there are increasingly stringent regulations on pollution from vehicles, such as carbon dioxide (CO_2), nitrogen oxides (NO_x) and particulate matter (PM). To meet these standards, efficiency improvements in ICEs are being made while limiting exhaust emissions by improving engine control, monitoring and management. Knowledge of mass injected in individual injections taken cycle-by-cycle and cylinder-by-cylinder in an engine can aid in delivering enhanced injector control for engine monitoring, performance and modelling to help achieve these efficiency improvements and limit emissions. Currently, there are no real-time and on-engine direct mass measurements of fuel flow in individual cylinders of an engine due to the lack of appropriate measurement techniques. To achieve this, in this thesis two potential solutions: pressure methods (One Pressure Transducer Method (OPTM) and Two Pressure Transducer Method (TPTM)) and direct measurement of mass flow rate using a Coriolis flowmeter (CFM) (Fast Next Generation Coriolis (FNGC)), were evaluated for future on-engine applications.

A spray rig was modified to run experiments for each of the solutions. First, the FNGC (CFM with Precise, Repeat Integral Signal Monitor (PRISM)) technique was implemented on the spray rig and used to measure injections of gasoline. Individual injections were detected, and a repeatability study was conducted on the injections. The work highlighted that the FNGC was capable of detecting features such as a negative mass flow rate at the start of injection (SOI) and partial injection detection. The tests showed the potential of FNGC for on-engine mass measurement in real-time.

The spray rig was then modified and used to conduct experiments to apply the OPTM and TPTM. Various pipeline setups were tested, and different injection detections methods were examined for finding the best technique to capture the injection in the pressure trace. Both the

OPTM and TPTM can be used to calculate the mass injected of individual injections, and the experiments showed that the pressure methods were capable of on-engine real-time injection mass measurement. At simulated engine speeds above 3500 rpm for the pipeline design implemented reflected pressure waves from the preceding injection influenced the current injection pressure measurement, this causes to the mass calculated to be significantly different to gravimetric measurement; this effect seen is a function of the pipeline design. A cursory model based on the Transmission Line Model (TLM) technique was developed to further understand and examine the impact of pressure reflections on OPTM and TPTM. The first pressure reflection after an injection was matched; however, a suitable match was not found for the consequent pressure reflections, limiting the application of the model.

Finally, the fuel pipeline was designed and deployed on an engine using the outcomes from the spray rig experiments. The OPTM and TPTM were applied to the pressure measurement data taken on the engine, and the mass injected per injection values were calculated at various engine speeds. The data confirmed no adverse impacts on the pressure methods due to engine vibrations.

Table of Contents

List of Abbreviations and Nomenclature

Abbreviations

AFR	Air Fuel Ratio
AIRG	Advanced Instrumentation Research Group
BEV	Battery Electric Vehicle
CFD	Computational Fluid Dynamics
CFM	Coriolis Flowmeter
CoV	Coefficient of Variance
DAQ	Data Acquisition
DNF	Dynamic Notch Filter
ECU	Electronic Control Unit
EGR	Exhaust Gas Recirculation
EOI	End of Injection
FNGC	Fast Next-Generation Coriolis
GDI	Gasoline Direct Injection
ID	Inside diameter
HC	Hydrocarbon
ICE	Internal Combustion Engine
LTFT	Long-Term Fuel Trim
MAF	Mass Air Flow
OBD	On-Board Diagnostics
OD	Outside Diameter
OPTM	One Pressure Transducer Method
PFI	Port Fuel Injection
PM	Particulate Matter
PRISM	Precise, Repeat Integral Signal Monitor
RST	Recursive Signal Tracker
SCR	Selective Catalytic Reduction
SI	Spark Ignition
SNF	Static Notch Filter
SNR	Signal to Noise Ratio
SOI	Start of Injection
T90	90% distillation temperature of the fuel
TPTM	Two Pressure Transducer Method
UBHC	Unburnt Hydrocarbon

Nomenclature

A	Pipe cross-sectional area
a	internal pipe radius
b	external pipe radius
c	speed of sound
c	cosine
D	Unwrapped width between the CFM sensors
d	diameter of pipe
F	Force
$\boldsymbol{F}$	Forcing vector
f	frequency
f	friction factor
fs	sampling rate
h	harmonic number
I_s	Inertia
J	Integral
K	CFM integration factor
K_s	spring constant
K_u	normal oscillation
l	Length of half tube of CFM
M	Mass of fluid
m	Characteristic frequency
$\boldsymbol{P}$	TLM pressure input
P	Fluid pressure
Q	Volume of fluid
q	phase
R	frequency ratio
R	Resistance
Re	Reynolds number
r	Radius of pipe
$\boldsymbol{S}$	Scattering matrix
s	scattering coefficients
s	sine
T	Time delay
T	Torque
t	Time
$\boldsymbol{u}$	TLM wave input
u	incident waves
u	Speed of fluid
V	Volume of chamber
$\boldsymbol{v}$	TLM wave output
v	emergent waves
x	Position in pipe
Y	Characteristic admittance

Greek

α	amplitude
Δ	step
Ω	angular frequency
κ	Bulk modulus
λ	ratio of AFR/stoichiometric
τ	shear stress
φ	phase
ν	Poisson's ratio
ρ	density
σ	stress
ω	driven frequency

Subscripts, superscripts, and accents

$diff$	difference
$down$	downstream
i	matrix coefficient
inj	injection
j	matrix coefficient
m	summation coefficient
n	summation coefficient
r	radial
$step$	step
up	upstream
w	Wall
θ	hoop
0	initial
$\bar{\ }$	space-averaged
$\langle \ \rangle$	time-average

1 Introduction

1.1 Motivation

The transport sector accounts for approximately 24% of global carbon emissions [1]. Between 1976 to 2016, the global vehicle population quadrupled [2], leading to an associated increase in air pollution. Figure 1.1 shows the percentage of cars registered in the UK by propulsion type, with nearly 97% powered by gasoline or diesel [3]. Further, the transport sector overall continues to rely almost entirely on ICEs (>99.9%) [4]. The current research priorities in internal combustion engines (ICEs) include advanced combustion technologies, improved engine control, alternative fuels to name a few. These are being developed to improve engine efficiency and limit exhaust emissions to meet the increasing tighter government guidelines on new vehicles produced [5], [6]. Environmental regulations such as EURO 6 [7] were introduced to limit pollutants, such as carbon monoxide (CO), oxides of nitrogen (NO_x) and particulate matter (PM), produced by ICEs, while regulations such as EC 443/2009 [8] were implemented to control CO_2 emissions.

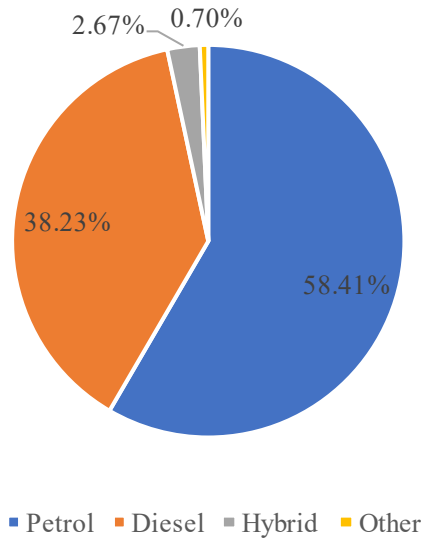

Figure 1.1: Percentages of the cars registered in the UK by fuel type. Data taken until the end of the year 2020. Data taken from [3]

While there is a drive for electrification of transport fueled by government policies such as bans on petrol and diesel cars [9], [10], the benefits of these Battery Electric Vehicles (BEVs) is less when a complete life-cycle analysis is conducted [4]. With ICEs being used more affordable and widely used than BEVs [5], improving the current generation of ICEs would be beneficial in increasing efficiency and reducing emissions, including greenhouse gases. In part, current legislative standards are met by the use of high-pressure fuel injection systems that improve fuel atomisation and enable injection strategies such as multiple injections, which optimise mixture preparation in the engine [11], [12]. Optimised mixture preparation leads to improved combustion and emissions performance. To further optimise and achieve higher efficiencies, injection strategies are required to be applied cycle by cycle for each cylinder of the engine [5]. This, therefore, requires precise knowledge of the fuel mass injected and the timing of each injection event.

There are currently no viable techniques available to measure the mass flow rate in individual injections directly, neither in real-time nor on-engine. This lack of capability is a barrier to the development of low emission and high-efficiency engines. Therefore, any development of real-time measurement capability will further the current understanding of injection events in multiple injection strategies. This data can be used to improve computational modelling tools used to study injection, mixing and combustion events in the engine.

In service, there are known to be injector ageing effects and deposit build-ups on injectors, which can reduce the amount of fuel injected into the combustion chamber. To efficiently operate the engine, global correction factors are applied to adjust the injection duration for the required mass per injection; this leads to a loss of efficiency due to the lack of individual injector control. Ferrari and co-workers [13] developed a control strategy using pressure measurement on the injector pipeline (connecting the fuel rail to the injector) to correct the fuel mass injected for a diesel engine. One manufacturer – Volkswagen – has also introduced a method to control individual injections based on fuel rail pressure measurement [14]. The method is not a direct

mass measurement method and relies on fuel rail pressure measurements to correct individual injections. However, this method still lacks information about the mass flow rate and remains a barrier to ascertaining complete information about the injection.

1.2 Objectives

This thesis aimed to design and evaluate high-speed techniques for measuring the injection mass flow rate on engines. The preferred technique will be required to measure individual injection events and determine the individual mass flow rates so as to deduce the total injected mass. Information about the injected mass will provide a further understanding of injector dynamics in engines and can be used to improve overall engine performance.

A recently developed direct mass measurement technique, Fast Next-Generation Coriolis (FNGC), and pressure to mass methods that are theoretically derived and developed by Ferrari et al. [13] have up till now only been implemented on diesel injector fuel lines and hence were implemented on a gasoline direct injection (GDI) injector spray rig. The lack of a spill line in the GDI injector fuel line required further characterisation of these methods. Further, Ferrari et al. [13] only provide a case specific application of the pressure methods; the work in this thesis conducts a complete analysis and evaluation of the pressure methods applied to a more comprehensive range of pipeline configurations and engine conditions (engine speed). Both the FNGC and the pressure methods were evaluated to understand the respective limitations for GDI on-engine application. These experiments were used to determine a suitable method for accurately calculating injected mass per injection. The chosen method was then be deployed on an optical engine for evaluation. The methods developed can be used to provide on-engine information about injections. This information will improve the understanding of injector mechanics, which can then be used to design injectors. Further, it can be used to develop new injection strategies for improved mixture preparation.

1.3 Gasoline engines

Current, state of the art, gasoline engines rely on the direct injection of fuel into the combustion chamber. GDI engines have been designed to improve the specific power output of a gasoline engine while having a higher engine efficiency compared to port fuel injected gasoline engines [15]. The motivation for their development comes from the need to comply with increasingly stringent emission requirements. The GDI engine was first implemented in a passenger car (Mercedes 300SL) in 1954 [16], [17] but was not developed further until the 1990s when the lower cost and increased access to electronics enabled GDI engine development [16].

In GDI engines, the fuel is directly injected into the combustion chamber; the liquid fuel spray evaporation cools the charge in the cylinder. This reduction in charge temperature results in an increased density of air that increases the air mass trapped in the cylinder per cycle. GDI engines, therefore, have an increased knock limit and/or lower octane rating requirements for fuels due to this charge cooling effect [18]. This effect allows for an increased compression ratio in the engine, which increases power output and reduces fuel consumption.

1.3.1 GDI engine operation

A GDI engine may be operated in the following modes: stratified, lean homogeneous, stoichiometric homogeneous and rich homogeneous. The mode of operation is dependent upon both the load and speed of the engine. Figure 1.2 shows the optimal modes and region of their operation for a MED7 GDI engine management system. Stratified charge mode, with late injection and small amounts of fuel, is used in low-load and low-speed conditions for improved fuel economy [18]–[22]. The fuel is injected late in the compression stroke, so a small region of near stoichiometric air-fuel mixture (Air Fuel Ratio (AFR) is equal to 1) is formed near the spark plug while the rest of the chamber is stoichiometrically lean ($\lambda > 1$)[15]. This, however, can cause localised rich mixtures causing an increase in soot formation [20] and requires

suitable designs of after-treatment systems for lean operation. In stratified mode, the overall air-fuel ratio may be as high as 65:1 compared to the stoichiometric ratio of 14.7:1 by mass [23]. Homogeneous modes are used for moderate to high load and speed conditions. The air-fuel mixture is formed uniformly throughout the cylinder. Although a lean homogenous mixture is the most economical fuel mixture, at high load and speed conditions, there is a reduced power output and potential overheating of the exhaust valve due to increased temperature in the cylinder caused by reduced charge cooling [15]. Ideally a stoichiometric mixture is used for high speed and load conditions, however this produces the hottest combustion products and can lead to engine overheating and knocking. A rich of stoichiometric mixture can be used to improve the power output at high speed and load conditions. The slightly rich of stoichiometric mixture can be used to ensure the engine is not overheated and reduce the potential for knocking due to the evaporative cooling of excess fuel.

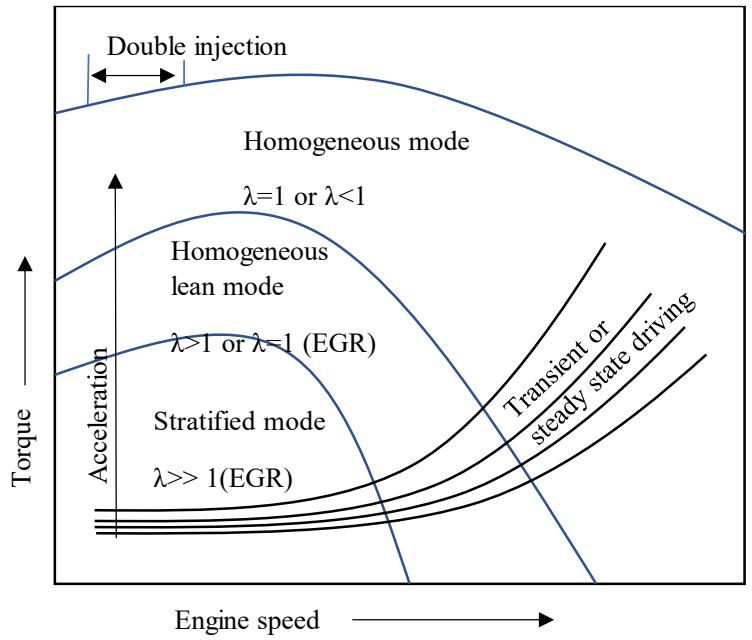

Figure 1.2: GDI engine operating modes from Motronic MED7, engine management system, adapted from [23]

GDI engine operation uses an electronic control unit (ECU). The ECU continuously monitors and controls the engine torque and speed in response to driver input. Engine monitoring uses inputs such as the throttle position, mass air flow (MAF) sensor and the lambda sensor. The

ECU uses the inputs with calibrated engine maps to determine the injection duration required for optimal Air Fuel Ratio (AFR). Any deviations of AFR for the operating point observed in the lambda sensor in the exhaust are corrected by changing the injection duration. Fuel correction in the ECU uses two types of fuel trims: the Short-Term Fuel Trim (STFT) and the Long-Term Fuel Trim (LTFT). The STFT is a dynamic correction parameter used to regulate immediate changes in demand while the engine is running and is done on a cycle to cycle basis to ensure optimal AFR. The STFT is initially used to influence the injection duration to achieve the required fuel input, and once the STFT reaches a limit set in the ECU, a long-term bias (LTFT) is introduced into the control. The LTFT is an adaptive parameter stored in the memory of the ECU, which compensates injection duration for deposit build-up and injector ageing to the original calibration [24].

1.3.2 Injectors

The most commonly used injector in GDI engines is the multi-hole injector. This optimises fuel distribution in mixture preparation for combustion; any changes of the spray pattern, spray angle, penetration distance, and droplet size distribution can negatively impact engine power output and increase emissions [25]. With the injector in the combustion chamber, there is a potential for deposit formation on the injector that can reduce the amount of fuel injected into the cylinder or alter the spray pattern further, causing increased emissions [25]. Deposits can also result in engine misfires and incomplete combustion; this is discussed further in Section 1.3.5.

1.3.3 Injection pressure

The fuel pressures of early GDI engines were in the range of 3-14 MPa [16]–[18], [23], with a common standard pressure of 10 MPa. The development of GDI systems over time has led to increased fuel pressure, with recent maximum fuel rail pressures going up to 35 MPa [14], [26]. Figure 1.3 shows the fuel pressures used in GDI engines over time. Literature shows that future

developments also aim to increase fuel pressure still further. While current production engines have a maximum fuel pressure of 35 MPa [14], [26], the effects of further increased fuel pressure up to 50 MPa have been examined on research engines [27]. Currently, injectors capable of injection pressures above 50 MPa are available in the market [28]; however, research has continued to increase injection pressures up to 200 MPa [29]. Increasing fuel pressure has been shown to improve the combustion process by improved mixture formation, caused by enhanced fuel atomisation, leading to lowered pollutant and particulate emissions due to better charge mixing [21]. The benefits of improved fuel efficiency, lower emissions are important factors in increasing fuel pressure [30], [31]. At higher pressures, faster evaporation is observed, and ignition timing can be further optimised for the best thermal efficiency [32]. Higher injection pressure also improves efficiency and lower emissions while maintaining performance in downsized engines and higher load conditions [29].

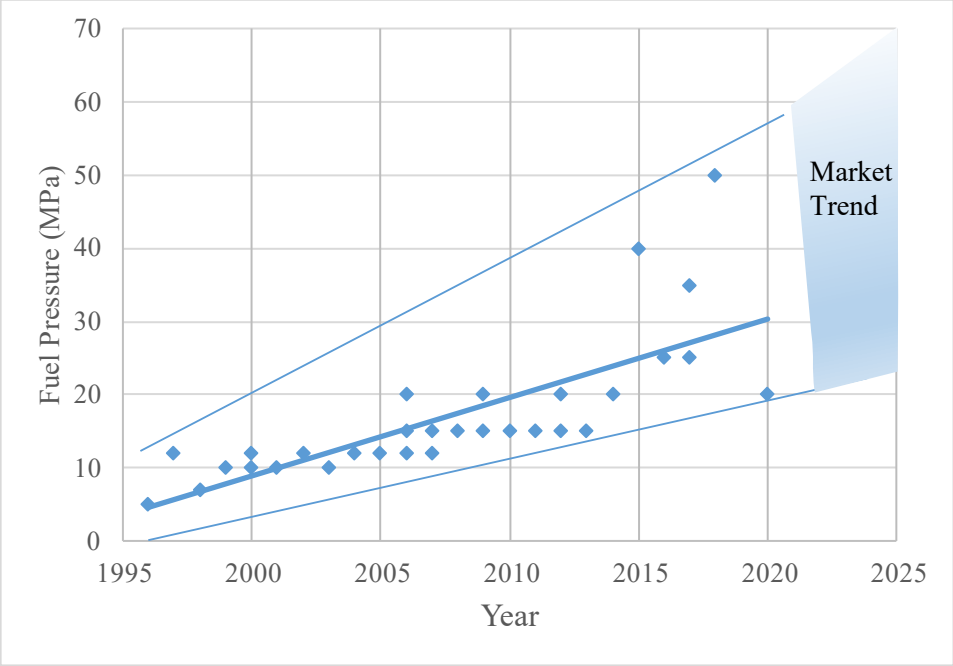

Figure 1.3: Fuel Pressure trends in GDI engines. Data taken from [15], [16]–[18], [21], [23], [27]

1.3.4 Emissions

Environmental regulations define the limits for each of the emission types found in the exhaust of an engine. In a GDI engine, the emissions observed contain unburnt hydrocarbons (UBHCs), soot and NO_x. However, when operated in a lean to stoichiometric mixture, there are low CO emissions in the exhaust [23].

The UBHC emissions observed in GDI engines are primarily due to liquid fuel impingement on cylinder walls or pistons, and the incomplete evaporation of fuel before combustion. This is a function of engine temperature, as the fuel evaporates faster at higher temperatures. In cold starts, low engine temperature impedes complete fuel evaporation [17], [23], which can lead to a rise in UBHCs. Distortion of the designed spray pattern due to injector fouling can also lead to locally rich regions, which are potential sources of UBHCs. This can be reduced by better fuel vaporisation, air-fuel mixture preparation and can be achieved with injector design to ensure there is no fuel impingement. UBHCs may also be formed in stratified operation if there are pockets of charge where the air-fuel ratio is outside the combustible limit of the fuel so that the flame front cannot propagate. In rich operation, due to excess fuel in the cylinder, UBHCs are present in the exhaust and would need after-treatment systems to minimise the amount being released at the end of the tailpipe into the atmosphere.

Particulate emissions in GDI engines arise from combustion generated products; these can be in solid form (soot, ash, carbon) or liquid form (UBHCs) [17]. If GDI mixture preparation is poor, rich areas may form, leading to the production of soot particles. These soot particles either coalesce and deposit in the cylinder or are pushed out through the exhaust. The deposited soot particles could act further as sponges, retaining fuel leading to rich flame combustion near the deposits, further increasing the problem [33].

NO_x emissions from an engine are dependent on both the load condition and the mixture preparation. The region around the spark plug and the flame front has high local temperatures

when the fuel is ignited and burned. These high temperatures lead to the formation of NO_x [23]. The formation of NO_x depends on the oxygen present after combustion and the temperature in the cylinder, with the maximum NO_x formation occurring in a mixture lean of stoichiometric.

To minimise exhaust emissions, a three-way catalyst is commonly used in gasoline engines [23]. However, this only works efficiently with stoichiometric engine operation. A new 'four-way catalytic converter' has been implemented as a solution to minimising emissions in the Volkswagen UP! [14]. It uses an additional particulate filter ahead of the conventional three-way catalytic converter, which would still require a stoichiometric operation. To reduce emissions while operating at lean compositions or stratified mode operation, more complex after treatment methods such as lean NO_x traps, exhaust gas recirculation (EGR) or Selective Catalytic Reduction (SCR) systems are needed [34]. In stoichiometric and rich compositions, the particulate emissions increase, requiring the use of particulate filters to remove them [35]. However, each after-treatment systems increase the cost of the engine and come with a fuel consumption penalty, which reduces the efficiency of the engine.

1.3.5 Injector deposits

GDI engines may suffer from a build-up of deposits on the injector [18], [25], [36], [37]. Injector deposits have been shown to reduce power output, increase fuel consumption and increase exhaust emissions [38]. Figure 1.4 shows the difference in spray pattern between clean versus coked injectors at different pressures. A longer penetration length, deformation in spray structure and a smaller spray cone are seen for the coked injectors (Figure 1.4) [39]. Figure 1.5 shows a Bosch injector with deposits used during tests at 150 bar fuel pressure. The referenced study showed that there was reduced fuel mass flow in injectors with deposits; there was also a higher droplet velocity during the injection event. The higher velocity liquid fuel can impinge on cylinder walls, which could result in higher UBHC or soot emissions [39], [40]. Early-stage injector fouling in this study increased UBHC by 30% and increased particulate matter

emissions; notably, there was a five-fold increase in PN. Higher pressure injections lowered PN emissions by at least threefold in 150 bar test when it was compared with 100 and 50 bar in a coked injection [37].

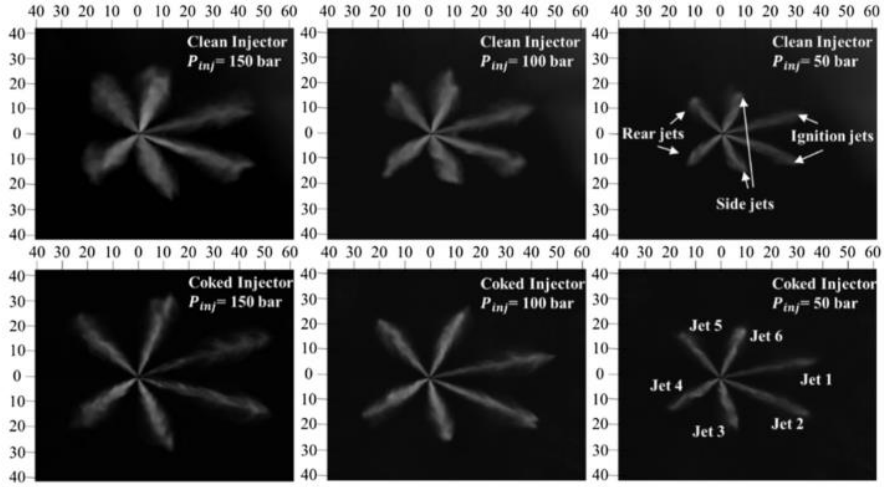

Figure 1.4: Bottom view of clean and dirty injector at EOI at different pressures [39]

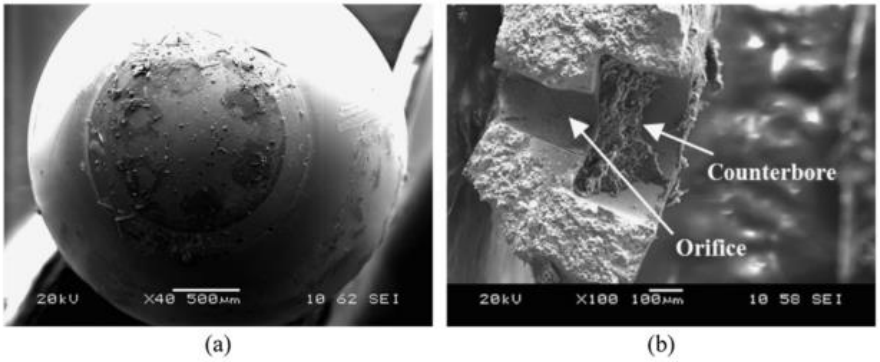

Figure 1.5: SEM picture of a coked injector (a) injector pin; (b) deposit inside nozzle and counter bore [39], [40]

Injector deposits can form in two ways [25]: low-temperature auto-oxidation and high-temperature pyrolysis, a process known as coking or carbon deposition. At low temperatures, oxidation generates alkyl radicals which form hydro-peroxides and other partially oxidised products. At higher temperatures, either the hydrocarbons decompose to their elemental forms or polymerise into larger polycyclic compounds. The high-temperature mechanism of deposit formation is commonly described using the 90% distillation temperature (T90 temperature of the fuel). Deposit precursors are mainly formed from molecules such as olefins (alkenes) and

aromatics due to their weak thermal stability. For fuel temperatures below the T90 temperature, deposit precursors are in solution, which means they cannot be deposited along the nozzle wall and are washed away. On the other hand, at temperatures above T90, the fuel evaporates and allow the precursors to agglomerate and deposit along the nozzle wall. Deposit formation increases with increasing temperature, although this relationship breaks down at much higher temperatures (above 173°C) [25], [41].

There are three aspects to be considered when trying to eliminate deposits in GDI engines: fuel detergents, injector design and the overall design of the engine. Fuel detergents have been shown to reverse deposit build-up in the injector [24], [38]. Typical fuel detergents compounds are amino amides, polyether and polybutene amines, alkyl and polybutene succinimides, and hydroxyl polyamino carbamates. The detergents attach to the surface of the injector creating a protective layer of hydrocarbons of the metal surface, preventing the deposition of precursors onto the surface [42]. Increasing injection pressures and cooled injectors have also been shown to reduce deposit build [25]. Finally, improving the in-cylinder mixing processes and reducing the number of fuel-rich regions will prevent the formation of soot particles and reduce deposit build-up. This would also improve the combustion process and reduce overall emissions.

1.3.6 Summary

Injector ageing and deposit formation influence the amount of fuel injected into the GDI combustion chamber. The amount of fuel injected and timing of the injection further influence mixture formation and, consequently, the combustion products emitted in the exhaust. It has been observed that deviations in the injection spray pattern or injected fuel mass influence the exhaust emissions [43]. Currently, a common method to correct the amount of fuel injected long term into the engine globally is by using the LTFT [24]. There is a growing requirement to improve the performance of engines along with reducing fuel consumption and emission, which further calls for individual injector monitoring as well as whole engine monitoring.

To enable individual injector control and enhance fuel injection, a fuel mass measurement device is required to apply correction factors on a cycle by cycle and cylinder by cylinder basis. On-engine measurement and management requires low flow rates, high accuracy and fast real-time measurement. This is discussed in Section 2.2.

1.4 Thesis structure

The thesis has been split into eight chapters. In the current chapter, the motivation, objectives and current state of gasoline engines are described. The gasoline engines section focuses specifically on engine operation, injectors, emissions, and injector deposits. In the next chapter, the current flow measurement techniques are discussed (Chapter 2), focusing on current fuel measurement techniques, the pressure to an injected mass method and Coriolis flowmeters. Chapter 2 also includes a description of the signal processing used in FNGC. Chapter 3 details the experimental equipment and setups used in this work. Chapter 4 describes the specific setup of the spray rig with the Coriolis meter, followed by a discussion of the experimental results. Chapter 5 focuses on pressure measurement to mass injected techniques. The different setups used are first described before the results for each are analysed. Chapter 6 focuses on the simulation of pressure data for different setups using Transmission line modelling (TLM). Finally, Chapter 7 describes the setup, followed by the results and analysis of the on-engine data of the pressure measurements techniques on an engine. The conclusions from the work undertaken are presented in Chapter 8. Each chapter begins with a short introduction of the work presented and is concluded with a summary.

2 Flow measurement

A flowmeter is generally defined as a group of components that have been used to determine the quantity or rate of fluid flow through a system. Many flow measurement techniques are used in industrial applications. The importance of choosing the correct flowmeter for the application is outlined by Baker [44]. In short, a specification is required to choose the flow measurement method to be used for the particular application. The purpose of the flowmeter plays an essential role in the specification. Considerations for the specification include the nature of the fluid, the range of operation required for the application, the required accuracy, the rate of measurement, and any losses introduced to the system due to the inclusion of the measurement device. Ideally, the flowmeter chosen should deliver accurate measurement in real-time, at the required rate and not induce losses in the system. However, this is far from reality, and it is important to reduce losses while the requirements for the application are being matched by the meter.

Baker [44] sub-divided the main types of flowmeters into three categories momentum, volume and mass measuring meters. Momentum meters measure a change in pressure or density which is used to calculate the flow rate, volume meters measure the volume flow rate by displacement or force change, and mass meters measure the mass flow rate directly. Although the mass flow rate is not directly given by the momentum and volume meters, it can be calculated from the fluid properties with some uncertainty. The amount of uncertainty would be dependent on the accuracy of the flowmeter measurement and the fluid properties used in the calculation.

A flowmeter for on-engine measurement and management will be used in a pulsating flow with low flow rates which requires the following qualities: high accuracy, fast real-time measurement, and a small size. Further, the flowmeter measurement needs to be robust to vibrational noise present in the on-engine environment. Table 2.1 outlines the required specification for on-engine mass flow measurement device. There are a few measurement

methods that are already being used in on-engine measurement applications. Probes that have the required data rate and accuracy are currently used in engines. These include pressure sensing for fuel pressure measurement and oxygen sensing using lambda sensors for measuring the AFR in the exhaust [45], however these don't measure fuel injected directly. Current fuel measurement methods are further discussed in the next section. CFMs and pressure transducers were recognised to meet the requirements for on-engine measurement, so these were chosen to be developed for injection mass flow measurement; these are described in Section 2.2 and Section 2.3.

Table 2.1: Specifications of flowmeter required for high speed flow measurement in GDI injectors

Flowmeter Property	Value
Response time	0.1 ms
Measurement resolution	1 g/s
Flow type	Pulsating flow, maximum pulse rate 60 Hz
Mass per injection	10-30 mg
Size	Compact (to fit onto an injection pipeline)
Vibration resistance	Yes

2.1 Current fuel measurement methods

Current fuel measurement methods can be separated into two categories: laboratory measurements or production on-engine measurements. Laboratory techniques are used for characterisation or measurement during the engine research, design and development process. Production on-engine methods utilise sensors to obtain global real-time measurement data for fuel injection and are currently used as part of the engine management system.

Coriolis flowmeters are already used for fuel measurements in many test cells and laboratories [46]–[48]. Fonseca et al. [49] developed two methods to measure the real-time fuel consumption of an engine using an orifice plate and MAF sensor with a wideband lambda sensor. The other common laboratory measurement technique is gravimetric. The total flow through the engine is calculated using a weighing scale with a suspended mass-spring system to measure the rate of fuel flow [47]. All of these methods measure the overall fuel consumption of the engine rather than individual injections. While these measurements are done in real-time, the instruments are typically required to be installed someway upstream of the engine and isolated from vibrations. These methods have a slow time response and read total engine fuel measurement rather than individual injection measurement.

Although production fuel injectors are extensively characterised during the engine development process, the mass flow rate through an individual in-service injector may vary from the norm due to manufacturing tolerances, ageing effects, or in-service damage or coking. Ideally, injectors should be optimised individually for best engine operation [50]. Many methods have been developed to measure fuel flow rate [51]–[56], with the Bosch and Zuech methods being the most commonly used. Bower and Foster [57] compared the two methods and concluded that both produced the same magnitude and rate shape. However, it also was concluded that while the Bosch method calculates the total mass injected, it attenuates high-frequency fluctuations seen in real injector behaviour when compared to the Zuech method [58].

The Bosch method, shown in Figure 2.1, measures the injection rate by recording the pressure wave caused due to injecting into a long measuring tube containing a compressible fluid. The pressure wave is measured by a pressure transducer near the injector mount. The size of the orifice is set to ensure that the measurement recorded by the strain gauge is not affected by a reflected pressure wave. The equation for the Bosch type rate injection is given by [51]:

$$\frac{\mathrm{d}Q}{\mathrm{d}t} = \frac{A}{c\rho}P \tag{2.1}$$

where A is the area, c is the speed of sound in the fluid, ρ is the density, P is the fluid pressure, and Q is the volume of fluid.

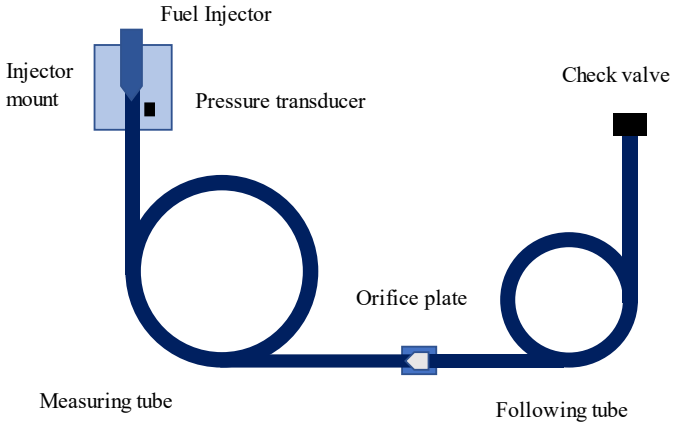

Figure 2.1: Bosch method rate metering schematic, adapted from [57]

In the Zuech method, shown in Figure 2.2, the pressure of the fluid is recorded as the injection occurs. The mass increase in the chamber increases the pressure inside the chamber. The derivative of this constant volume chamber pressure is proportional to the injection rate. Figure 2.2 shows a schematic for the Zuech method rate shape meter. The meter records both temperature and pressure using the temperature and pressure probes. The equation for the Zuech method is given by [57]:

$$\frac{\mathrm{d}M}{\mathrm{d}t} = \frac{\rho V}{\kappa}\frac{\mathrm{d}P}{\mathrm{d}t} \tag{2.2}$$

where M is the mass of fluid, ρ is the fluid density, V is the volume of the chamber, κ is the bulk modulus and, P is the pressure of the fluid in the chamber.

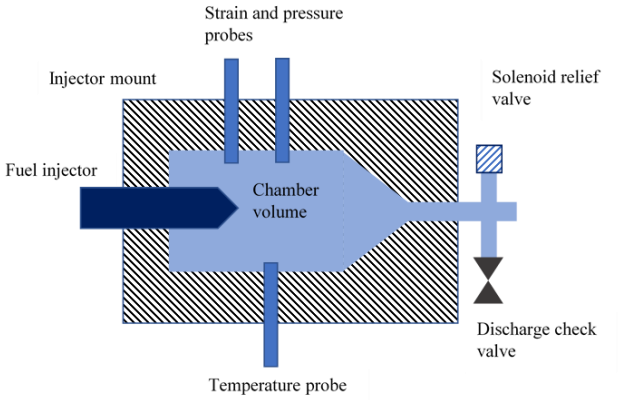

Figure 2.2: Zuech method rate shape meter schematic, adapted from [57]

2.2 Pressure to mass injected

Rail pressures have previously been used for injector diagnosis and monitoring to correct for deviations in the fuel injected [14], [59]. Ferrari et al. [13] developed a method using the pressure-time history of injector pipelines (between the fuel rail and injector) to calculate the instantaneous mass flow rate of the fuel injected using one or two pressure transducers. The instantaneous mass flow rate was used to calculate the mass injected. For small mass injections, a single pressure transducer was used for the calculation, while for larger injections, both of the pressure transducers were used. The requirement for one vs two pressure transducers for injected mass calculations is discussed in section 2.2.3.

The following sub-sections aim to derive an instantaneous mass injected estimation based on pressure traces. This will provide an estimate for mass injected per injection, which can be applied online to be able to correct the mass injected on a cycle by cycle basis. First, pressure wave theory in liquids is derived for the mass flow rate calculation from pressure-time history for a single pressure transducer method (Section 2.2.1), and this is compared with the Ferrari one-pressure method [60] (Section 2.2.3). Further, the two-pressure method described by Ferrari et al. [61], [62] is derived (Section 2.2.3).

2.2.1 Pressure waves in liquids

A pressure wave in a liquid occurs when there is a sudden change in the velocity of the fluid, for example, a sudden partial or complete closure of a pipe valve [63]. Before the valve is closed, the fluid can be assumed to be flowing with a uniform velocity through the pipe. The sudden change of velocity means the fluid near the valve pushes against the constriction causing a pressure wave (pressure increase), which is pushed to the next layer of fluid and throughout the pipeline. This pressure wave is transmitted through the whole pipeline at the speed of sound of the fluid. The kinetic energy in the fluid is transformed into elastic strain energy downstream of the pressure wave. Upstream of the wavefront, the fluid remains at its original conditions as before the partial closure, while downstream of the pressure wave, pressure, density, and the area of the pipe (however, this does not have a significant effect in metal pipelines) increase with reduced velocity. Figure 2.3(a) shows the conditions in the pipeline upstream and downstream of the pressure wave. From a stationary point of view, the wavefront (shown in red) is moving at the speed of $c - u$.

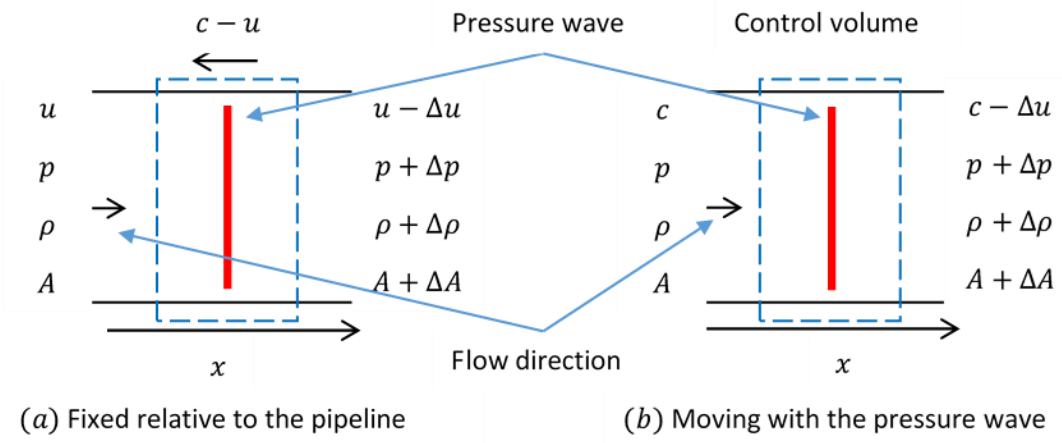

Figure 2.3: Pressure wave (pressure increase) in a pipeline caused due to partial closure in pipeline; (a) stationary frame of reference, (b) wave-front frame of reference

Converting the pressure wave into a steady control volume (shown in blue) by taking the wavefront frame of reference (Figure 2.3(b)), the mass equilibrium and momentum balance can be taken across the pressure wave.

Then, mass equilibrium is given by:

$$\dot{M} = \rho A c = (\rho + \Delta\rho)(A + \Delta A)(c - \Delta u) \tag{2.3}$$

where $\dot{M}$ is the mass flowrate, ρ is the fluid density, A is the cross-sectional area of the pipe, c is the speed of sound, and $\Delta\rho$ is the change in density, ΔA is the change in the area of the pipe and Δu is the change in the speed of the fluid caused by the pressure wave.

And the momentum balance is given by:

$$pA - (p + \Delta p)(A + \Delta A) = \dot{M}[(c - \Delta u) - c] = \rho A c \Delta u \tag{2.4}$$

where p is the original pressure in the pipeline and Δp is the change in pressure due to the partial closure of the valve at the end of the pipeline. The mass flow rate equation is given by substituting into Equation 2.3. Assuming the pipeline is relatively rigid $\Delta A/A \ll 1$ then Equation 2.4 can be simplified to:

$$\Delta p = \rho c \Delta u \tag{2.5}$$

Finally, the instantaneous mass flow rate through the pipeline across the propagating pressure wave in $x < 0$ direction is given by:

$$\dot{M} = -\rho A \Delta u = -A\frac{\Delta p}{c} \tag{2.6}$$

Substituting Δu from Equation 2.5 into Equation 2.6, the mass flow rate can be related directly to the change of pressure across the pressure wave.

2.2.2 Speed of sound in the pipeline

The change of density is directly related to the bulk modulus by the following equation [63]:

$$\frac{\Delta\rho}{\rho} = \frac{\Delta p}{K} \tag{2.7}$$

where K is the bulk modulus of the liquid.

The speed of the wavefront can be derived by substituting Equation 2.7 and Equation 2.5 into Equation 1 and rearranging:

$$\rho c^2 = \frac{\Delta p\left(1+\frac{\Delta A}{A}\right)\left(1+\frac{\Delta p}{K}\right)}{\frac{\Delta p}{K}\left(1+\frac{\Delta A}{A}\right)+\frac{\Delta A}{A}} \tag{2.8}$$

Considering $\Delta A/A \ll 1$ and $\Delta p/K \ll 1$ (incompressible fluid) then the equation can be further simplified, and the speed of the pressure wave is:

$$c = \sqrt{\frac{\Delta p}{\frac{\Delta p}{K}+\frac{\Delta A}{A}}} \tag{2.9}$$

For a perfectly rigid pipe $\frac{\Delta A}{A} = 0$. However, for a thick-walled pipe, the change in areas is given by:

$$\frac{\Delta A}{A} = \frac{\pi(a+\Delta a)^2}{\pi r^2} \approx \frac{2\Delta a}{a} \tag{2.10}$$

where a is the internal pipe radius, and Δa is the change in pipe radius due to increased pressure. For a thick-walled pipe with internal stress, only the hoop stress σ_θ and the radial stress σ_r at the internal radius a are given by the following equations [64]:

$$\sigma_\theta = \frac{\Delta p a^2}{b^2-a^2}\left(1+\frac{b^2}{a^2}\right) \tag{2.11}$$

$$\sigma_r = \frac{\Delta p a^2}{b^2-a^2}\left(1-\frac{b^2}{a^2}\right) \tag{2.12}$$

where a is the internal pipe radius, and b is the external pipe radius. In a plane stress condition, the axial stress is zero as $\sigma_z = 0$. Then, in these boundary conditions, the following equation can be used to calculate the change in radius:

$$\Delta a = \frac{a}{E}\frac{\Delta p a^2}{b^2 - a^2}\left(\left(1 + \frac{b^2}{a^2}\right) - \nu\left(1 - \frac{b^2}{a^2}\right)\right) \tag{2.13}$$

where E is Young's modulus of the pipe material, and ν is the Poisson's ratio of pipe material.

2.2.3 Ferrari pressure method

The velocity and pressure time history in the pipeline requires two locations of measurement as boundary conditions [60]. In cases where the pressure wave is travelling in a single direction, a single location can be used to find out the flow rate history. The derivation for the one pressure transducer method (OPTM) described by Ferrari et al. [60] is similar to the Bosch method and the same as the pressure wave derivation shown above in Section 2.2.1.

The requirement of the two pressure transducer method (TPTM) arises when the injection duration increases and there are reflected pressure waves within the injection duration due to limitations of the pipe length between the fuel rail and the injector [60]. The pressure waves then do not have a single direction of travel nor a definite speed due to the reflections, and hence, the single transducer to the injected mass calculation cannot be used. This would require pressure measurements at two locations to calculate the instantaneous mass flow rate. The two pressure transducers are placed distance l apart at x_{up} and x_{down} as shown in Figure 2.4. The distance between the two sensors to provide a high-quality measurement should be in the range of $5ct$ to $7ct$, where t is the defined as the reciprocal of the frequency of acquisition [61], [62]. The direction of flow is shown by the arrow in the pipeline (Figure 2.4). Taking the mass conservation (Equation 2.14) and momentum (Equation 2.15) for a slender pipe [61]:

$$\frac{d\rho}{dt} + \rho\frac{\partial u}{\partial x} = 0 \tag{2.14}$$

$$\frac{\partial u}{\partial t} + u\frac{\partial u}{\partial x} + \frac{1}{\rho}\frac{\partial p}{\partial x} = -\frac{4\tau_w}{\rho d} \tag{2.15}$$

where u is the velocity in the pipeline, t is time, x is the coordinate along the pipe, ρ is the density of the liquid, p is the pressure of the liquid, and τ_w is the pipe wall shear stress.

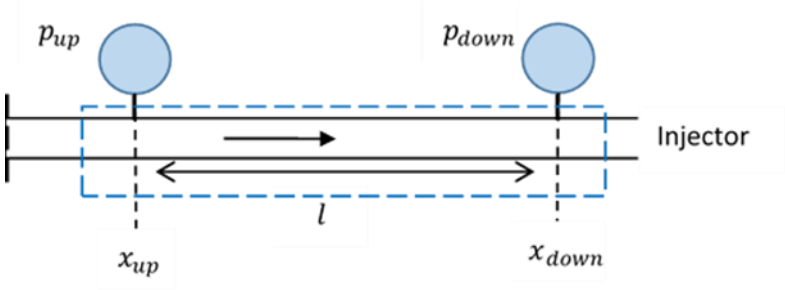

Figure 2.4: Two-pressure transducers installation

Ferrari et al. [61] assume the liquid is locally incompressible, $d\rho/dt \approx 0$ and $\partial\rho/\partial x \approx 0$. Hence, only mean pressure variations influence the density and pressure fluctuations near the mean pressure are disregarded. This assumption holds when the fluid velocity is much lower than the speed of sound of the fluid. From this assumption, the continuity equation (Equation 2.14) simplifies to $\partial u/\partial x \approx 0$ and the momentum equation (Equation 2.15) reduces to:

$$\frac{\partial u}{\partial t} + \frac{1}{\rho}\frac{\partial p}{\partial x} = -\frac{4\tau_w}{\rho d} \tag{2.16}$$

Multiplying Equation 2.16 by ρA and integrating over the length, l, between the pressure transducers in the control volume and dividing the same length, the equation can be rearranged to obtain:

$$\frac{d\dot{m}}{dt} = \frac{A}{l}p_{diff} - \pi d\bar{\tau}_w \tag{2.17}$$

where $p_{diff} = p_{up} - p_{down}$. Further, space averaged terms ($\dot{m}, \bar{\tau}_w$) are a consequence of the continuity approximation taken above.

Substituting the Darcy-Weisbach formula [65] for steady-state wall friction, the wall shear stress can be written as:

$$\bar{\tau}_w \approx \frac{\bar{f}}{8\rho A^2}|\dot{\bar{m}}|\dot{\bar{m}} \tag{2.18}$$

In unsteady flow, the time-averaged steady-state friction is taken along with a frequency-based friction component. However, this component is small and so ignored to simplify the calculation. This simplification reduces Equation 2.17 to the following:

$$\frac{d\dot{\bar{m}}}{dt} = \frac{A}{l}p_{diff} - \pi d\frac{\langle\bar{f}\rangle}{8\rho A^2}\langle\dot{\bar{m}}\rangle|\langle\dot{\bar{m}}\rangle| \tag{2.19}$$

Integrating Equation 2.19 over time:

$$\dot{\bar{m}}(t) = \frac{A}{l}\int_0^t p_{diff}\,dt - \pi d\frac{\langle\bar{f}\rangle}{8\rho A^2}\langle\dot{\bar{m}}\rangle|\langle\dot{\bar{m}}\rangle|\,t \tag{2.20}$$

The mass flow rate calculation relies upon the ability to calculate the friction factor, which is dependent on the time-averaged mass flow rate. To be able to approximate the friction value, the integral is done over a complete working cycle (injection period) with the assumption of ideally periodic flow. Then the friction term is given by:

$$\frac{A}{l}\langle p_{diff}\rangle = \pi d\frac{\langle\bar{f}\rangle}{8\rho A^2}\langle\dot{\bar{m}}\rangle|\langle\dot{\bar{m}}\rangle| \tag{2.21}$$

The flow is not ideally periodic as there is an injected mass in the cycle. However, if an injection train (multiple injections in series) is considered, then the flow is periodic with the same injected mass for each injection cycle. The approximation provides an estimate for the friction term for overall cycle flow loss. The time-averaged pressure difference is non-zero due to the injected mass, and this term is equated to the overall friction due to the mass flow rate. This substitution enables the calculation of the mass flow rate with the use of pressure data directly rather than an iterative process required to calculate both the friction factor and the mass flow rate.

2.3 Coriolis Flow Meter

The inertial force or “Coriolis force” was first observed and reported by the French scientist Gustave-Gaspard Coriolis in 1835 [66]. A modern Coriolis flowmeter utilises a pair of vibrating tubes to calculate the mass flow rate by measuring the phase difference between two points due to the flow, using velocity transducers. From the first Coriolis meters, major developments were made to digitise and improve the accuracy of the meter in liquid, gas and two-phase flows [67], [68].

Coriolis flowmeters are generally operated in a beam mode. This assumes the tubes as beams and are both vibrating at the resonant frequency in a bending mechanism. This is the most common type of Coriolis meter, and there is normally only a single mode of vibration. The fluid flow through the tubes causes a phase delay between the velocity transducers (sensors) of the Coriolis meter, which is proportional to the mass flow rate. This sensor operates on a principle of a moving magnet, where the output voltage is proportional to the velocity of the magnet.

Baker [44], [67] explains the Coriolis flowmeter measurement technique and provides a simple physical and mathematical theory for understanding. Commonly, U-tube flowmeters have two U-bend tubes which the flow is split into at entry. Taking one of the tubes of a U-tube flowmeter, assuming the flow is split equally, the forces will be half of the total force. In the tube, the fluid moves outwards in one half of the tube (Figure 2.5). Consider a small fluid element that is moving outwards in an upward moving tube; the angular momentum of the fluid is increased as it moves away from the hinge and has an increased lateral velocity. This change in angular momentum creates a force upwards on the fluid from the tube, which in turn creates an opposite downward force on the tube from the fluid. A similar argument can be made for the fluid coming back towards the hinge in the other half of the tube, which creates a force downwards on the fluid from the tube due to reducing momentum and an equal upwards force on the tube from the fluid. The Coriolis acceleration created from the fluid flow is measured as

a phase difference at the sensors. The flowmeter operates in vibration, which is produced by drivers on the flowtube, rather than pure rotation creating alternating forces. As the tube rises, the forces and the twist are maximum in the mid-plane of the vibrations and zero in maximal points from the mid-plane. The flowtube vibrates symmetrically, with no twist when there is no flow and the transit time is zero. The twist from the forces causes a delay in the transit time of the tube (phase difference), which is measured by sensors on the tube. As fluid flow increases, the forces in the tubes are greater, and the twist observed increases. This transit time (twist) is measured, which then is directly proportional to the mass flow through the tube.

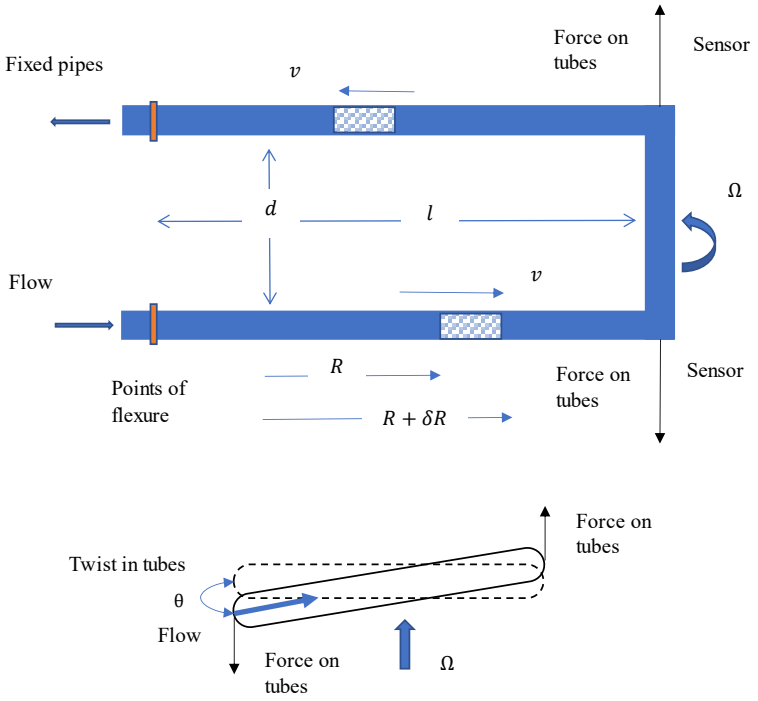

Figure 2.5: U-tube Coriolis meter motion and forces. Adapted from [44], [67]

Taking a more mathematical approach to understanding the analysis [44], [67]. If the flow velocity is v and the angular velocity caused by the vibration is Ω. Then a small element of mass δM at radius R will have a lateral (tangential) velocity of $R\Omega$. An increase of radius by δR, then increases the lateral velocity to $(R+\delta R)\Omega$ (Figure 2.5). This increase in angular momentum due to the liquid flowing is $2R\delta R\delta M\Omega$, assuming the δR^2 term is negligible, the fluid mass would take $\delta R/v$ seconds to move across δR causing the pipe to experience a force:

$$\mathrm{d}F = 2\Omega v \delta M \tag{2.22}$$

The other half of the tube will experience the same but opposite force. The mass of the fluid is $\delta M = \rho A \delta R'$, where $\delta R'$ is the length of the tube which is used to calculate the mass of fluid. Then the torque on the flowtube tube is:

$$T = 2K\Omega \rho A v d l \tag{2.23}$$

where, d is the unwrapped width of the U-tube (between the sensors), and l is the length of each half of the tube. K is the integration factor that allows for the distortion due to Coriolis forces not forming a straight integration. This multiplier considers the material properties of the fluid and physical properties of the flowtube. The flow rate in the tube is as $\dot{M} = \rho A v$ by continuity. Then the torque is related to flowrate by:

$$\dot{M} = \frac{T}{2K\Omega d l} \tag{2.24}$$

Considering the tube is in an oscillating motion, the following substitution for angular velocity can be made: $\Omega = \Omega_o \cos\omega t$ where ω is the driving frequency, and t is the time. This can be substituted into Equation 2.23.

For a U-tube configuration, ignoring any damping effects, the torque can be related to the twist, θ, due to Coriolis acceleration in the tube by the general equation of motion:

$$I_s \frac{d^2\theta}{dt^2} + K_s \theta = T \tag{2.25}$$

where, $I_s$is the inertia and K_s is the spring constant of the tube in oscillation.

Assuming a solution of the form $\theta = \theta_o \cos\omega t$. Then from Equation 2.23 and Equation 2.25 and the substitution for Ω in T, we can obtain the following expression:

$$\theta_o = \frac{2K\Omega_0 \dot{M} d l}{K_s - I_s \omega^2} \tag{2.26}$$

where θ and Ω are in phase. This matches with the twist being maximum at the mid-plane and zero in the maxima. The frequency of free vibration is given by $\omega_s = (K_s/I_s)^{\frac{1}{2}}$.

The time of transit (phase difference) between the two sensors:

$$\tau = \frac{\theta_0 d}{\Omega_0 l} \tag{2.27}$$

where, $\Omega_0 l$ is the velocity of the sensor and $\theta_0 d$ is the displacement due to twist. Then the mass flow in terms of the transit time is:

$$\dot{M} = \frac{K_s \tau (1 - \omega^2/\omega_s^2)}{2Kd^2} \tag{2.28}$$

A similar equation can be derived for oscillation without flow. This can be used to find the natural frequency of the U-tube, given by [44], [67]:

$$\omega_u = (K_u/I_u)^{1/2} \tag{2.29}$$

where, K_u is the spring constant in normal oscillation and I_u is the inertia in the plane. The inertia is proportional to the mass and, this is related to the density of the fluid. This natural frequency can be used to find the fluid density.

The analysis above suggests, the higher the fluid flow, the greater the twist observed in the system (Equation 2.27). The twist is measured using the velocity sensors from which the mass flow rate can be calculated using Equation 2.29. In most flowmeters, the two tubes oscillate in anti-phase at zero flow.

Over the years, there have been other theories developed on the operating principles of the Coriolis flowmeter. Some of these include: a weight vector theory for simple configurations [69] and using beam element methods to predict the Coriolis effect on the meter [70]. These theoretical developments were further reviewed in [44], [68].

Coriolis meters have many attractive features: they are accurate (most present-day Coriolis mass flowmeters have a 0.1% uncertainty or less at full scale and a turndown ratio – the ratio of maximum flow rate to minimum flow rate that can be measured – of up to 100:1), they can be used in bidirectional flows (as the measurement can be achieved by looking at the phase difference), they are compact and have low maintenance requirements. Furthermore, the Coriolis meter is a multi-parameter measurement device as it measures mass flow rate, density and temperature (with a thermocouple). On the negative side, secondary containment is required to make the device safe at high temperatures and pressures, the maintenance process when required is complex if the tubes are clogged or need to be replaced, and for specialised applications, the device might have a very high initial cost and require calibration for certain fluids that have a substantially different fluid density from the calibration fluid. Coriolis meters also require a separate power supply for the drivers and sensors and a computer for processing the data – all adding to the initial and running costs.

Different external factors which influence Coriolis meter calibration, and hence the measured mass flow reading, have been reported in the literature. Cheesewright et al. [71] concluded that the Coriolis frequency of the meter and the frequencies which indirectly excites the Coriolis frequency affect the calibration and measurement—where the drive frequency of the meter is defined as the frequency at which the tubes are excited using drivers, while the Coriolis frequency is defined as the resonant frequency corresponding to the shifted (full flow) mode shape [72].

Methods, such as filtering techniques to improve noise suppression [73] and integrated active vibration isolation using a secondary driver [74], have been developed to improve the performance of the Coriolis meter in response to frame noise and other external vibrations—likely significant factors for an on-engine application. Recently, a novel, Oxford-patented signal processing method called precise, repeat integer signal monitor (PRISM) was used with a CFM. The PRISM processing method is discussed further in Section 2.4.1. A feasibility study

using the combined PRISM/CFM technique, together known as Fast Next Generation Coriolis (FNGC), reported tracking diesel injections up to simulated engine speeds of 4000 rpm, with injection durations of 4 ms at a pressure of 100 MPa [75], [76]. The technique successfully detected individual injection pulses in a pulse train. However, it was found that injections were extended in time (due to the flowtube acting as a mechanical filter and filtering due to the driving frequency in the signal processing scheme) and, accordingly, the FNGC technique 'as is' significantly over-predicts the injected fuel mass inferred from the injection duration. It has been suggested that using a higher frequency flowtube would improve the time response and hence, the mass measurement of the fuel-injected [75], [76].

2.4 Signal processing

Signal processing is the modelling and analysis of data representations of physical events [77]. Electronic sensors are required to collect, process and communicate the measured data for devices to function. In the case of the Coriolis meter, the sensor data is required to be processed to calculate the required input for the drivers and the flow properties of the fluid.

With an increasing ability to take measurements at high speeds, fast and efficient online signal processing methods assume ever-increasing significance. The storage of large amounts of data taken at high speeds is both expensive and time-consuming. Real-time processing can reduce these storage requirements and enable better control of devices. However, the cost and resource requirements for online data processing are often prohibitive. In the case of a Coriolis meter applied to measure fuel flow on engines, high-frequency data acquisition is required, and this data needs to be processed in real-time with minimal delay and relatively low computational power.

Many signal processing methods have been developed to be used with Coriolis meters. Techniques including Fourier transform, Digital Phase-Locked Loop, Digital Correlation, Adaptive Notch Filter, and the Hilbert transform have all been used [78]; however, these

methods are not suitable for batched measurement where the batch length is shorter than the drive period of the Coriolis meter. Typical update rates range from 10 to 100 Hz, whereas update rates in the kHz range would be required for fuel measurement. For this challenging application, PRISM is recognised to have the capabilities required [79]. The PRISM method is further described below.

2.4.1 PRISM signal processing

The PRISM signal processing method is a finite impulse response (FIR) method which can be used to track and filter sinusoid signals. In the FNGC technique the PRISM is implemented to add low pass and notch filters with a signal tracker to the CFM output signals from the velocity sensors. These signal can then be used to find the phase difference between the sensors and hence the mass flow rate as discussed in Section 2.3.

PRISM uses a double Fourier type integration, which has six individual integration blocks to calculate two output time series (Figure 2.6). The inputs are taken in at a sampling rate fs and outputs at the same rate are generated. The inputs are multiplied by the modulation function hm (h is the harmonic number and m is the characteristic frequency), and this product is stored and is integrated over a window of $1/m$ s. The PRISM can be taken as a pair of FIR filters in series for a data window with a total duration of $2/m$ s (one per each Fourier type integral). The output is computed after every new input value from each integral. The computation burden is small for each calculation, as only one multiply and one accumulate operation is used in the filter. The filter time required per sample remains the same even when the sample rate increases compared to non-recursive FIR filters [80], making it attractive to be used in high-frequency data filtering.

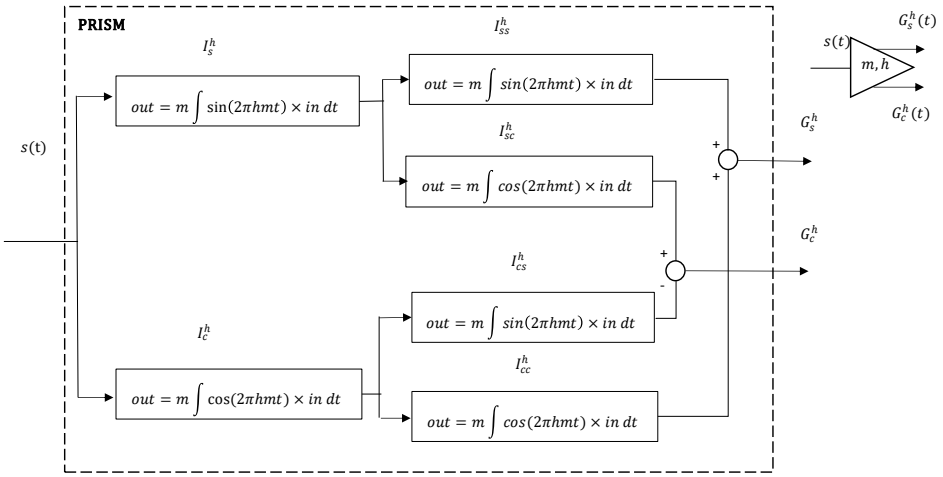

Figure 2.6: PRISM Structure and symbol used for PRISM structure, adapted from [80]

Mathematically, the PRISM integration can be represented by the equation below:

$$I^h_{[S|C][S|C]} = m^2 \int_{-\frac{1}{m}}^{0} [\sin|\cos](2\pi\ hmt + q) \left(\int_{t-\frac{1}{m}}^{t} [\sin|\cos]\,(2\pi\ hmt + q).\, s(t) dt \right) dt \quad (2.30)$$

where the $[s|c]$ the subscript notation is for the selection of sine and cosine modulation functions. The superscript h is the harmonic number, which is a small positive integer giving the number of modulation function periods ($1/hm$ s) within an integration period $1/m$ s. For PRISM implementation fs/m (the number of samples) need to be a whole number while q is an arbitrary initial phase. Finally, taking $s(t)$ as a sinusoidal input:

$$s(t) = \alpha \sin(2\pi f t + \varphi_i) \quad (2.31)$$

Then the integrals can be combined to make the following analytical expressions [80]:

$$G_s^h(t) = I_{ss}^h + I_{cc}^h = \alpha\ \mathrm{sinc}^2(r) \frac{r^2}{r^2 - h^2} \sin(\varphi(t) - 2\pi r) \quad (2.32)$$

$$G_c^h(t) = I_{cs}^h - I_{sc}^h = \alpha\ \mathrm{sinc}(r) \frac{rh}{r^2 - h^2} \cos(\varphi(t) - 2\pi r) \quad (2.33)$$

where the instantaneous phase $\varphi(t) = 2\pi ft + \varphi_i$ and $r = f/m$ the frequency ratio. The two analytical expressions form orthogonal pairs with the same linear phase delay. From inspection, Equations 2.32 and 2.33 are true irrespective of the initial phase q of the modulation function. This makes it possible to evaluate each integral as a 'sliding window', in which the oldest value is replaced by the newest value and the data window integral value is updated with an accumulation calculation for every input [80].

The gain of the functions, shown in Figure 2.7, can be calculated by removing the sine and cosine terms from the analytical functions (Equations 2.32 and 2.33). The gains are negative below m Hz and positive after, with notches at m and its multiples including DC.

The only requirement for the PRISM signal processing designs are knowledge of the frequency and bandwidth of the measured signal [79], and then the filters can be designed in real-time [81], making this filtering technique suitable for a wide range of applications. The PRISM technique has previously been used with the CFM to measure the mass flow in a diesel injector [75], [76]. In these cited works, the sensor data was read at a rate of 48 kHz, and the PRISM method was used to perform signal tracking, online notch filtering and low pass filtering required for instantaneous mass flow rate measurements from the CFM. The signal tracking is achieved using Recursive Signal Tracker (RST), which is described fully in [75]. The notch filtering is achieved either by Static Notch Filtering (SNF) or Dynamic Notch Filtering (DNF). SNF is accomplished by placing a PRISM in the signal path with parameters m and h; this acts as a static notch filter on the input signal with notches at all multiples of m HZ. Each PRISM added to the signal path add a delay of $2/m$ seconds to the signal. While DNF uses one or more PRISM in parallel to create more notches without losing further dynamic response in the signal. The DNF algorithm is described in detail in [82], [83].

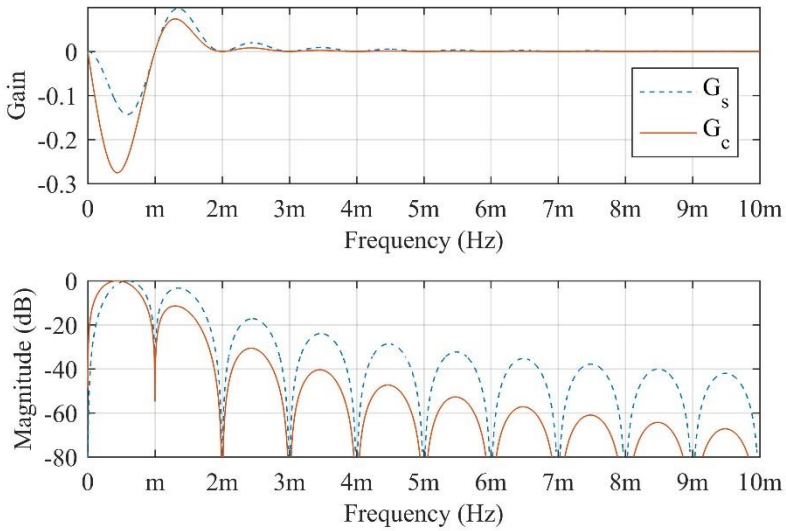

Figure 2.7: Gains of PRISM at different frequencies for analytical functions

2.5 Summary

In the current chapter, the specification for the flow measurement device was set out before current fuel measurement techniques were reviewed. Most current techniques rely on being isolated and upstream of the engine or off-engine analysis on the injector. Current injection correction methods do not have individual injected mass corrected based on mass flow rate measurements in GDI engines. This is a barrier to the further development of higher efficiency engines. OPTM, TPTM and FNGC (CFM with Prism signal processing) were recognised to provide these measurement capabilities. An initial feasibility study on diesel injectors using FNGC was conducted previously [75], [76]. This study has shown both the potential and the limitations of this technology. The technology is to be tested GDI spray rig for viability and further investigation of the limitations to determine the improvements required in this method. The OPTM and TPTM will also be developed and tested on a GDI spray rig to determine the constraints of the methods on mass flow rate calculation. The two methods were then compared to determine the best method for implementation on-engine. The next chapter describes the details of the experimental equipment used in the tests conducted.

3 Experimental equipment

3.1 Oxford spray rig

The Oxford spray rig [84] was originally designed and built for gasoline fuel spray imaging experiments as a bench-top GDI injector-based rig. The rig provided improved optical access. The spray chamber was designed to be used with a fused quartz optical liner with an inner diameter of 89 mm and outer diameter of 117 mm. The fuel is sprayed into the chamber at room temperature and atmospheric pressure. The injector could be operated continuously to inject at engine frequencies with continuous purging of fuel vapour. The chamber has four slot holes on the top of the chamber to form the air inlet. The fuel injector is vertically mounted with the air-fuel mixture extraction at the bottom of the spray rig. Figure 3.1 shows the 3D model of the spray chamber with the supporting pillars. Further details of the geometry of the spray rig are discussed in [84].

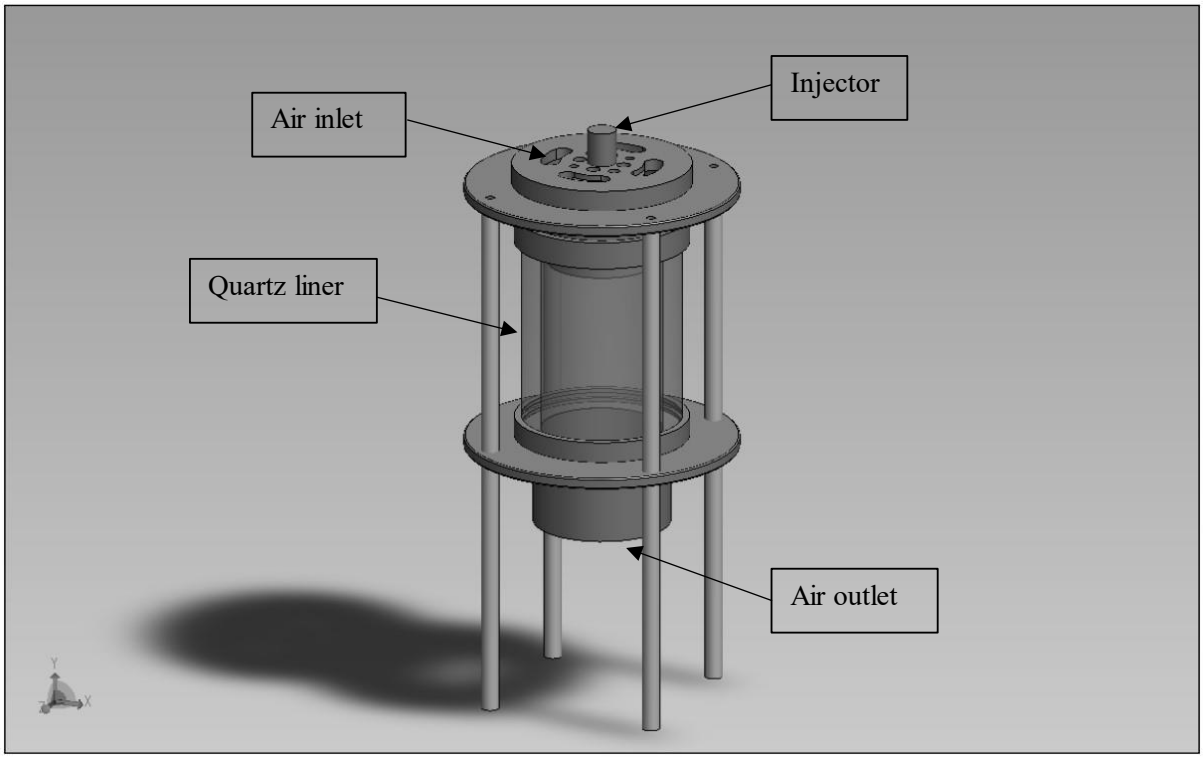

Figure 3.1: Spray chamber model in 3D with supporting pillars. Adapted from [84]

Modified versions of the Oxford spray rig [84] were built to check the feasibility and understand the limitations of fuel measurement techniques. The mass injected measurements are required to evaluate the measurement techniques. The optical liner from the original setup was removed, and an aluminium enclosure with a removable side was installed around the spray chamber. This gives access to include a glass jar for weighing the injected fuel mass while ensuring any vapours that are not caught in the jar do not escape the spray chamber and are sucked into the exhaust. Figure 3.2 shows the installed aluminium enclosure and the glass jar in the spray rig. A fuel pipeline is connected between the injector and pressure pump. This includes the flow measurement devices (described in more detail in sections 3.1.4 and 3.1.5). The equipment used in the experiments is described below. Further, the details of the modifications made to the spray rig and the exact setups are described in individual measurement technique chapters.

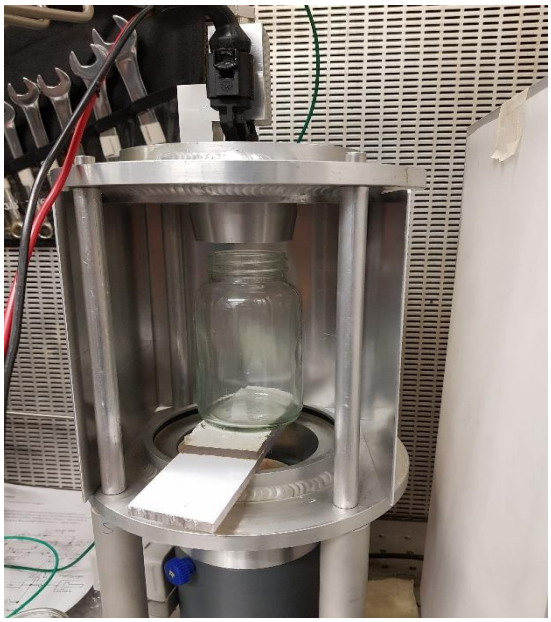

Figure 3.2: Aluminium enclosure around the spray chamber with access to glass jar to measure the mass of injected fuel.

3.1.1 Pressure accumulator

Initially, the fuel pressure accumulator designed for the spray rig was used to pressurise the fuel [84]. The injection pressure used in this work is 150 bar, with the maximum operating fuel pressure of the pressure accumulator being 350 bar. The design used a piston arrangement to magnify the fuel pressure statically using pressurised air or nitrogen. The ratio of air and fuel side areas is used to achieve a pressure ratio of 1:61.6 between the air and fuel side. Pressurised nitrogen from a gas bottle was used in the experiments. Figure 3.3 shows a simplified schematic of the pressure accumulator. A regulator is attached to the air side to control the inlet air pressure. To measure the fuel pressure, a pressure transducer, P0, was fitted on the fuel side; details of the pressure transducer are given in section 3.1.5. As the fuel is injected, the piston travels upwards to maintain fuel pressure. Once the piston reaches the top of its travel (at the top of the pump's air side), the accumulator is effectively empty and needs to be refilled. The procedure of use and complete specification of the pressure accumulator is described in [84]. The pressure accumulator holds approximately 25 cm^3 of fuel, limiting the number of injections before the accumulator is empty. This is a problem when the setup is to be installed for on-engine measurement, and a fuel pump is required for any further experiments.

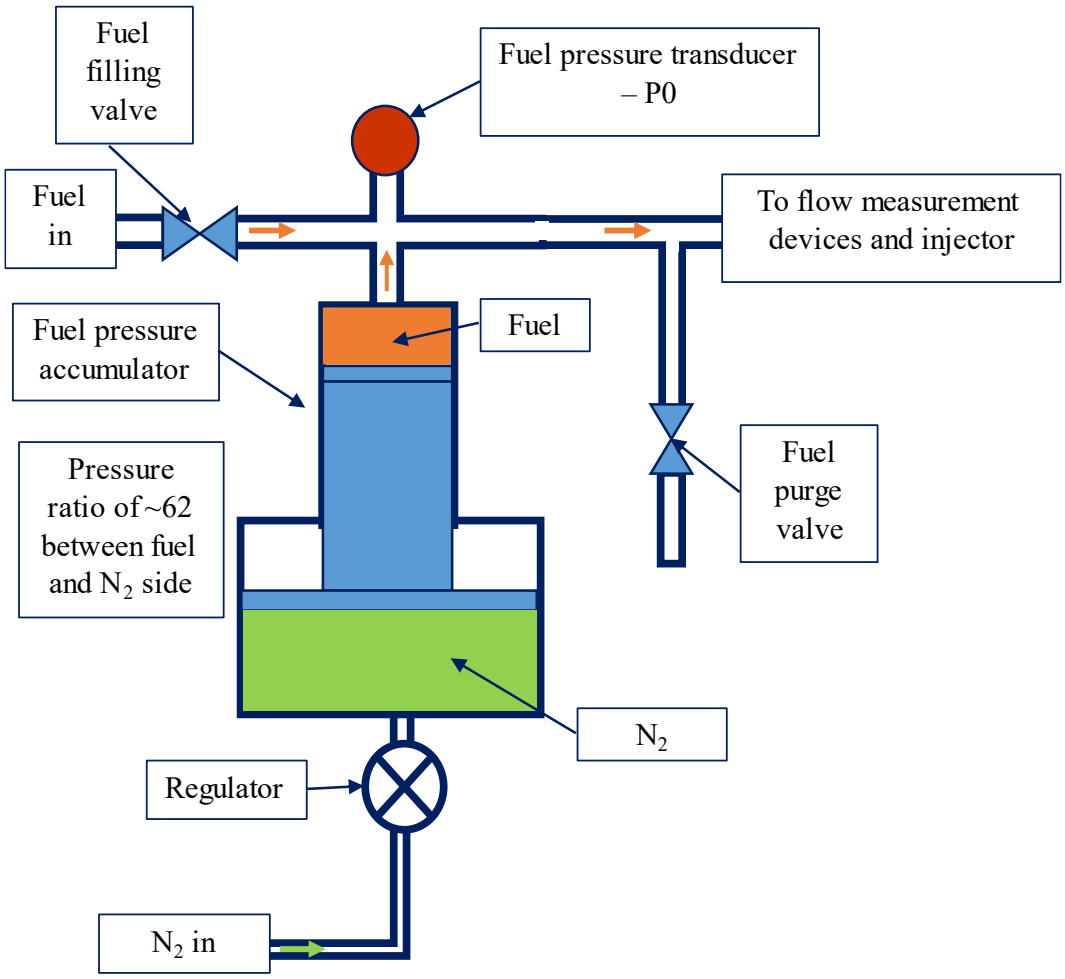

Figure 3.3: Simplified schematic of the fuel accumulator. The fuel pipework including the fuel fill side and fuel purge is shown above. The pipeline continues to the flow measurement devices attached which is connected to the injector. A regulator is attached on the N_2 side to control the fuel pressure. Not to scale.

3.1.2 Fuel pump

An air-driven pump (HEYPAC KR20 [85]), which can also be used on an engine, was added to the system to replace the pressure accumulator in the pressure measurement experiments. The fuel pump has a pressure ratio of 1:20 between the air and fuel sides with a maximum fuel pressure of 170 bar.

The HEYPAC pump is a double-acting pump where the compressed gas (nitrogen) is applied on each side of the piston one after the other. This delivers flow on both the upstroke and downstroke of the pump mechanism. The air-side piston is connected to a smaller diameter fuel side piston. Like the fuel accumulator, the ratio of diameters between air and the fuel side is the

pump's intensification ratio. A set of valves inside the pump control the reciprocating pump action to ensure the pump delivers the fuel at the required pressure. The pump has zero energy and air consumption (assuming no leaks) when the pump has no demand and cycles automatically based on the demand. The pump speed increases with increasing flow rates. The pump has the highest flow rate at low pressure and reduces as the pressure increases. The fuel pump has a maximum pressure fuel of 170 bar and a maximum flow rate of 2.5 L/min [86]. For the fuel injection experiments, the flowrate is much smaller than the maximum, and hence this pump can be used in the setup. To measure the fuel pressure, the same pressure transducer (P0) (as on the pressure accumulator) was installed on the pipeline near the pump's fuel outlet.

3.1.3 Fuel injectors

Two GDI fuel injectors were used during the experiments. Table 3.2 below shows the specifications of the two injectors. The first injector used is a multi-hole production Bosch injector (HDEV-5-1LE). It is a 6-hole injector with a maximum injection pressure of 150 bar [84]. The majority of the experiments were conducted with HDEV-5-1LE. The injector was either driven by a BOSCH ECU or National Instruments (NI) Direct Injector Driver System (DIDS) through NI LabVIEW software which was used to control the injection duration and injection period.

Table 3.2: Specifications of injectors used in the experiments

Injector number	Type	Maximum fuel pressure (bar)	Injector holes
1	BOSCH HDEV 5.1	150 [84]	6
2	BOSCH HDEV 1.2	200 [87]	1

The second injector used is a single hole swirl-type injector BOSCH HDEV1.2 injector. This injector has been previously used for experiments of injection pressure of 100 bar [88]. However, the maximum pressure for the injector is 200 bar [87]. The injector was driven using

an NI DIDS system through NI LabVIEW software which was used to control the injection duration and injection period.

3.1.4 Coriolis flowmeter

The RHM015 from Rheonik GmBH was the Coriolis meter used in the experiments. It has a drive mode frequency of approximately 150 Hz. The flowmeter has omega-shaped tubes with a torsion rod to generate the oscillatory movement [89]. The flowmeter uses a torsional oscillation. The torsion rods twist, causing the two flow conduits to oscillate. Figure 3.4(a) shows the structure of the flowtube with its components. The flow tubes oscillate exactly 180° out of phase when there is no flow. With flow, the force from the fluid creates a deflection from zero flow oscillation which is seen as a phase difference in the two signals. Figure 3.4(b) shows the waveforms from the sensor signals in a flow and no-flow case [90]. The phase difference is directly proportional to the mass flow rate through the tube.

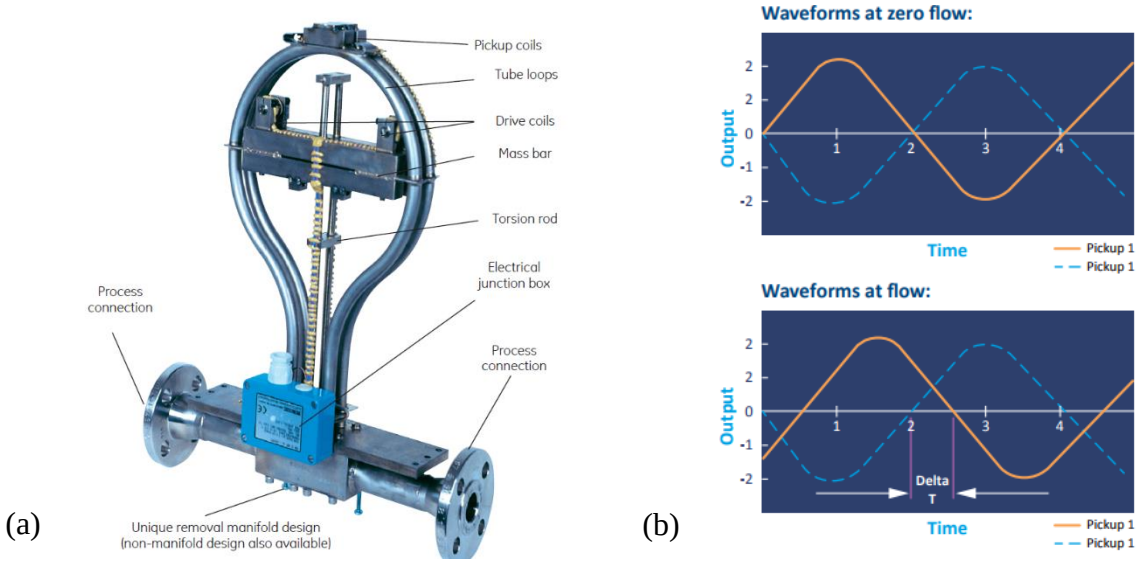

Figure 3.4: (a) Rheonik flowtube with components labelled. The pickup coils act as the sensors and the drive coils are used to excite the CFM. The electrical junction connects to the CFM control unit [4] (b) Sensor waveform signals for zero flow and flaw cases, the phase difference (Delta T) shown in the image is exaggerated [89]**.**

3.1.5 Fuel pressure transducers

Fuel pressure transducers were used for both monitoring fuel pressure and for pressure data acquisition (DAQ) in order to derive mass flow rate. Table 3.3 below shows the specifications for the sensors used. A pressure transducer was installed on the fuel side of the pressure accumulator, and near the output of the fuel pump was used to monitor the fuel pressure during pressurisation to ensure that the correct nominal pressure was reached. This transducer had a range of 0-400 bar with a response time of 1 ms. This transducer is labelled as P0 in the experimental setup.

Table 3.3: Pressure sensors specification

Sensor number	Transducer labels	Number of sensors	Manufacturer	Type	Range (bar)	Maximum response rate (kHz)
1	P0	1	Gems Sensor	3100	0-400	1 [91]
2	P1, P2	2	Kistler	4067E	0-3000	>40 [92], [93]
3	P1, P2	2	Kistler	4007D	0-250	>20 [93], [94]

For faster fuel pressure measurements to derive mass flow rate, two Kistler piezoresistive pressure transducers were used. Kistler 4067E sensors were initially used as these were previously used in the CFM [75]. The SNR in the pressure data was high as only a small range of the 4067E sensor was being used (50-200 bar of a 0-3000 bar range). These were replaced with Kistler 4007D sensors with a lower pressure range (0-250 bar) that is closer to a pressure range of interest. All of these Kistler pressure transducers gave high-frequency (>20 kHz) information about the pressure in the pipeline during injection and were to be used to develop a pressure-based mass measurement technique. The Kistler sensors also give a slow temperature output, which was used to adjust the speed of sound for the mass calculation for temperature variations.

The Kistler 4067E and 4007D sensors have a natural frequency that is greater than 200 kHz and 100 kHz [92], [94], respectively. For a piezoresistive transducer, an amplitude rise of 5% is expected at a fifth of the natural frequency [93]. The sensor behaves like an underdamped spring-mass system with a single degree of freedom. The Kistler transducers are connected to a Kistler 4624A amplifier to convert the pressure transducer's pressure measurement into voltage 0 – 10 V.

3.1.6 Current clamp

A Pico TA018 AC/DC current clamp was used to monitor the injector current profile [95]. The current probe is clamped onto the current-carrying wire, and the signal is recorded along with the pressure measurements. The low input range (10mA to 20A) is selected, which gives a voltage output in the range of 1mV – 2 V for the current observed.

3.1.7 Airflow mass control

An airflow control system was used as a safety device to ensure sufficient air extraction before injections. It is necessary to extract and sufficiently dilute the fuel spray below the flammability limit of the fuel before the next injection. A defined minimum airflow rate (2.5 L/s) was set for an injection event to occur. This minimum flow rate value was chosen in [84] to ensure the droplets and fuel vapours are extracted before the next injection; this can be set in the LabVIEW program used to control injection. While the injection frequency was increased above 5 Hz (corresponds to an engine speed of 600 rpm), the exhaust airflow rate was not increased. The injected fuel was collected in a glass bottle instead of being released into the spray chamber, so the exhaust was only used as a safety device to ensure that any spray that was not caught in the glass jar was safely extracted.

3.1.8 Data acquisition and control

The data acquisition (DAQ) and control system requirements are summarised in Table 3.4.

Table 3.4: DAQ and control system requirements for the Oxford spray rig experiments

System	Input or output signal	Requirement
Fuel pressure measurement and acquisition	Input	Continuous reading of the from Gems sensor transducer to check fuel pressure (P0) and recording fuel pressure from Kistler sensors at a minimum of 20 kHz (P1 and P2)
Temperature measurement	Input	Record fuel temperature during injections from the Kistler sensors (P1)
Air flow rate	Input	Continuous reading for checking volume flowrate
Injector control	Output	Digital pulse generation for the injections at required injection duration, frequency, and the number of injections. The pulses are sent to a BOSCH ECU or the NI DIDS, which was used to actuate the injector
Injector driver	Input and Output	Input from the Injector control box to NI DIDS, which is converted into a current signal for the injector
Current clamp	Input	The current clamp data is recorded to check that the correct injector profile is being delivered to the injector

Injector control

Injector control was achieved using a National Instruments LabVIEW program. A National Instruments USB-6211 DAQ module [96] was used for the inputs from the sensors (fuel pressure, air mass flow rate) and to give an output signal for injection time. This was used in the original control program designed by Camm [84].

The USB-6211 DAQ module has 16 analogue inputs (8 differential analogue inputs) with a 16-bit analogue to digital converter, 2 analogue outputs, 4 digital inputs, 4 digital outputs and 2 counter channels. The USB module has the capability of capturing 250 kilo samples per second.

The setup for the injector control on the USB-6211 was the same as in [84]. The input from the P0 pressure transducer used for real-time monitoring and the air flow rate are connected as analogue inputs into the DAQ. The inputs for the period (injection repetition rate) and pulse width (injection duration) were provided by the user, which was used to create an infinite pulse train using a counter channel, and an analogue output is used to create a finite pulse of the required injections which is triggered by the user. A logical AND gate is used to combine the analogue output and counter channel; this combined signal is sent to the injector driver to provide the required injections. Since the injection experiments were only performed at room temperature, this program was subsequently simplified from the original [84] only to control the injector timing. Figure 3.5 shows the LabVIEW program used for injector control.

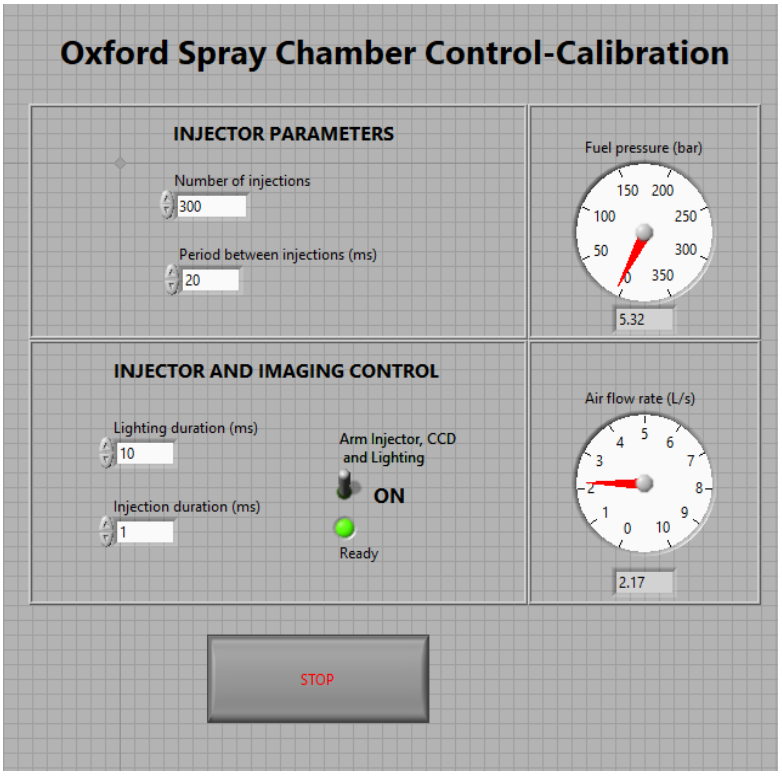

Figure 3.5: Simplified LabVIEW program for injector control.

Injector driver

Bosch ECU

The signal from the DAQ module is connected to provide input to the Bosch ECU. Optical isolator circuits were used to ensure there was no physical wire connection between the ECU and DAQ to ensure that no large current was sent into the DAQ. While the ECU could deliver injection current profiles for different injection duration, it was found to be limited to delivering injections at a maximum simulated engine speed of 3000 rpm. To be able to conduct experiments above this simulated engine speed, a NI DIDS-2103 system was used.

NI DIDS-2103

The NI DIDS-2103 system was based on a NI cRIO-9066, NI 9751 Direct Injection (DI) driver and a NI 9411 digital input module. The system is capable of delivering an injection profile synchronised with cam position sensors [97]. The system can also be used to inject using the external digital command signal sent using the LabVIEW program above. The NI cRIO-9066

was powered with a DC 24V supply and 13.8V, 10A supply for the DI driver. The NI DIDS system is connected to the laptop using the USB and Software Calibration Manager Toolkit (NI SCM) to set up the required injector profile.

The DI driver was set up to receive a digital signal to control the injector trigger. This was connected to the NI 9411 module. The injector current profile and voltage were set up in the driver setup window. Figure 3.6 shows the DI driver setup for a maximum of 2 ms injection for the multi-hole GDI injector used in the spray rig. The current profile was matched with the ECU output to trigger the injection using the NI DIDS.

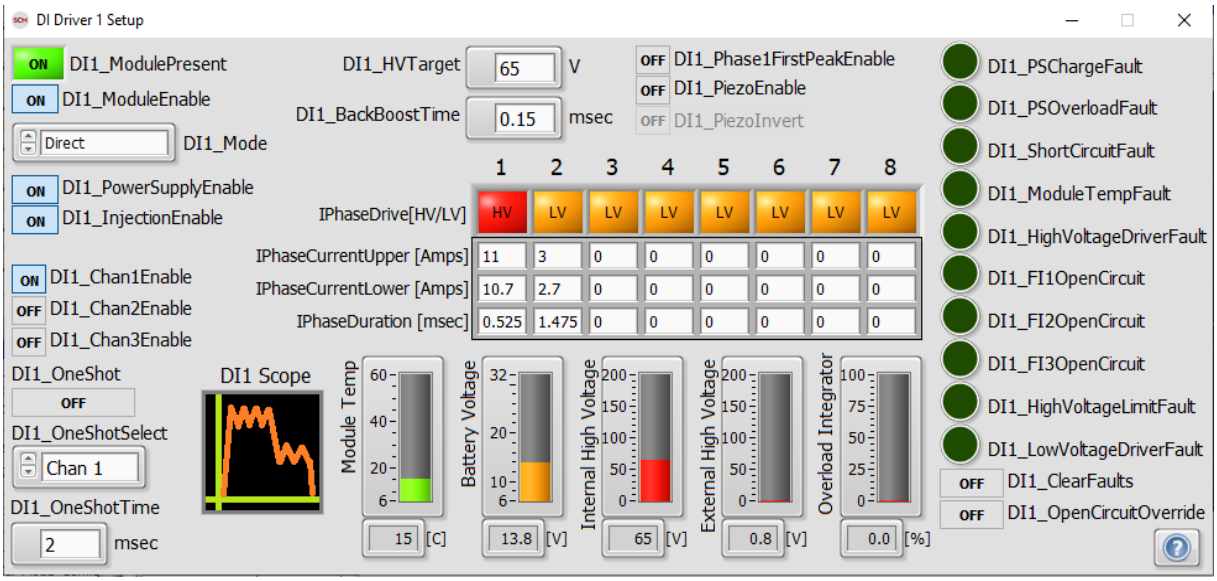

Figure 3.6: NI SCM console DI driver setup window for injector current profile setup.

Coriolis Meter

The Coriolis meter was controlled through a prototype transmitter based on a Zynq-7000 chip [98] designed by the AIRG. This uses 2 ARM Cortex-A9 processors, on which one of the processors was used for real-time calculation and flowtube control using PRISM signal processing. The second core was used for data archiving and web interface to control the Coriolis setup. The measurement data for the Coriolis meter was sampled at 48 kHz and was chosen by AIRG. The measurement data from the flowmeter was used to calculate frequency, phase, and amplitude. These are used for controlling the flowtube in real-time and calculating

the mass flow rate through the flowmeter. The collected data was initially processed by the AIRG using PRISM signal processing. Each set of injections were recorded as an individual file, and these were converted into MATLAB data files for calculating the phase difference during the injections.

Pressure measurements

A second USB-6211 module was used for data acquisition. The injection request from the injector control was set up as the trigger for data collection. The analogue input channels were used to record the voltage output with respect to the ground pin in the USB-6211. The pressure measurements from the pressure transducers (P0, P1 and P2), temperature measurement from the P1 pressure transducer and the current clamp outputs were recorded. Figure 3.7 shows the LabVIEW program for pressure data acquisition. The number of samples required, the sample read rate (Hz) and the filenames were set to be user-defined. The samples recorded include 100 pre-trigger samples. Each set of injections was recorded as an individual file, and these were converted into MATLAB data files for applying the pressure methods (OPTM and TPTM) onto the data.

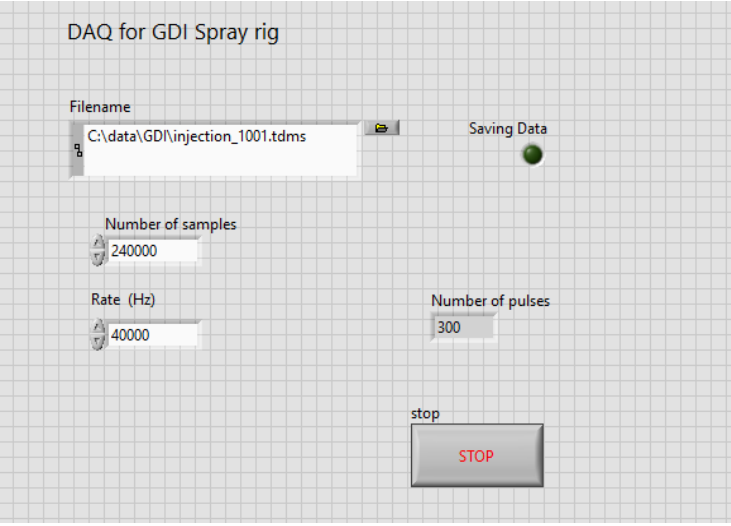

Figure 3.7: LabVIEW program for pressure data acquisition for the pressure measurements.

3.2 Single-cylinder Engine

A single-cylinder optical engine was used to run the on-engine pressure measurement experiments. The design of the engine was based on a 5 litre AJV8 GDI engine. The engine has a pent-roof combustion chamber with four valves and a centrally mounted injection, and a spark plug. The details of the AJV8 engine is described in [99]. For this work, the engine uses an injector with the same specifications as injector 1 (Table 3.2). Figure 3.8 shows the engine components.

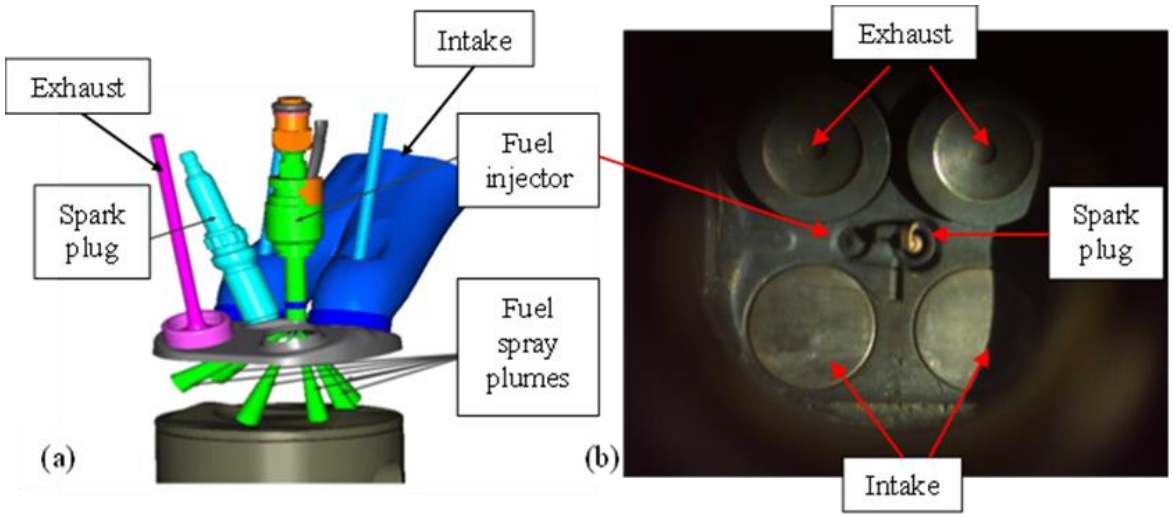

Figure 3.8: (a) AJV8 engine combustion system, adapted from [84]**, originally from** [99]**. It shows a central mounted injector, and the injector spray plumes (green), a spark plug (cyan), intake ports and values (blue) and an exhaust valve (magenta). The orientation of the injector is parallel to the crankshaft axis. (b) Engine valves, injector and spark plug from below.**

The engine used in the experiments is not thermodynamically equivalent to a multi-cylinder engine. The different materials used can impact the surface temperature and heat transfer. While this is the case, these experiments can be used to validate the pressure methods application for research purposes. The speed is, however, limited to 2000 rpm due to the long, heavy piston used in the engine. Further details on the engine physical layout are described in [84]. The engine parameters are summarised in Table 3.5.

Table 3.5: Engine specifications

Engine parameter	Value
Bore x Stroke	89 x 90.3 mm
Displacement	562 cm^3
Valves	2 intakes, 2 exhausts
Compression ratio	11:1
Fuel pressure	150
Valve timing (°CA ATDC)	IVO 24°, IVC 274°, EVO 476°, EVC 6°
Injection start (°CA ATDC)	90°
Spark ignition (°CA ATDC)	315°

The engine has a crank angle marked flywheel; this is connected to a dynamometer (from DC Control Techniques) for torque and speed control. The dynamometer and majority of the engine are controlled by the Taylor $DynPro_2$ control system [100]. The system has the capability of taking in pressure, temperature, other analogue and frequency inputs. The system is also connected to a dynamometer and other control values (throttles and coolant) and has operations control for starting the engine dynamometer. The majority of the input signals are used for closed-loop control and engine monitoring. The engine is controlled by a PC remotely outside the engine bay where the throttle valve opening, engine speed and torque and coolant circuits parameters can be set and monitored.

The injector and the spark plug are separately controlled from the shaft encoder signal using a Berkeley Nucleonics Corporation (BNC) model 725 [101]. This multi-trigger digital delay generator was used to create TTL pulses required for injector and spark plug triggering in the engine. Using two signals, 0.5°CA and the 0° flag (described when the engine is at the bottom dead centre) from the shaft encoder, the injection timing, duration and spark timings were set

at the end of the compression stroke. The timerPRO software which comes along with BNC, was used to control the timing device [101]. The injection trigger from the BNC is sent to the NI DIDS- 2103 for injector actuation.

The data acquisition was made using an AVL X-ion high-speed modular data acquisition platform [102]. A shaft encoder was mounted onto the crankshaft with a resolution of 0.1°CA for timing in relation to the engine. The AVL X-ion has 16 input channels that can acquire signals at a sampling rate of 2 MHz per channel. This system has an input range of +/- 10 V, and the data can be sampled based on time or crank angle. The signal from the shaft encoder, cylinder, barrel, and fuel pressure transducers and the injection signal from the BNC were all connected for data acquisition. The AVL IndiCOM software [103] was used for data recording while the engine was run.

3.3 Fuels

GDI injectors typically are run using unleaded gasoline (ULG) as the fuel on the engine, and previously ULG was used as the fuel in spray rig experiments [84]. For the CFM experiments, white spirit was used as a safer alternative to ULG due to its higher flash point, which also allowed it to be used safely for injection mass calibration. However, using single-component fuels in pressure measurement experiments makes it easier to calculate the speed of sound at different pressures, as these can be readily found in the literature. The single-component fuel iso-octane is available and can be used for the optical engine tests during on-engine experiments. However, iso-octane has a flashpoint of 4.5°C [104]; this is below the lab's room temperature (~20°C). In this case, part of the injected fuel can be in vapour form, and any escaped fuel from the glass bottle can form an ignitable fuel mixture at room temperature in the lab. To remove the risk of potential ignition of any vapours, undecane, which has a flashpoint of 62°C [105], was chosen as a replacement for iso-octane for the spray rig experiments. Iso-

octane was used for the optical engine experiments as undecane is not suitable for gasoline engine operation. Table 3.6 shows the flash points of the fuels used in the experiments.

Table 3.6: Flash points of the fuels used in the experiments

Fuel	Flash Point (°C)
Unleaded Gasoline (ULG) [106]	< -40
White Spirit [107]	40
Undecane [105]	62
Iso-octane [104]	4.5

3.3.1 Undecane

The speed of sound of undecane as the temperature and pressure changes are shown in Figure 3.9. The data for the speed of sound was taken from [108] and was used in the pressure methods calculations for the spray rig setup data.

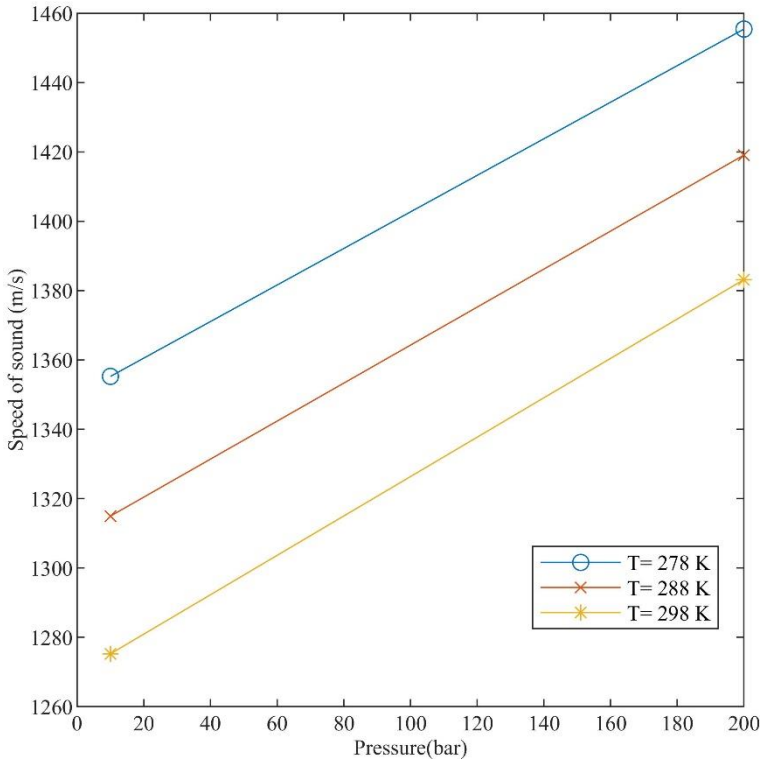

Figure 3.9: Speed of sound for n-Undecane at different pressure and temperatures. Adapted from [108]**.**

3.3.2 Iso-octane

The speed of sound of iso-octane as the temperature and pressure changes are shown in Figure 3.10. The data for the speed of sound was taken from [109] and was used in the pressure methods calculations for the optical engine data.

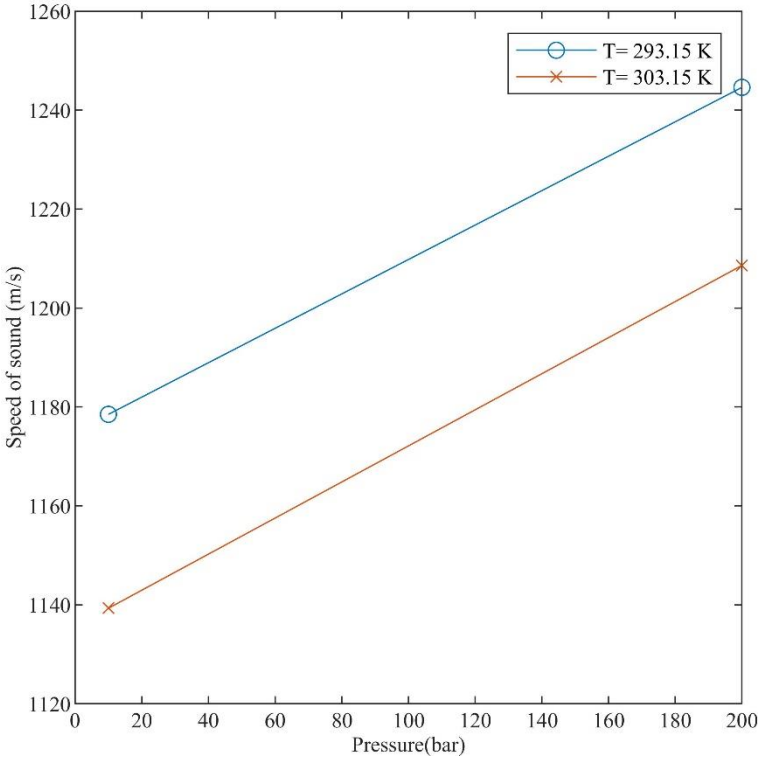

Figure 3.10: Speed of sound for Iso-octane at different pressure and temperatures. Adapted from [109]**.**

3.4 Summary

In this chapter, the experimental hardware used has been described. The specific setups made for fuel flow measurement experiments are described in the specific chapters before the results are discussed. The optical engine used for the on-engine experiments was also discussed. Finally, the fuel choices for the different experiments are also discussed.

4 Coriolis flowmeter for measuring mass flow rate

Experiments were conducted to understand the usage of the current generation of CFM for fuel measurements. First, the experimental methodology is described, including the setup used in the experiments. Then the results from the experiments are analysed and discussed. Finally, a summary of the CFM experiments is discussed, along with the limitations.

4.1 Experimental setup

4.1.1 Test Rig

The experimental setup used was a modified version of the spray rig described in Section 3.1. It was modified to include a Coriolis flowmeter and fuel pressure transducers between the fuel pressure accumulator and the fuel injector. Figure 4.1 shows the setup used for gasoline experiments with the CFM. White spirit was used as an alternative to unleaded gasoline (ULG) in the CFM experiments; this was discussed further in Section 3.3. The setup used the fuel pressure accumulator for fuel pressurisation. The control box shown in Figure 4.1 was used to control the injector using a Bosch ECU and for data acquisition of pressure data from P1 and P2 (Kistler 4067E) pressure transducers. CFM data was recorded using a prototype transmitter designed by AIRG described in Section 3.1.9.

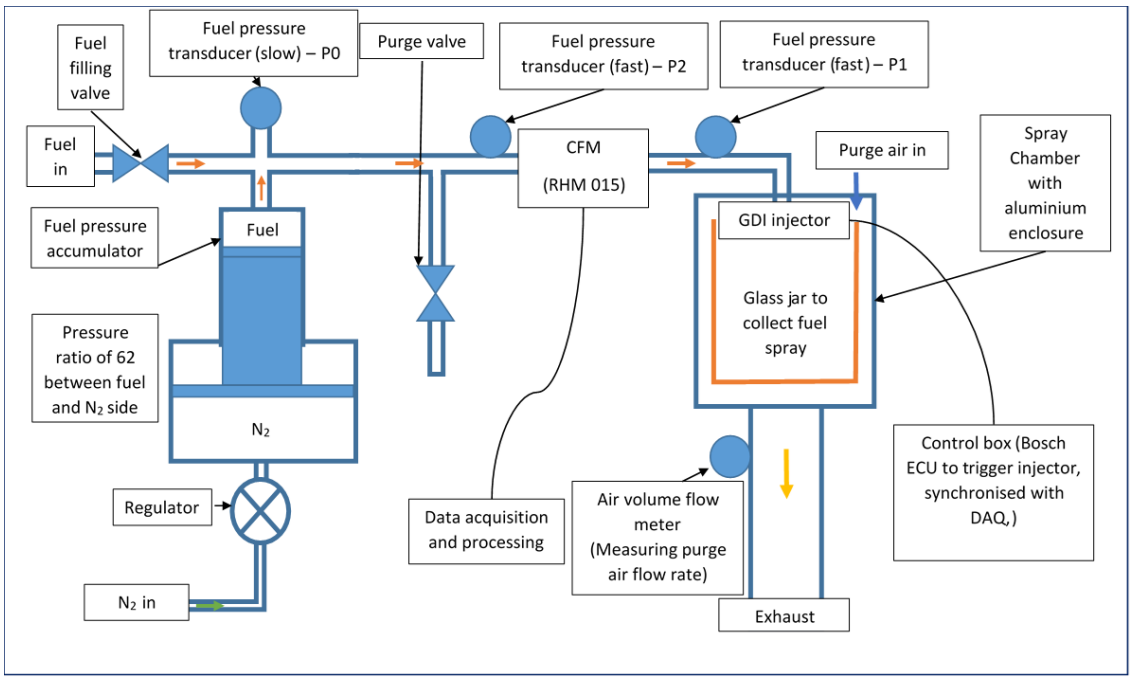

Figure 4.1: Experimental set up for modified Oxford spray rig for CFM experiments. The CFM was fitted with two pressure transducers, upstream and downstream of the CFM. The CFM was installed as close to the injector as possible. Not to scale.

It was found after initial testing that the rig assembly caused external vibrations during injections. The lack of a return line, such as in the previous diesel injection experiments [75], [76] in the current gasoline setup, caused a hydraulic shock at the start and end of injections (this is discussed in section 4.2.7). This added vibrational noise to the signal. Additional cross-bracing was installed to keep the CFM rigidly in place, and rubber clamps were added to provide damping from external vibrations from the surroundings (Figure 4.2).

Figure 4.2: Spray rig setup with support and clamps on CFM for external vibration isolation without the aluminium enclosure.

4.1.2 Test conditions

The experiments were conducted at GDI engine operating conditions with the maximum rated pressure of the GDI injector (150 bar). Single shots and series of injections were fired at simulated GDI engine operation frequencies to evaluate the performance of the Fast NGC technique for mass measurement. During initial experiments, the peak height of the phase difference results from the CFM was observed to be a function of the flowtube phase and peak injection duration; this was also observed in [76]. To ensure the flowtube phase did not influence the injections, the injection periods were chosen to be a multiple of the oscillation period of the flowtube. In drive mode at the fuel pressure (150 bar), the flowtube frequency was approximately 149 Hz; this was used to calculate the flowtube period (6.7 ms) and hence the injection period. Table 4.1 summarises the experiments conducted.

Table 4.1: Experimental conditions for CFM experiments

Simulated engine speed (rpm)	**Single shot**	**1788**	**2978**
Injection Frequency (Hz)	n/a	14.9	24.8
Injection period (ms)	n/a	67.1	40.3
Injection duration (ms)	1.0, 2.0	2.0	1.0, 1.5, 2.0
Injection pressure (bar)	150	150	150

4.1.3 Mass calibration results

Experiments were conducted to evaluate the average injected mass per injection to be able to compare this to the values calculated by using the CFM. The CFM setup was used to inject 200 injections at 150 bar at three injection durations in the CFM experiments. Each test condition was repeated three times, and injected mass was measured on a weighing scale and averaged. The results from the total injected mass per injection are given in Table 4.2.

Table 4.2: Mean mass injected per injection at 150 bar, averaged over 3 repeats (each repeat has 300 injections)

Injection duration (ms)	Mass injected per injection (mg)	Standard deviation (mg)
1.0	13.84	0.17
1.5	20.89	0.12
2.0	27.36	0.21

4.2 Results

The CFM results were first processed using PRISM signal processing (Section 2.4.1, [110]) by AIRG. Due to the injection duration being shorter than the oscillation period of the CFM, the phase difference was a function of both the injection duration and the instantaneous phase of the flowmeter. The phase difference observed in the CFM signal is proportional to the mass injected, however as the injection was smaller than the oscillation period, the position in the cycle where the injection occurs determines the phase difference measured due to the injection. Further, the injection duration observed in the phase difference was stretched in time to approximately 16 ms, with the end of injection (EOI) occurring within this stretched time envelope. The stretch was caused by a combination of the flowtube oscillations acting as a mechanical filter and signal processing acting as a digital filter. This stretch was observed irrespective of the injection duration, and so the signal cannot be used to measure injection duration directly. These complications do not allow for a derivation of the instantaneous mass flow rate. However, the phase difference is directly proportional to the mass flow rate when the injection occurs at the same instantaneous phase of the flowmeter. Hence, the area of the individual injections would be proportional to the mass injected in the units of °s. While this unit is directly proportional to mass injected in grams for the injection, the peak height for the same injected mass injection is different at different instantaneous phases, so the mass injected as the peak height is also a function of the instantaneous phase and hence was not used for the mass injected calculation.

4.2.1 Signal processing of raw signals

The effect of Prism signal processing on the raw data can be seen in Figure 4.3. The grey line is the raw data signal, while the blue line shows the filtered signal (a series of injections at 24.8 Hz, which is equal to 2978 rpm engine speed).

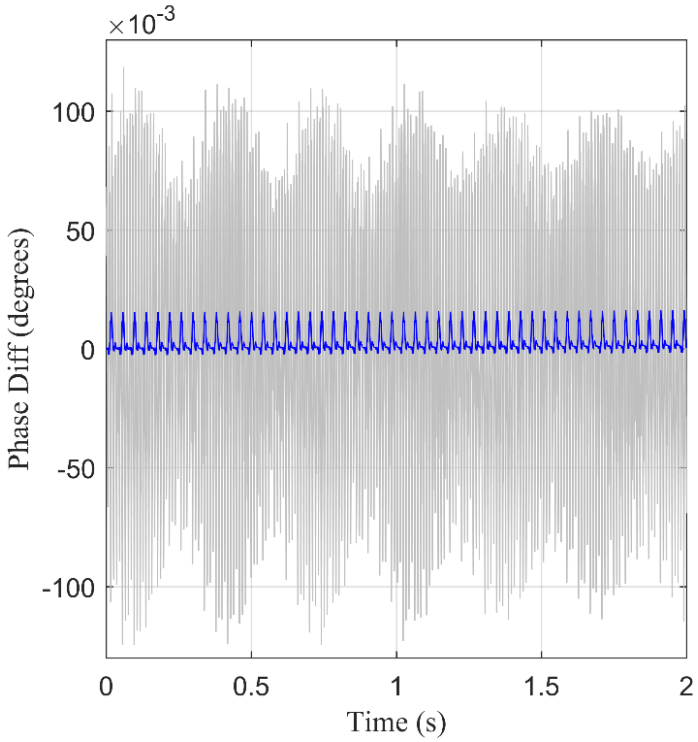

Figure 4.3: Raw vs Filtered signal for 2ms injection train at 2978 rpm.

The raw signal was pre-filtered with four PRISM notch filters designed by AIRG. Static Notch Filters (SNFs) were applied at 245.0 Hz and 262.6 Hz. Additional Dynamic Notch Filters (DNFs) were applied at 114.3 Hz with $m = 622.9$ Hz and at 298.0 Hz with $m = 447.1$ Hz [82]. An RST is finally applied to the filtered signal to get the phase difference data [76]. Due to the limitations of the bandwidth of the ARM core and all the results presented are from offline post-processing of the data. Figure 4.4 shows the sensor signal with no notch filters applied (a) and with notch filters applied (b). The signal magnitude reduced by seven orders of magnitude approximately. CFM generally uses the signal directly to calculate the mass flow rate, due to the reduction in signal strength, a calibration factor would be required to calculate the mass

flow rate. However, compared to raw signals, the SNR had improved to three orders of magnitude from less than one order of magnitude due to the filtering enabling the FNGC technique to identify individual injections.

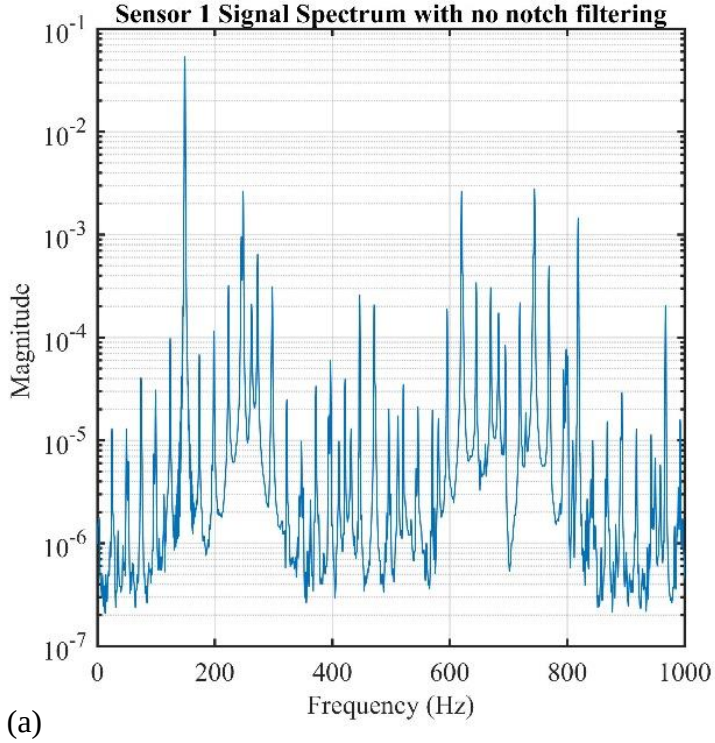

(a)

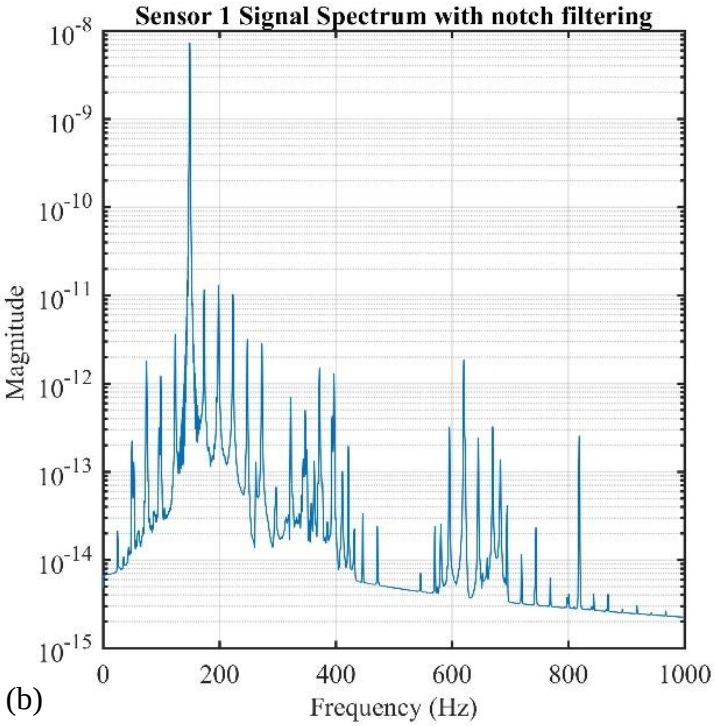

(b)

Figure 4.4: CFM sensor 1 signal spectrum; (a) with no notch filters applied, (b) all notch filters applied.

4.2.2 Single shots

Figure 4.5 shows the measured phase difference for 1 ms and 2 ms single injections. After injection, there was a signal offset that subsides approximately 200 ms, returning to zero. This was caused by the CFM control returning the flowmeter to its original oscillation. The difference in post injection response was caused due to the injection occurring at a different instantaneous phase of the CFM. The initial negative phase difference in the signal (circled in red) was not observed in the diesel tests due to the inclusion of a spill line [76]; this was likely associated with needle lifting at the start of injection (SOI). The initial flow at this point would be inwards (into the fuel pipeline) from the injector before the injection as the needle lifts. These details being observed shows the potential of this technology to be further developed for mass measurement.

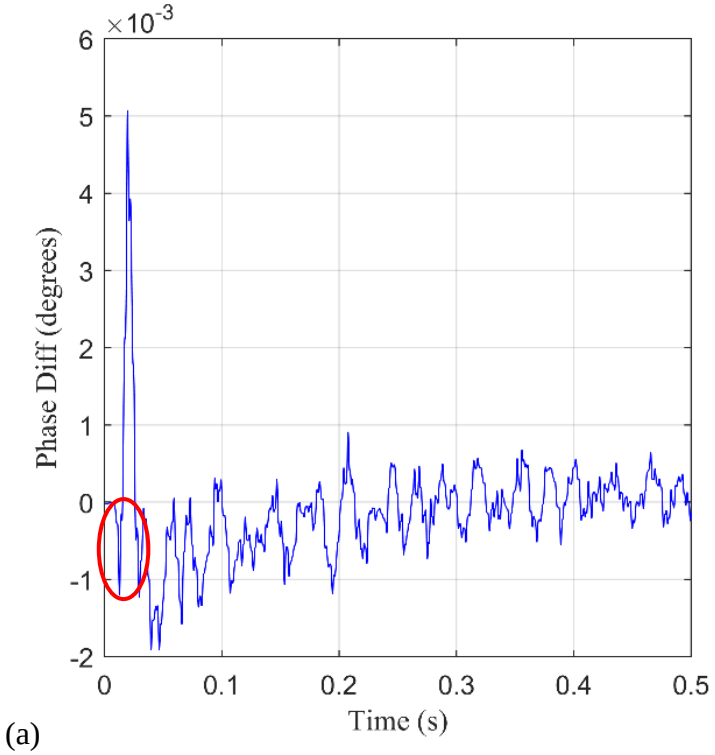

(a)

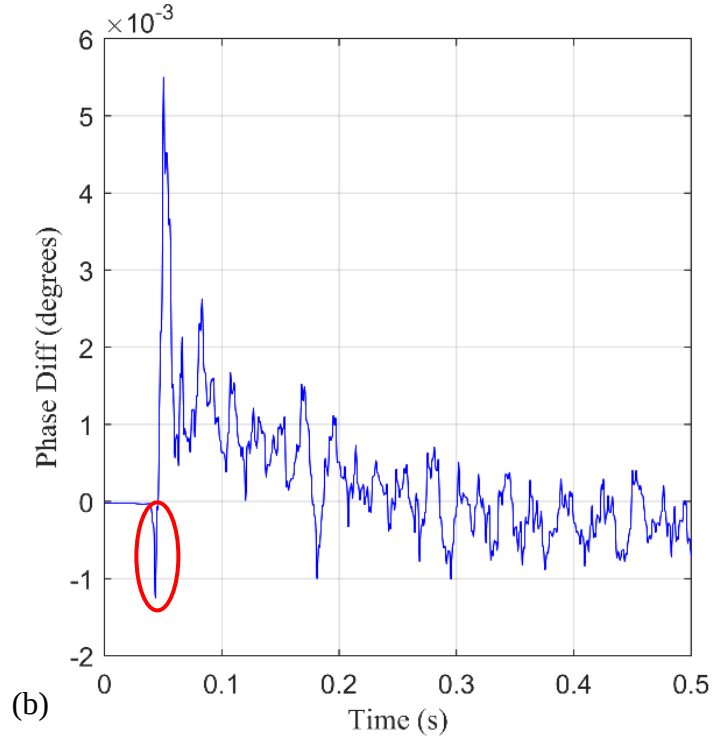

(b)

Figure 4.5: Single injection at 150 bar (a) 1 ms injection, (b) 2 ms injection (DC offset corrected).

4.2.3 Injection trains

As mentioned in Table 4.1, the injection frequencies were chosen to be 1788 rpm and 2978 rpm, which are one-tenth and one-sixth of the flowtube frequency, respectively. The injection occurs at approximately the same flowtube phase minimising the effect from the flowtube phase on the injection.

Figure 4.6 (a) shows a 2 ms injection at 2978 rpm with the DC offset corrected, and Figure 4.6 (b) shows a magnified image of the injections. The individual injections were distinguishable in the injection train, with the spacing between each peak matching the requested injection period. The variations in individual injections seen around the peak in Figure 4.6 (b) were attributed to slight deviations in injection timing as only an approximate multiple of the flowtube period was used and the shot-to-shot variations in the injected mass.

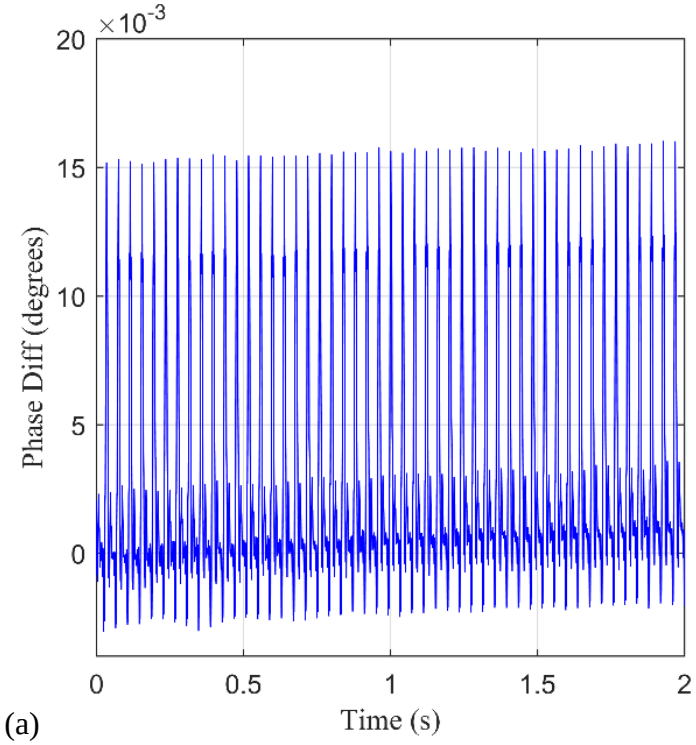

(a)

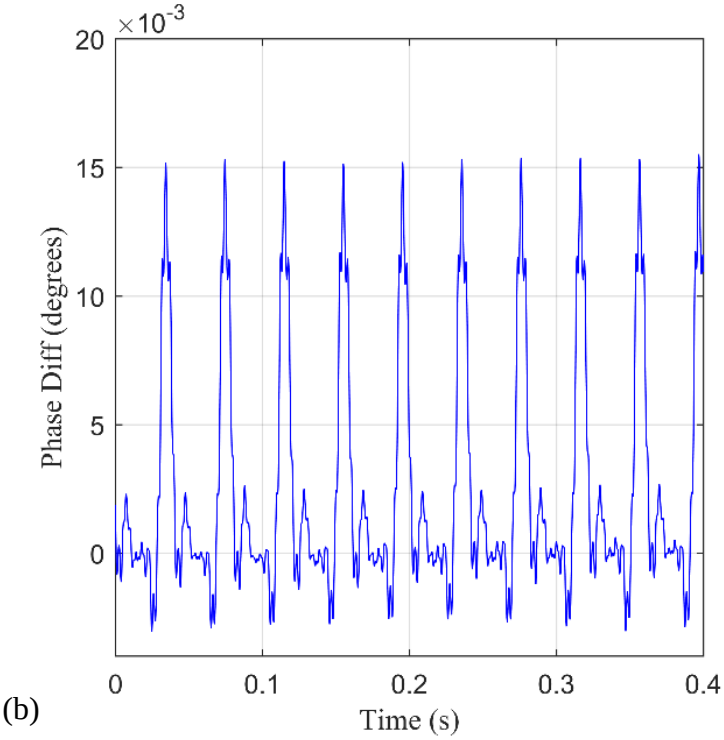

(b)

Figure 4.6: Phase difference for a series of 2 ms injections at 2978 rpm equivalent speed (a) injection train, (b) detailed individual injections (DC offset corrected).

4.2.4 Effect of phase on injections

The instantaneous flowtube phase was suggested to influence the height and offset in the phase difference observed [76]. The injection period was offset deliberately from a multiple of approximately 24.8 Hz (2978 rpm) to 24.72 Hz (2966 rpm equivalent engine speed) in one of the experiments to test this hypothesis. Figure 4.7(a) shows the results as a phase difference plot for this case and Figure 4.7(b) shows individual injections in the CFM signal. After the injections started at 4.5 s, the measured phase difference follows a sinusoidal shape. To understand the effect of the sinusoidal shape observed in the phase difference signal, the peak heights of each injection were plotted with the instantaneous phase of the flowtube at the point of peak in the injection in Figure 4.8. The peak detection method used on the signal is described in section 4.2.5.

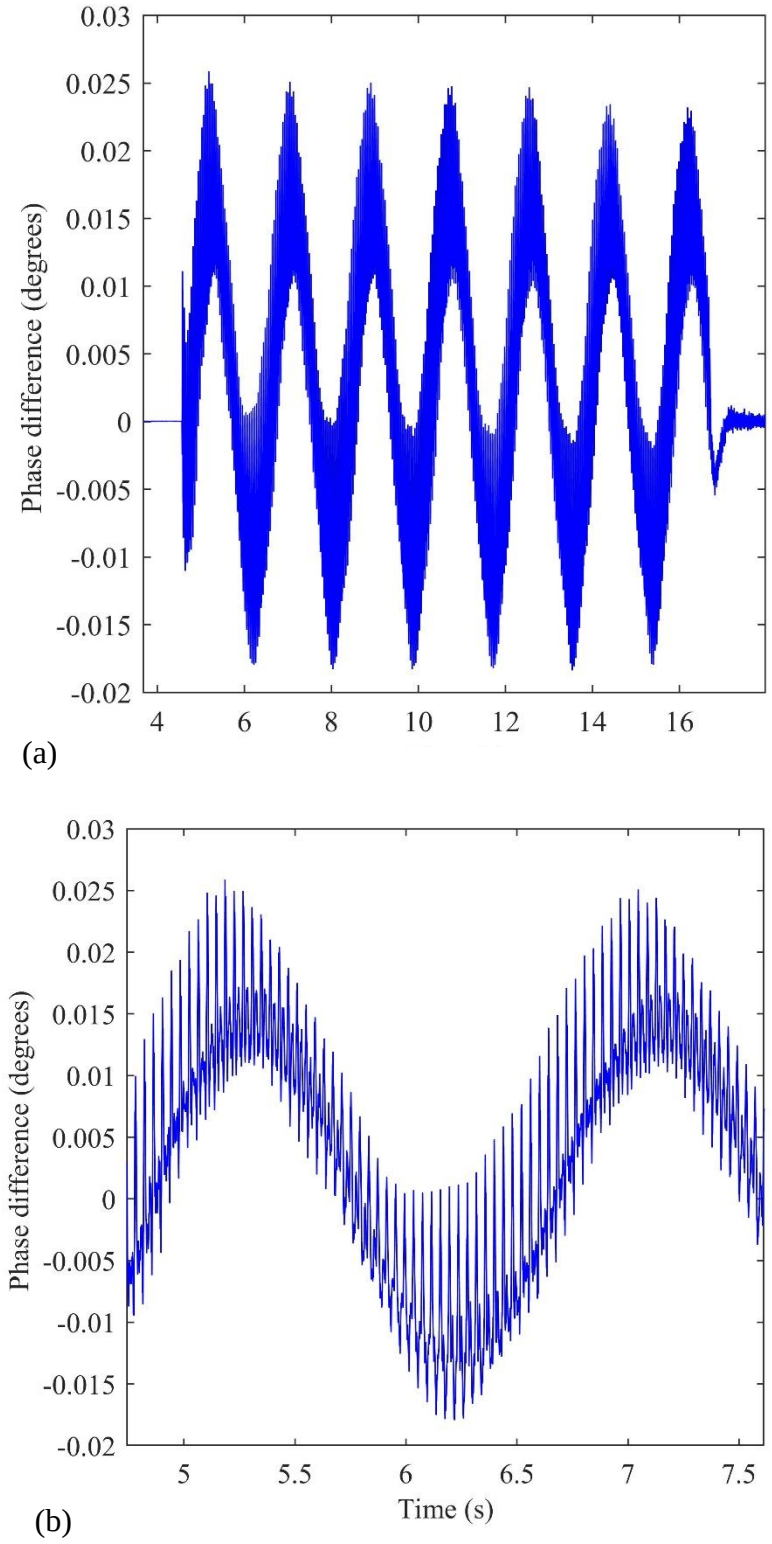

Figure 4.7: A series of 2 ms injections at an offset of flowtube period multiple (2966 rpm) (a) injection train, (b) detailed individual injections.

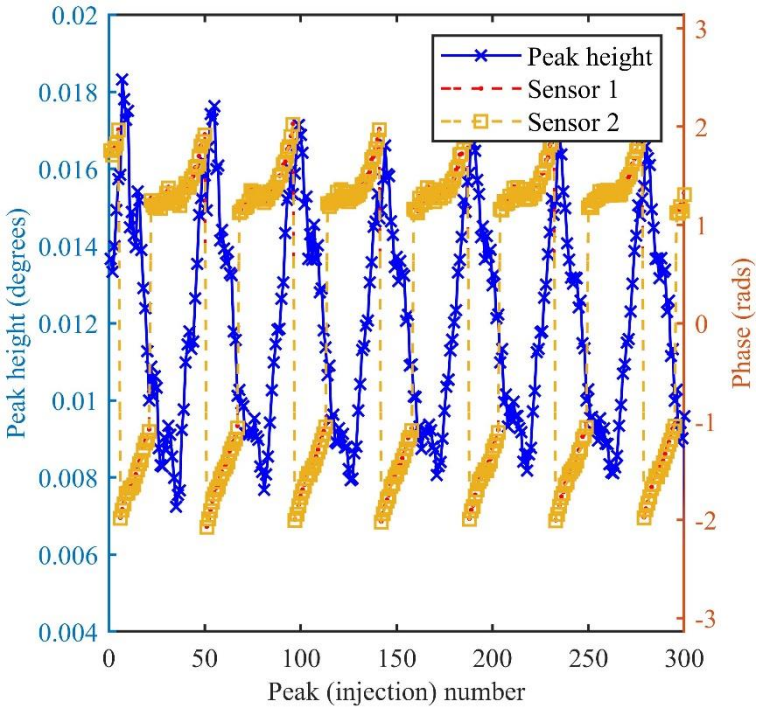

Figure 4.8: Peak height of each peak plotted with the instantaneous phase of the flowtube at the peak for 2 ms injections at 2966 rpm.

The change of peak height for each peak shows that both the phase difference in the CFM measurement (Figure 4.7) and the peak height are influenced by the instantaneous phase changes. The peak height was calculated using the technique described in Section 4.2.5. In Figure 4.8, the peak heights change sinusoidally as the injection location in CFM changes; this CFM phase, however, was not sinusoidal. This shows the limitation of the technique, as only equivalent engine speeds at integer multiples of the flowtube period have peaks near the same instantaneous phase, and only these cases can be used for injection mass calculations. Further work is required to find a relationship between the peak height and instantaneous phase for enabling the peak height to be directly related to the mass flow rate of injection.

4.2.5 Repeatability

For injections being injected at a given phase (i.e. injections at a multiple of flowtube period), the measured phase difference of the CFM is proportional to the mass flow rate through the

flowmeter. Then, the areas obtained from the phase difference signal peaks would be the total mass injected per injection. This was represented in the units of °s in the analysis. The data was post-processed for injection trains of 1788 rpm and 2978 rpm for testing the repeatability of the measurement system.

To identify an injection in the phase difference CFM signal, a baseline was calculated by removing the noise surrounding the injection; this is shown in Figure 4.9. The peaks were first identified (shown in yellow) and then removed by replacing an 8 ms (half the injection stretch observed) section before and after the peak with a linear interpolation between these two points. For the baseline, a median filter across a 75% injection period on the no peaks signal (for the 2978 rpm signal, the median signal was applied over 30 ms)— the intersection with the baseline and the signal before the peak was taken to be the SOI and the intersection after as EOI (this is shown in Figure 4.10 (a)).

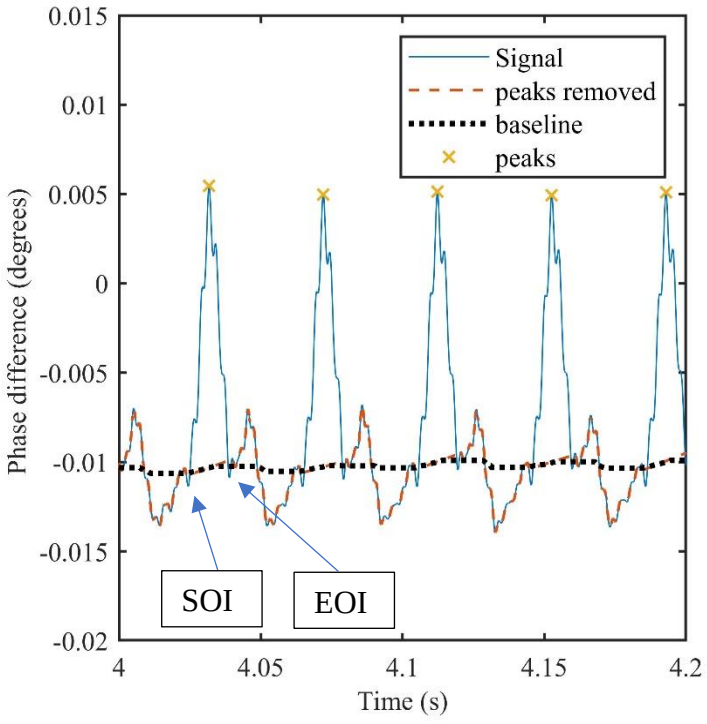

Figure 4.9: Baseline calculation used for repeatability test for CFM phase difference signal (2 ms injection at 2978 rpm with no correction on DC offset).

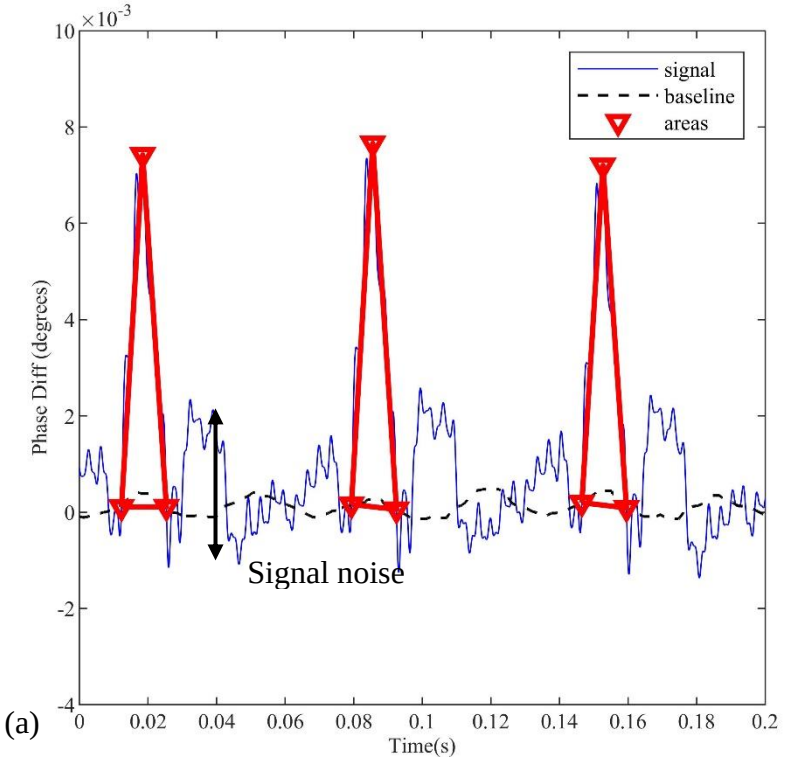

(a)

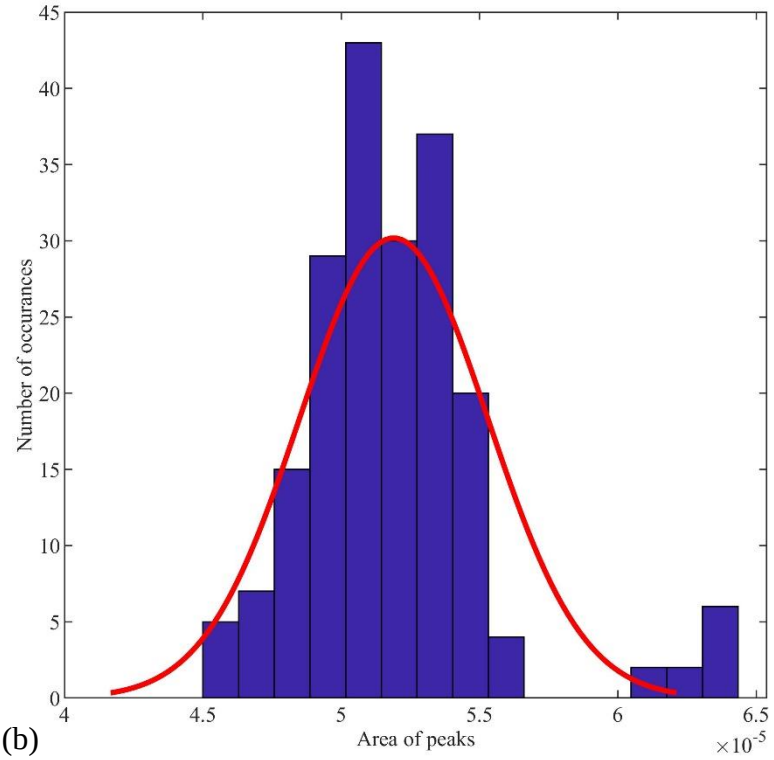

(b)

Figure 4.10: Repeatability analysis for individual injections at 1788 rpm for 2 ms injections (a) calculated areas from signal, (b) histogram of the integrated area representing injected masses (DC offset corrected).

The three points (SOI, peak, EOI) were used to create a triangle and the triangle was then integrated to find the approximate area of each peak, which is proportional to the mass injected per injection. The triangle was used to calculate the mass injected; this is taken as a suitable approximation to represent the signal for the first calculation of mass injected. Figure 4.10 (a) shows the signal in blue, the baseline in black and the triangle, of which the area calculated in red for 2 ms injections at 1788 rpm. As seen in Figure 4.10 (a), the area integrated closely represented the signal integral. This further enabled the use of the repeatability measurement when there was a DC offset observed in the signal (Figure 4.9). Figure 4.10 (b) shows the histograms of the integrated areas for the 1788 rpm. The same repeatability analysis was conducted on 2978 rpm (Figure 4.11, Figure 4.12 and Figure 4.13 for injection duration of 2 ms, 1.5 ms and 1 ms, respectively).

Table 4.3 shows the data statistics for the 1788 rpm and 2978 rpm data. The distribution of most of the areas of the integrated injections was within 1×10^{-5} °s, a coefficient of variation (CoV) of 6.6% for the 1788 rpm data. The areas are proportional to the injection duration for the 2978 rpm as expected, suggesting that as the injection duration increases, the injected mass increases. The peak height observed in the signal in the three 2978 rpm cases increased linearly with increasing injection duration (Figure 4.11, Figure 4.12 and Figure 4.13). It was noted that as the injection duration increased from 1 ms to 2 ms, the SNR improves, and the CoV reduced from 5.23% to 0.94% for 200 injections. This, even with higher SNR, demonstrates good repeatability for mass measurement. In the 1.5 ms injection train at 2978 rpm, only 199 injections were used for repeatability testing due to a partial injection present in the injection train. This is further discussed in section 4.2.6.

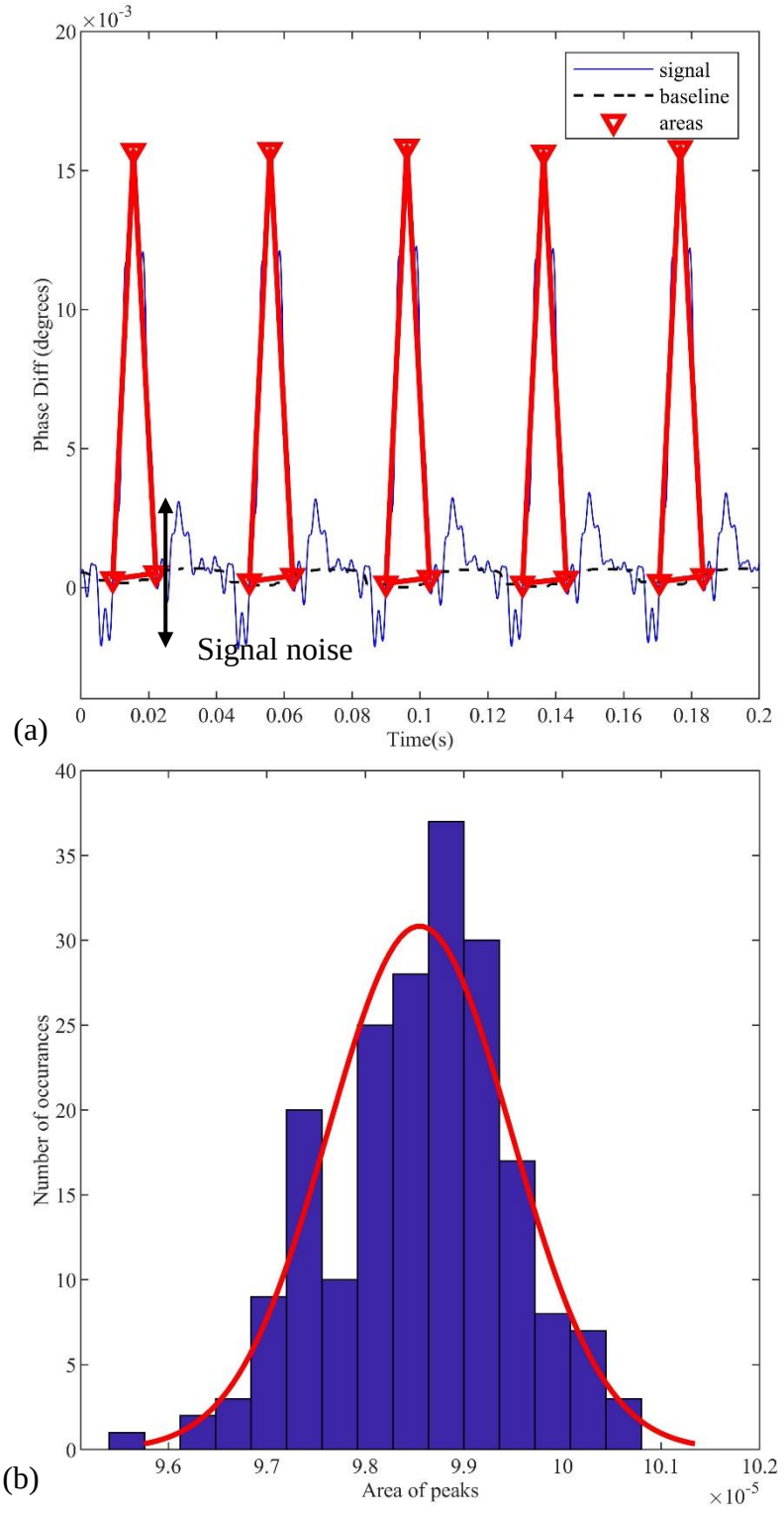

Figure 4.11: Repeatability analysis for individual injections at 2978 rpm for 2 ms injections (a) calculated areas from signal, (b) histogram of the integrated area representing injected masses (DC offset corrected).

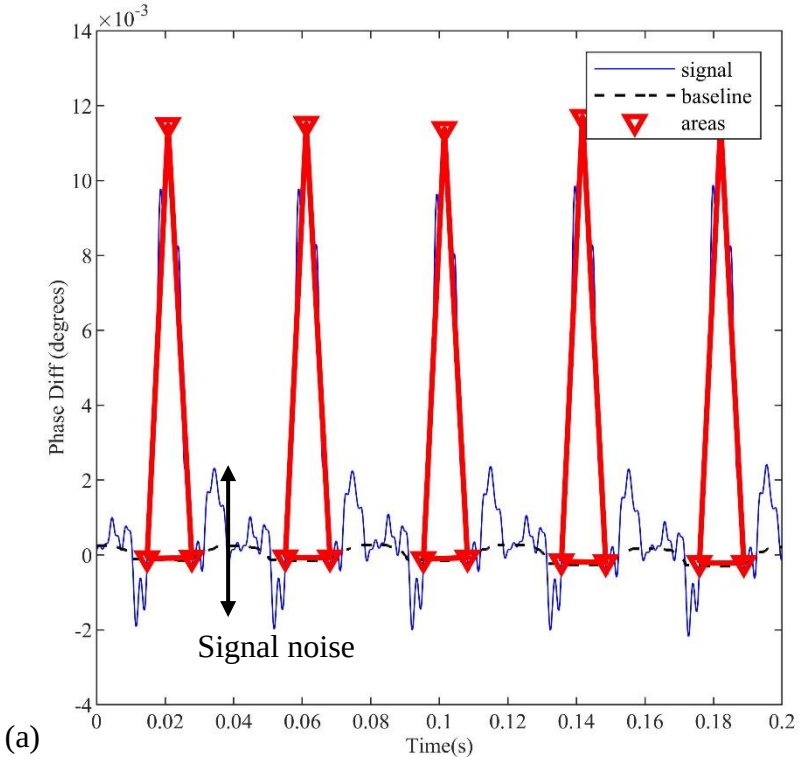

(a)

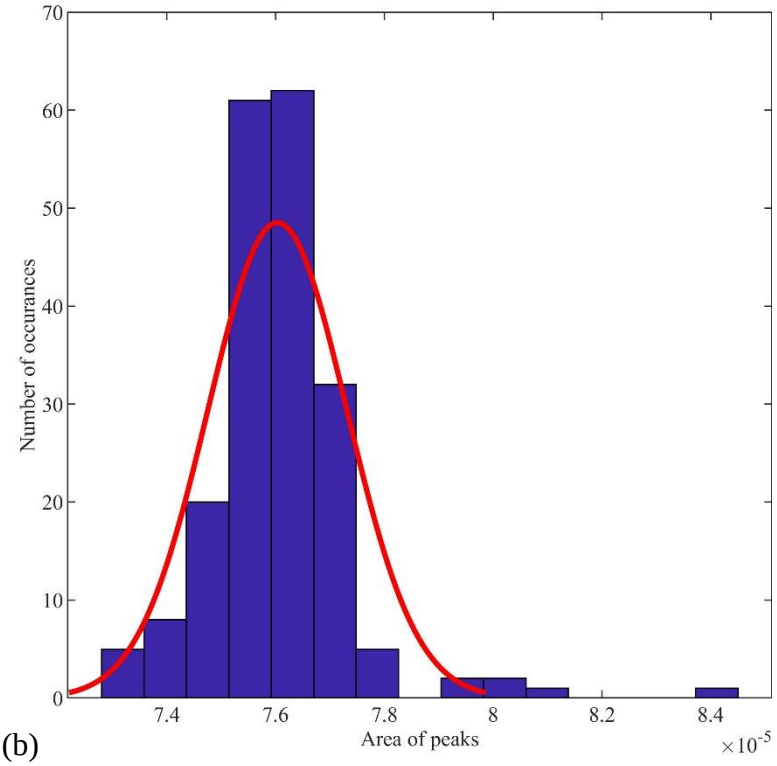

(b)

Figure 4.12: Repeatability analysis for individual injections at 2978 rpm for 1.5 ms injections (a) calculated areas from signal, (b) histogram of the integrated area representing injected masses (DC offset corrected).

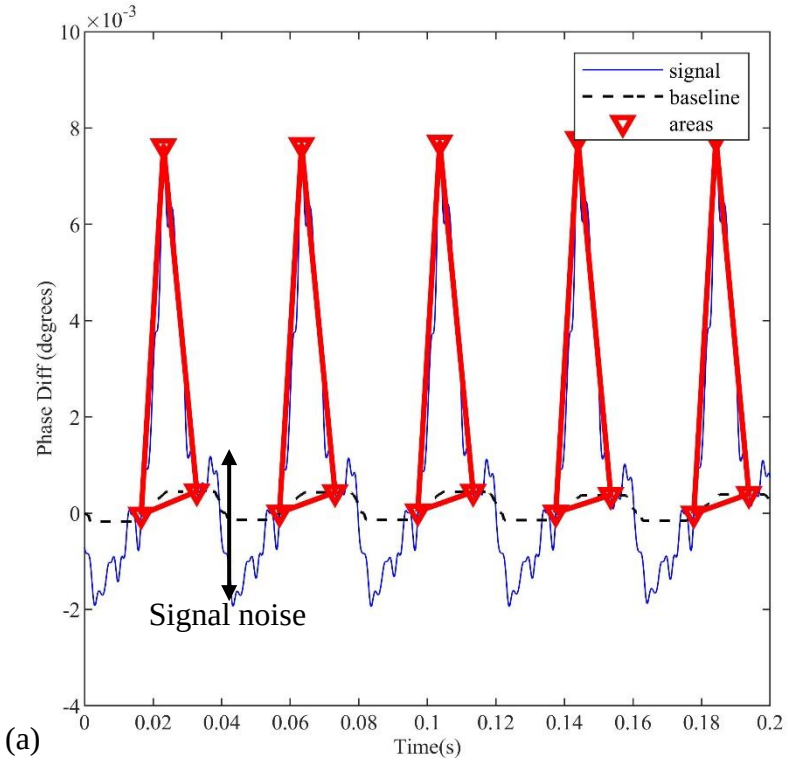

(a)

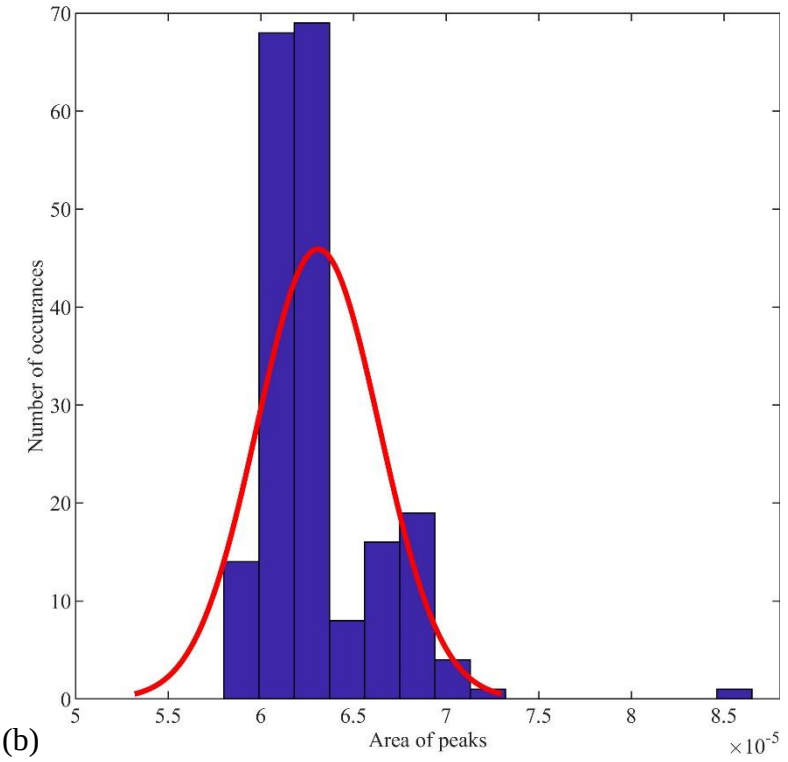

(b)

Figure 4.13: Repeatability analysis for individual injections at 2978 rpm for 1 ms injections (a) calculated areas from signal, (b) histogram of the integrated area representing injected masses (DC offset corrected).

Table 4.3: Data statistics for injections at 1788 rpm and 2978 rpm equivalent speed

Injection length (ms)	**2**	**2**	**1.5**	**1**
Simulated engine speed (rpm)	1788	2978	2978	2978
Number of injections	200	200	199	200
Mean (°s)	5.19e-05	9.86e-5	7.60e-5	6.31e-5
Median (°s)	5.14e-05	9.87e-5	7.63e-5	6.22e-5
Standard Deviation (°s)	3.41e-06	9.31e-7	1.27e-6	3.30e-6
CoV (%)	6.57	0.94	1.67	5.23

For 2 ms injection train, the CoV was over six times higher in 1788 rpm (Figure 4.10) data than 2978 rpm (Figure 4.11) data. There was a difference in the peak height between the two injections trains, which was attributed to the different flowtube phases for the two tests. The level of noise (~ 3-4×10^{-3}°) observed was the same in all the test cases suggesting it was independent of the flowtube phase and injection duration (shown in Figure 4.10 - Figure 4.13 with the black arrow). The peak height observed in the 2 ms injection was much larger than the noise surrounding the signal. This larger observable peak compared to the signal directly improves the SNR. However, the peak height was influenced by the instantaneous phase, the 1788 rpm data, while also having the 2 ms injections, the peak height is much lower, which increases the SNR. As expected, the SNR observed in the 1788 rpm case is higher, causing a broader range in areas calculated, increasing the data's CoV.

After the first peak, the secondary peak was observed; this was caused by the hydraulic shock (a pressure wave) in the tube after injector closure and signal processing. This will need to be understood for the use of CFM in fuel mass measurement. Further investigation on the flowtube was done by taking pressure measurements upstream and downstream of the Coriolis meter. The results from this are discussed in 4.2.7.

4.2.6 'Misfire' detection

In the injection train of 1.5 ms injections at 2978 rpm equivalent speed, a 'misfire' occurred (where a full injection did not occur within the injection train). This was heard as an audible difference during the experiment. This event was picked up by the CFM and is shown in Figure 4.14, marked by the red rectangle. The 'misfire' was distinct from the noise and the injections, seen on either side of the 'misfire'. This shows the capability of the Fast NGC technique for error detection of injections.

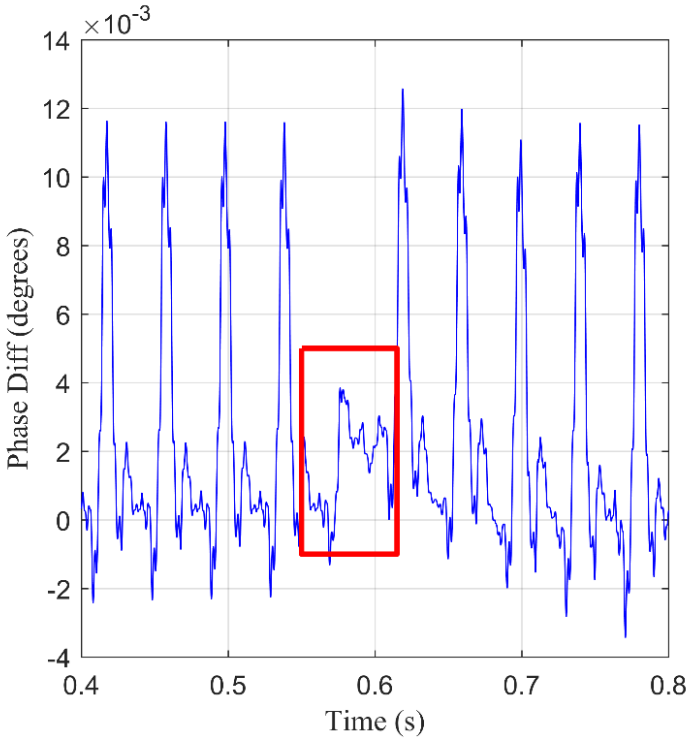

Figure 4.14: Misfire in the injection train at 2978 rpm of 1.5 ms injection duration.

4.2.7 Pressure measurements

Pressure measurements were taken upstream and downstream of the Coriolis Flow Meter to understand the effect of the hydraulic shock (pressure wave caused due to sudden closure of the injector) on the mass flow measurement. Figure 4.15 shows the pressure trace downstream (P1) and upstream (P2) of the CFM for a single injection of 2 ms with SOI at 5 ms. There was a significant pressure increase after the EOI, suggesting a pressure wave travelling back into the

fuel pipeline. For reference, the EOI is at the bottom of the P1 signal. Further, the P1 and P2 traces difference shows that the Coriolis meter acts as a damper. This damping effect by the Coriolis meter would influence the phase difference measurement due to the energy dissipation through the flowtube (caused due to the geometry of the CFM). Due to the lack of spill line the energy dissipates in the CFM and increases the noise observed in the signal and needs to be considered in a GDI setup.

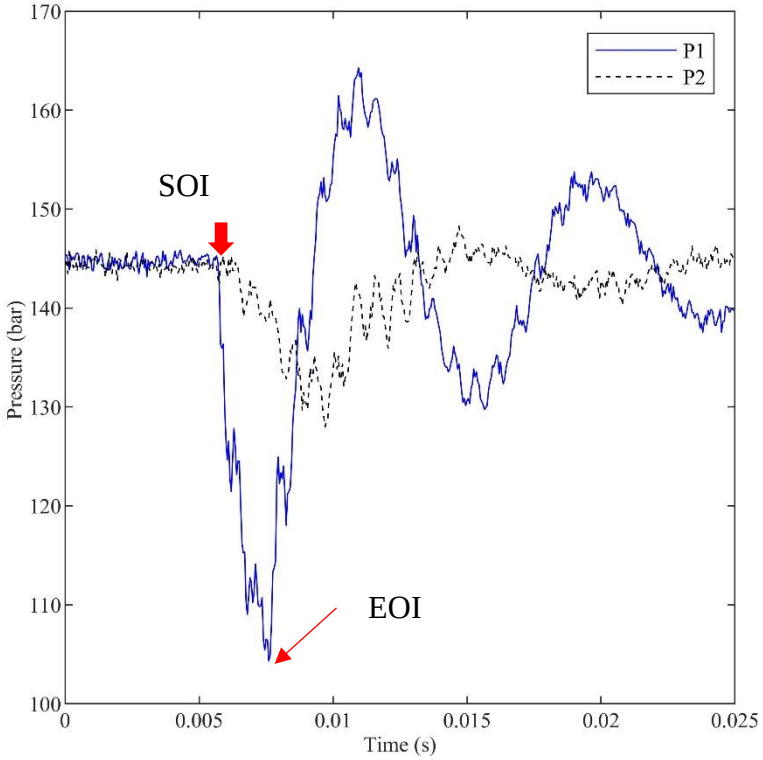

Figure 4.15: Single injection pressure traces pressure measurement of the fuel injection for 2 ms with the injection SOI request at 5 ms. The SOI of the injection shown with the red arrow.

Figure 4.16 shows the pressure difference for 100 injections (P2-P1). These pressure traces show matching details observed in the phase difference data, such as the reverse flow observed at SOI showing the capability of the Coriolis flowmeters in injected mass measurement (Figure 4.5). The repeatability of the injections can also be observed as the pressure traces follow the same profile. A minor negative pressure drop (i.e. pressure rise) suggests reverse flow due to needle lift at the SOI (shown by the black circle), which was also observed in the CFM data.

The secondary peak was caused due to the reflected pressure wave after the EOI (shown by the red square). This reflection occurs when there is a discontinuity in the pipe network, the junction between the fuel pipeline and the CFM. The cause and implications of pressure reflections are further discussed in the next chapter (Chapter 5).

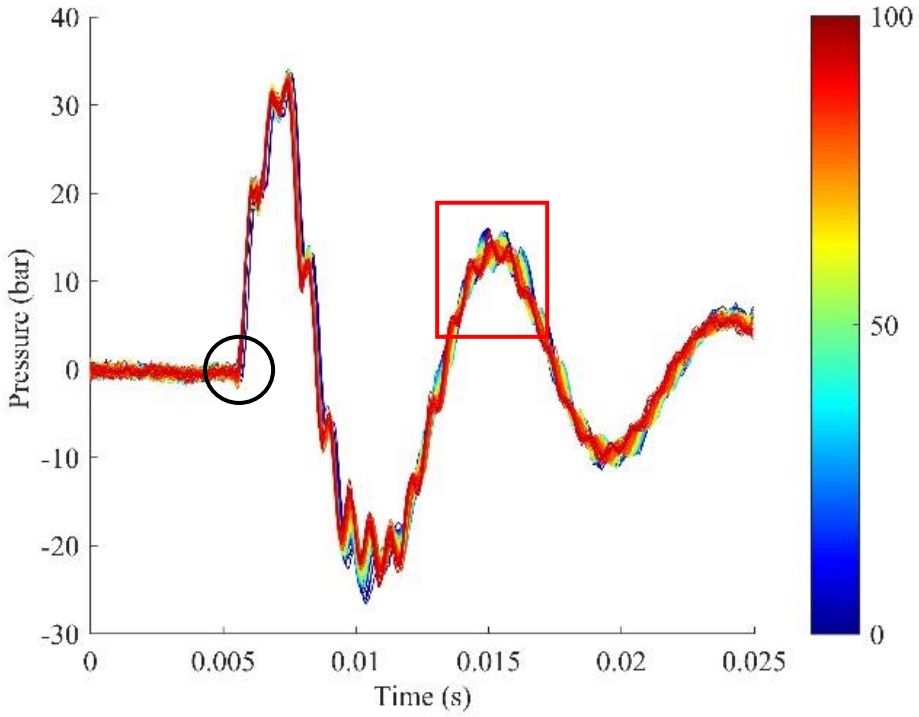

Figure 4.16: Pressure difference of the 100 injections (P2-P1) for 2ms injections at 150 bar. Black circle shows SOI with a small negative pressure also seen in CFM data. Red rectangle shows the reflected pressure wave.

4.3 Chapter summary

A CFM was installed into the GDI spray rig, and injections with an injection pressure of 150 bar were tested. Further, pressure sensors were also installed to gather data on injection pressures during the Coriolis tests. The pressure data recorded during the mass calibration data was used to observe the pressure traces upstream and downstream of the CFM. The initial signal processing of the CFM data with PRISM was completed by AIRG. This data was then used to analyse the FNCG method for GDI applications.

The FNGC technique measured and differentiated individual injections in both single injections and injection trains at simulated engine speeds of 1788 rpm and 2978 rpm. There were some notable features in work undertaken for GDI experiments. Negative mass flow due to needle lift at SOI was observed. The system was also capable of fault detection by observing a misfire in an injection train at 2978 rpm.

The technique was successful in detecting individual injection pulses in a simulated pulse train up to 2978 rpm. AIRG processed the raw data CFM data. The data from AIRG was then post-processed to assess repeatability with the method described above. Individual injections were integrated as triangles for the first approximation of the mass injected. A CoV between 0.94% to 6.6% was observed in these preliminary tests indicating the potential use of Fast NGC in fuel measurement.

The injections could, however, only be measured when injected at multiples of the flowtube oscillation period due to the instantaneous phase of the flowtube affecting the DC offset and measured peak phase difference. The data presented in this chapter discounted the DC offset. It was observed that the injection duration and the flowtube phase influenced the peak height.

The lack of a spill line in the GDI setup significantly increased the mechanical vibrations at SOI and EOI. This required designing and careful mounting of the flowtube to reduce vibrations. Additional Prism filters stages (two DNFs) before the RST were included in the signal processing of the data. AIRG did the offline analysis of the CFM raw data to implement all the required Prism stages to remove the noise in the measurement. This processed data was presented in the chapter.

The injections were measured to be approximately 16 ms wide, while the actual injection durations were much shorter (1 ms to 2 ms). The elongation of the injection width observed was attributed to mechanical and digital filtering of the injection caused by the flowtube oscillation period being longer than the injection duration.

The pressure difference seen across the CFM shows that the CFM acts as a plenum damping the pressure waves caused by the injection upstream of the CFM. This shows that the CFM absorbed part of the pressure wave energy of the hydraulic shock and was damped through the flow meter, which influences the phase difference signal. This was seen as increased noise in the signal. The negative mass flow rate at SOI due to needle lift was also detected in the pressure signal as a tiny pressure difference at the start of injection. The features observed in the phase difference data also appear in the pressure data, confirming that the pressure wave caused at the EOI influences the phase difference measurement.

In the current form, the FNCG technique fails to meet the criteria compared to the specification required for on-engine measurement discussed in Table 2.1. The slow drive frequency caused a mechanical filter reducing the response time. The PRISM digital filtering further includes a stretch in the signal. With the dependency observed in the CFM phase, the mass injected per injection cannot be directly calculated with the data. This is further coupled with the requirement of vibration isolation in the setup for clean measurement. Due to current limitations, Coriolis meters cannot provide the mass flow rate for injectors.

The CFM, however, shows the potential to be used in GDI injection mass measurement applications. This method requires further improvements to enable injection rate shape measurement. One way to improve this method is with CFMs with an increased frequency of oscillation (order of kHz). This increase in the drive frequency can be achieved by increasing the ratio of stiffness to the second moment of inertia (K/I). While the CFM stiffness, K, can be increased by increasing the wall thickness with the current CFM size, this will also further increase the inertial component, I. However, by reducing the overall size of the CFM, I is reduced while the K term can be scaled to match. This design reduces the size of the CFM, making it a more suitable option for on-engine deployment of this measurement technique. The increased drive frequency with this improved design and a smaller CFM size will enable a

broader range of injection frequency and reduce the injection stretch in time that has been observed in the experiments. The next chapter explores techniques using the fuel pipeline pressure measurement to infer mass flow rate directly.

5 Applying continuity to pressure measurements for mass injected calculation on GDI injectors

Pressure measurements can directly be used to calculate the mass flow rate and hence the injected mass; the theory for this is discussed and derived in Section 2.2. The mass injected per injection can be calculated using the one-pressure transducer method (OPTM) and two-pressure transducer method (TPTM) from pressure measurements taken in the fuel pipeline. Experiments were conducted to understand the limitations of both the pressure methods described. The following section describes the experimental methodology, including the setups and test conditions of the experiments conducted. Then, the results of these tests were analysed and discussed. Finally, a summary of the investigations undertaken was presented. These conclusions were used to design the apparatus used for the on-engine application.

5.1 Experimental methodology

The initial setup was a modified version of the Oxford spray rig [84] described in Section 3.1. Experiments were conducted to develop the pressure method theory and to better understanding the limitations of each pressure method. The robustness of the methods was tested by incrementally adding sources of error that might be present in a realistic setup. It is known that any sudden radial changes in the pipelines are sources of pressure reflections and energy loss. Hence, the initial setup was modified to eliminate any pressure reflections caused due to sudden changes in the pipeline's radius near the injector. This ensured that the pressure drop measured due to injection was detected with minimal energy losses and enabled the evaluation of the pressure methods accurately with a close to ideal setup. The injector mount used to connect the fuel pipeline to the injector was redesigned with a 1:48 ratio tapered section internally to enable a smooth transition of diameter from the injector internal diameter (ID) (4.75 mm) to pipeline ID (4 mm). The measurement pipeline was then installed flush with the end of the tapered

section to ensure no discontinuity (sudden radial change) between the pipeline ID and injector mount; this ensured minimal energy was lost between the injector mount and the pipeline. The Swagelok fitting used to connect the pipeline to the injector mount was modified by increasing the ID to enable the pipeline to go through the fitting. Figure 5.1 shows the redesigned injector mount with the fitted fuel pipeline into the injector mount.

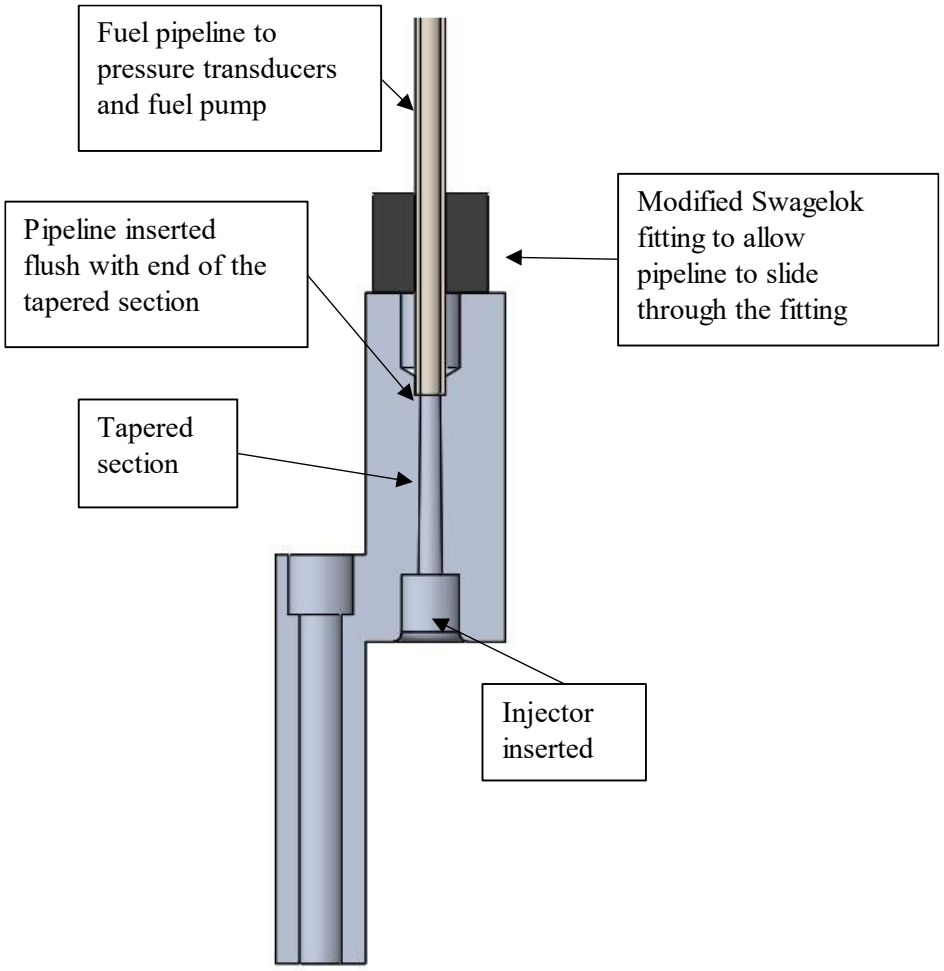

Figure 5.1: Redesigned injector mount section view with a 1:48 ratio tapered section between the injector side and pipeline side. The pipeline is installed flush end of the tapered section to reduce any sudden radial changes. A Swagelok fitting was modified by increasing the diameter to enable the pipeline to slide through the fitting.

The initial experimental setup used for the test campaign is shown in Figure 5.2. The initial design includes a pipe length of 3 m from the injector mount to the first Swagelok fitting, and was fitted onto the mount with no discontinuities, as shown in Figure 5.1. The pipeline was not

bent till the ceiling to ensure as long a straight section of pipe as possible. The straight pipe length, L, was 1.75 m before the first bend. This pipe had two Kistler pressure transducers installed that were used for pressure measurements. The length between the pressure transducers P1 and P2 was calculated to be in the range of $5ct$ to $7ct$ (where c is the speed of sound and t is time-step (reciprocal of frequency of data acquisition)) [61], [62] to enable high-quality data acquisition at 20 kHz. The pressure transducers were installed at a distance, l, of 400 mm from each other, with P1 being installed 50 mm from the top of the injector mount. In this setup, the Kistler 4067E pressure transducers were used. A further 6 m (2 x 3 m pipes) of the coiled pipeline was installed upstream of the measurement pipeline to minimise reflections from the fuel pressure accumulator or pump within the injection window. This coiled pipeline increased the transmission time of the pressure drop, due to injection, to the fuel pump and, in turn, increased the time taken for the reflected pressure wave to be observed by the pressure transducers. A third pressure transducer, P0, was installed near the fuel accumulator to monitor the fuel pressure during the experimental runs. The specification of the P0 transducer was discussed in Section 3.1.5.

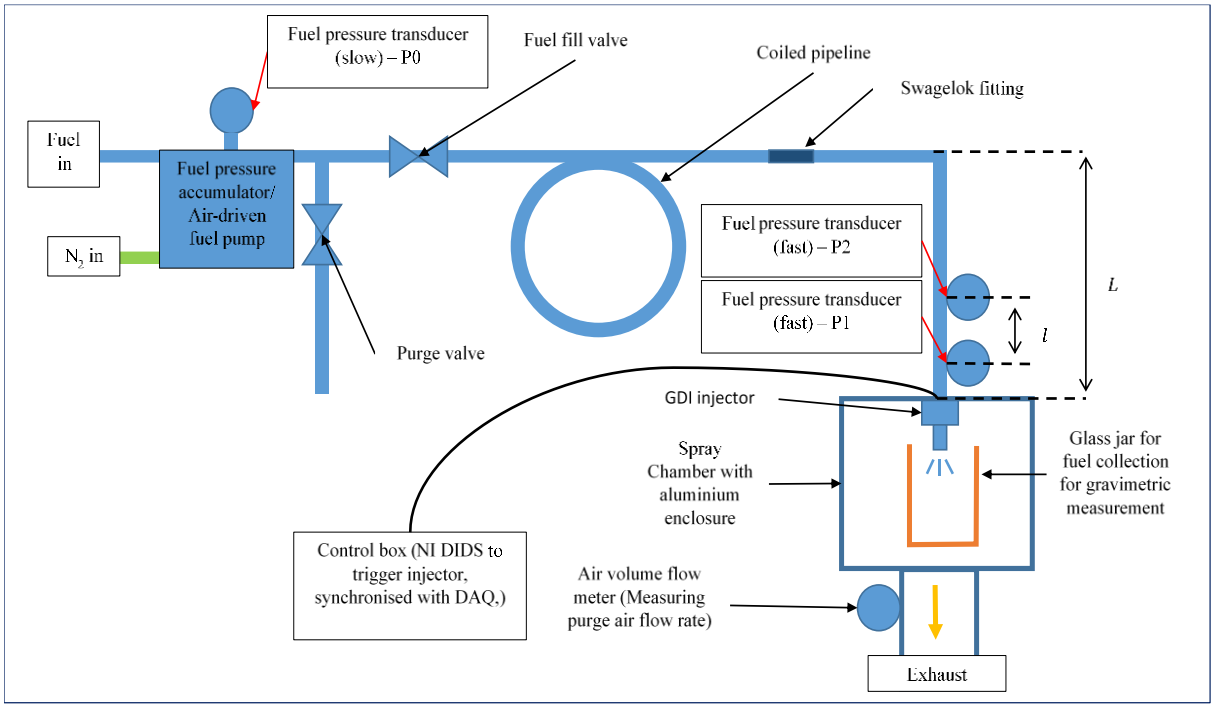

Figure 5.2: Modified Oxford spray rig setup for initial pressure measurement experiments. A pipe length, *L*, 3 m from the injector mount to the first Swagelok fitting with a straight pipe length is 1.75 m before the first bend. This was used for setup 1,2 (Table 5.1). Not to scale.

Sources of noise and discontinuities were added to the setup described above to understand their effects on the pressure measurements. Table 5.1 shows the different changes made to the original setup (Figure 5.2) used in the experiments. The changes were done incrementally with the changes being made on the preceding setup. Initially, a fuel pressure accumulator was installed to pressurise the fuel to the desired level. However, this limits the amount of fuel that can be injected, especially when the setup is to be installed for on-engine measurement. The fuel pressure accumulator was replaced with an air-driven pump (HEYPAC KR20 [85]), which can be used on an engine (setup 2, Table 5.1). The double-acting pump increased the fuel capacity for the on-engine application.

Table 5.1: Experimental setups used in the pressure method experiments. The changes described are made incrementally on the Oxford spray rig.

Experimental setup	Change description
1	Original setup with a fuel pressure accumulator, Figure 5.2
2	Original setup with HEYPAC fuel pump replacing the pressure accumulator, Figure 5.2
3	Discontinuity of 3.5 mm between injector mount and measurement fuel pipeline by cutting the pipeline in the injector mount, Figure 5.3
4	Fuel pipeline with measurement pressure transducers reduced to length, *L*, of 0.92 m
5	The pipeline between the sensors bent with 4 90° bends creating a loop
6	2.4 m measurement fuel pipeline with 200 mm between P1 and P2 pressure transducers with 90° bends at every 100 mm. The Kistler 4067E sensors replaced with Kistler 4007D sensors. This setup is used for 40 kHz data acquisition experiments.
7	Single-hole injector at 100 bar injections

Pressure waves reflect at discontinuities, such as sudden changes in pipe diameter (caused by pipe fittings) and pipe bends [111]. A dead volume was introduced near the injector mount (setup 3, Table 5.1) to quantify the impact of small discontinuities in the pipeline caused due to sudden radius changes. This was achieved by cutting the pipeline in the injector mount by 3.5 mm to give a volume of 98.96 mm^3 and two sudden diameter changes from 4 mm to 6 mm and the inverse. Figure 5.3 shows the injector mount section with the pipeline discontinuity.

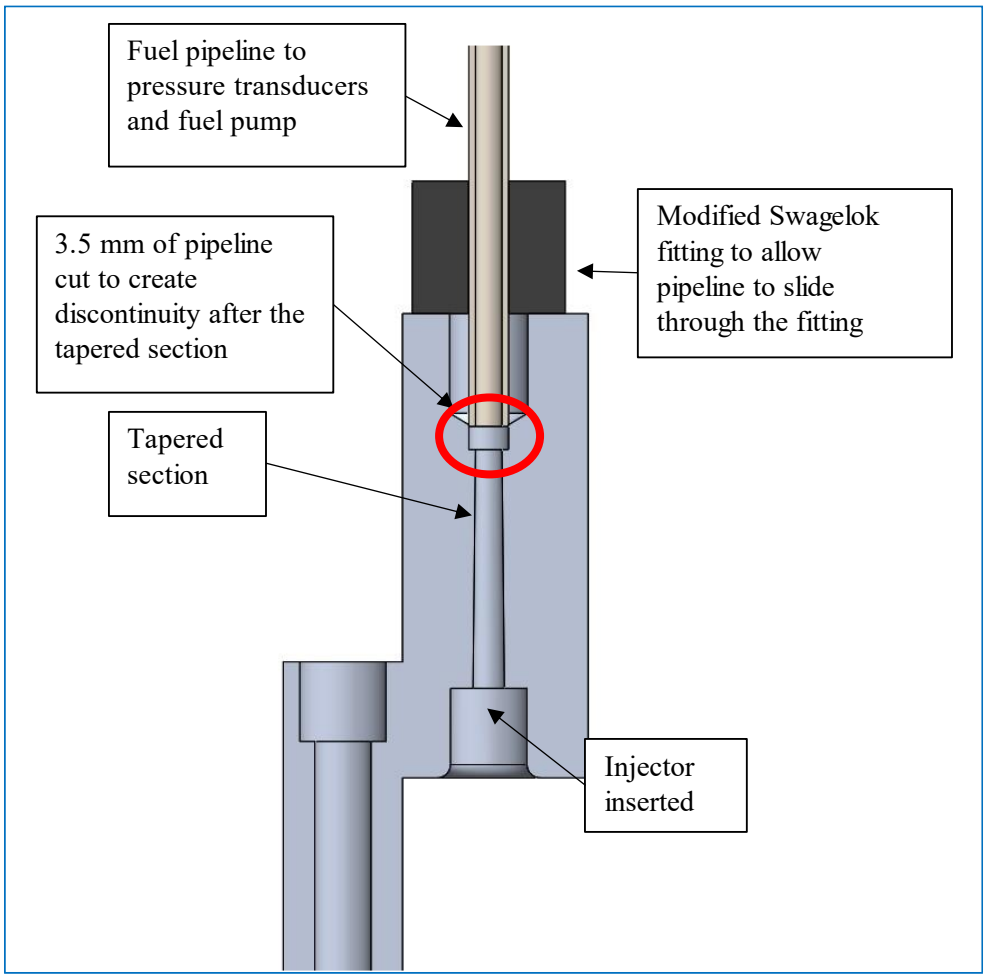

Figure 5.3: Injector mount with a discontinuity at the end of the tapered section caused by cutting 3.5 mm from the pipeline. This refers to changes made for setup number 3 (Table 5.1).

Setup 3 was modified (Table 5.1) by shortening the pipe length, *L*, to 0.92 m to induce reflections in the injection window and to observe the effects of these on the pressure methods (setup 4, Table 5.1). Finally, the pipeline between the sensors was coiled to study the effects caused by bends between the sensors. The pipeline was bent into a loop with four 90° angle bends between the two pressure sensors (setup 5, Table 5.1). Creating a loop with the fuel pipeline reduced the physical length required whilst maintaining the pipeline's effective length. This makes the pressure method's setup more compact and suitable for on-engine implementation. Figure 5.4 shows the diagram of the experimental setup 5.

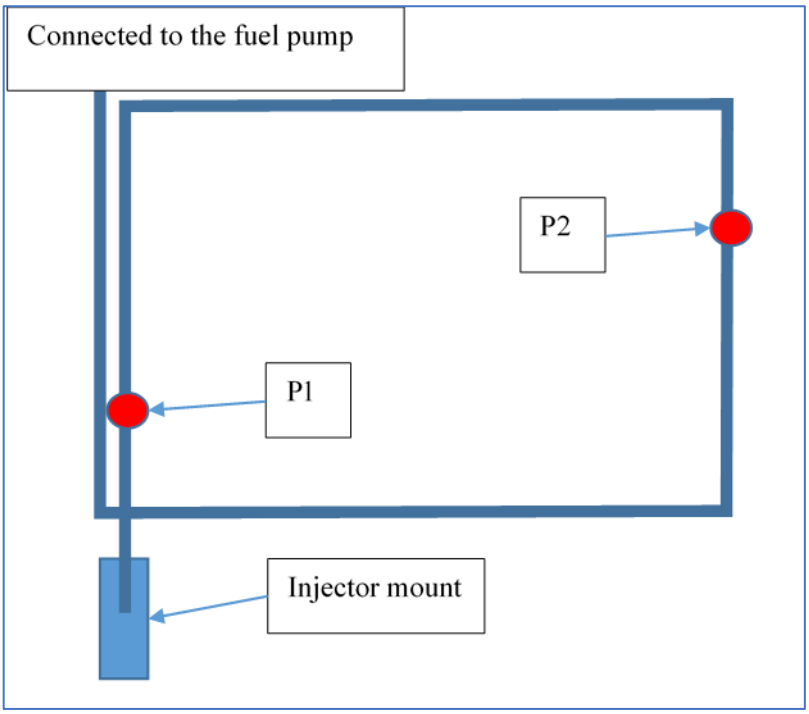

Figure 5.4: Measurement pipeline bent into a loop with a total length of 0.92 m. This refers to experimental setup 5 (Table 5.1).

For experimental setups 1 to 5, the experiments were performed at three injection durations of 2 ms, 1.5 ms, and 1 ms with an injection period of 200 ms during the experiments. The injection period of 200 ms corresponds to 600 rpm engine speed. Initially, each test included 150 injections, but this was increased to 300 injections to reduce the uncertainty caused in the gravimetric measurement. After each test, the mass of the glass jar was recorded to compare with the pressure methods. The weighing machine's accuracy was 0.1 g, and the uncertainty in the gravimetric method for 1 ms injection reduced from 5% to 2.5% (maximum error) by doubling the number of injections. Further, by doubling the number of injections, the uncertainty in the average mass injected calculations from the pressure method reduced from 8.2% to 5.8% ($1/\sqrt{number\ of\ injections}$). Table 5.2 below shows the conditions used for the pressure measurement experiments for setups 1 to 5. Further tests with injection periods of 120 ms, 80 ms and 60 ms (which correspond to simulated engine speeds of 1000 rpm, 1500 rpm and 2000 rpm, respectively) were conducted on the experimental setup 5.

Table 5.2: Experiment conditions for experimental setup numbers 1 to 5

Experiment conditions	Value
Injection duration (ms)	1, 1.5, 2
Injection period (ms)	200
Injection pressure (bar)	150
No of injections	150, 300

For the experimental setups 1 to 5, the pressure data was acquired at 20 kHz for each channel. The LabVIEW program's injection request triggered the pressure data acquisition from the control box (Figure 5.2). Initially, 500 samples were recorded, with 100 pre-trigger samples collected before each injection for each injection signal. However, this limited data acquisition speed and only saved part of the data at simulated engine speeds experiments higher than 1000 rpm. The program was changed to continuous recording to save the simulated engine speed data.

Once the 20 kHz experiments were completed, the pipeline was changed for a higher data acquisition rate of 40 kHz, using the limit of $5ct$ to $7ct$ for high quality data acquisition [61], [62] the distance between the sensors, l, was reduced to 200 mm. The Kistler 4067E pressure transducer were replaced with Kistler 4007D sensors. The pipeline length was 2.4 m to the first Swagelok fitting without any discontinuity at the injector mount. The pipeline was bent every 100 mm with 90° bends, creating a coil (experimental setup 6, Table 5.1). This pipeline was then directly connected with no discontinuity to the injector mount, as shown in Figure 5.1. The coiled pipeline between the measurement pipe and the fuel pump was also removed. Figure 5.5 shows the coiled pipeline in the setup used for these experiments. The data acquisition was continuous for each injection train. A GDI engine can operate at high engine speeds up to around 7000 rpm. Hence, the experiments were conducted at the same injection repetition rates

as for experimental setup 5 (600 rpm, 1000 rpm, 1500 rpm and 2000 rpm) and continued at intervals of 500 rpm up to 7000 rpm.

Figure 5.5: Coiled measurement pipeline used in experimental setup 6.

Finally, to verify that the pressure methods work with different injectors in experimental setup 7, the multi-hole injector was replaced with a single-hole swirl hole injector (Section 3.1.3). The experiments with this setup were conducted at 100 bar with the injection repetition rates equivalent to 600 rpm, 1500 rpm, 3000 rpm and 6000 rpm simulated engine speeds.

Using single-component fuels in the experiments makes it easier to calculate the speed of sound at different pressures, as these can be readily found in the literature [108]. Undecane was used for all the pressure method experiments on the spray rig; this was discussed in Section 3.3.

5.2 Results and Discussion

The data collected during the experiments was imported and processed in MATLAB for calculating the mass injected. The raw pressure traces and the current trace for a single injection of 2 ms are shown in Figure 5.6. The injector current signal is plotted in red, and the pressure traces are shown in solid blue (P1) and dashed black (P2). The current signal was first sent to the injector, and the pressure change caused by the injection lag behind this current signal (red dot-dash). The P1 pressure trace has a sharp reduction of pressure caused at the start of injection (SOI), and at the end of injection (EOI), there was a pressure rise in the P1 signal. The same trend is observed in the P2 trace (dashed black) with a time delay, as seen in the figure. The delay in injection pressure drop between P1 and P2 was due to the additional distance travelled by the pressure wave between the two pressure transducers.

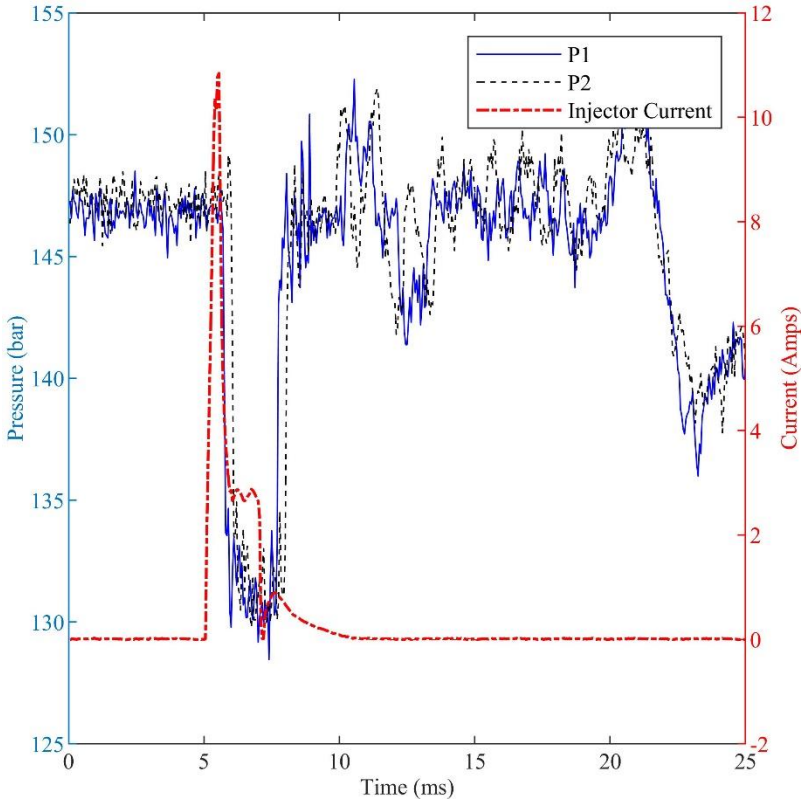

Figure 5.6: Single injection pressure data from P1 and P2 for 2 ms injection along with the current profile for the injector at 20 kHz acquisition rate on experimental setup 1.

5.2.1 Effects of the sensor range

The range of the sensor affected the noise observed in the sensor. Figure 5.7 shows the P1 signal for a single 2 ms injection in both the 4067E sensor with a range of 0-3000 bar and 4007D sensor with a 0-250 bar. While the setup used were the same in both experiments, using the 4007D sensor shows reduced noise in the signal. The small differences observed in the reflection is due to using single injection data.

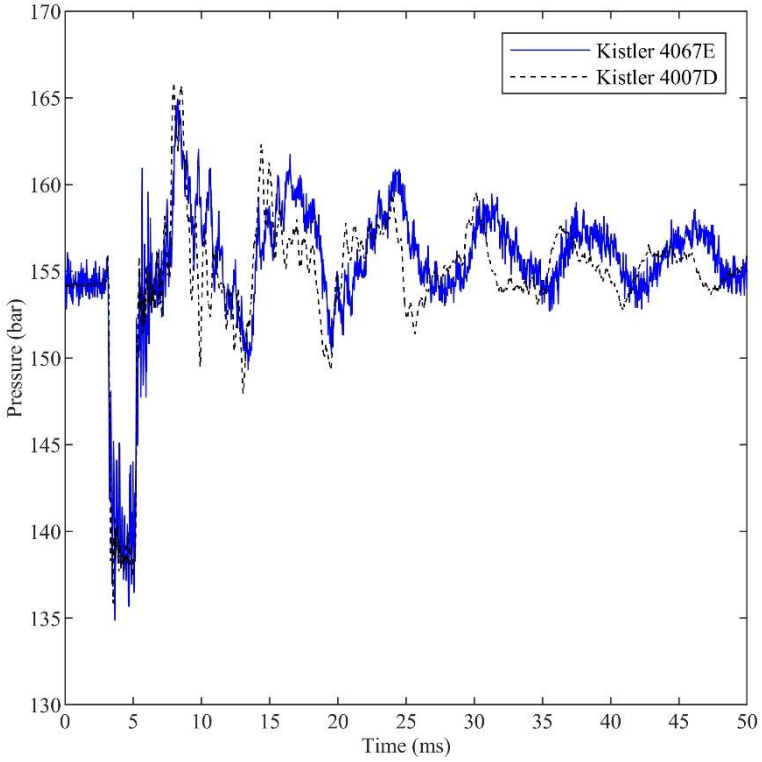

Figure 5.7: Sensor comparison between Kistler 4067E and Kistler 4007D for a 2 ms injection at 40 kHz acquisition rate.

5.2.2 Injection detection algorithms

Average pre-injection fuel pressure

The SOI and EOI can be detected using the average fuel pressure calculated for each injection. The SOI was defined as the last data sample above the pressure average, while the EOI was defined as the first data sample above the pressure average. Figure 5.8 shows a 2 ms injection SOI and EOI using the average fuel pressure. The method to calculate the average pre-injection fuel pressure is described in Section 5.2.3. While the method works to detect the SOI and EOI

of most injections, the SOI and EOI detection fails when falling or rising injections are caused by the fuel pump cycle. These injections were ignored as they form less than 1% of the overall injections. The method, however, degrades at injection repetition rates higher than 2000 rpm simulated engine speeds. This was due to pipe reflections after the injection influencing the following pressure trace; such that, most of the injections were not detected using the average pre-injection fuel pressure method.

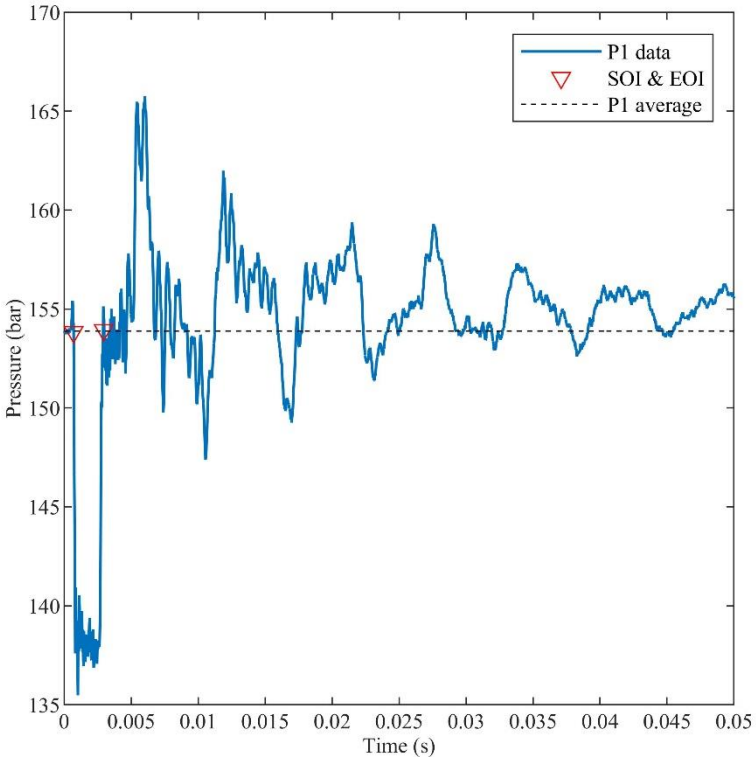

Figure 5.8: SOI and EOI detection using the average fuel pressure for 2 ms injection at 600 rpm engine speed.

Injector current signal

Ferrari et al. [13] used the current signal to define the SOI of the injection. Similarly, the injector's SOI and EOI can be detected by the rise and fall of the injector current signal. This can be used to look for an SOI and EOI in the pressure signal in a window after a certain time delay observed after the current signal (Figure 5.6). The SOI and EOI were defined as the first value higher than the average pressure drop after the current signal are above 0.5 A and below 0.5 A, respectively. This method, however, requires a secondary signal to be monitored and can

be influenced by the injector and the pipeline setup used. Figure 5.9 shows the injector current signal SOI and EOI detection.

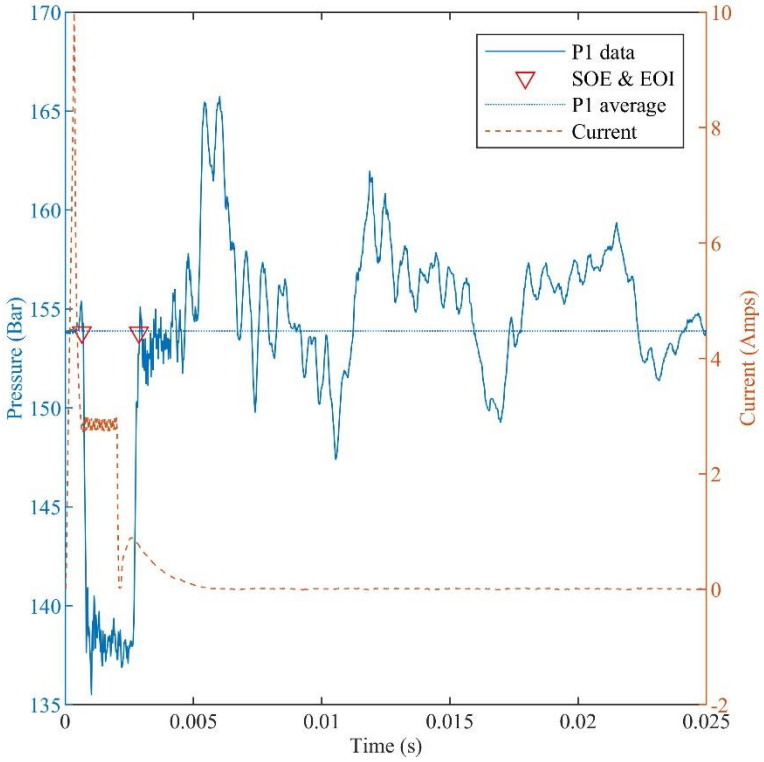

Figure 5.9: SOI and EOI detection using the current signal for a 2 ms injection at 600 rpm engine speed.

The gradient of pressure trace

The gradient of the P1 pressure signal can also be used for SOI and EOI. A median filter on the P1 data was applied before finding the gradient. The large changes in gradient caused by the pressure wave were used to detect the SOI and EOI. This captures all the injection pressure waves at higher injection repetition rates. Figure 5.10 shows the SOI and EOI detection using the gradient of P1 pressure signal. The peaks in the P1 gradient correspond to pressure drop and pressure rise in the P1 pressure signal caused due to SOI and EOI.

While the gradient method detects the SOI and EOI of all injections, it was limited by the level of noise in the signal. To ensure that it is not affected in the results, the average fuel pressure method was used in the analysis of the data in the experimental setups 1 to 5. The gradient method was used from experimental setup 6 onwards due to the smaller range sensors'

inclusion. While all three injection detection techniques have the same SOI and EOI at engine speed of 600 rpm, the gradient method demonstrated improved injection detection at higher engine speeds.

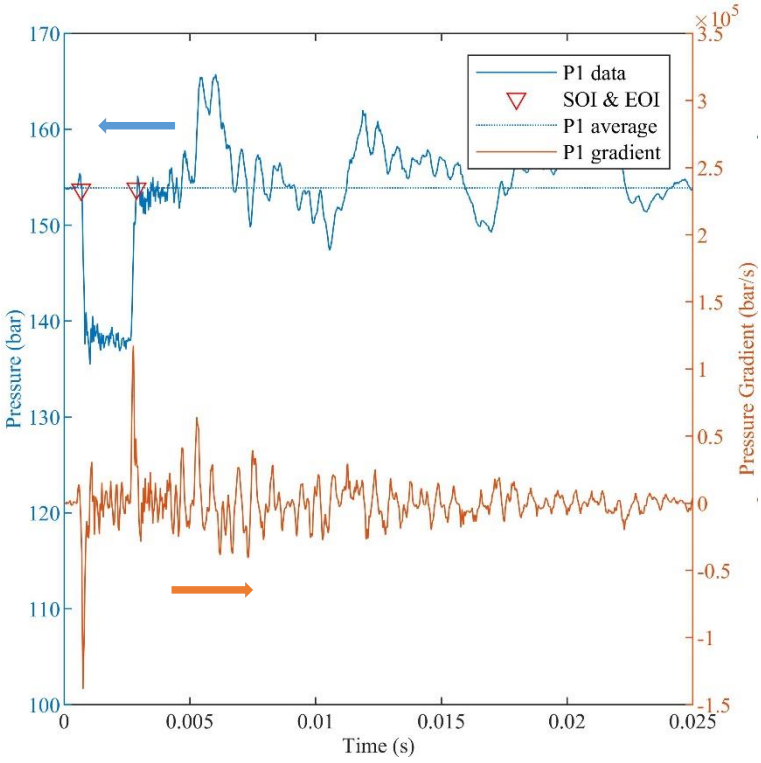

Figure 5.10: SOI and EOI detection using the P1 pressure signal gradient for a 2 ms injection at 600 rpm engine speed.

5.2.3 Calculation of average fuel pressure

The average fuel pressure was used to find the SOI and EOI in the pressure data and calculate the mass injected as described previously. The SOI was observed approximately 0.5 ms after the injection request from LabVIEW. This delay in pressure signal is a constant value and depends on the injector needle lift and the pressure sensor's distance from the injector tip. For the 20 kHz data, 100 pre-trigger and 10 post-trigger samples together can be used to find the average fuel pressure. However, with the inclusion of a fuel pump, the stroke might have falling or rising pressure waves during the injection; this effect is further discussed in Section 5.2.8. To ensure that this effect is considered, the minimum number of samples required to determine the 'true' average while still compensating for the pump stroke cycle was determined. Figure

5.11 shows the error in average pressure calculation as the number of samples used changes for 300 injections. The pressure average of each injection pressure was calculated using 110 samples, and was compared with a pressure average with a reduced number of samples. The samples remove the pre SOI samples, reducing to only using the last 5 post-trigger samples. It was found that 1 ms of data (20 samples at 20 kHz) can be used to find the mean fuel pressure for the one pressure method. This was chosen as the minimum number of samples required for the error to be within 0.5 bar of the true mean. Simultaneously, any injection with rising or falling pressure can still be detected and used for the pressure with the modified pressure average calculation. There is still a potential that there might be an injection that occurs during a pump stroke. However, this happens with less than 1% of the injections where the pump interacts with the injector, and these injections were ignored.

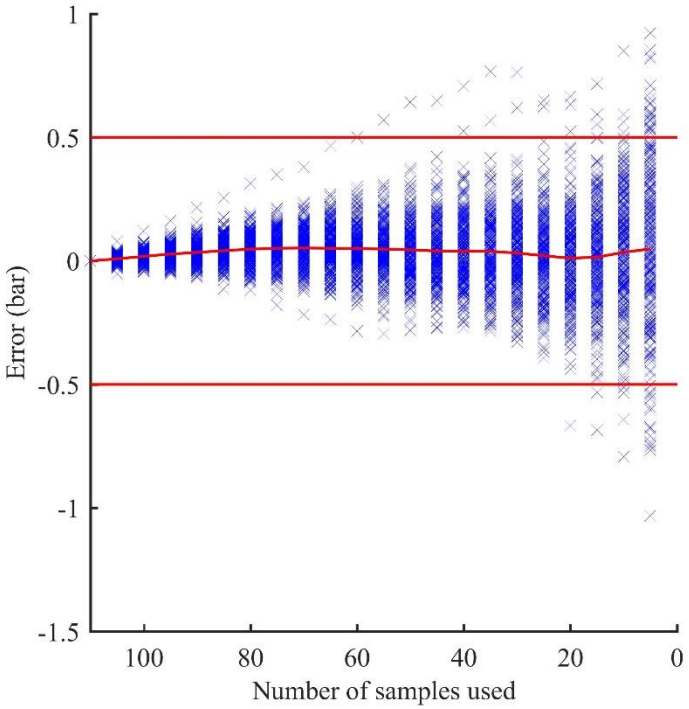

Figure 5.11: Error calculation in pressure average calculation with the inclusion of fuel pump (experimental setup 2). The outliers in the average are the cycles where the fuel pump cycle influences the average pressure calculation.

5.2.4 Speed of sound

The speed of sound data for undecane at different temperatures and pressures was calculated from the literature [108] for each P1 pressure transducer data point; and this speed of sound was used to calculate mass injected using the OPTM.

5.2.5 One pressure transducer method

The spray rig design enabled a single pressure transducer (OPTM) to calculate the mass injected as there are no pressure reflections present in the injection; the pressure wave travels only in one direction. The OPTM calculates the instantaneous injected mass flow rate using Equation 2.6. The average fuel pressure calculated was used as the original fuel pipeline pressure for the injection. The SOI and EOI are detected using the average fuel pressure for experimental setups 1 to 5 and the gradient method for experimental setups 6 and 7. Figure 5.12 shows the injected mass flow rate with SOI and EOI marked for the P1 pressure data. The mass flow rate is integrated between the SOI and EOI, as shown in Equation 5.1, to find the mass injected for the injection.

$$m_{injected} = \int_{SOI}^{EOI} \dot{m}\ dt \tag{5.1}$$

Pressure method applied to signal P1 & P2

The OPTM was also applied to the P2 pressure signal. Figure 5.12 shows the instantaneous mass flow rate calculation on the P1 pressure and P2 pressure signal. P2 pressure data had a time delay in the instantaneous mass flow rate recorded, as expected from the pressure traces shown in Figure 5.6. Calculating the mass injected from the P1 and P2, the pressure method gave a lower mass injected than gravimetric measurement. Table 5.3 compares the OPTM applied to both P1 and P2 data and the gravimetric measurement. While P2 data calculated a lower mass injected than P1 data, the difference was small, and this was due to the energy lost in the pressure wave as P2 is further upstream compared to P1. The difference between P1 and

P2 data calculation usually was much smaller than the difference between gravimetric and the OPTM. Since P1 data has a smaller delay, this was used in the OPTM calculations.

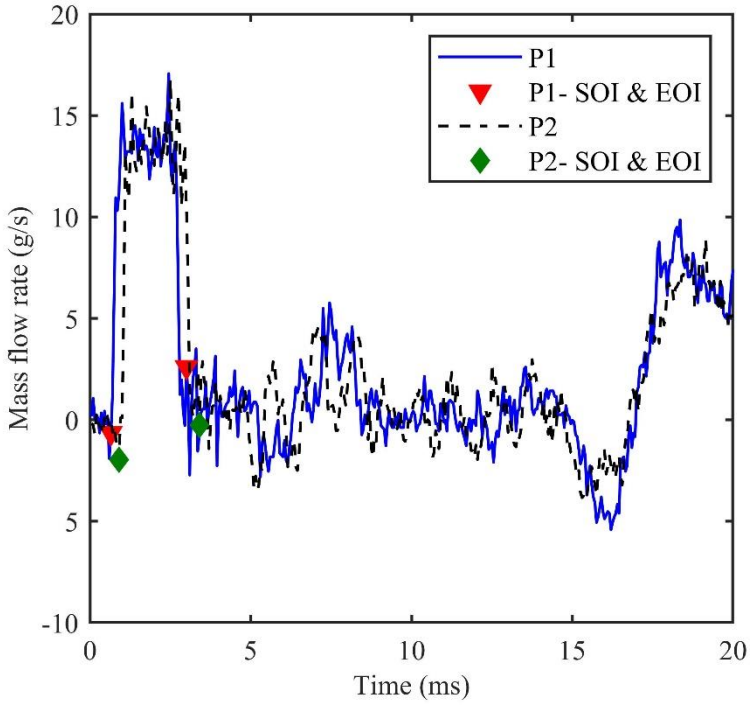

Figure 5.12: OPTM applied on P1 and P2 data of a single 2 ms injection on experimental setup 1.

Table 5.3: OPTM on P1 and P2 pressure data and the gravimetric measurement of the data.

Method	Mass injected per injection (mg)
P1 data	26.5
P2 data	26.4
Gravimetric	27.2

Pipe elasticity effects

The pressurisation of the pipeline from atmospheric to 150 bar increases the cross-sectional area of the pipe elastically. The change in radius caused by this pressure increase was determined to be 59.2 nm from Equation 2.13. The increased radius was included in the OPTM and had increased the mass injected by 0.016 mg in the P1 data used. The mass injected increase

was smaller than the difference between OPTM and gravimetric measurement (0.06%). Hence, the pipe elasticity effects were ignored in the mass injected calculations.

5.2.6 Two pressure transducer method

The TPTM is applied using both P1 and P2 pressure sensors. Equation 2.20 with friction term substituted (Equation 2.21) was used to calculate the mass flow rate. The SOI and EOI were defined from the P1 pressure signal. Figure 5.13 below compares the OPTM and TPTM mass flow rate calculated from the data. There was a slower response in the two-pressure method due to the time delay between the two sensors. However, as defined by Ferrari et al. [61], the EOI was not at the mass flow rate signal's peak. This was only an effect of the setup, and the EOI was defined according to the P1 signal.

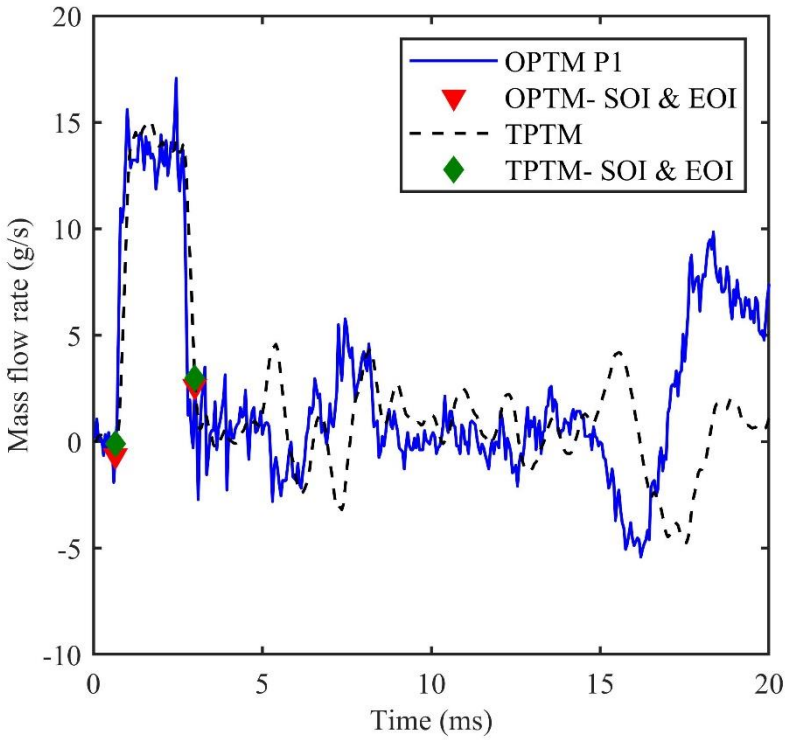

Figure 5.13: Comparison of OPTM and TPTM for a single 2 ms injection on experimental setup 1.

Pipe elasticity effects

The increased radius was included in the TPTM and had increased the mass injected by 0.03 mg. The mass injected difference was smaller than TPTM and gravimetric measurement (0.12%). Hence, the pipe elasticity effects were ignored in the mass injected calculations.

5.2.7 Comparison of pressure methods to gravimetric measurement

Figure 5.14 compares the OPTM and TPTM with gravimetric measurement on experimental setup 1. Each test point mass is averaged over 150 injections, and three repetitions were conducted for each injection duration (1 ms, 1.5 ms, 2 ms). The OPTM underestimates the mass injected by approximately 1.4%, while the TPTM overestimates the mass injected by approximately 0.4% compared to gravimetric measurement. This difference is within the uncertainty bounds in the gravimetric measurement. The OPTM underestimates the mass flow as there is still some energy lost in the transmission of the pressure wave, specifically in the injector. This error is expected in the TPTM results, however the TPTM calculates the mass flow rate with a fluid bulk (between the two sensors), the further loss of energy between P1& P2 sensors leads to the overestimation of mass injected. However, there was also a larger standard deviation observed in the TPTM compared to the OPTM. Two sensors create two sources of noise that are not temporally coupled, so the sensor noise propagated and compounded in the integration values. The plot below shows that the pressure method calculations gradient to be close to unity, showing that both pressure methods can calculate the mass injected.

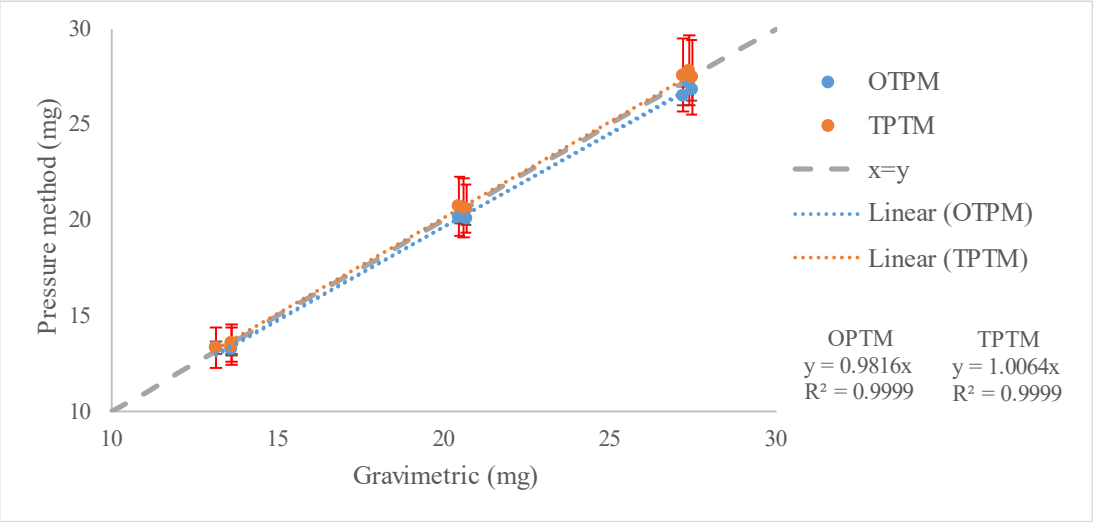

Figure 5.14: Comparison of gravimetric and pressure method for experimental setup 1 with each test point averaged over 150 injections at 150 bar. Tests were conducted over 1 ms,1.5 ms and 2 ms injection durations with a 200 ms injection period between injections. ±One standard deviation is plotted for the pressure method calculations.

5.2.8 Fuel pump

The fuel accumulator was replaced with an air-driven double-acting fuel pump (experimental setup 2, Table 5.1) that was to be used on the optical engine. During the injection train, pumping cycles reduced the fuel pressure from the injection pressure of 152 bar to approximately 137 bar. Figure 5.15 shows the calculated average pressures in an experiment with 300 injections plotted as a histogram. Over 70% of the injections average pressure was between 150 bar and 152 bar (requested injection pressure was 152 bar), while the rest of the injections occur in the pumping up to injection pressure—the fuel pump cycles at the end of the piston travel. However, the inclusion of the fuel pump cycles did not impact the mean calculation in pressure methods. The pumping causes two distinct injection pressure regions in the fuel injections, caused by the fuel pump's upstroke and downstroke.

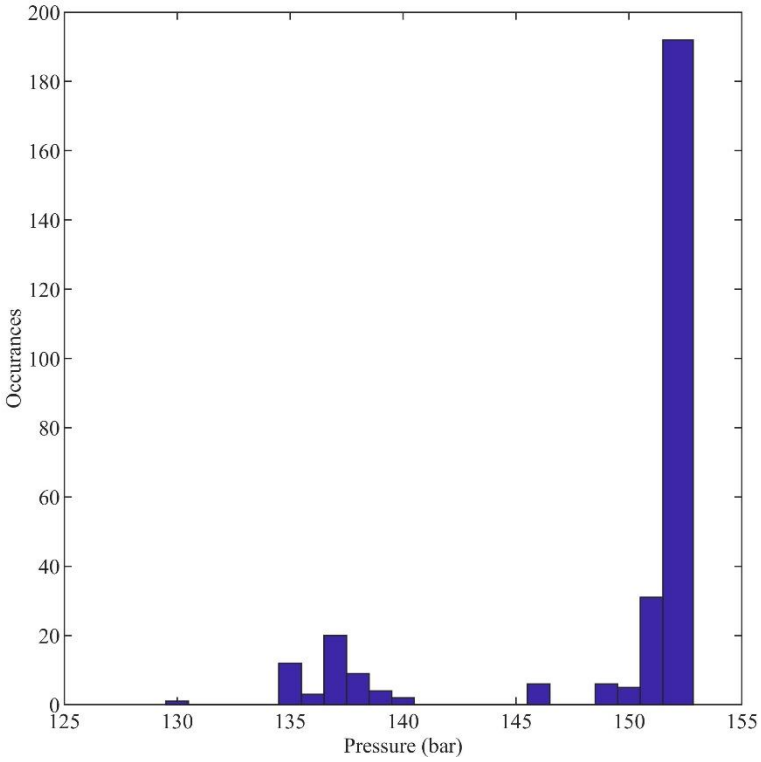

Figure 5.15: The calculated average pressure for 300 injections with the inclusion of the fuel pump.

Figure 5.16 shows the comparison of the inclusion of the pump in the pressure calculation versus gravimetric measurement. The difference of the pressure methods on experimental setup 2 compared to the gravimetric data remained the same as initial the experimental setup. However, the standard deviation increased in both the OPTM and TPTM; this was caused due to the different mass injected at different pressures in the pump's strokes.

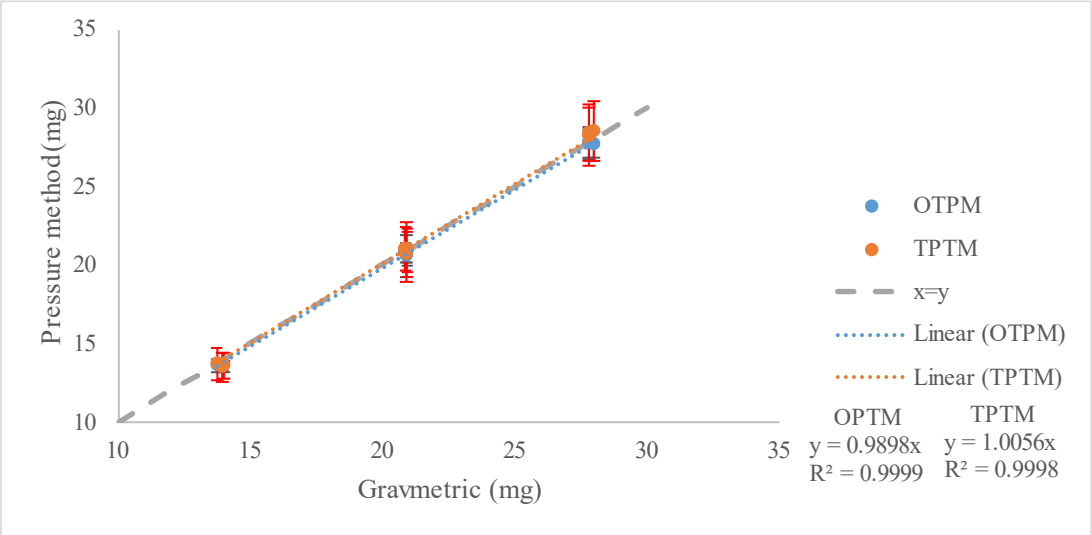

Figure 5.16: Comparison of pressure methods with gravimetric measurement for fuel pump setup (experimental setup 2) with each test point averaged over 150 injections at 150 bar. Tests were conducted over 1 ms, 1.5 ms and 2 ms injection durations with a 200 ms injection period between injections. ±One standard deviation is plotted for the pressure method calculations.

5.2.9 A pipe discontinuity

A dead volume was created by removing a pipe section to create a discontinuity in the injector mount (experimental setup 3, Table 5.1). This dead volume fills with fuel, and energy was partially dissipated into this section of the pipeline in the form of pressure reflections. This loss of energy was not picked up by the sensors upstream of the discontinuity and will increase the error in the mass injected calculation. Since the discontinuity was small, the energy loss was minimal. Figure 5.17 shows the average difference between the pressure methods when compared to gravimetric measurement. Each of the OPTM and TPTM average difference bars was averaged over nine injection trains (3 each of the 3 different injection durations) with 150 injections. Fuel pump and the pipe discontinuity difference compared. The following equation defines the difference for the injection set:

$$Difference\ (\%) = \frac{pressure\ method\ calculated\ mass\ -\ gravimetric}{gravimetric} * 100 \quad (5.2)$$

The calculated mass injected value was reduced by over 2% in both the pressure methods, but the error was still within 5%. The error in both methods was smaller than the uncertainty in both the gravimetric measurement and pressure method calculation. Hence, both methods can be implemented even with small discontinuities within the pipeline.

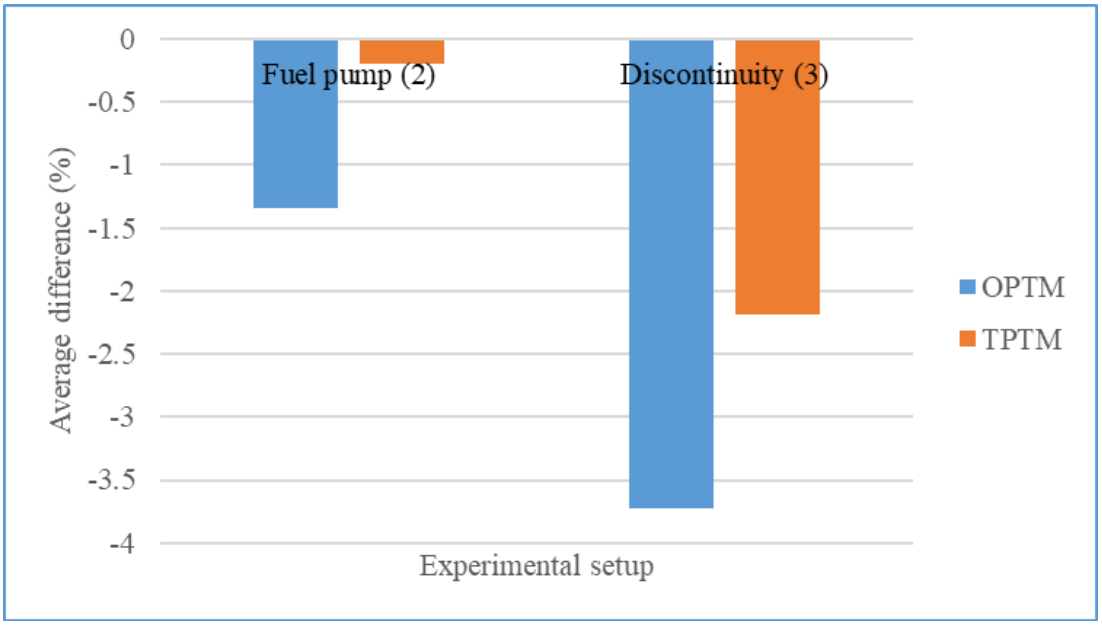

Figure 5.17: Average difference between pressure method calculation and gravimetric measurement for fuel pump setup and pipe discontinuity setup for both OTPM and TPTM.

5.2.10 Pressure reflections in the injection window

The effect of pressure reflections within the injection window would influence the setup and the pressure method for calculating the mass injected. It was observed in the pressure traces that pipe bends upstream of the pressure sensors did not cause any significant reflections in the injection and on the measurement. In contrast, pipe fittings caused an observable reflection. So, pressure reflections were forced within the injection window by reducing the pipeline's length to the first fitting (experimental setup no. 4, Table 5.1). The reflected pressure wave was expected to be first observed in P2 data, followed by P1 data. The pressure reflection is shown in Figure 5.18. The returning pressure wave was first observed in the P2 signal before the P1 signal. The pipeline's length was reduced so that the 2 ms injection has a reflection, as shown in the figure, while the 1 ms injection was not affected by any reflections.

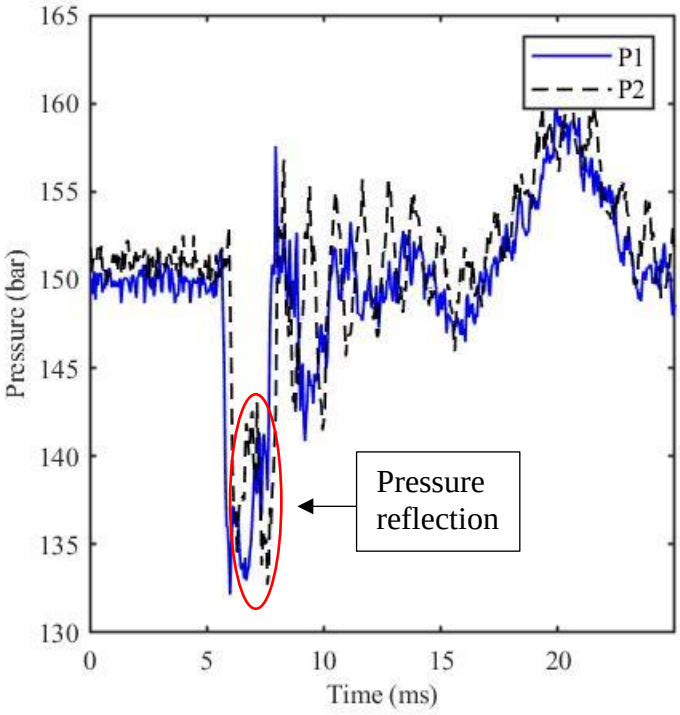

Figure 5.18: Pressure reflections in injection window of a 2 ms injection with injection period of 200 ms. The reflected pressure wave is observed in P2 signal and then is observed in the P1 signal on experimental setup 4. The pressure reflection is circled in red.

In theory, the OPTM can only be applied when there are no reflections during the injection (injection window). With the reflections in the injection window due to a shorter pipeline, the original OPTM required modification to be applied to the injections. The P1 signal after SOI was averaged for 20 samples (1ms); this average was forced for the rest of the injection for the 1.5 ms and 2 ms injections until EOI. However, this method causes issues, specifically when the injection duration matches the duration taken for the reflection to be observed at P1. This will increase the error; the pressure wave caused by EOI will interact with the reflected wave, and the EOI detected will not be accurate. However, the proposed corrected OPTM reduces the error. Using the original OPTM gives an error of 13.5%, while the compensated method reduces the error to less than 0.5% for a test with 2 ms injections. The P1 mass injected calculation with and without correction for OPTM for a 2 ms injection is shown in Figure 5.19.

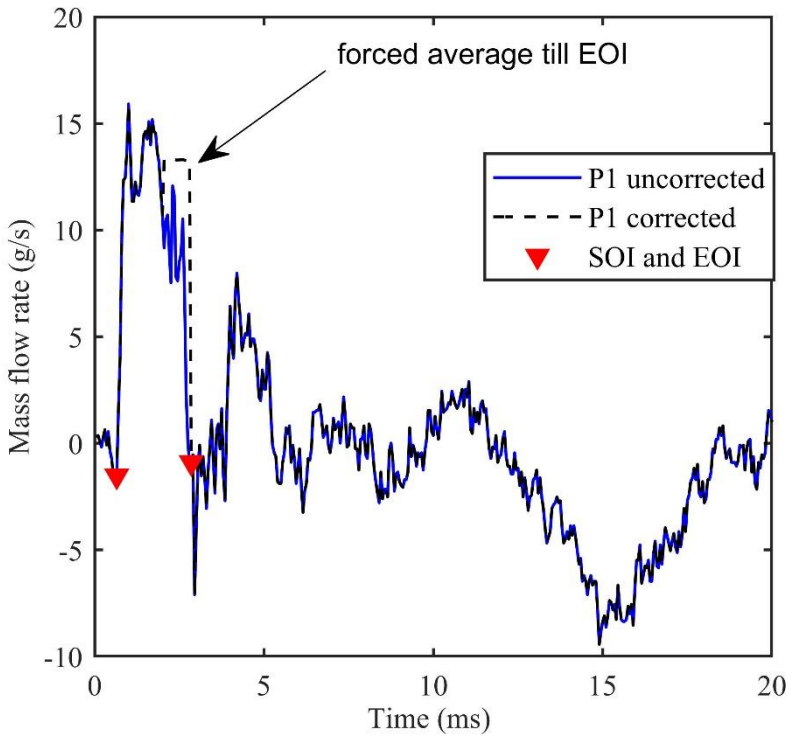

Figure 5.19: OPTM corrected and uncorrected applied to a single injection on experimental setup 5. The pressure method is applied on a 2 ms injection with an injection period of 200 ms between each injection. The forced section of the average is identified to show the change in OTPM due to the correction.

The TPTM can be directly applied as this method compensates for any reflections present in the injection. Each of the OPTM and TPTM average difference bars was averaged over nine injection train tests with 300 injections. Figure 5.20 shows the average error comparison between fuel pump results and shorter pipeline (which induce pressure reflection) results. With the presence of pressure reflections, the TPTM overestimates the mass injected as expected due to the bulk flow calculation even in the presence of reflections. In comparison, a compensated OPTM, the average difference and the standard deviation were similar to the original method. The compensated OPTM also had a similar average difference as the fuel pump inclusion results. This shows that the compensation can be used to calculate the mass injected even with reflections within the injection window.

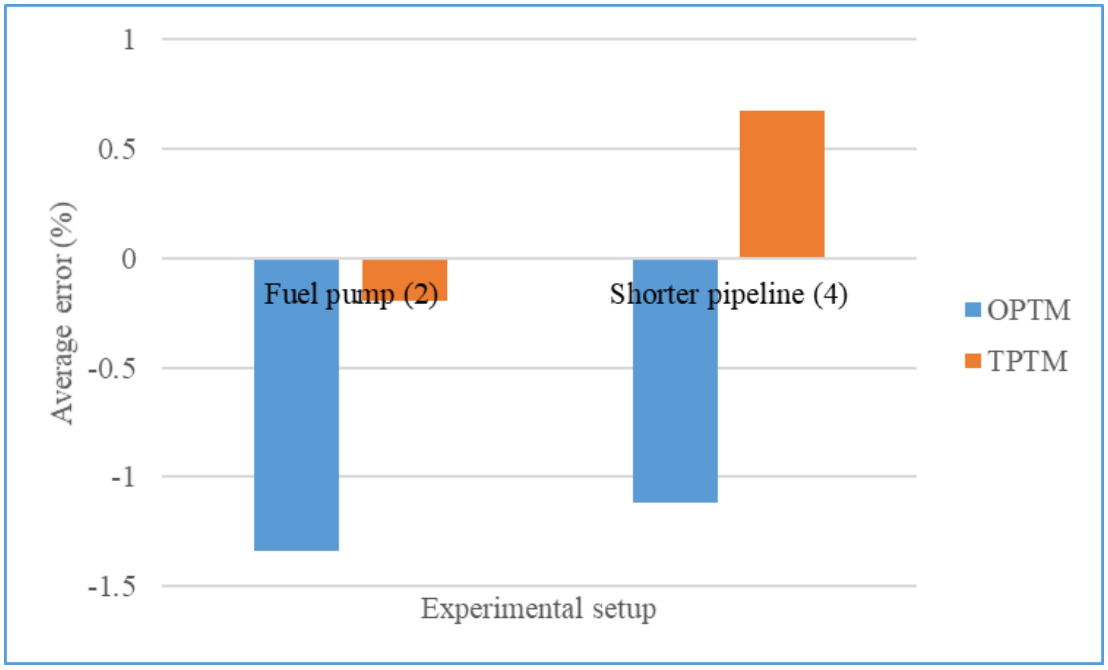

Figure 5.20: Average difference between pressure method calculation and gravimetric measurement for fuel pump setup and shorter pipeline (to induce reflections in the injection window) setup for both OTPM and TPTM.

5.2.11 Curved pipelines between sensors

The physical space requirements for the measurement system can be reduced by bending the pipeline while the pipe length remains the same, enabling the pressure methods to be used for on-engine applications. The pipeline was bent four times at 90° at 100 mm intervals to reduce the space required with no change to the length of pipe (experimental setup 5, Table 5.1). Figure 5.21 below shows the comparison of the average error in pressure methods. There were no significant differences observed in the pressure signals, and there are also no changes observed in average error caused due to the bends in the pipeline on both the pressure methods. The pipe bends even between the two pressure transducers, causing minimal pressure reflections. This shows that the pipeline can be coiled while the pipeline's effective length was the uncoiled length of the pipe. The 0.6% difference observed in TPTM between the shorter and coiled pipeline results was attributed to the uncertainty present in the pressure and gravimetric measurements.

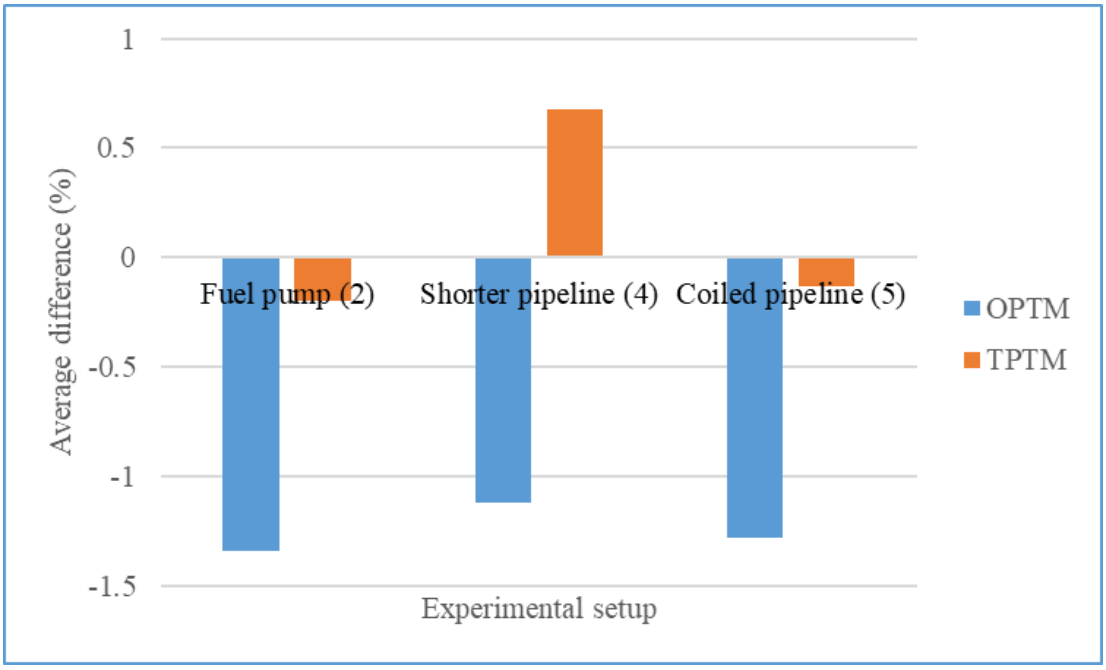

Figure 5.21: Average difference between pressure method calculation and gravimetric measurement for fuel pump setup, shorter pipeline (to induce reflections in the injection window) and coiled pipeline setup for both OTPM and TPTM.

5.2.12 Simulated engine speed operation

Simulated engine speed tests of 1000 rpm (120 ms), 1500 rpm (80 ms) and 2000 rpm (60 ms) were performed on experimental setup 5 to understand the effects of pressure waves on the increased injection frequency. Figure 5.22 shows the OPTM results for the three engine speed tests. The OPTM calculation was not affected at higher engine speeds. The 1 ms injection had the most significant difference (~5%) in the mass injected calculation compared to the gravimetric measurement. The gravimetric measurement error for a 1 ms injection is 2.5%, compounded with the uncertainty in measuring 300 injections (5.8%) is within the range of uncertainty present in the experiment. A few injections interacted with the fuel pump cycle during the pump stroke during the simulated engine test. The average fuel pressure method for SOI and EOI technique described in Section 5.2.2 enabled the calculation of mass injected for most of the injections. In a few injections, this was not possible, and these injections were ignored.

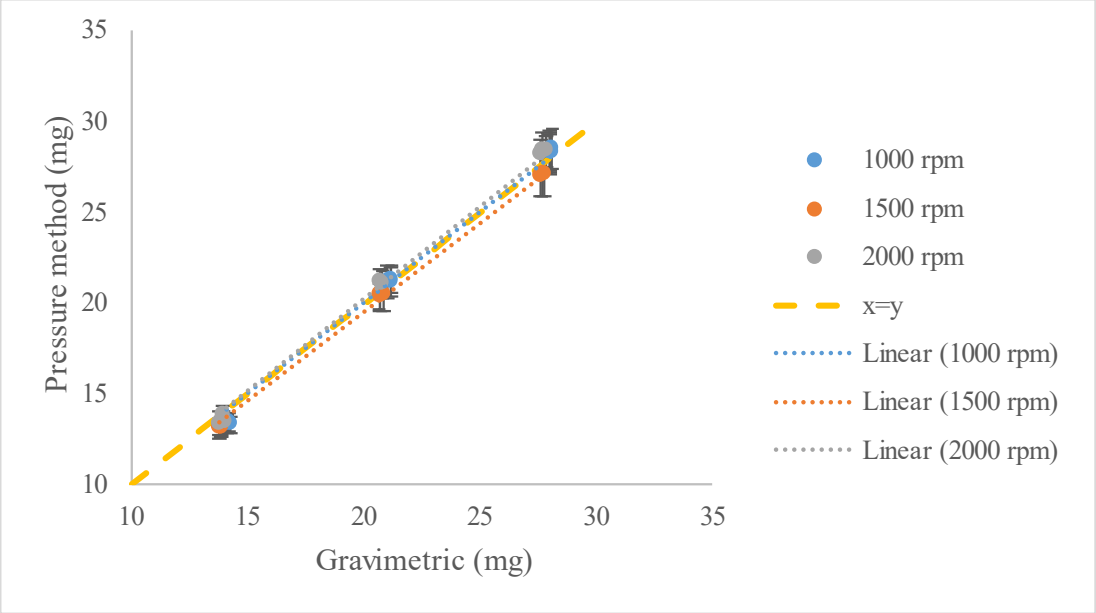

Figure 5.22:Comparison of gravimetric results to OPTM simulated engine speed results of 1000 rpm, 1500 rpm and 2000 rpm on experimental setup 5. ±One standard deviation is plotted for the pressure method calculations.

The TPTM results are shown below in Figure 5.23. The maximum error in the method was less than 3%. At 1000 rpm, the mass injected was overestimated; however, the mass-injected was underestimated as simulated engine speed increased. This is caused due to higher noise in the signal from using the Kistler 4067E sensors, leading to an error in the SOI & EOI detection using the average pre-injection pressure. This issue is resolved by using the smaller range pressure transducers, Kistler 4007D. However, the mass difference in the mass injected calculation was less than 5%, so the method can still be applied successfully.

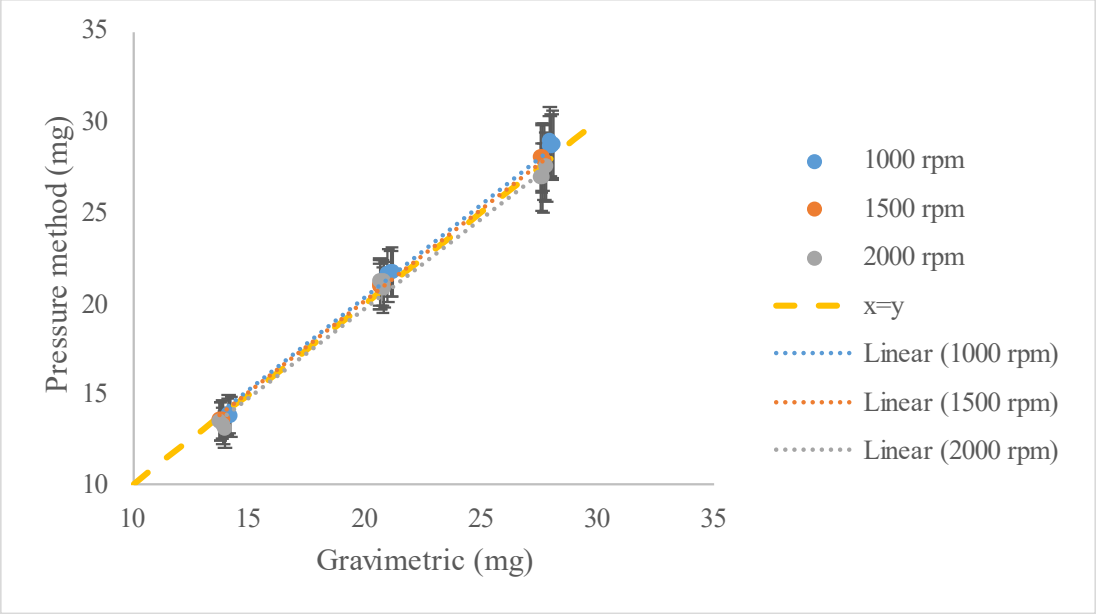

Figure 5.23: Comparison of gravimetric results to TPTM simulated engine speed results of 1000 rpm, 1500 rpm and 2000 rpm on experimental setup 5. ±One standard deviation is plotted for the pressure method calculation.

5.2.13 Higher acquisition rate experiments

Increasing the data acquisition rate reduced the required distance between the two pressure sensors while increasing the pressure data's resolution. The acquisition rate was doubled to 40 kHz, and the distance between the sensors was decreased proportionally. The OPTM and TPTM were applied to the data and compared with the gravimetric measurement. The experiments were conducted on experimental setup 6 and were run to simulated engine speeds up to 7000 rpm—the gradient method used to detect each injector's SOI and EOI.

Figure 5.24 shows the OPTM and TPTM compared with the gravimetric measurement on experimental setup 6. Three injection durations (1 ms, 1.5 ms and 2 ms) were tested with three repetitions for each simulated engine speed test. The OPTM underestimated the mass injected for most simulated engine speeds except at 3500 rpm, 5500 rpm and 6000 rpm. The TPTM overestimates the mass injected except in 3000 rpm, 3500 rpm, 4500 rpm and above 6000 rpm. However, the average difference in both pressure method increases above 5% after 2500 rpm and significantly increase from 4500 rpm, with the largest average difference around 5500 rpm.

The average difference becomes negative at 6000 rpm deviating further from the gravimetric measurement as the engine speed increases. This was caused due to the impact of returning pressure reflection of the previous injection on the current injection pressure signal.

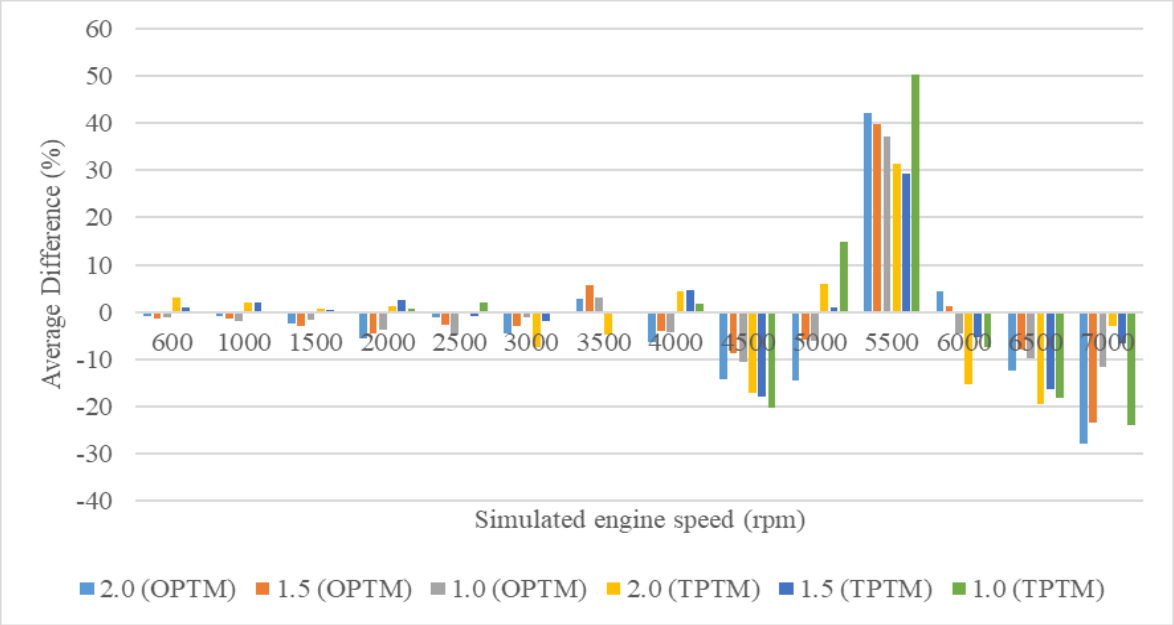

Figure 5.24: Higher acquisition rate experiments on experimental setup 6. OPTM and TPTM are applied on 3 injection durations of 1 ms, 1.5 ms and 2 ms. Each average difference bar has 3 tests with 300 injections in each test.

The simulated engine speed of 5500 rpm had the highest difference from the gravimetric measurement. Figure 5.25 shows the first five injections of a 2 ms injection train. The reflected wave and the injection pressure wave join constructively at the location of the P1 pressure transducer. This increased the instantaneous mass flow rate and overestimated the mass injected at this simulated engine speed. Similarly, at 7000 rpm, the injection coincides with a pressure reflection peak between 17 and 19 ms, leading to underestimating the mass injected calculation in both pressure methods. For effective use of OPTM and TPTM at higher simulated engine speeds, these reflection effects need to be further understood.

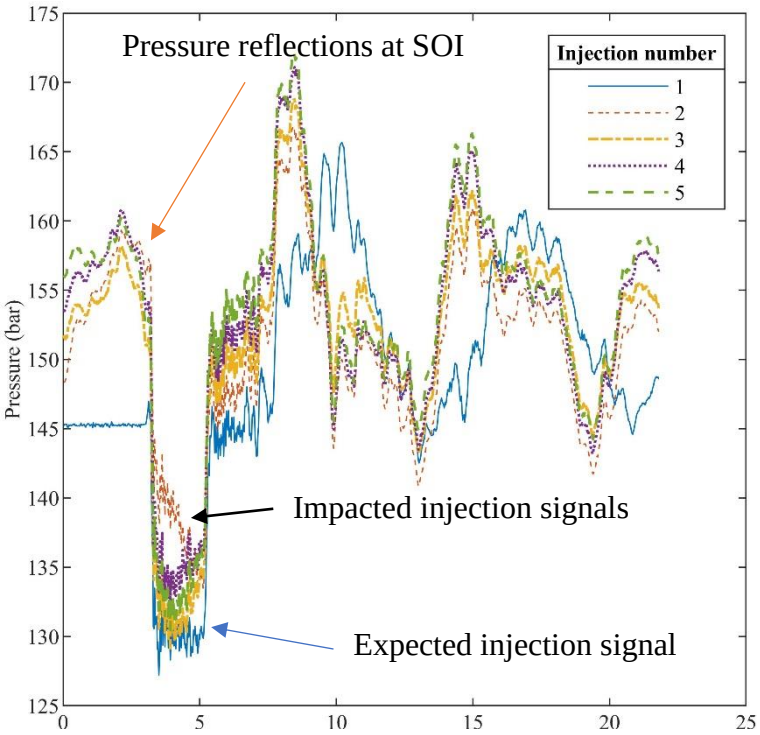

Figure 5.25: Five 2 ms injections data at P1 pressure transducer at 5500 rpm simulated engine speed on experimental setup 6.

5.2.14 Single-hole injector

Single-hole injector experiments were conducted with experimental setup 7. The tests were conducted at 100 bar and at four different simulated engine speeds of 600 rpm, 1500 rpm, 3000 rpm and 6000 rpm. The simulated engine speeds were chosen such that they represent engine speeds at idle, low speed, medium speed, and high-speed operation on the engine. Figure 5.26 shows the average difference for the OPTM and TPTM when compared to gravimetric measurement. The OPTM underestimated the mass injected at 600 rpm while overestimating the mass injected for the rest of the engine speeds, while the reverse trend was observed in the TPTM. However, the difference range observed for the tests with the single-holed injector matches the multi-holed injector used in experimental setup 6. The reduction in pressure changes the fuel pump behaviour, impacting the location and amplitude of reflections and, hence, the injected mass calculations.

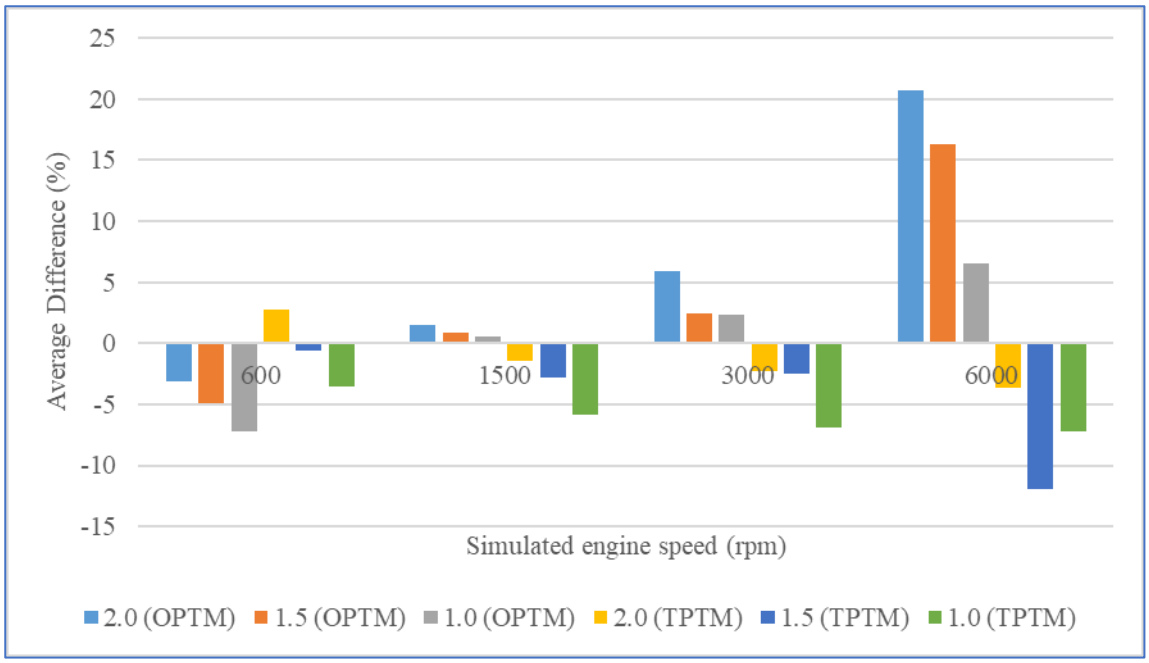

Figure 5.26: Higher acquisition rate experiments on experimental setup 7 for 4 simulated engine speeds. OPTM and TPTM are applied on 3 injection durations of 1 ms, 1.5 ms and 2 ms. Each average difference bar has 3 tests with 300 injections in each test.

5.3 Chapter summary

The Oxford spray rig was modified, and a vertical spray rig was successfully built to minimise pressure reflections and enable the application of pressure history to mass flow rate calculation. This setup was used to collect and analyse pressure data during injections to compare with the gravimetric measurement of injected mass. Sources of noise were added to the setup incrementally to test the robustness of the pressure methods. Initially, the data was acquired at 20 kHz before doubling this to 40 kHz.

The two fast pressure transducers (P1 and P2) used on the spray rig for the experiments had a range of 0-3000 bar (Kistler 4067E), while the tests were only conducted at 150 bar. Since such a small range of the pressure transducers was used, the signal to noise ratio (SNR) is high. To reduce the SNR and improve the pressure methods, smaller range pressure transducers with a range of 0-250 bar (Kistler 4007D) were used. These sensors provided an improved resolution to observe the smaller pressure reflections in the fuel pipeline. This improvement in SNR improved the pressure reflection information in the signal and enabled a gradient method for

injection detection at simulated engine speeds higher than 2000 rpm. Kistler 4067E sensors were used on experimental setups 1 to 5, and Kistler 4007D sensors were used on experimental setups 6 and 7.

The OPTM was initially applied to the pressure data to calculate the mass injected. The upstream fast-pressure transducer (P2) data and the downstream fast-pressure transducer (P1) data were individually used to calculate the instantaneous mass flow rate. The mass injected was calculated to be similar, while the P2 trace mass flow rate rise was delayed due to the distance upstream from the injector. Hence, the P1 trace was used in further analysis of the one-pressure method. Further, the effect of the increased area due to the increased pipeline pressure was compared. Nevertheless, this difference was found to be small (0.06%), and hence, it was ignored in the mass flow rate calculation.

The TPTM was applied to the pressure data and was used to calculate the mass injected. Similar to the OPTM, the increased area caused by the pipeline pressure was found not to cause any significant impact (0.12%) on the TPTM and was ignored in the mass flow rate calculation. Both pressure methods could be used to successfully calculate the mass injected with a maximum error of 2%. However, the TPTM has a larger standard deviation compared to the OPTM as there is no temporal coupling between the two sensors.

Then, a fuel pump was integrated, replacing the fuel accumulator in the spray rig to understand the effects on both methods. The impact of this was minimal on the calculation but increased the standard deviation of both approaches. A small discontinuity was introduced at the injector mount. This dissipated the energy within the discontinuity. But this was small and reduced the mass injected calculation by 2% in both the pressure methods. However, this difference could be ignored as this is within the uncertainty range of the pressure method and the gravimetric measurement.

A pressure reflection was induced within the injection window by reducing the pipe length to the first pipe fitting. This increased error in the OPTM but did not influence the TPTM. The OPTM was modified to correct for the reflection, and the modified method could successfully calculate the mass injected. Then, the pipeline between the two-pressure transducers (P1 and P2) were bent. The bends within the pipeline did not influence the injected mass calculations, and finally, simulated engine speeds were tested with this setup.

A pipeline with reduced spacing between the pressure transducers, P1 and P2, and a higher acquisition rate (40 kHz) was built with Kistler 4007D pressure transducers. The experiments on this setup were conducted from 600 rpm to 7000 rpm simulated engine speed. The gradient method was used for injection detection (SOI and EOI detection), and OPTM and TPTM could be successfully applied. At simulated engine speeds higher than 3500 rpm, the reflected pressure waves from the preceding injection influence the current injection. This effect was the worst, around 5500 rpm, when the reflected waves and pressure waves from the injection are constructive, leading to overestimating the mass injected in both pressure methods. The TPTM calculation for a 1 ms injection case is the worst at nearly 50% overestimation of the mass injected. The reflected pressure waves are destructive at simulated engine speeds between 6000 rpm and 7000 rpm, leading to underestimating the mass injected in both pressure methods. These results shown that OPTM and TPTM can currently not suitable to be used at higher engine speed. Further the experiments showed that the TPTM could only be used where small pressure reflections are present. Experiments with a single holed injector were conducted to check for compatibility across different injectors and injection pressure, and the OPTM and TPTM were applied. Simulations using Transmission Line Modelling (TLM) are required to be completed to understand the effects of pressure reflections on pressure methods.

Finally, a single holed injector was used instead of the multi-holed injector, and four simulated engine speeds were tested. The injection pressures were also lowered to 100 bar from 150 bar in the previous tests. OPTM and TPTM were applied. The OPTM underestimated mass injected

except at 6000 rpm, while the reverse trend was observed in TPTM. Further analysis needs to be completed using TLM to understand the difference in the results.

The experiments showed that OPTM and TPTM could successfully be implemented on gasoline fuel pipelines at different injection pressures and injector types. The length of the pipeline plays a crucial role in choosing the pressure method used and influenced the location of pressure reflections. Overall, the OPTM offers a smaller standard deviation in the results, while the TPTM is generally more robust to small reflections near the injections. When there are pressure reflections present within the injection window, the TPTM was better suited; however, this comes at the cost of a larger standard deviation in the calculated mass flow rate. It was observed that pipe bends have minimal impact on pressure reflections while pipe fittings induce reflections. The design of the pipeline and locations of these fittings impact the pressure reflections observed and the mass injected calculations, especially at higher engine speeds.

Both the OPTM and TPTM methods meet the criteria set out in Table 2.1 for high-speed measurement requirements for GDI injectors and hence were chosen for on-engine implementation. For implementation on the optical engine of the pressure methods, the pipeline should ideally have no discontinuities near the injector mount, and it should be long enough to ensure there are no reflections in the injection window. The pipeline can be coiled to save physical space, similar to experimental setup 6 (Table 5.1), as pipe bends did not produce any significant reflections in the pressure waves. While the optical engine has a maximum engine speed of 2000 rpm, the OPTM and TPTM can be implemented using the gradient method for injection detection using the smaller range sensors (Kistler 4007D).

Further study is required to understand the cause of the large difference observed at simulated engine speeds higher than 3000 rpm. The effect of pressure reflections on the injection pressure waves needs to be understood to successfully implement the pressure method on the full range

of engine speeds. A TLM model will help provide the source of the reflections and the effect of this on the mass injected calculation.

6 Transmission line modelling for fuel pipeline pressure measurement

6.1 Introduction

It was previously discussed how pressure transients occur when there is a sudden change in fluid velocity (in this case, the fuel in the pipeline) (Chapter 2). This change in fluid velocity is caused by the sudden opening or closing of a pipe valve. The generation of sudden pressure waves can be used to calculate the mass of fluid injected in an injection. However, to further understand the fuel pipeline system's influence on the propagation of this pressure wave and the reflections caused by it, the system needs to be modelled. Hydraulic pipeline models can be assumed to be one-dimensional flow [111], [112]. This makes the analysis more straightforward and can be performed in the time or frequency domain.

Many approaches can be used to model one-dimensional wave propagation, such as the method of characteristics (MOC) [111], bond graph modelling [113] and transmission line modelling (TLM) [114], [115]. While the MOC is commonly applied for modelling pressure waves, TLM is more straightforward, efficient, and easy to implement on time-varying pipeline components [114], for example, injectors. The general solution to the wave equation is the sum of two bidirectional waves [111], and if they only undergo linear operations, the two waves can be operated on independently. As the wave equation is linear, the sum of any solutions with linear operations on the waves can be superimposed. The component waves can then be summed when physical data (e.g., pressure or mass flow rate) is required. On the other hand, the MOC uses the net flow and pressure as the solution variables. The elementary waves from the wave equations are uncoupled and recombined inherently, so they cannot be handled separately.

TLM is computationally efficient and can model a wide range of wave phenomena and physical geometries. TLM solves in the time domain and can be directly implemented for applications of flow modelling in fuel pipelines. TLM relies on the time delay in each pipeline section which is proportional to the pipe's length, and the computation is only done at junctions. At a junction, the waves' propagation, dissipation and reflection are calculated, and resultant waves are propagated with the appropriate delays to the next junction. The TLM technique was identified as an ideal modelling tool for determining the pressure waves' locations and understanding the impact of reflections on the pressure methods in the experimental setups tested in Chapter 5.

In this chapter, the background and the derivation of TLM are described, and then a validation case is implemented. Subsequently, the model setup for the fuel pipelines is described. Penultimately, the results are discussed, including different methods used for improving the model. Finally, in the summary section, the lessons learnt about TLM are discussed.

6.2 Background

In the following section, the history of TLM was examined before the derivations of the equations used for TLM. The derivation and the equations presented in this section was directly drawn from the work of Ghazali [116] and Beck et al. [114].

6.2.1 History

The TLM method is based on transmission line theory and was first used in circuit modelling to find voltage and current in each circuit component [117]. The complete derivation of TLM can be found in [117]. Auslander [115] first adapted and applied this technique for elementary fluid lines modelling. The approach was adapted further and stylised for topographical implementation with junction descriptions which are used in this work. These junction descriptions led to the application of TLM to pipeline networks without complications in the mathematical modelling of the physical components in the network [114], [118], [119].

6.2.2 Theory and formulation

The implementation of TLM on pipelines is based on the work of Auslander [115] and was further developed by Beck et al. [114]. The wave equation's general solution can be taken as the sum of two bidirectional waves [114]. In TLM, the pipelines are treated as lossless, with the effect on a wave in the pipe being only a time delay. Any operation on the waves, including friction effects, only occurs at junctions. These junctions are generally at the position of physical junctions where any friction effects can be lumped. For improved accuracy of pipeline friction, fictitious friction junctions can be included. These friction junctions are not different computationally from the physical junctions present in the pipe network. These friction junctions and the physical junctions form the scattering matrix. A pressure wave at a junction is partially absorbed, reflected into the same pipe section and transmitted to the other pipes connected to the junction. The degree of wave attenuation, reflection and transmission are based on the physical geometry of the junction. The scattering matrix coefficients used in TLM satisfy resistance, momentum, and continuity equations.

The wave equation derivations for approximate flows in hydraulic systems can be found in [111], [112]. The approach for TLM is an extension of using lumped dynamic elements for each pipeline. The flow equations derived are almost identical to the equations derived for transmission lines [111], [112]. Figure 6.1 shows a pipeline length of l, with upstream pressure, P_1 and flow, $\dot{m}_1$, and downstream pressure, P_2 and flow $\dot{m}_2$.

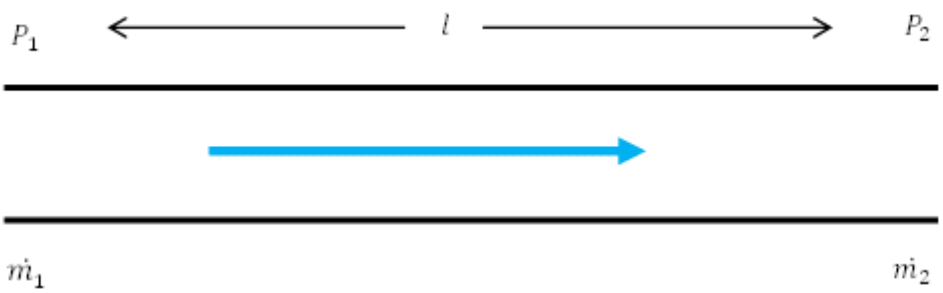

Figure 6.1: Pipe with upstream and downstream pressure and flow rates. The direction of the blue arrow shows the direction of fluid flow, adapted from [116]**.**

The equations governing the effect of a wave entering the pipeline on the pressure and mass flow can be written as the following transfer function [116]:

$$\begin{vmatrix} P_1 \\ \dot{m}_1 \end{vmatrix} = \begin{vmatrix} \cosh\left(\frac{l}{a}\right)\frac{d}{dt} & \left(\frac{a}{A}\right)\sinh\left(\frac{l}{a}\right)\frac{d}{dt} \\ \left(\frac{A}{a}\right)\sinh\left(\frac{l}{a}\right)\frac{d}{dt} & \cosh\left(\frac{l}{a}\right)\frac{d}{dt} \end{vmatrix} \begin{vmatrix} P_2 \\ \dot{m}_2 \end{vmatrix} \tag{6.1}$$

Where A is the cross-sectional area of the pipe, and a is the speed of sound of the pressure wave in the fluid. For a general fluid line, the characteristic admittance, Y, is defined as the ratio of flow change to pressure change [114]:

$$Y = \frac{A}{a} \tag{6.2}$$

Then the delay time, T, along the pipeline is defined as [114]:

$$T = \frac{l}{a} \tag{6.3}$$

The TLM method has two component waves (referred to as u and v waves), which are operated on at the junction and are tracked through the pipe network. They are combined where the pressure and mass flow rate outputs are required as an output. The transformation matrix between the component waves and the pressure and mass flow rate can be written as:

$$\begin{vmatrix} u \\ v \end{vmatrix} = \begin{vmatrix} \sqrt{\frac{Y}{2}} & \sqrt{\frac{1}{2Y}} \\ \sqrt{\frac{Y}{2}} & -\sqrt{\frac{1}{2Y}} \end{vmatrix} \begin{vmatrix} P \\ \dot{m} \end{vmatrix} \tag{6.4}$$

The inverse of Equation 6.4 can be written as:

$$\begin{vmatrix} P \\ \dot{m} \end{vmatrix} = \begin{vmatrix} \sqrt{\frac{1}{2Y}} & \sqrt{\frac{1}{2Y}} \\ \sqrt{\frac{Y}{2}} & -\sqrt{\frac{Y}{2}} \end{vmatrix} \begin{vmatrix} u \\ v \end{vmatrix} \tag{6.5}$$

Substituting Equation 6.5 into Equation 6.1 and performing a Laplace transform, the following equation is obtained:

$$\begin{vmatrix} u_1 \\ v_1 \end{vmatrix} = \begin{vmatrix} e^{sT} & 0 \\ 0 & e^{-sT} \end{vmatrix} \begin{vmatrix} u_2 \\ v_2 \end{vmatrix} \tag{6.6}$$

In a transmission line, the relationship between a wave entering and leaving is a time delay that is dependent on the length of the pipeline and the speed of sound in the line. As the two waves are decoupled, neither influences the other in the line. Then, by considering Equation 6.5, the wave variables have the dimensions of the square root of the power flowing in opposite directions [114].

In a complex system, pipes of different lengths are used, hence different delay times in each pipe. For computational efficiency and removing the need for interpolation, synchronous processing of the events is required. This is achieved by setting a common time delay – by setting a length of a pipe segment in which all the pipes' sections can be divided. The length should be chosen so that even the shortest pipe length is an integer multiple of the pipe segment. Small pipe segment lengths can reduce the modelling errors, but in turn, increase the computation time. The ideal segment length will give the required spatial and temporal resolution in the simulation at the frequency of interest.

6.2.3 Junctions

At junctions in TLM, the wave propagation and direction are calculated. A pipeline network typically would consist of multiple junctions, and the boundaries of the network are also defined as junctions. The relative admittance of each pipeline connected to the junction will determine the transmission of the incident waves into all the pipes connected to the junction. To enable the data structure implementation of TLM to pipeline, the junction types need to be standardised and are based on the implementation of bond graphs. Table 6.1 shows the common junctions adapted from [114].

Table 6.1: Common junctions, adapted from [114]

Code	Number of ports	Function
O	$2, \dots, n$	Simple junction (type zero)
OR	$2, \dots, n$	Simple junction with resistance
E	$1, \dots, n$	Constant pressure (effort) junction
ER	$1, \dots, n$	Resistive constant pressure junction
F	1	Constant flow junction
B	1	Blocked junction

The simplest is an O type junction; it is a perfect (ideal) junction joining multiple pipes together. The OR type is a junction with resistance with losses at one or more connections. Based on Beck et al. [114], the OR junction is constrained by the conservation of mass and common pressure to exist for all the for all pipes at the junction:

$$\sum_{i=1}^{n} \dot{m}_i = 0 \tag{6.7}$$

and

$$p_i - p_0 = R_i \dot{m}_i , \qquad i = 1, \dots, n \tag{6.8}$$

where R_i represents the resistance of the junction, and p_i, the pressure on the other side of the resistance on the ith pipe of that junction.

Substituting from Equation 6.5 for mass flow rate and solving v_1, the first wave gives

$$v_1 = u_1 + \sum_{i=1}^{n} \sqrt{\frac{Y_i}{Y_1}} (u_i - v_i) \tag{6.9}$$

where u_i are the incident and v_i are the emergent waves. Substituting further and using symmetry produces the following general result for the OR junction emergent wave [114]:

$$v_i = \sum_{i=1}^{n} s_{ij} u_j \,, \qquad i = 1, \dots, n \tag{6.10}$$

where the scattering coefficients are given by:

$$s_{ij} = \frac{2K_i K_j}{\sqrt{Y_i Y_j} \sum_{m=1}^{n} K_m} \,, \qquad i \neq j \tag{6.11}$$

and

$$s_{ij} = \frac{K_i}{Y_i \sum_{m=1}^{n} K_m} \left\{ 2K_i + (R_i Y_i - 1) \sum_{m=1}^{n} K_m \right\}, \qquad i = j \tag{6.12}$$

where

$$K = \frac{Y_i}{1 + Y_i R_i} \tag{6.13}$$

Setting $R_i = 0$ gives the scattering coefficient of a simple O junction.

The E type junction is a constant pressure junction which is a boundary condition. The input for the junction includes a limit on pressure; an example is a valve open to atmospheric conditions. While the ER type is a junction with resistance in at least one connection. In these junctions, the mass flow rate is unconstrained while the junction pressure, p_0, remains constant or a function of time. Any pipes connected to the junction do not influence the other pipes. From Equation 6.5, 6.7, 6.8, the relationship between the waves in an ER junction is:

$$v_i = \frac{R_i Y_i + 1}{R_i Y_i - 1} u_i + \frac{\sqrt{2Y_i}}{R_i Y_i + 1} p_o \,, \qquad i = 1, \dots, n \tag{6.14}$$

The second term in the equation is a forcing term derived from Equations 6.1 and 6.4. Setting the resistance as $R_i = 0$ yields the E type junction result.

The F type junction is another boundary condition where the pressure is unconstrained (e.g., a blocked end with friction or valve with the mass flow restricted), and mass flow is a constant or a function of time and is known $\dot{m} = \dot{m}_o$. Solving Equation 6.5 for the emergent wave gives:

$$v = u + \sqrt{\frac{2}{Y}\dot{m}_0} \tag{6.15}$$

The B type junction is a blocked end where there is no flow out, so setting the second term to zero gives the relation between the two-component waves.

6.2.4 Network representation

A scattering matrix, $\boldsymbol{S}$, can be constructed for all the junctions as the relationship between the incident and emergent waves are known. The matrix operates on the incident wave vector, $\boldsymbol{u}$, and in the following time step, they (incident vectors) produce the emergent wave vector, $\boldsymbol{v}$. Any frictionless joints with only two pipe connections (O type junctions) can be removed to improve the calculation speed by reducing the matrix order, and the waves are delayed by the required number of time steps. The forcing terms are stored in a vector $\boldsymbol{F}$ for the TLM implementation. The overall method can be represented by:

$$\boldsymbol{v} = \boldsymbol{S}\boldsymbol{u} + \boldsymbol{F} \tag{6.16}$$

To extract any physical values, Equation 6.5 can be used to transform the component waves.

6.2.5 User input and assumptions in TLM

The primary required input for the TLM is the resistance values, and these must be carefully selected and optimised to improve the accuracy of the model. There are three types of resistance that are inputs in TLM; distribution resistance (friction in the pipes), lumped resistance (losses associated with junctions), tabulated function (fluid control devices, valves, filters etc.). Most of these losses are non-linear and can impact the results observed. Further information on this is given by Beck et al. [114].

The fixed time delay in the TLM technique ignores the effect of dispersion of the waves propagating at different speeds caused by changes in the speed of sound due to pressure changes. This potentially reduces the accuracy of the model as the time delay cannot be changed during the calculations. This effect, however, is small when small pipelines are used, as the time delay remains small.

6.3 TLM validation case

To understand and use the TLM technique for fuel pipeline and to verify the code, validation cases were set up and tested to compare the three results of the three configurations shown in [118]. First, a simple pipeline with a chamber was modelled shown in Figure 6.2 (system 1). The model shows a 3 m long pipe with a 0.15 m diameter was connected to a 64 m^3 chamber. Table 6.2 shows the model parameters used in this example. The delay time chosen for the model was equal to the time of transmission in the pipeline ($\Delta t = 8.67$ ms). The boundary condition at the open end of the pipeline is given by:

$$u_1 = -v_1 + \sqrt{2Y_1}(P_0) \tag{6.17}$$

At the blocked end inside the chamber, the boundary condition was given by the following equation:

$$v_2 = u_2 \tag{6.18}$$

Table 6.2: Model parameters for a transmission line and chamber for system 1 (Figure 6.2), adapted from [118]

Line	d	Y
1	0.15	5.11×10^{-5}
2		6.16×10^{-2}

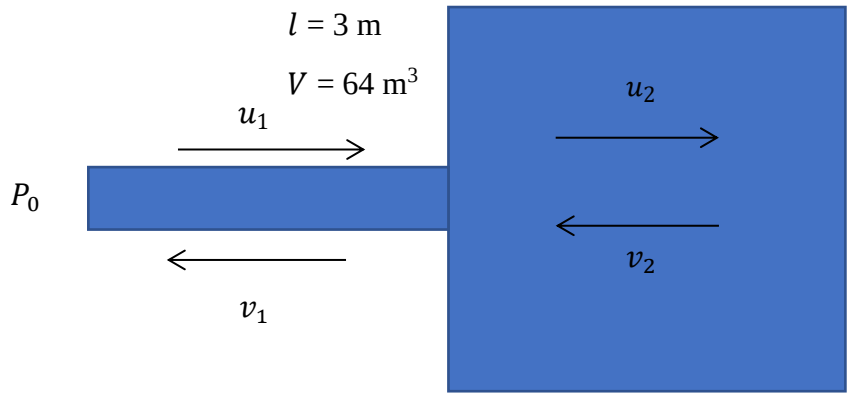

Figure 6.2: Lossless pipeline connected to a chamber (system 1) where the pipeline length is 3 m and the chamber volume is 64 m^3. Adapted from [118]**.**

With the boundary conditions (Equation 6.17 and 6.18) and the scattering coefficients calculated using the O junction, the overall model (system 1) can be described using the following matrix [118]:

$$\begin{pmatrix} u_1 \\ v_1 \\ u_2 \\ v_2 \end{pmatrix}_{t+\Delta t} = \begin{pmatrix} 0 & -1 & 0 & 0 \\ -0.9983 & 0 & 0 & 0.0575 \\ 0.0575 & 0 & 0 & 0.9983 \\ 0 & 0 & 1 & 0 \end{pmatrix} \begin{pmatrix} u_1 \\ v_1 \\ u_2 \\ v_2 \end{pmatrix}_t + \begin{pmatrix} 0.0101 \\ 0 \\ 0 \\ 0 \end{pmatrix} \begin{pmatrix} P_0(t) \\ 0 \\ 0 \\ 0 \end{pmatrix} \quad (6.19)$$

The matrix was implemented in a 'FOR' loop with the next time step ($t + \Delta t$) is calculated using the resultant vector from the previous time step (t). This ensured that the pressure waves are traversing in the pipelines are calculated correctly. At time $t = 0$ the open end had a step increase input pressure of 100 Pa, and the response to this input was calculated from Equation 6.19 as a function of time. Figure 6.3 shows the response on system 1 in the chamber (line 2) for a step input pressure of 100 Pa. This matched the results shown in [118].

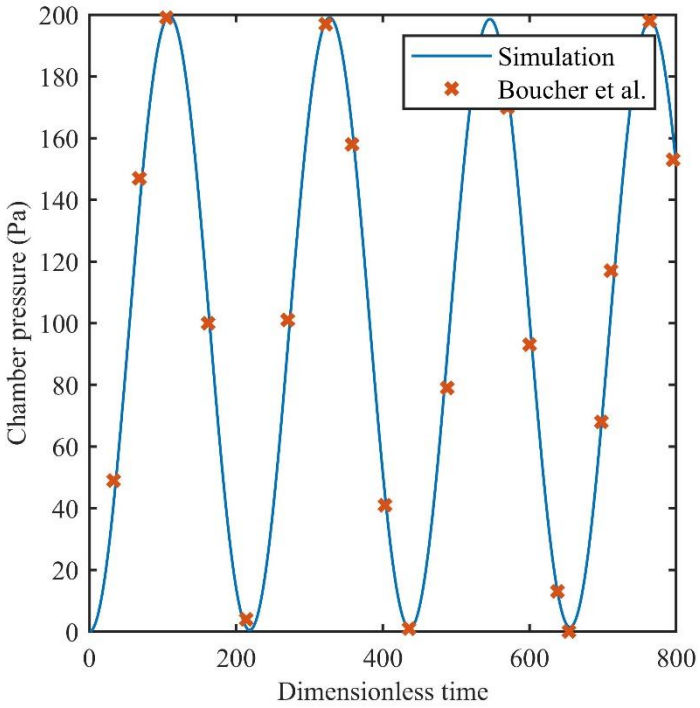

Figure 6.3: Response of system 1 to a step input pressure of 100 Pa in the chamber (line 2).

The second model (system 2) had two open-end transmission lines with a chamber in the centre, and the transmission lines were assumed to be 'lossy' (pressure loss in the pipeline), and the resistance for the transmission line was lumped at the junctions to the chamber. As per [118], the chamber was modelled as an 'ideal' transmission line. Both lines were open at the end to atmosphere, with one end having a step input of 100 Pa pressure (P_0). Figure 6.4 shows the model described, and Table 6.3 details the parameters used. The delay time for this model was kept the same as the previous model. The overall system can be described using the following equation:

$$\begin{pmatrix} u_1 \\ v_1 \\ u_2 \\ v_2 \\ u_3 \\ v_3 \end{pmatrix}_{t+\Delta t} = \begin{pmatrix} 0 & -1 & 0 & 0 & 0 & 0 \\ -0.9980 & 0 & 0.0575 & 0 & 0 & 0.0006 \\ 0 & 0 & 0 & 1 & 0 & 0 \\ 0.0575 & 0 & 0.9982 & 0 & 0 & 0.0192 \\ 0.0006 & 0 & 0.0192 & 0 & 0 & -0.9964 \\ 0 & 0 & 0 & 0 & -1 & 0 \end{pmatrix} \begin{pmatrix} u_1 \\ v_1 \\ u_2 \\ v_2 \\ u_3 \\ v_3 \end{pmatrix}_t + \begin{pmatrix} 0.0101 \\ 0 \\ 0 \\ 0 \\ 0 \\ 0.0034 \end{pmatrix} \begin{pmatrix} P_0(t) \\ 0 \\ 0 \\ 0 \\ 0 \\ 0 \end{pmatrix} \quad (6.20)$$

Table 6.3: Model parameters for transmission lines and chamber for system 2 (Figure 6.4), adapted from [118]**.**

Line	d	Y	R
1	0.15	5.11×10^{-5}	3.764
2		6.16×10^{-2}	0
3	0.05	5.67×10^{-6}	304.9

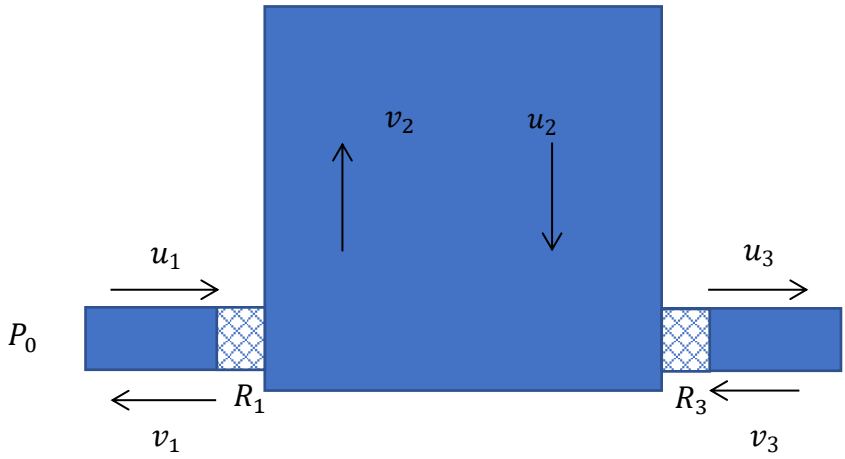

Figure 6.4: Two open end pipelines connected to a chamber with resistance at junctions connecting to the chamber (system 2). Adapted from [118]**.**

The matrix was implemented in a 'FOR' loop, with the next time step $(t + \Delta t)$ being calculated using the resultant vector from the previous time step (t), similar to system 1. At time $t = 0$, the open end had a step increase input pressure of 100 Pa, and the response to this input was

calculated from Equation 6.20 as a function of time. Figure 6.5 shows the response on system 1 for a step input pressure of 100 Pa. This matches the results shown in [118].

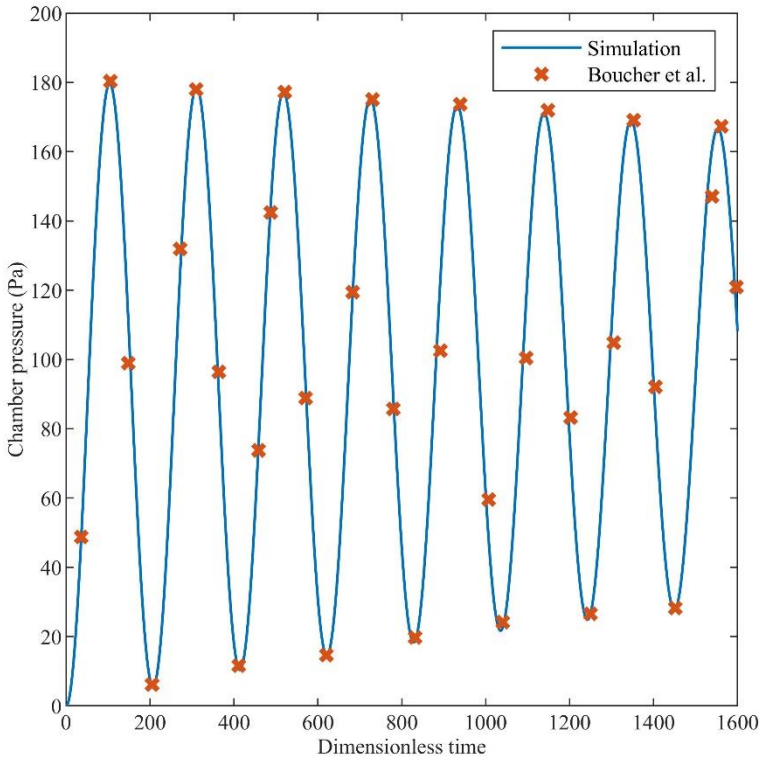

Figure 6.5: Response of system 2 to a step input pressure of 100 Pa in line 2.

The final validation model (system 3) had two open-end transmission lines and a closed transmission line with a chamber in the centre, and the transmission lines were assumed to be 'lossy'. The resistance for the transmission line was lumped divided equally at the two ends of each transmission at the junctions (ends of the line). The chamber was modelled as an 'ideal' transmission line with a blocked end. Both lines were open at the end to at the atmosphere, with one end having a step input of 100 Pa pressure (P_1). The pipelines 1 and 3 are 6 m and 9 m in length, respectively, and were divided into multiple pipe segments. Figure 6.6 shows the model described, and Table 6.4 details the parameters used. The delay time for this model had been kept the same as the previous model (the pipe segments are each 3 m in length).

Table 6.4: Model parameters for transmission lines and chamber for system 3 (Figure 6.6), adapted from [118]

Line	d	Y	R
1	0.15	5.11×10^{-5}	3.764
2	0.1	2.27×10^{-5}	19.01
3	0.05	5.67×10^{-6}	304.9
4		6.16×10^{-2}	0
	$\boldsymbol{R_v} = 40 \times 10^3$		

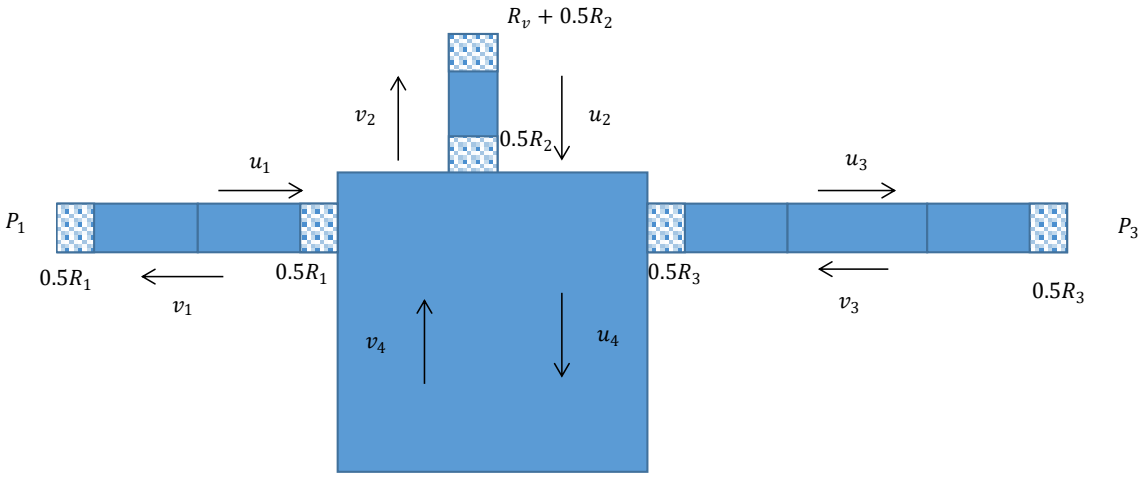

Figure 6.6: Two open end pipelines and a blocked end pipeline connected to a chamber with resistance at junctions (system 3). Adapted from [118]**.**

The scattering matrix was calculated using the boundary condition and the model parameters (Table 6.4). However, due to the different pipeline lengths in system 3, the pressure waves were delayed based on the segments in the transmission line. The delays implemented for calculating the system 3 response are shown in Equation 6.21 below.

$$\begin{pmatrix} u_1 \\ v_1 \\ u_2 \\ v_2 \\ u_3 \\ v_3 \\ u_4 \\ v_4 \end{pmatrix}_{t+\Delta t} = \boldsymbol{S} \begin{pmatrix} u_{1_{t-\Delta t}} \\ v_{1_{t-\Delta t}} \\ u_{2_t} \\ v_{2_t} \\ u_{3_{t-2\Delta t}} \\ v_{3_{t-2\Delta t}} \\ u_{4_t} \\ v_{4_t} \end{pmatrix} + \boldsymbol{PF} \tag{6.21}$$

The matrix was implemented in a 'FOR' loop with the next time step $(t + \Delta t)$ is calculated using the resultant vector from the previous time steps (t) with delays as described in Equation 6.21. At time $t = 0$, the open end had a step increase input pressure of 100 Pa, and the pressure response to this input was calculated in line 3 (Figure 6.7). This matches the results shown in [118].

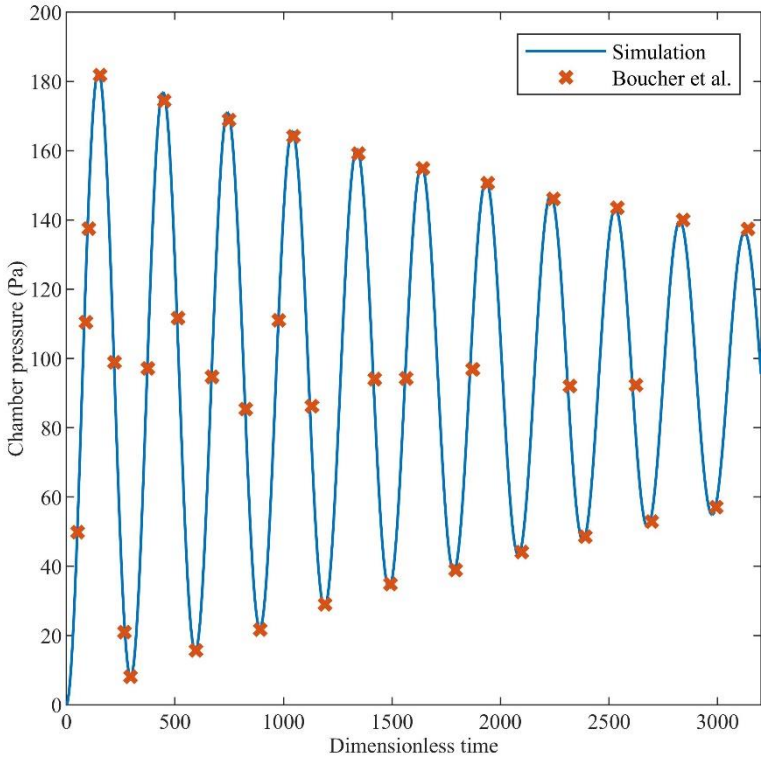

Figure 6.7: Response of system 3 to a step input pressure of 100 Pa in line 3.

6.4 Pressure measurements on fuel pipeline TLM setup

After the validation study, a TLM model was built using the principles described above to understand the influence of reflections on pressure measurement methods used for fuel mass injected calculations. Experimental setup 6 was used to assume values of the resistance parameters initially and subsequently the key parameters optimised in the model for further studies. This setup's pressure data was recorded continuously at 40 kHz, so the entire injection period is captured even at a simulated engine speed of 600 rpm. Figure 6.8(a) shows the complete injection captured in the experiment, and Figure 6.8(b) shows the injection trace

magnified to show the pressure reflections. This data showed the complete pressure reflections in the pipeline between two injections. This data was used to optimise the TLM model as the complete decay of pressure reflections at the pressure transducers was recorded.

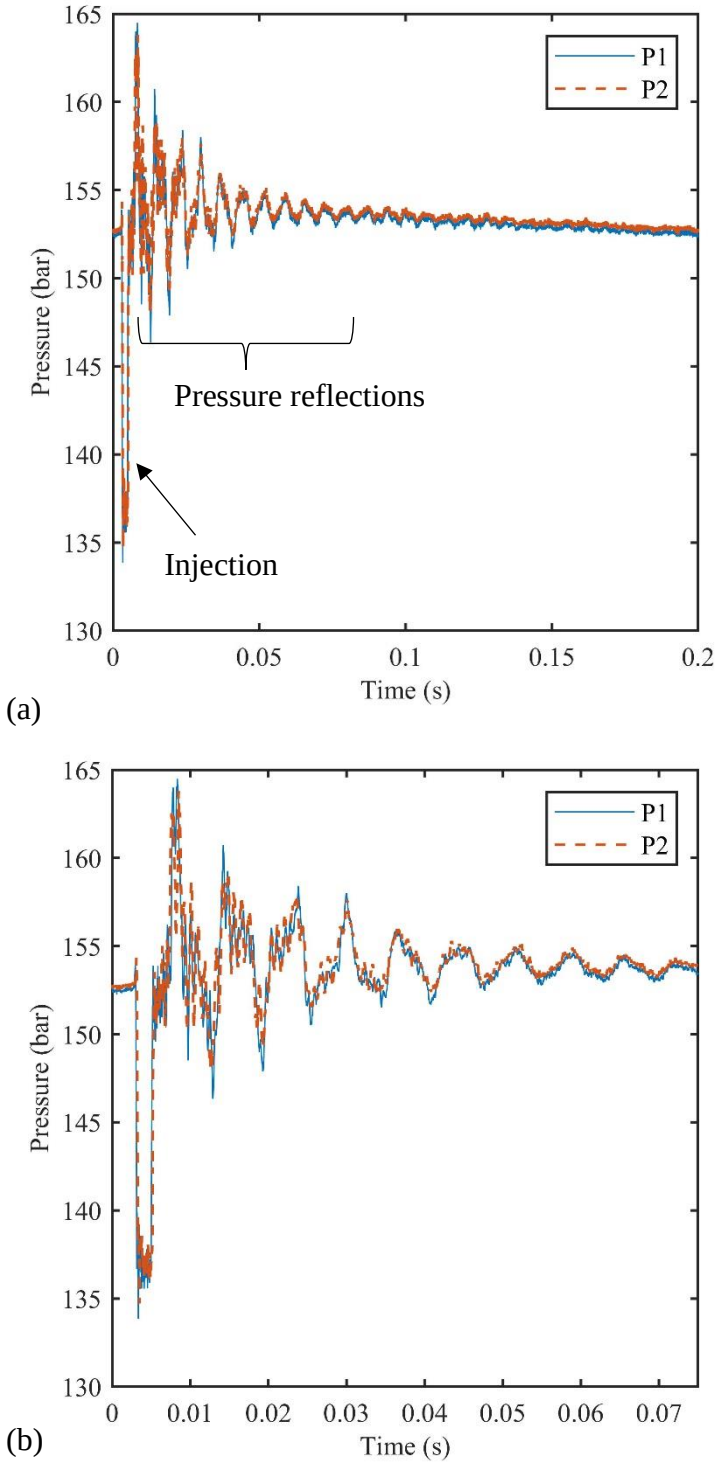

Figure 6.8: (a) A complete injection trace at 600 rpm simulated engine speed experimental data from setup 6. The reflections caused by the injection decay over time to before the next injection. (b) magnified injection trace to near the pressure reflections

Figure 6.9 shows the simplified setup used for the fuel pipeline in the TLM model. T-junctions and an elbow junction connected the pipes. The looped pipeline (4 loops) was modelled as junctions at the bends (21 bends in total), so resistance can be added to check its impact on the pressure measurements. At the pressure transducers' locations, the component waves were added to generate the pressure data to compare to the experimental data.

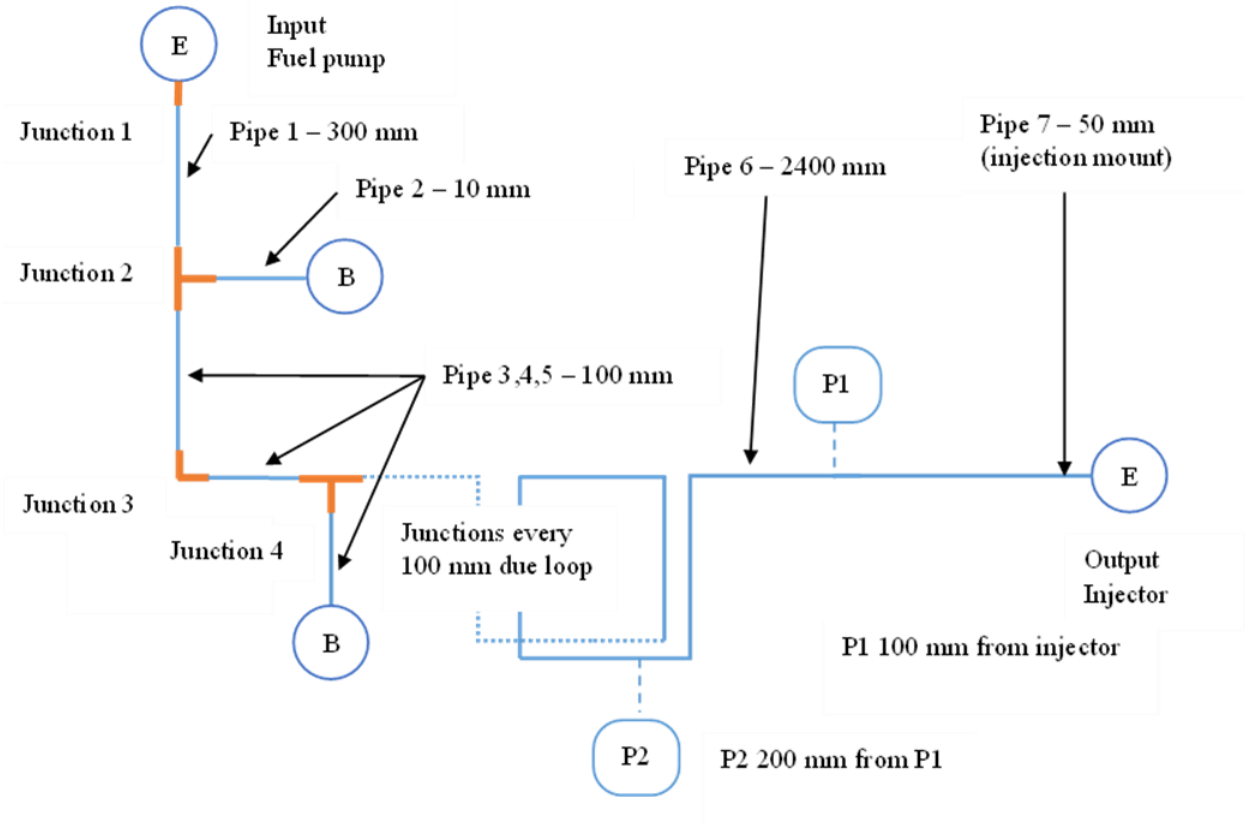

Figure 6.9: Simplified diagram of the modelled fuel pipeline for validation based on experimental setup 6 from the pressure measurement experiments. Junctions are shown in orange (OR type junctions). Not all the loops are included in the image (the experimental setup had 5 loops with 21 junctions). Not to scale.

The smallest pipe segment was the pipe fitting used in the fuel pipeline, which had a length of 10.5 mm and an internal diameter of 4.8 mm. Figure 6.10 shows a diagram of a pipeline-to-pipeline Swagelok connector. To enable the integer division of pipeline segments, 10 mm was used as the standard length of the pipe segment for the model. The speed of sound for undecane was approximated to 1400 m/s and was used to calculate the time delay in each pipe (7.14 µs).

On the fuel input side, the pressure was chosen to be 153 bar to match the pressure set by the fuel pump. As discussed in section 5.2.8, when the pump was in pressure stroke (at requested fuel pressure), the injections had the same injection pressure. Hence, any pumping effects caused due to the fuel pump were ignored in this model, and the fuel pressure at the inlet was assumed to be constant. This enabled the pipeline reflections to be caused only due to injections rather than the pump.

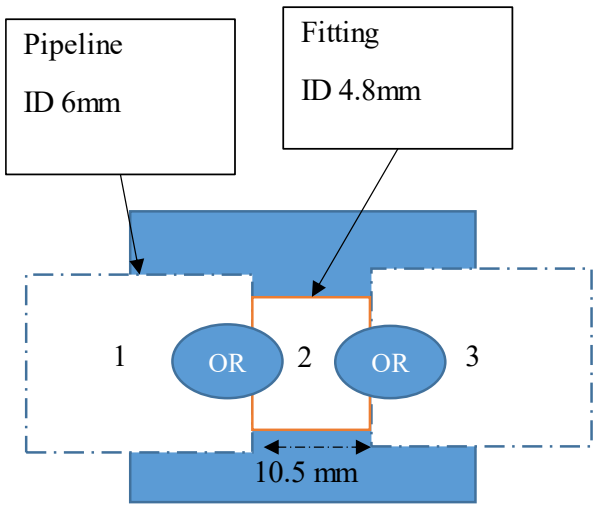

Figure 6.10: Swagelok fitting dimensions used in the pipeline for a pipeline-to-pipeline fitting.

On the injector side, a pressure drop of 10% of the fuel pressure was forced during an injection event. The injection started at the same pressure and drops by 10% to simulate the observed pressure drop in the pressure transducers. This was not modelling the operation of the injector during experiments and used an approximation. An injection request of 2 ms on the injector control produced an actual injection duration of 2.2 ms (~ 0.2 ms needle closing time, this was observed in the pressure signal in the experiments conducted). The output junction (injector) was modelled as a blocked junction when the injector was closed (i.e., no injection). Two blocked junctions (B) were present in the pipeline. These were the location of bleed valves that remained closed during the experiments (end of pipe 2 and pipe 5). Table 6.5 shows the parameters used for setting up the TLM fuel pipeline model. The input, output and blocked

junctions were dimensioned with the fitting diameter, and the injector mount was dimensioned with the pipeline diameter. While the injector mount was a tapered section, the tapered section was taken with the same diameter as the pipeline to reduce the complexity of the model. The tapered section was included in the experiment to remove sudden discontinuities to reduce energy dissipation. Hence, this approximation makes no impact on the model as there were thought to be negligible energy losses in these components.

Table 6.5: Parameters used for setting up the model for the simulation.

Parameter	Value
Speed of sound (m/s)	1400
Length of pipe segment (mm)	10
Fuel pressure at the input (bar)	153
Pressure drop due to injection(bar)	15.3
Sensor distance (mm)	200
Fitting diameter (mm)	4.8
Pipe diameter (mm)	4.0
Injection duration (ms)	2.2
Time delay (μs)	7.14

The T-junctions used for the setup posed a challenge to model in the TLM technique due to the change in diameter in the fitting and the flow direction. To solve this, the junction was split into the resistive junction (OR) between the pipeline and the fitting and the three-way resistive junction (OR) in the centre with a segment length of 10 mm in the fitting. Figure 6.11 shows the flows present in the T-junctions for the TLM pipeline model. The following equations relate the waves in the three-way OR junction (marked in red):

$$\begin{aligned} v_1 &= s_{11}u_1 + s_{12}v_2 + s_{13}v_3 \\ u_2 &= s_{12}u_1 + s_{22}v_2 + s_{23}v_3 \\ u_3 &= s_{31}u_1 + s_{32}v_2 + s_{33}v_3 \end{aligned} \tag{6.22}$$

where the scattering variables were calculated using Equations 6.11 and 6.12.

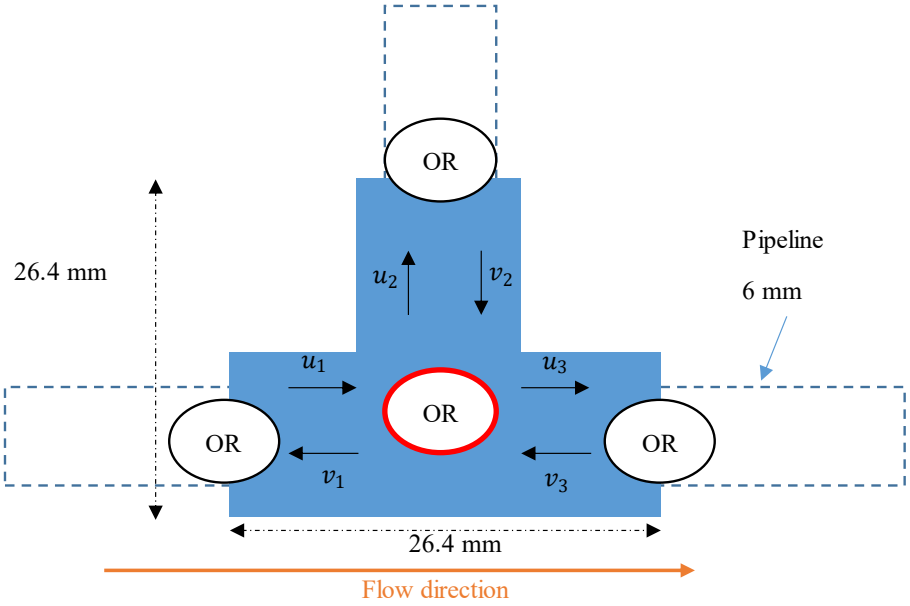

Figure 6.11: Details of flow in T-junction for TLM model, (junction 2 and 4 in Figure 6.9).

The scattering matrix for the pipeline was derived from the theory for the model and coded into MATLAB in the format of Equation 6.16. Initially, the resistance for each part was approximated based on the geometry of the junction and the experimental data. The T-junction resistance was split to favour flow direction in the straight compared to the perpendicular (90°) in the fitting. The code for the pipeline model is provided in Appendices (Appendix 10.1). Table 6.6 shows the approximated first guess resistance parameters used in the TLM pipeline model. The choice of resistance values and the sensitivity is discussed in section 6.5.3.

Table 6.6: Initial resistance parameter values used for the pipeline model.

Resistance parameter	Value $(m\ s)^{-1}$
Input	5e04
Output	5e04
Fitting	3e06
Bends	0

Elbow	5e05
Blocked end fitting	1e05
T-junction straight	5e06
T-junction 90°	10e06
Pipeline	0

6.5 Results and Discussion

The TLM simulation data for P1 and P2 pressure sensors were plotted along with the data from the experiment; this is shown in Figure 6.12. The forced injection section is marked with a red rectangle, while the rest of the simulated data was a result of the simulation. As seen in the figure, the forced injection matched the injection observed in the experiments on the pressure drop at the start of injection and pressure rise at the end of injection. For the injection duration, the forced injection input in the simulation data matched the average pressure observed in experimental data but does not include any of the noise observed in the experimental signal. This noise in experimental data was attributed to the needle lift, pressure signal noise and imperfections in the experimental setup.

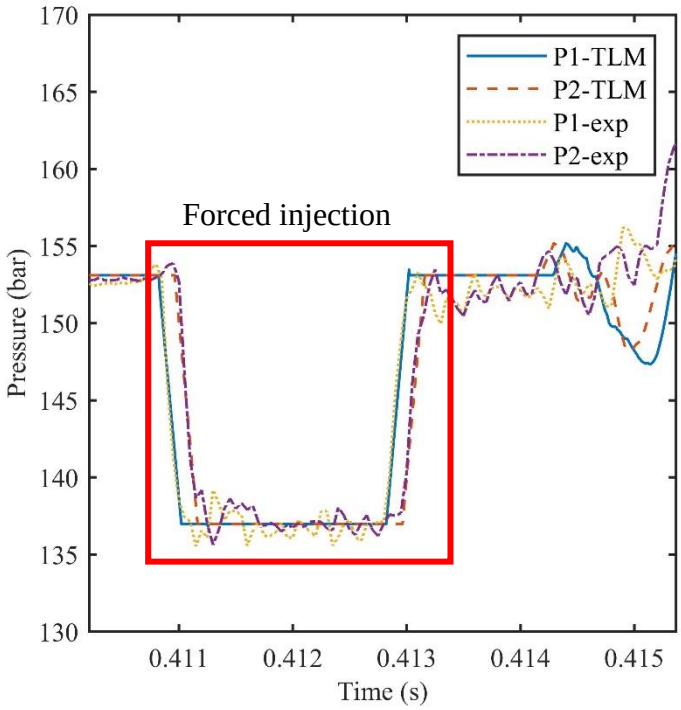

Figure 6.12: TLM data plotted along with the pressure measurements taken during experiments for a 2 ms injection on experimental setup 6 at 600 rpm simulated engine speed. The forced injection section matches the injection pressure drop observed in the experimental data.

To compare the model predictions of the reflections, the predicted P1 data from the TLM technique and the measured experimental data are plotted in Figure 6.13. The TLM accurately predicts the location of the first reflection but started to break down around the second peak as the low-frequency reflections decay while the higher frequency reflections were still present (0.445 s). The first reflection peak in the TLM was much longer and higher than observed in the experiments. This shows that further optimisation was required to match the peak height and the low-frequency reflections after the first reflection. The lack of matching after the first reflection will not enable the model to be used for designing the pipelines for higher engine speed applications (above 2500 rpm) of the pressure methods. Above 2500 rpm engine speed, the pressure reflections in the pipeline from the preceding injection, which are observed in the experimental data pressure signal, influence the pressure wave measured in the current injection. As these reflections were not matched in the current model, the predicted pressure

waves were not accurate; this limited the use of the model to engine speeds below which the pressure waves influence the next injection.

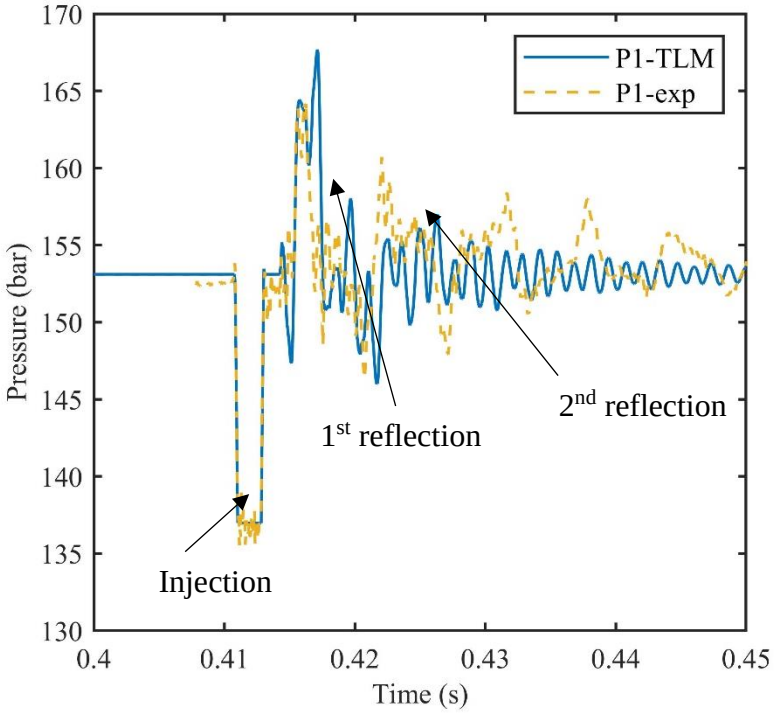

Figure 6.13: P1 pressure transducer predicted data (TLM) plotted with experimental data for a 2 ms injection at 600 rpm simulated engine speed.

Below 2500 rpm (48 ms between injections), the pressure reflections were sufficiently decayed for the next injection not to be impacted (Figure 6.8 shows the decay of pressure reflections after an injection). However, these reflections have been observed to cause a considerable impact in the pressure measurements at higher simulated engine speeds (above 2500 rpm) in experiments as the reflections present in the pipeline from the current injection impact the next injection. Figure 6.14 shows the P1 pressure signal from experiments at 2500 rpm and TLM prediction data. As the prediction data had a similar decay pattern before SOI, the injections had a similar profile. However, the difference in the decay of pressure reflections between injections in the experimental data lead to different injection profiles during injection (different pressure drop during injection).

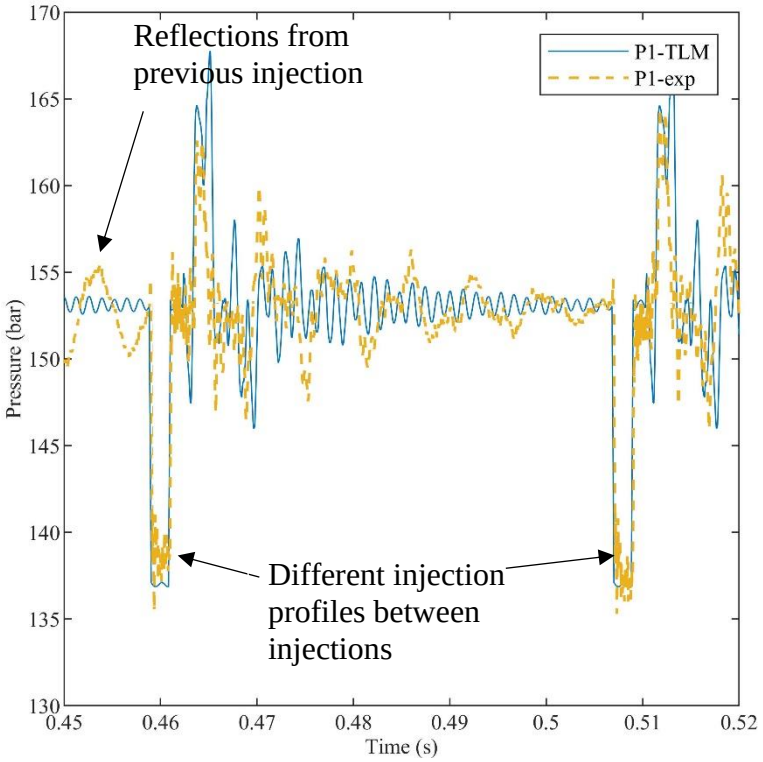

Figure 6.14: TLM data vs experimental data of P1 pressure signal at 2500 rpm for a 2 ms injection. The impact of reflections from the previous injections is visible in the experimental data as there are different injection profiles.

The lack of matching after the first reflection was further highlighted at higher engine speed. Figure 6.15 shows the P1 pressure signal from experiments at 5500 rpm and TLM prediction data. The difference in reflections and the injection profile was significantly different. The experimental pressure data showed the reflections clearly influencing subsequent injection; however, this was not matched in the pipeline model. This highlights the importance of accurate pressure reflection predictions in the pipeline model at higher engine speeds.

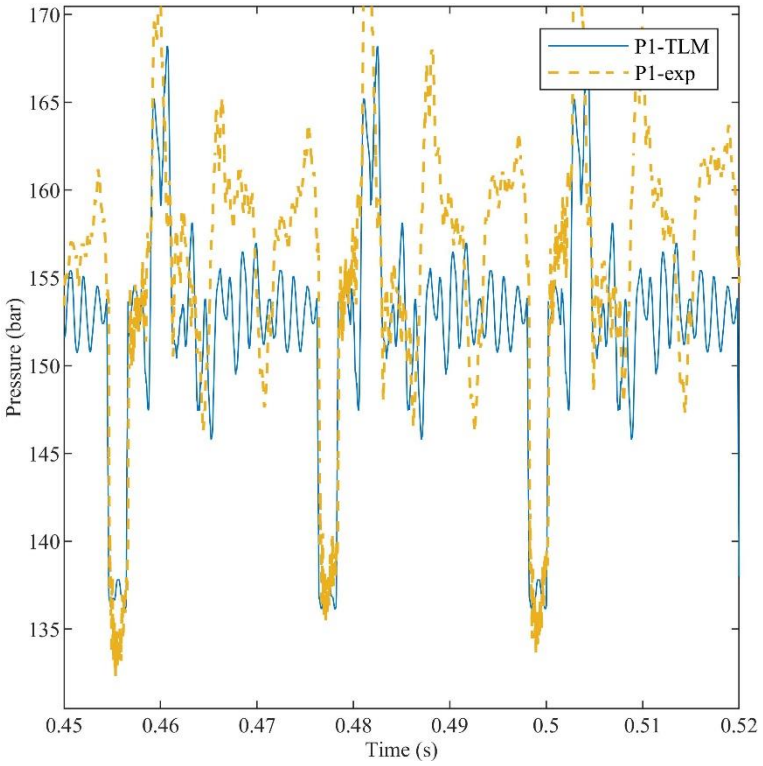

Figure 6.15: TLM data vs experimental data of P1 pressure signal at 5500 rpm for 2 ms injection. The impact of reflections from the previous injections is visible in the experimental data as there are different injection profiles.

To compare the TLM model with experimental data, the OPTM and TPTM were applied to the simulated pressure data, shown in Figure 6.16. While the SOI and EOI can be found using the gradient detection technique used for the experimental data (Section 5.2.2), as the information for the injection was defined in the model setup; this can directly be used to define the injection window. The SOI and EOI were directly defined from the pipeline model, the injection was delayed from the injector to match the P1 pressure transducer location. While the OPTM EOI sat at the end of the injection, the TPTM EOI was indicated within the injection window. The EOI was defined at the P1 pressure sensor same as in the experimental injection detection method. This difference was negligible (<0.1%) in calculating the mass injected in the TLM model, so it was ignored.

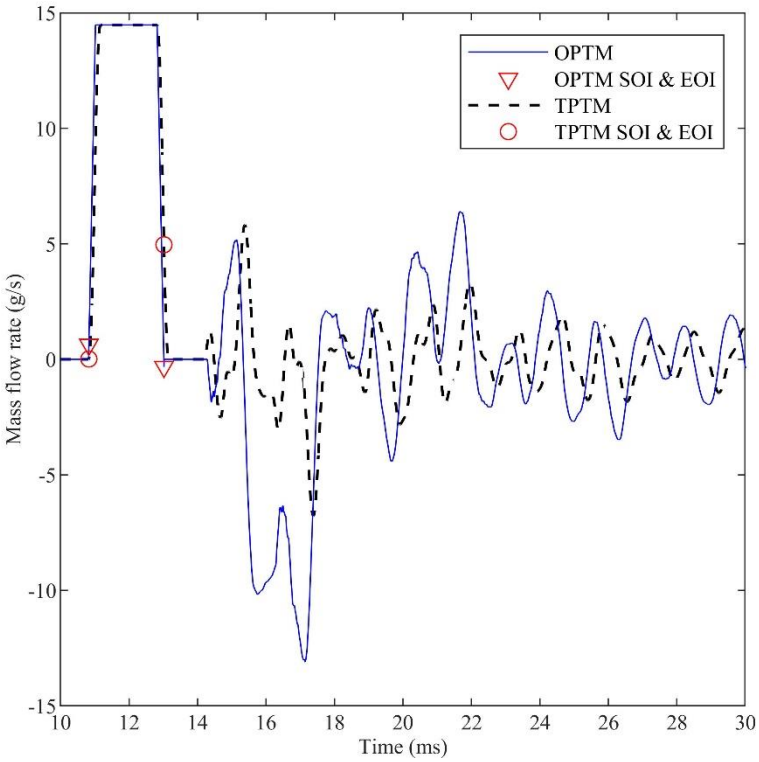

Figure 6.16: OPTM and TPTM applied to the simulated pressure data from the TLM model for a 2 ms injection at 600 rpm simulated engine speed.

While there were pumping cycles observed in the experiment (fuel pressure below the requested injection pressure due to fuel pump filling and pressurisation), the pressure for the TLM simulation at the input was fixed. The reduced pressure during pumping results in a lower injected mass. As the experimental data included the pumping cycles in the mass injected calculation, the initial mass injected was lower than if the pressure was fixed at the requested injection pressure (no pumping). For the 2 ms injection case presented in Figure 6.16, 70 injections were affected by the fuel pump (Section 5.2.8). This caused an over approximation of the mass injected by 2% in TLM estimates of the OPTM compared with the experiment. Further, the pipeline model does not account for the pressure changes caused due to needle movement (pressure rise at SOI) as injector geometry was assumed as an ideal valve at the injector. This assumption of the ideal cases leads to an over-approximation of mass injected in the OPTM and TPTM calculations when compared with the gravimetric measurements.

The pipeline model was applied to injections at 600 rpm simulated engine speed. The three injection durations (1.0 ms, 1.5 ms, and 2.0 ms) were matched to the experiment cases. Figure 6.17 compares the 600 rpm simulated engine speed mass injected calculations from experimented with TLM calculated data. The plot shows that the TLM calculations overapproximate the mass injected, but this was within one standard deviation of the injected mass value calculations from the pressure methods.

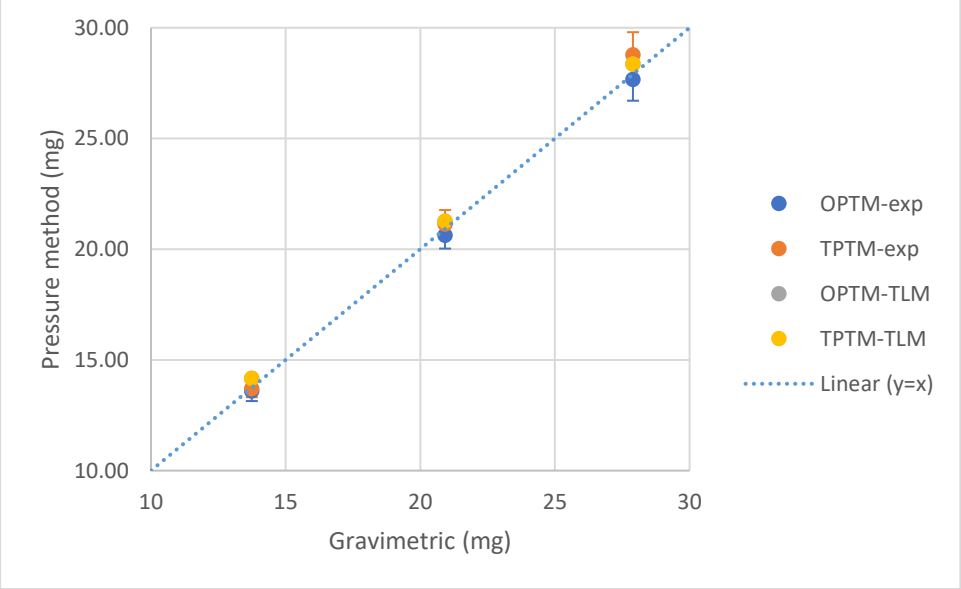

Figure 6.17: 600 rpm simulated engine speed experimental and TLM calculated data compared with gravimetric data for setup 6. ±One standard deviation is plotted for the pressure method calculations.

The TLM calculation was applied at different engine speeds to compare with experimental data till 2500 rpm. Figure 6.18 shows the difference between the experimental gravimetric mass measurement results to the TLM calculation. The fuel pump effects were observed in the experiment; this was not replicated in the model, and the pressure for the TLM simulation at the input was fixed. This caused the TLM estimates of the OPTM and TPTM to overapproximate the mass injected (~2%) as mentioned previously. However, the error was observed to increase as the simulated engine speed increased. This was expected as the impact

of pressure reflections increased as the engine speed increased, as shown in Figure 6.14 and Figure 6.15. However, the mass injected calculation of the TLM is within the uncertainty level of the gravimetric measurement (5.8%) till 2500 rpm.

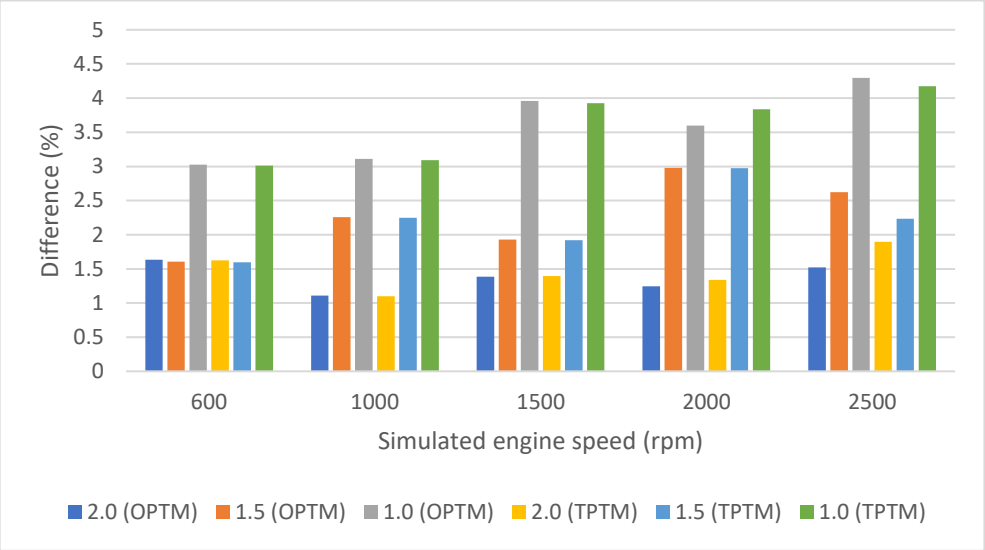

Figure 6.18: Difference in percentage for the experimental gravimetric mass injected measurement to the TLM calculation of the OPTM and TPTM for 3 different injection durations (2.0 ms, 1.5 ms, 1.0 ms).

6.5.1 Speed of sound

The speed of sound in undecane at different pressures was shown in Section 3.3. The input for the model assumes an average speed of sound of 1400 m/s regardless of the change in pressure of the fluid. However, the pressure traces observed in Figure 6.13 shows a match in the location of pressure waves in compassion to the experimental data. This confirmed that a fixed speed of sound is an appropriate solution, and the model was insensitive to fluctuations in speed of sound due to pressure reflections in the pipeline.

6.5.2 Friction in pipeline

The pressure drop due to friction in the pipeline was calculated using the Darcy-Weisbach formula [65]. Assuming a maximum peak flow rate of 20 g/s during injection, the density of undecane at 757.6 kg/m^3 at 20°C and 150 bar [108], and a viscosity of 1.098 mPas [120], the Reynolds number was approximately 8900. Using a turbulent flow condition in the pipeline and

assuming a pipeline's absolute roughness of 6 µm [121], the friction factor was calculated by the Colebrook equation [122]. During injection, the friction factor is calculated to be 0.0325, leading to a pressure loss of 0.23 bar. As this is less than 0.15 % of the fuel pressure, the friction resistance in pipelines, which damps the pressure reflections observed, has been ignored in the model, and hence the resistance parameter is set to 0, as shown in Table 6.6.

Bends in pipelines cause pressure drops in the fluid after the bend. To quantify the pressure drop, the Darcy-Weisbach formula [65] was used. However, as this was a coiled pipeline, the friction factor is calculated using the following relationship from Mishra and Gupta [123]:

$$f = \frac{0.079}{Re^{0.25}} + 0.0075\left[\frac{d}{D}\right]^{0.5} \tag{6.22}$$

where, f is the friction factor, Re is the Reynolds number, d is the pipeline diameter, D is the coil diameter. With the coiled pipeline, the coil diameter is assumed to be 0.1 m, the pressure drop per loop was estimated to be 0.00855 bar. Even with the five loops used in the pipeline, the pressure loss accounts for less than 0.03 % of the fuel pressure; hence the pipeline bend parameters were also set to 0 in the pipeline model Table 6.6.

6.5.3 Parameter sensitivity analysis and optimisation

Resistance parameters

The resistance parameters chosen for the pipeline model shown in Table 6.6 were estimated initially. A sensitivity analysis was conducted on all the parameters to understand the validity of the chosen resistance values. Individual resistance parameters were changed to understand their influence on the pressure predictions of the pipeline model.

The input and output junctions were chosen to be near ideal junctions (>99.5 % reflection). As there were minimal losses at the junction at the current resistance value, when the resistance value was set to 0 for each junction (100 % reflection), the model prediction remains the same for the pressure signals. The effect of doubling the input and output parameters from Table 6.6,

individually were tested. Figure 6.19 shows the plots for the changed resistance values. When the resistance at the input was increased, the pressure drop during injection was larger (Figure 6.19 (a)). An increased resistance at the input reduced the energy available in the pipeline, increasing the energy lost at the output when the injector was open. However, an increase in resistance in output reduced the pressure drop, as less energy was removed from the pipeline (Figure 6.19 (b)). Nevertheless, minimal changes are observed in the pressure reflections when the input and output parameters are changed. This impact on reflections was limited as the junctions were still near perfect at the increased resistance. Further, it was observed that the reflections were caused due to the sudden radius change in the pipeline caused by the fittings.

The pipeline model was observed to be sensitive to the fitting resistance as the fittings define the pressure reflections strength and location. The reflection of the wave at the initial estimated value was 14.4 %. An increase in resistance value only made a difference in the pressure reflections while the injection pressure remained unchanged. The pressure reflections amplitude increased as the resistance reduced, as shown in Figure 6.20 (a), increasing the maximum pressure observed in the first reflection and the subsequent waves, while the reverse trend was observed with reduced resistance (Figure 6.20 (b)). Reducing the resistance value reduced the energy lost in the joint, and a higher proportion of the pressure wave energy was reflected into the pipeline due to the discontinuity present in the junction (radius change). Changes in fitting parameter resistance only impacted the magnitude of the pressure reflections while the phase remained unchanged.

Next, the T-junction parameter resistances were varied to understand the influence on the model. The T-junction straight parameter was found to have an impact on the pressure reflections amplitude while T-junction 90° had minimal impact on the pressure reflections. Like the fitting resistance, the T-junction straight resistance decrease led to increased magnitude in the pressure reflection. However, the magnitude increase in pressure amplitude was smaller compared to the fitting resistance change. The change was smaller as the majority of the wave

energy transfer occurs in the fitting compared to the T-junction. This was shown in Figure 6.21(a). The difference in T-junction 90° resistance set to 0 is shown in Figure 6.21(b). There was no visible change caused by the increasing or decreasing of the T-junction 90° resistance parameter.

To understand the impact of the T-junction on pressure reflections, both the T-junctions were replaced with a straight junction. The removal of the third pipe had negligible impact on the first pressure reflection (increasing the peak pressure by 0.5 bar). However, the consequent reflections in the pipeline were phase-shifted while the magnitude of these remained the same. This phase shift increased as the pressure waves interacted in the pipeline. Figure 6.22 shows the P1 pressure data of the optimised TLM versus the straight junction substitution in the model. The T-junctions acted as a buffer (capacitance) absorbing the pressure reflections partially between the input and output sides of the model and delayed the pressure reflections due to the presence of this third pipeline.

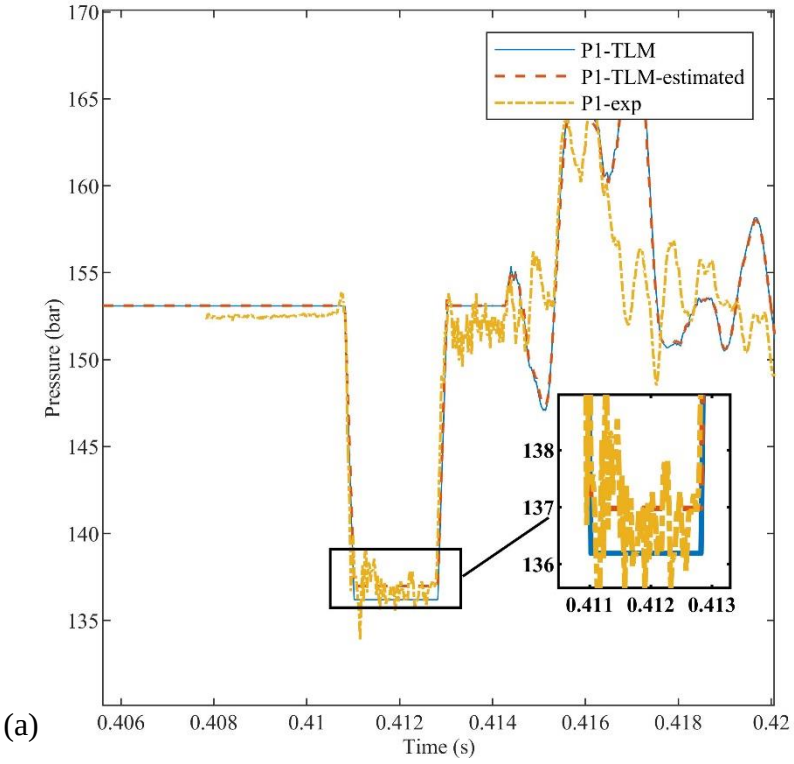

(a)

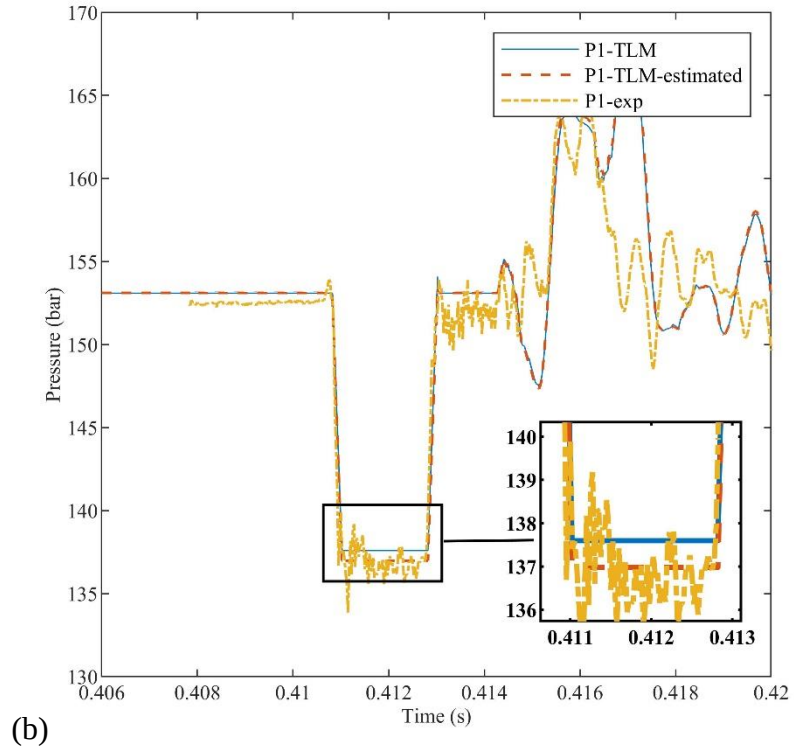

(b)

Figure 6.19: Parameter sensitivity in input and output. The optimised TLM is shown in orange, experimental data is shown in yellow, and blue shows the model with the changed resistance value. (a) The input resistance value is doubled (10e04), (b) the output resistance value is doubled (10e04).

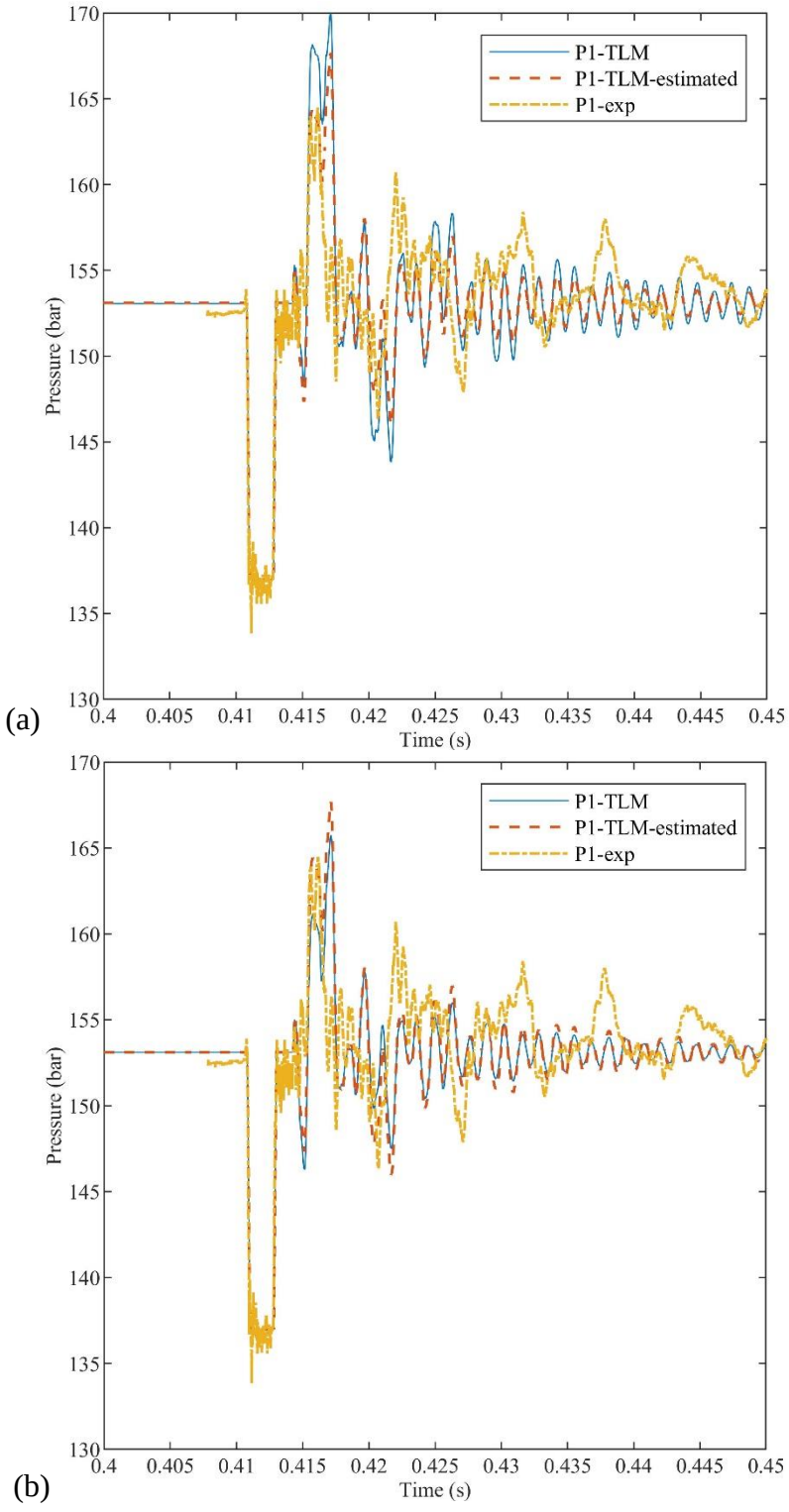

Figure 6.20: Parameter sensitivity in fitting. The optimised TLM is shown in orange, experimental data is shown in yellow, and blue shows the model with the changed resistance value. (a) The fitting resistance reduced by 1e06 (33% increase), (b) the fitting resistance increased by 1e06 (33% decrease).

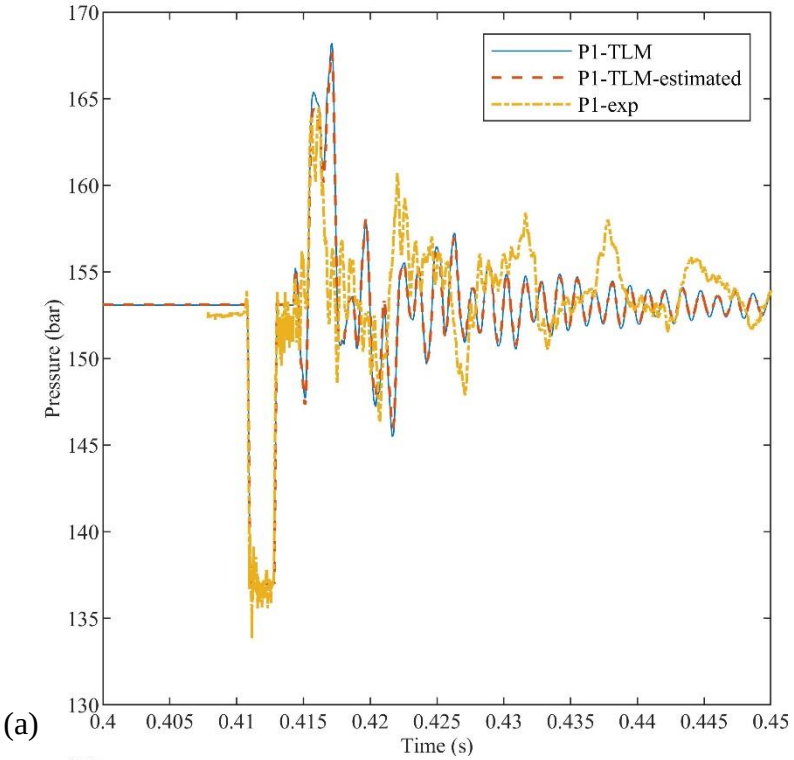

(a)

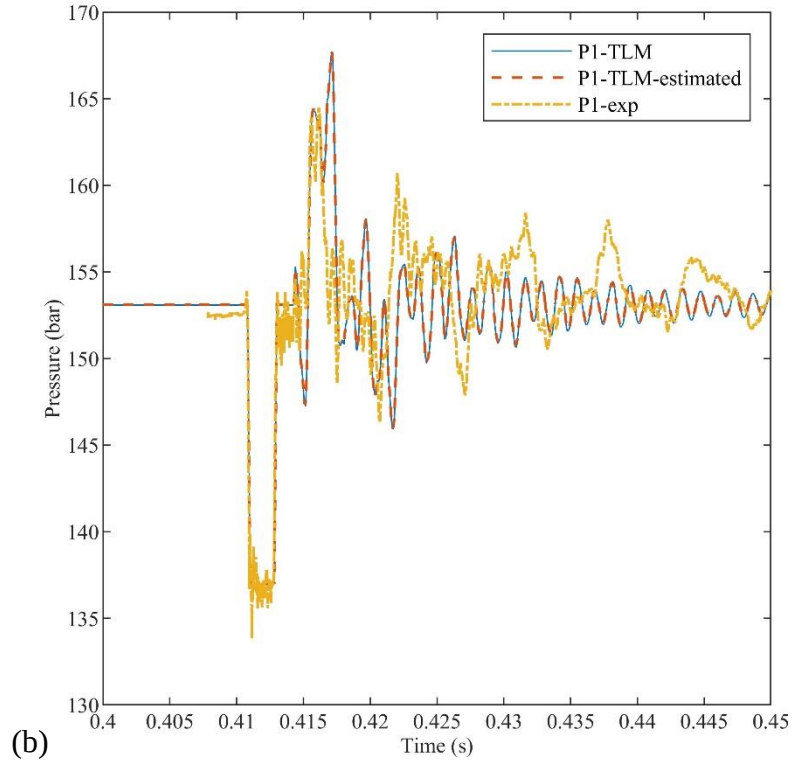

(b)

Figure 6.21: Parameter sensitivity in T-junctions. The optimised TLM is shown in orange, experimental data is shown in yellow, and blue shows the model with the changed resistance value. (a) The T-junction straight resistance is reduced by 1e06 (20% decrease), (b) the T-junction 90° resistance is set to 0.

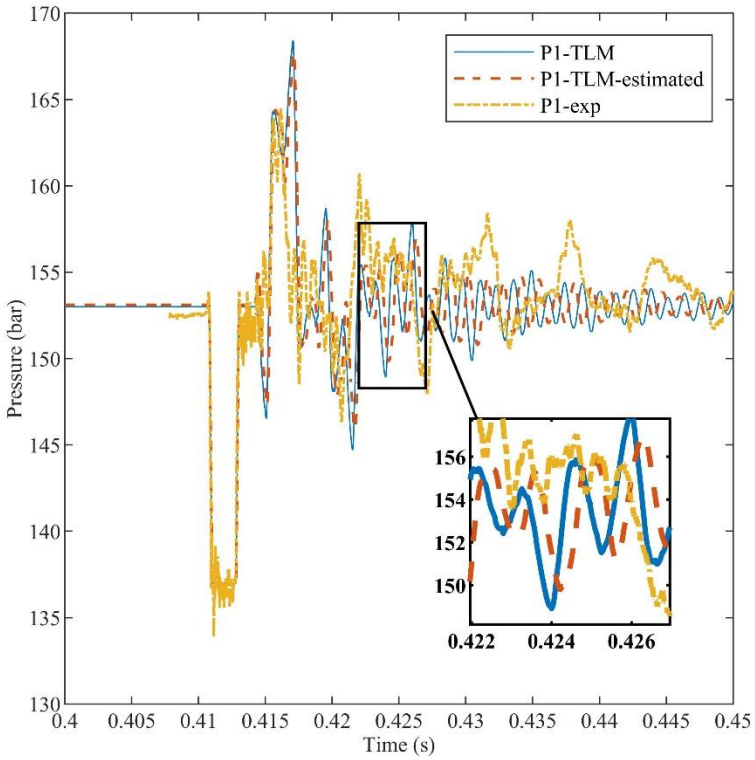

Figure 6.22: Parameter sensitivity study by removing the third junction in the T-junction to consider the impact on the pressure reflections. A phase shift (continually preceding the pressure trace) in the consequent pressure reflections after the first pressure reflection.

Optimisation

The analysis conducted above indicated that pressure wave reflections were most influenced by the fitting and T-junction resistance parameters. An optimisation study was conducted to match the pressure wave beyond the first reflection. The 'FMINCON' function in MATLAB was used to optimise the fitting and T-junction variables. The input function was chosen as the TLM code used to calculate the pressure wave with an error function defined by the error between the P1 pressure transducer TLM and the experimental data collected. The error function is shown in Equation 6.23. The error is calculated for data between EOI and 0.45 s for the case shown in Figure 6.12 (until approximately 35 ms after injection). This enabled the error to be calculated where the reflections were deemed to have the most significant impact. The parameters were optimised with different start points to ensure the error was minimised and a global minimum was found. The optimised parameters are shown in Table 6.7. The value of the fitting parameter

increased during the optimisation search while the T-junction parameters were reduced. This would reduce the peak of the first pressure reflection.

$$error = \frac{1}{length\ of\ P1_{TLM}} \left(\sum |P1_{TLM} - P1_{exp}| \right) \tag{6.23}$$

Table 6.7: Optimised fitting and T-junction parameters

Resistance parameter	Estimated value (m s)$^{-1}$	Optimised value (m s)$^{-1}$
Fitting	3e06	4.58e06
T-junction straight	5e06	4.65e06
T-junction 90°	10e06	9.65e06

The results of the TLM model with the newly optimised resistance parameters, the original, optimised TLM, and the experimental pressure traces were plotted in Figure 6.23. The first reflected wave was reduced as predicted compared to earlier; however, the TLM pressure waves decay was still not accurately modelling the reflections during the second wave. This suggested that more information about the fittings was required to develop an accurate TLM model. While the geometry of the pipeline and fittings was available, further information about the pressure reflections amplitude was required around the junctions to improve the resistance estimates used.

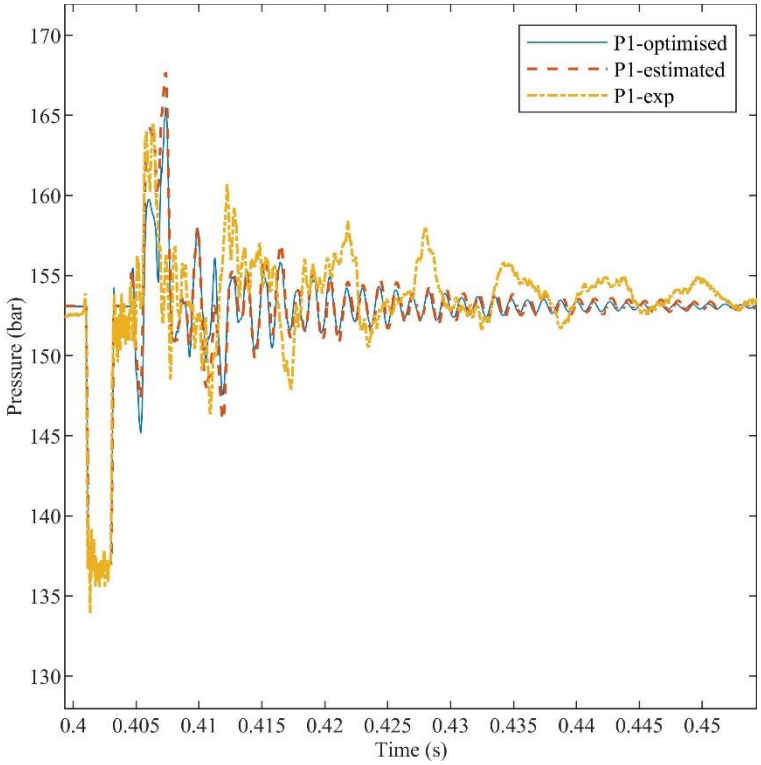

Figure 6.23: TLM P1 pressure trace with optimised parameters plotted, with experimental data and original TLM pressure trace. The plot shows a 600 rpm 2 ms injection at injection pressure of 153 bar.

Length variation study

The length of pipeline 4 (Figure 6.9) was increased by 0.2 m to test for sensitivity in pipeline lengths in the model. This increased the pipeline length by 200% to understand the impact on the pressure reflection locations. Figure 6.24 shows the TLM pressure traces with a changed length compared with the original length in the model (Figure 6.9). The change in the length, as expected, delayed the first reflected wave (0.14 ms delay). This shows the importance of accurate input of the pipeline lengths in the pipeline model. However, this change of length also led to a faster decay of the reflected waves in the model. This change in pipeline 4 length showed a destructive interference of pressure reflections leading to faster decay. If the TLM model accuracy was improved, this could be used to determine optimal pipe lengths for faster decay of pressure wave reflections in the fuel pipeline.

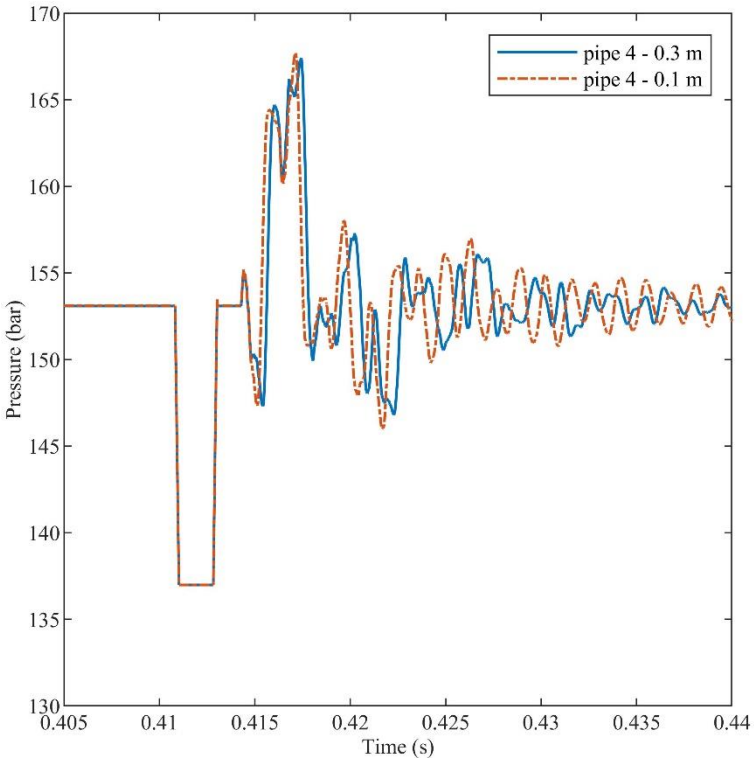

Figure 6.24: TLM pressure traces with optimised parameters and changed pipeline 4 length.

6.5.4 Other experimental setups

To further understand the current limitation of the model, other experimental setups were modelled. Figure 6.25 shows the TLM prediction and the experimental pressure data for P1 for setup 1 (Section 5.1). While location of both the first pipe fitting reflection and the reflection from the fuel pump are matched between the TLM and experimental data, there was a lack of matching in the magnitude. This showed that the model needs to be improved at the fittings to match the experimental data better.

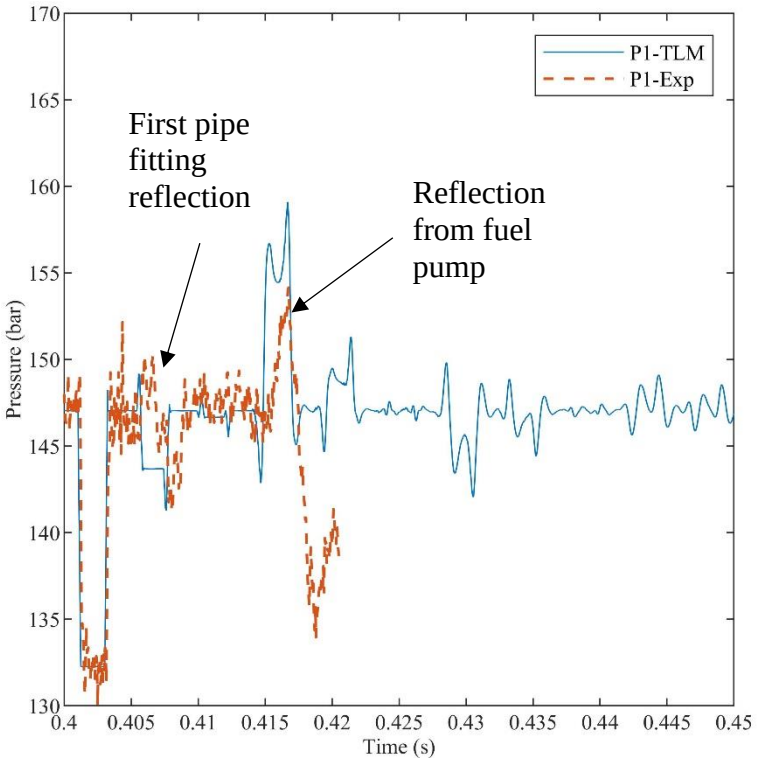

Figure 6.25: Setup 1 P1 TLM pressure trace and experimental pressure trace plotted for 2 ms injection at 600 rpm simulated engine speed.

Setup 4 (Section 5.1) was also modelled in the pipeline to check for the reflection prediction within the injection window caused due to the use of a shorter measurement pipeline. Figure 6.26 shows the TLM prediction and the experimental pressure data for P1 for setup 4. The location and the pressure reflection within the injection window was well predicted; however, the magnitude of the reflection from the fuel pump required an improved match. While the location of the pressure waves was matched in both cases, the model needs to improve to predict the reflection shape better. This would require further experiments to characterise the pipeline fitting resistances to improve the model.

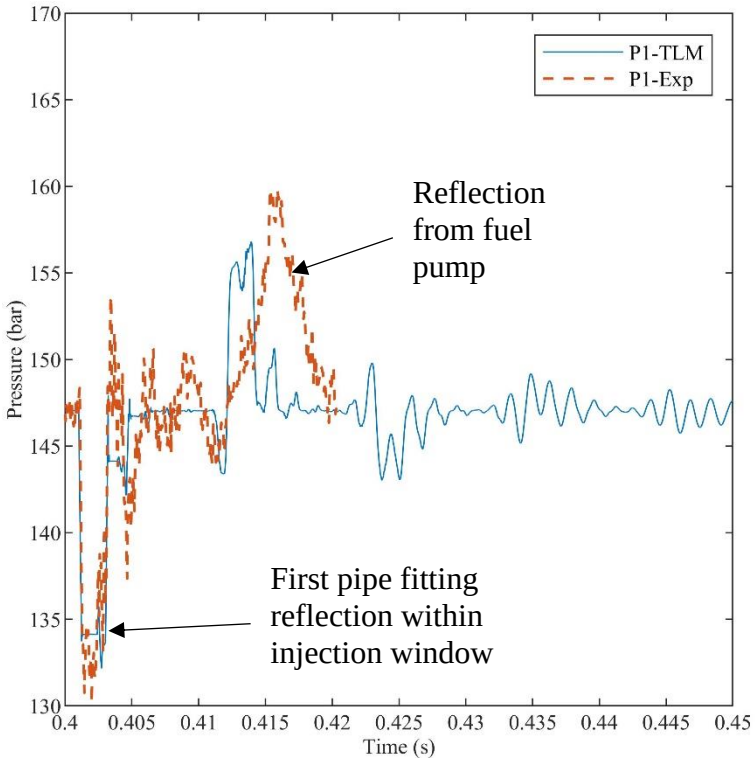

Figure 6.26: Setup 4 P1 TLM pressure trace and experimental pressure trace plotted for 2 ms injection at 600 rpm simulated engine speed.

6.6 Summary

The derivation of the TLM technique was initially presented, and the merits of the scheme were discussed. A validation case study was conducted to understand the implementation of TLM. Then, TLM was used to develop a fuel pipeline model based on the experimental setup. The model setup was described, and initial approximations were completed on the resistance parameters using experimental data. TLM simulated pressure data reasonably matched the experimental data after EOI until the end of the first pressure reflection. The low-frequency pressure reflections decayed faster in the model than the higher frequencies.

Both OPTM and TPTM were applied to the simulated engine speed data up to 2500 rpm with a forced injection approximation. The difference between the experimental gravimetric measurement and the simulated was within 5%, showing the TLM application's potential for fuel pipelines even with a forced pressure drop at the output. The fuel pressure at the input is

fixed in the model, while the injections in the experimental data are subject to pump effects; this caused the mass injected values to be over approximated compared to the experimental values. However, the calculated mass injected values are within the uncertainty level of the gravimetric measurement.

In the pipeline model, it was acceptable to use a fixed speed of sound as the pressure fluctuations in the pipeline lead to an average speed of sound similar to that used in the model. The pressure losses due to friction in the pipeline and bends were quantified and found to have a negligible effect on fuel pressure. Hence the pipeline friction resistance and bends resistance were set to zero in the model.

A sensitivity study on the different resistance parameters showed that the pressure reflections were most impacted by fitting and T-junction parameters. A multi-variable optimisation was done on the pipeline model in MATLAB. While this improved the reflected wave performance in the first wave, the lower frequency wave reflections continued to decay faster than experimental data. To improve the matching of the reflected waves, further experiments are required to understand the response of the fittings, specifically the T-junctions used in the experimental setup. This will enable an improved resistance matching enabling better TLM technique application for fuel pipelines with short pressure reflections.

A sensitivity analysis on pipe 4 was conducted by changing the length. The model was shown to be sensitive to length, specifically to the decay of pressure reflections. With an accurate model, an optimised solution for fast decay of pressure reflections in the pipeline design can be implemented. This would reduce the error observed in the pressure methods at higher engine speeds.

While TLM could provide a starting point for pressure wave reflection predictions, further experiments and characterisation of components would be required to improve the simulation results' accuracy of pressure reflections. TLM technique's application to the fuel pipelines

requires further experiments to obtain data on pressure waves caused due to each component. This data is required to enhance the accuracy of resistances used in the model. This closer examination of each component will enable accurate implementation of the TLM technique for fuel pipeline applications. The precise representation requirements of components (such as the injector) for the TLM technique would increase the complexity of the model and potentially increase the computation cost and time required for modelling.

7 On-engine pressure measurement

The pressure methods (OPTM and TPTM) were previously applied on a spray rig (Chapter 5). The conclusions from the experimental data were used to design the fuel injection pipeline used on a single-cylinder engine to enable the use of both OPTM and TPTM. While the engine was not thermodynamically similar to a commercial engine, the tests conducted will provide evidence for confirming the utility of the pressure methods for on-engine applications in research. The pressure measurement setup used on the engine for the experiments is first described, followed by results and discussion.

7.1 Experimental methodology

7.1.1 Fuel pipeline

The same pipeline as used in setup 6 in the pressure measurement chapter was used on the optical engine (Section 5.1), as this setup could be used to calculate the mass injected using both the pressure methods. Table 7.1 lists the different dimensions and setup used for the optical engine experiments. The measurement pipeline was 2400 mm long with 200 mm between the P1 and P2 pressure transducers. The P1 was 100 mm from the end of the pipeline going into the injector mount. The pipeline had 90° bends every 100 mm to create a coiled pipeline. The Kistler 4067E pressure transducers were used for the pressure measurement data. The measurement pipeline was connected to a fuel purge valve and the fuel pump with a T-junction. Figure 7.1 shows the setup used for the optical engine experiments. The injection signal was delivered using the NI DIDS system, the duration and timing are controlled using the BNC device described in Section 3.2.

Table 7.1: Measurement pipeline setup used for the optical engine experiments

Measurement pipeline parameter	Value
Length (mm)	2400
Distance between P1 & P2 sensors, l (mm)	200
Distance between injector mount and P1 (mm)	100
Distance between bends (mm)	100
Number of bends	21
Type of P1 & P2 sensor	Kistler 4067E

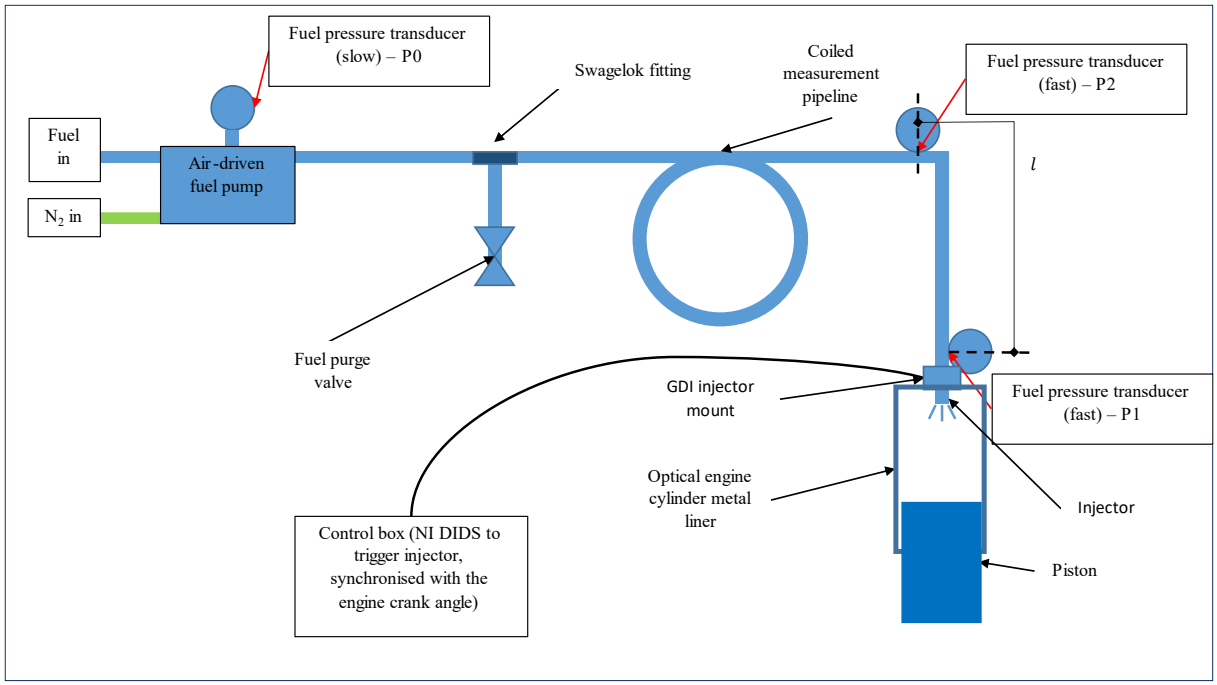

Figure 7.1: Simplified schematic of the fuel pipeline setup used for pressure measurement experiments on the optical engine. The air-driven (Heypac) fuel pump is used for fuel pressurisation. The fuel pressure transducers P1 and P2 are recorded during the experiments while P0 is used to monitor fuel pressure before injection. Not to scale.

7.1.2 Experimental conditions

The optical engine was motored (where the engine dynamometer was used to run the engine) during all the pressure measurement tests. Five different engine speeds with three injection

duration, which were used in the spray rig experiments, were tested. Each test had 300 injections recorded, the same as the spray rig. Table 7.2 shows all the conditions used for the pressure measurement experiments on the optical engine. Iso-octane was used for the experiments at 150 bar injection pressure, same as the spray rig.

Table 7.2: Experimental engine conditions for the optical engine tests.

Engine parameter	Value
Engine speed (rpm)	1060, 1210, 1505, 1725, 2020
Injection duration (ms)	1.0, 1.5, 2.0

The data for the experiments was recorded with the AVL X-ion system using the AVL IndiCOM software. The pressure measurements from the P1 and P2 transducers were recorded at 0.1 °CA resolution. The temperature signal from the P1 pressure transducer was recorded every 1.0 °CA, and the digital trigger signal sent to the NI DIDS system was recorded every 0.2 °CA. The measurements were saved for each engine cycle and are converted into a MATLAB data file for post-processing.

7.2 Results and Discussion

The injection pressure traces were processed in MATLAB to analyse and calculate the mass injected per injection. Figure 7.2 shows a single 2 ms injection at 1060 rpm engine speed. The P1 and P2 pressure traces are shown in blue solid and black dashed, respectively, in Figure 7.2 (a). The injection signal sent to the DIDS system is shown in red in Figure 7.2 (b). The injection request was sent to the DIDS system at -280 °CA, and this is followed by the injection seen in the pressure signals.

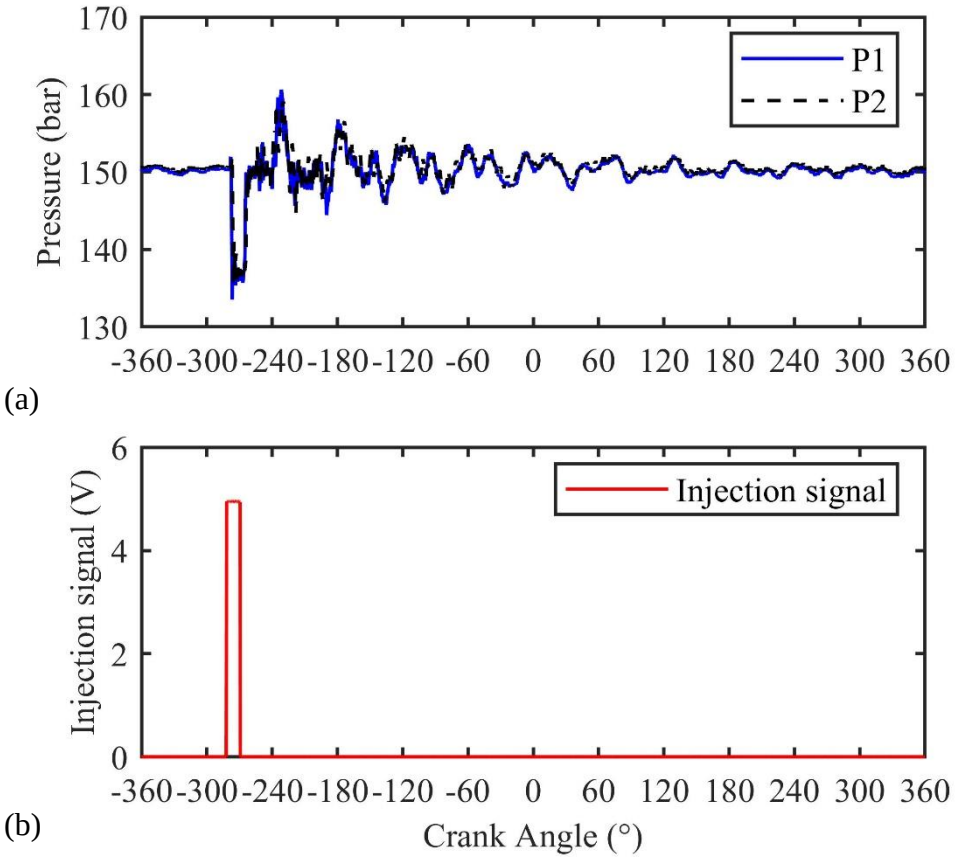

Figure 7.2: Single injection of 2 ms injection duration at 1060 rpm with 150 bar injection pressure, (a) the pressure traces for the injection from both the P1 and P2 pressure transducer. (b) the injection signal sent from the BNC control box to the LabVIEW DIDS.

The pressure signals observed in Figure 7.2 had a similar shape as observed in the spray rig experiments, and both the OPTM and TPTM were be applied to the pressure data. Figure 7.3 shows a magnified injection trace where there was a small phase difference observed in the P1 and P2 pressure traces as seen in the spray rig experiments in Chapter 5. There was also an observable delay between the injection signal sent from the NI DIDS and the pressure drop due to injection; this was caused due by delays in injector actuation and the pressure measurement being taken upstream of the injector.

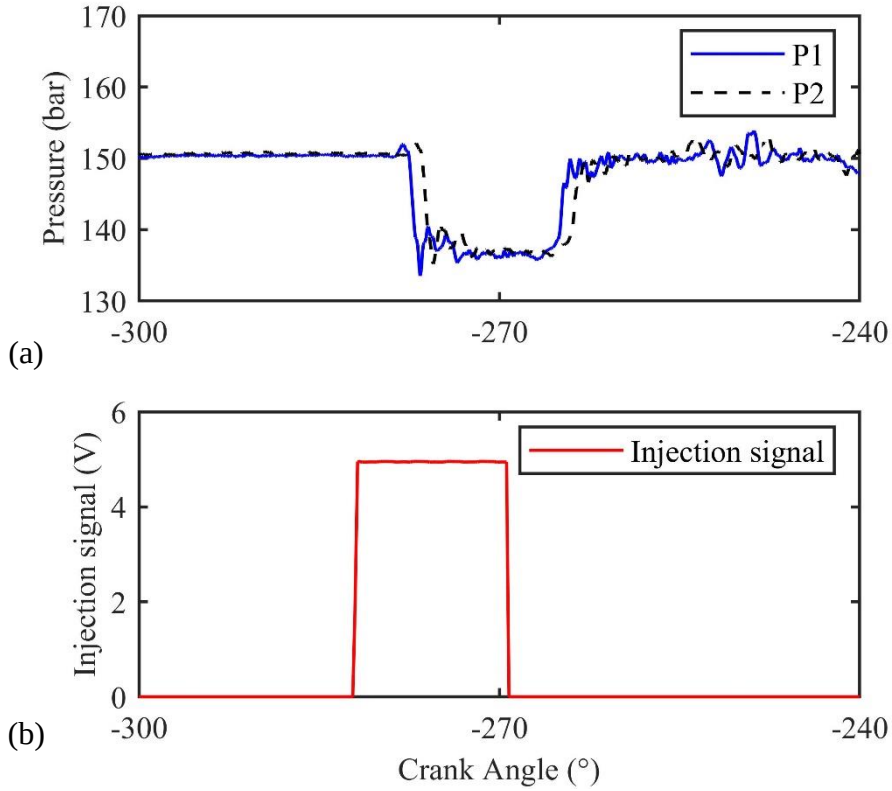

Figure 7.3: Single injection of 2 ms injection duration at 1060 rpm with 150 bar injection pressure magnified, (a) the pressure traces for the injection from both the P1 and P2 pressure transducer. (b) the injection signal sent from the BNC control box to the LabVIEW DIDS.

The engine data was recorded in reference to engine crank angles, and this means that for the same injection duration, the injection signal will be a more significant proportion of the engine cycle at higher engine speeds. Figure 7.4 shows a 2 ms injection at an engine speed of 2020 rpm. While the injection duration in milliseconds is the same for both injections, the injection signal in engine crank angles is approximately 25 °CA for the injection at 2020 rpm, while its duration is 12.5 °CA at 1060 rpm. To use the OPTM and TPTM for calculating mass injected, the pressure data needs to be converted into a time-domain signal. The time step (t_{step}) for 0.1 °CA was given by equation 7.1 below.

$$t_{step} = \frac{engine\ cycle\ duration}{7200\ samples\ per\ engine\ cycle} \tag{7.1}$$

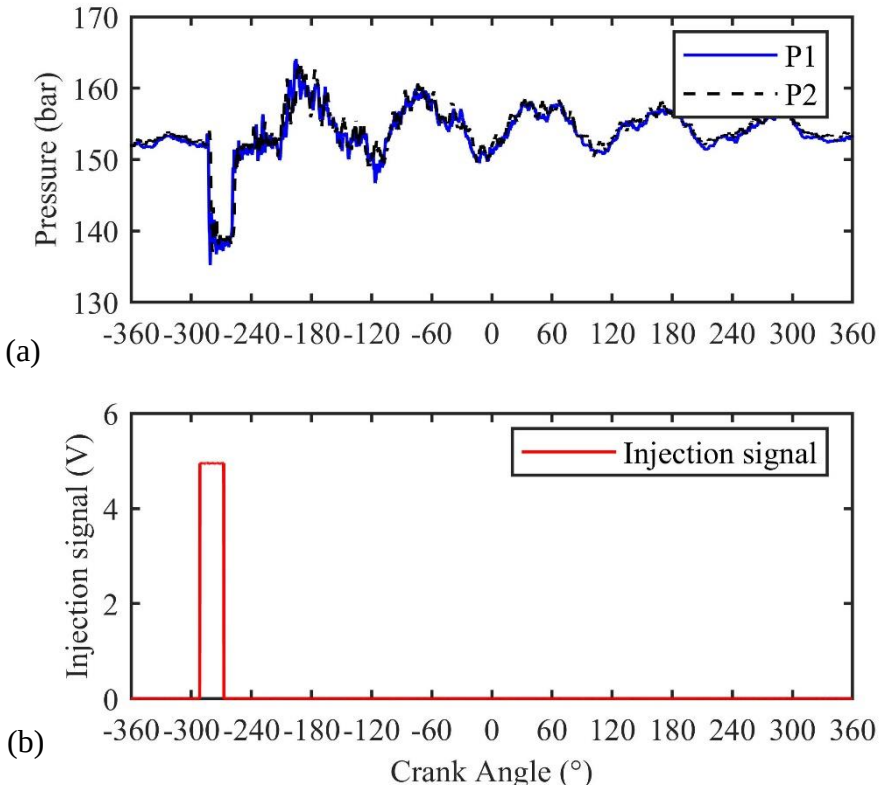

Figure 7.4: Single injection of 2 ms injection duration at 2020 rpm with 150 bar injection pressure, (a) the pressure traces for the injection from both the P1 and P2 pressure transducer. (b) the injection signal sent from the BNC control box to the LabVIEW DIDS.

The gradient of the P1 pressure trace was used to determine the SOI and EOI of injection (Section 5.2.2) to calculate the mass injected per injection. The average pressure was calculated using the SOI and using 1 ms worth of the pressure trace prior to the SOI (~6.25 °CA at 1060 rpm). The SOI and EOI were detected similarly to the DAQ data; the change in gradient was detected after -300 °CA. Figure 7.5 shows a 2 ms injection at 1060 rpm marked with the SOI an EOI detected using the gradient method with the marked pressure data used for the average fuel pressure calculation. The EOI detected was below the SOI pressure suggesting the EOI detected was during injector closure; this might lower the mass injected calculated. While the impact of the current EOI detection on the mass injected calculation can be calculated, the difference to actual injected mass can on be quantified if there is a secondary mass measurement

method used for the OPTM calibration on the setup. Hence, the current EOI detected was used in the mas injected calculations.

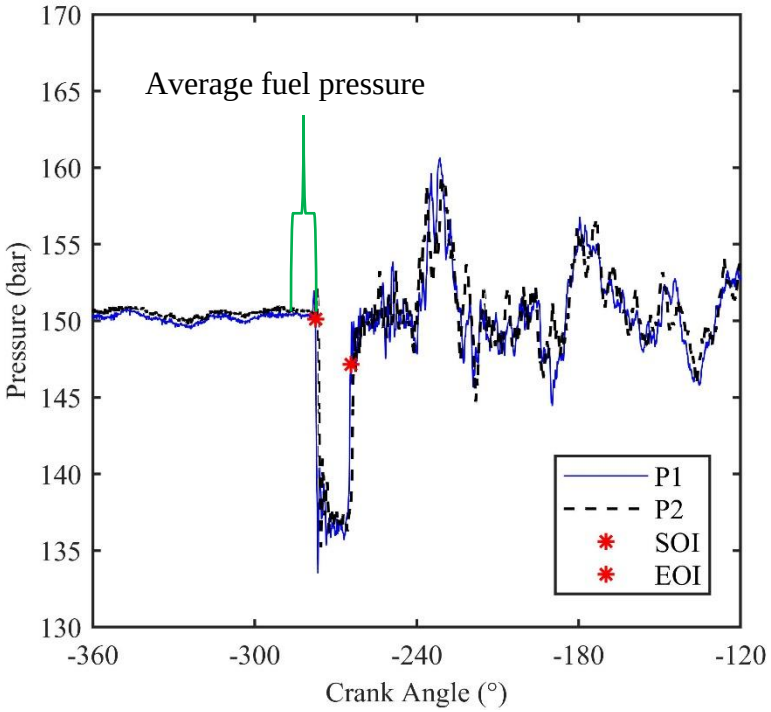

Figure 7.5: Single 2 ms injection at 1060 rpm pressure signals with the SOI and EOI of the injection marked. Average fuel pressure is taken over 1 ms (marked by the green section).

The OPTM and TPTM were applied to the pressure measurement taken on the engine. Figure 7.6 shows the OPTM and TPTM applied to the 2 ms injection pressure data plotted in Figure 7.5. The mass injected was calculated for each injection and averaged for each data set. The TPTM EOI was detected during the flow rate drop as shown in Figure 7.6 when using the gradient method for SOI and EOI detection. The impact of this, as mentioned earlier, will further need to be investigated with a secondary mass measurement technique. Any injections where the SOI and EOI cannot be deduced due to the fuel pump stroke were removed from the calculation, similar to spray rig experiments (Section 5.2).

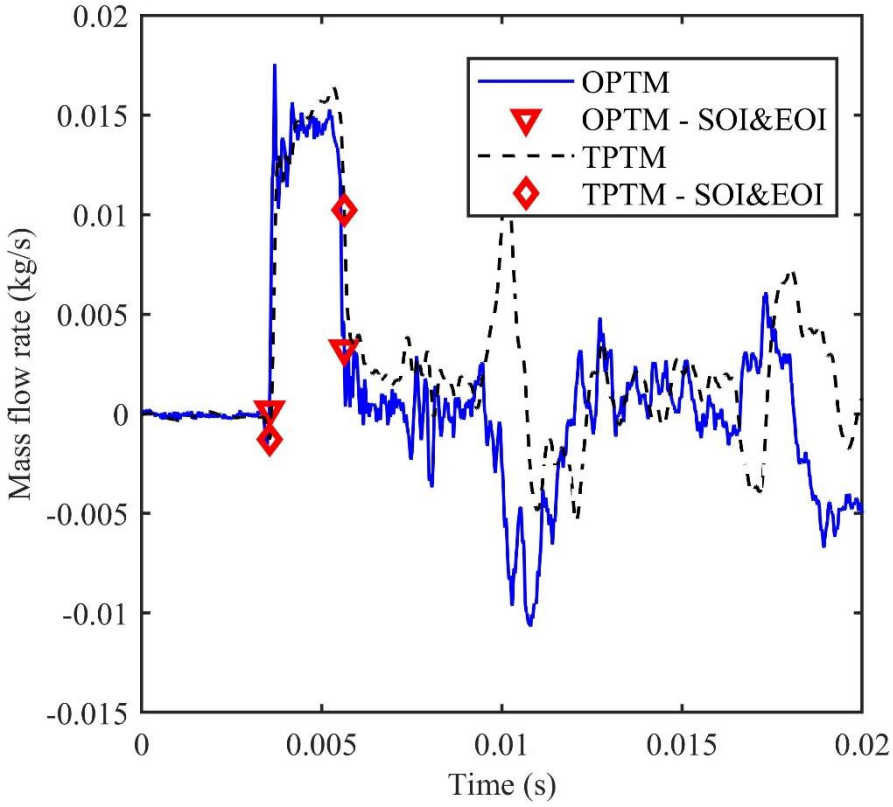

Figure 7.6: OPTM and TPTM applied to a single 2ms injection at 1060 rpm.

The pressure methods were applied to the data collected with the different test conditions. While processing the pressure data, a few of the datasets were not synchronised (shifted injection timing and extended pressure signal delays between P1 and P2). Figure 7.7 shows a single injection with these effects. The shift in injection timing indicated an issue with BNC control, while the increased delay between the pressure signals was caused due to errors in the data acquisition system. While the OPTM was not affected by this shift, in the current from the TPTM cannot be applied to this data. However, this data was used by shifting the P2 pressure signal to correct the time delay. The P2 pressure signal was advanced manually to the correct position with an approximate time delay calculated using the distance between the sensors. This correction, however, relies on knowing both the distance and the expected time delay between the P1 and P2 sensors. This was observed explicitly in the 2 ms injection data above 1500 rpm, as shown in Figure 7.7. Further changes were made in the BNC control by setting a faster

sampling rate for the BNC input to correct the timing of the injection and avoid this problem for other injection duration tests.

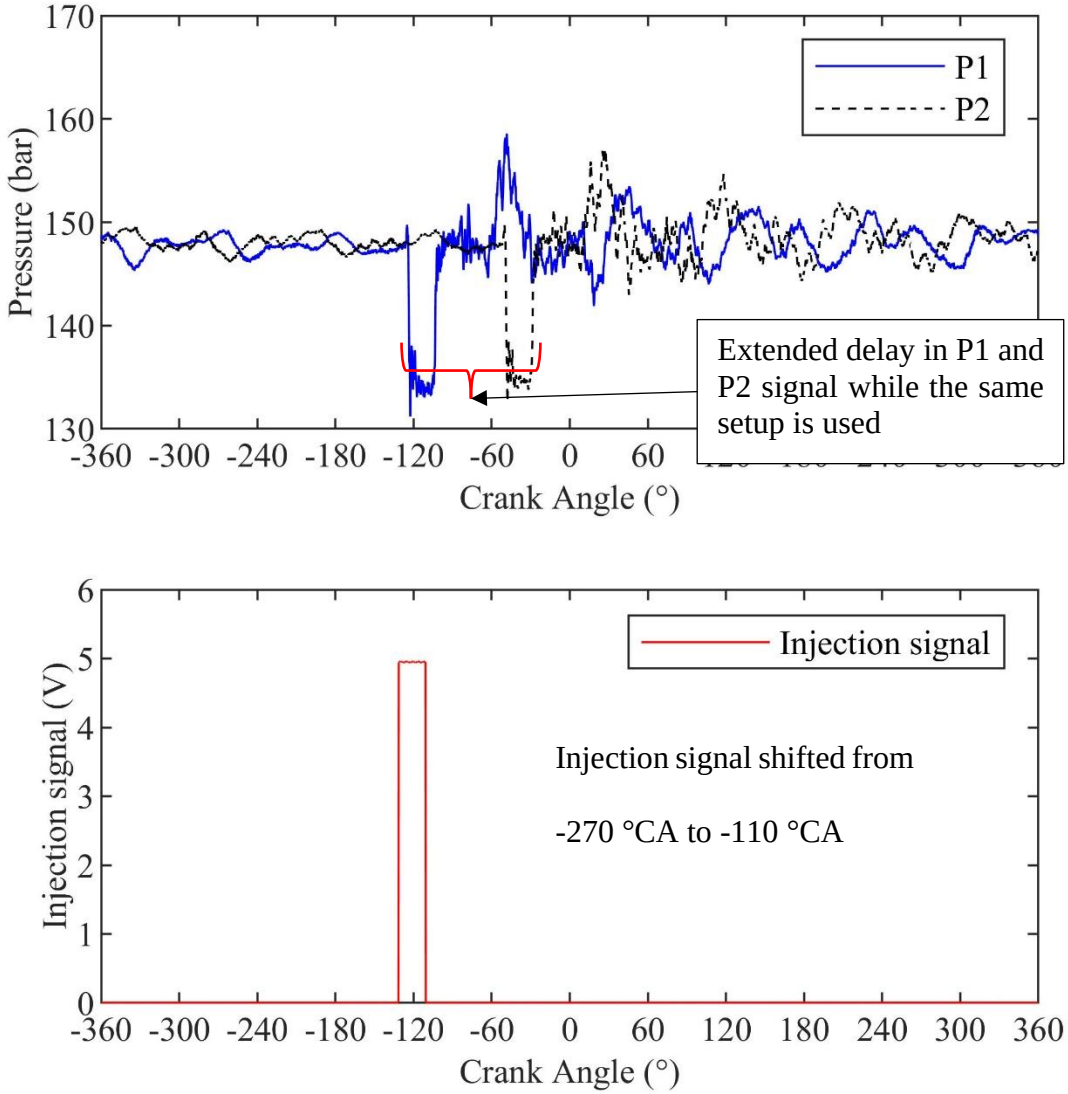

Figure 7.7: Single 2 ms injection at 1725 rpm. The injection timing has been delayed and the delay between the P1 and P2 increased.

Figure 7.8 shows the calculated mass injected for the engine data using both OPTM and TPTM. The three injection durations are plotted at different engine speeds. The OPTM and TPTM calculate similar mass injected values at all the tested engine speeds, showing the pressure methods' applicability for mass injected calculations. One standard deviation from the mass injected calculation was plotted on each data set. The most significant standard deviation is

observed in the 2 ms TPTM higher engine speed cases (1505 rpm and 2020 rpm). This variation was attributed to the time delay correction applied to the P2 pressure signal. While the time delay was corrected, this was a manual correction and was a source of the large standard deviation caused in mass injected values. Further tests would be needed to get improved data sets at the 2 ms injection duration.

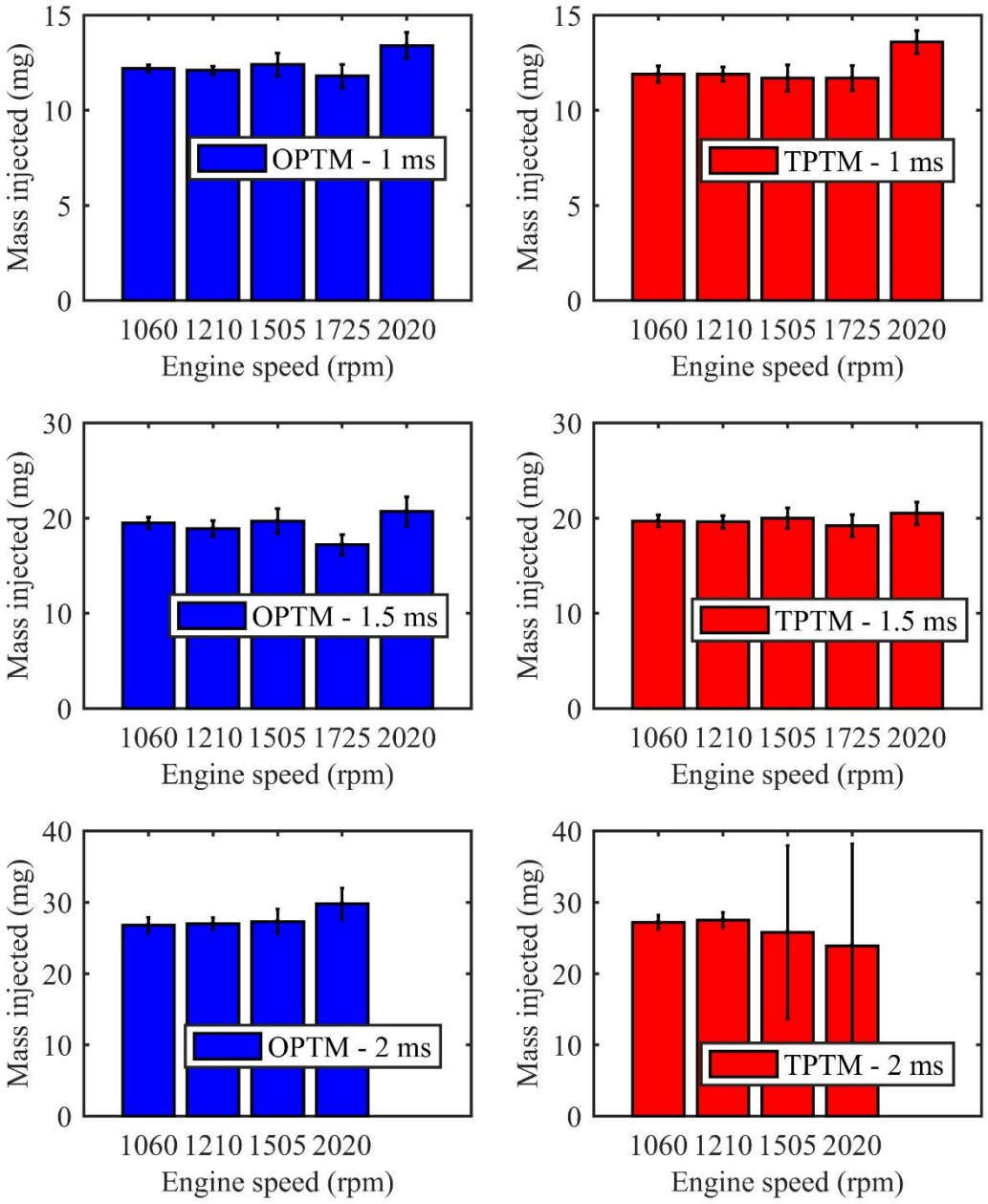

Figure 7.8: Calculated mass injected at different engine speed using OPTM and TPTM. 3 different injection duration results are shown. ±One standard deviation is plotted for the calculated injected mass have been plotted on the individual bars.

Figure 7.9 shows the OPTM and TPTM averaged mass injected values. The mass injected value across all engine speeds were used to calculate the average. The plot shows both the methods calculate a similar mass injected, and any discrepancies between the two calculations were within the one standard deviation of the average. This shows that both the pressure methods can be used to calculate on-engine mass injected values. A secondary mass measurement technique is required to assess the accuracy of the mass injected calculation of the pressure methods. While both methods can be used for injected mass measurement, the OPTM was easier to implement and required data only a single pressure transducer. OPTM also offered a lower standard deviation in the results compared to the TPTM. With the current pipeline design, the OPTM can be used to calculate the mass injected values for on-engine data. Further, the OPTM was also more robust to any errors in data acquisition and does not require additional data or knowledge for injected mass calculation.

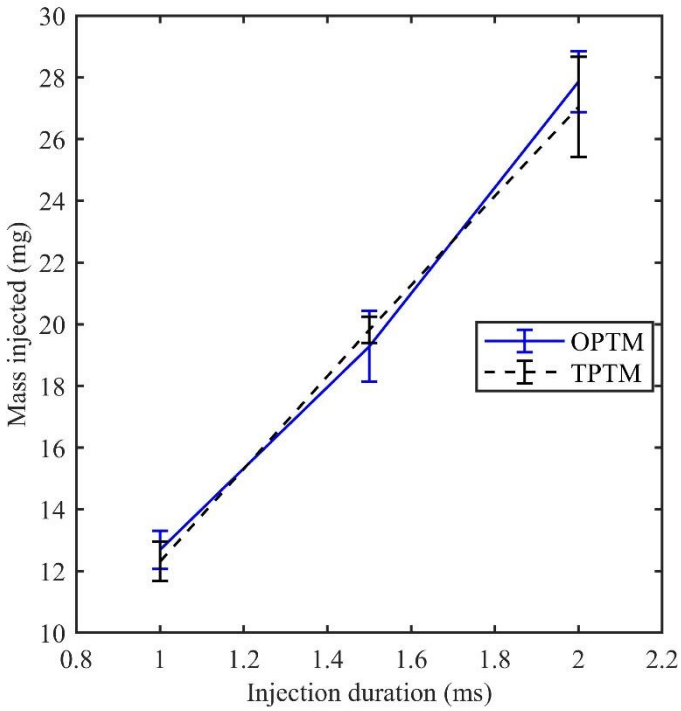

Figure 7.9: Averaged mass injected values across the engine speeds for different injection durations. ±One standard deviation is plotted for the pressure method calculations.

7.3 Chapter summary

Initial pressure measurement data were taken from the on-engine deployment of the pressure transducer setup. The experiments were conducted in a motoring engine for three injection durations at five engine speeds.

The OPTM and TPTM were both applied to the pressure data collected, and the injected mass per injection was calculated offline after data collection. With the 2 ms injection tests at engine speeds higher than 1500 rpm, there was a shift observed in the injection timing and the time delay in the data acquisition of the P2 pressure signal. This was manually corrected by reducing the delay and shifting the SOI and EOI detection to the new injection timing for pressure methods implementation on this data.

The mass injected calculations show that OPTM and TPTM can be successfully implemented on the initial pressure data taken on-engine. Both the pressure methods gave similar averaged values of mass injected across the engine speeds tested at the three injection durations.

Further tests are required to correct the injection trigger and get further data at different injection duration. Tests would need to be completed for comparing the mass injected calculation from the OPTM and TPTM to the engine consumption using a second fuel measurement method. For example, a CFM or the exhaust lambda sensor and the volumetric air flow meter measurement at intake together used to measure the average engine consumption for this comparison. Once these tests are completed, the pressure methods would need to be implemented for real-time fuel measurement and correction of the injection duration. Real-time fuel measurement requires on-engine implementation and monitoring of the pressure data.

8 Originalities, Conclusions and Future work

8.1 Originalities

1. A repeatability test was developed on The data collected from Coriolis Flow Meter (CFM) experiments, and this provided novel insights into the current CFM limitations. This demonstration of the repeatability in measurement was not previously reported in the literature. This work highlighted and quantified the current shortcomings, showing the FNGC technique's unsuitability in measuring the mass injected in GDI injections. Design suggestions were made to improve this technique for applicability for fuel injection measurement. Further, this work demonstrated that the CFM could distinguish the reverse flow at the start of injection (SOI) and that the measurement technique was capable of partial injection (‘misfire’) detection.
2. Ferrari et al. [13] suggested that either a One Pressure Transducer Method (OPTM) or a Two Pressure Transducer Method (TPTM) should be used for flow measurement depending on the mass injected. However, the current work has demonstrated that both the OPTM and the TPTM can be applied to a broad range of injection events in GDI injectors with appropriate modifications to the pipeline setup. This work has extended the range of applicability of both the OPTM and TPTM beyond that which has previously been reported with different pipeline designs. Additionally, the SOI and end of injection (EOI) detection methods used by Ferrari et al. [13] were found to be inaccurate, particularly having no physical basis for the assignment of EOI. Hence, three alternative SOI and EOI detection methods were proposed and investigated. While all three methods could be used, the study found that a gradient-based method was preferable as it could accurately detect the SOI and EOI positions from the pressure signal alone at all the simulated engine speeds examined. The identification and inclusion of physically justifiable SOI and EOI events into the pressure method

calculations are crucial for accurate mass injected calculations and represent a significant improvement over the state-of-the-art represented by [13].

3. A Transmission Line Modelling (TLM) for fuel pipelines was developed and implemented on the experimental setups tested in the pressure measurement experiments. However, in this TLM technique implementation, a suitably good match beyond the first pressure reflection after injection was not achieved, limiting the fuel pipeline model application.
4. The pressure measurement pipeline was deployed on an optical engine, and the OPTM and TPTM were applied to the data collected. The data has confirmed that there are no adverse effects from engine vibration on the pressure methods.

8.2 Conclusions

This work presented an investigation of two potential flow measurement techniques for determining the mass of fuel injection through injectors in individual injection events. Pressure methods (OPTM and TPTM) and FNGC (CFM with PRISM for filtering) were recognised to provide these measurement capabilities and were considered for on-engine flow measurement applications. These technologies were chosen to be tested on the Oxford spray rig with a GDI injector for viability and further investigate the limitations to determine the improvements required in the methods for on-engine implementation.

8.2.1 Coriolis Flowmeters

CFM and pressure sensors were installed on the Oxford spray rig and tested to gather Coriolis and pressure data during injection to understand the impact of including a CFM in a fuel pipeline. The pressure data recorded was used to observe the CFM's pressure traces upstream and downstream.

The FNGC technique measured and identified individual injections in single injections and injection trains at simulated engine speeds of 1788 and 2978 rpm (multiples of flowtube period).

The CFM data was post-processed, and the data indicated repeatability of the measurement technique, demonstrating the potential use of FNGC in fuel measurement. However, as previously observed in [75], [76], the FNGC technique was limited in the GDI setup as injections could only be injected at multiples of the flowtube oscillation period due to the instantaneous phase of the flowtube affecting the DC offset and measured peak phase difference. It was observed that the injection duration and the flowtube phase both influenced the peak height. The mechanical and digital filtering of the injection caused by the flowtube oscillation period and signal processing respectively elongated the injection observed in the CFM signal irrespective of injection duration. Consequently, the CFM data could not be used to calculate the injected mass.

The work reported some notable features from the GDI experiments conducted using the FNGC. Negative mass flow due to needle lift at SOI could be differentiated from the injection in the CFM data. The pressure signal also showed this as a pressure rise (reverse flow at needle lift) at SOI due to needle lift. Further, partial injections in an injection train could also be identified, demonstrating the potential of FNGC for injector monitoring uses.

The pressure difference seen across the CFM showed the CFM acts as a plenum damping the pressure waves caused by the injection upstream of the CFM. This revealed that the CFM absorbed part of the pressure wave energy, which was observed as increased noise in the CFM signal.

While the FNGC technique shows the potential for mass flowrate measurements, it cannot be used with the current CFM available due to the limitation of the flowtube frequency. With the current limitations, CFMs cannot provide the direct mass flow rate measurement for injectors. This method requires further improvements, such as higher oscillation frequency CFM (by reducing the size of CFMs) to enable injected mass calculation and injection rate shape measurement.

8.2.2 Pressure methods

The Oxford spray rig was modified to include an injector mount to minimise pressure reflections near the injector and enable the application of pressure measurements to mass flow rate calculation. This setup was used to collect and analyse pressure data during injections to compare with the gravimetric measurement of the injected mass. Sources of noise (fuel pump, a small discontinuity near the injector, and pressure reflections within the injection window) were added to the setup incrementally to test the robustness and characterise the pressure methods. Initially, the data from the transducers was acquired at 20 kHz before doubling this to 40 kHz to improve the pressure data resolution, with two fast pressure transducers (P1 and P2) on the spray rig. Three different SOI and EOI detection methods were proposed and examined, and the gradient method was chosen for injection detection methods, as injections at higher simulated speeds could be detected effectively.

The OPTM and TPTM were applied to the pressure data to calculate the mass injected. Both pressure methods could be used to calculate the mass injected successfully. However, the TPTM had a bigger standard deviation in the injected mass calculations than the OPTM as there was no temporal coupling between the two sensors. The following conclusions were taken from the experiments conducted:

- The inclusion of a fuel pump in place of the fuel accumulator in the spray rig had minimal impact on the accuracy of the mass calculation but increased the standard deviation of both approaches.
- Introducing a small discontinuity at the injector mount dissipated part of the energy within the discontinuity (before the pressure transducers) and reduced the mass injected calculation in both the pressure methods.
- The inclusion of pressure reflections induced within the injection window increased the error in the OPTM but did not influence the TPTM. The OPTM was required to be

modified to correct the reflection with a forced average, which then could be used to calculate the mass injected. This modification required knowledge of the expected reflection interaction with the signal.

- Bends in the fuel pipeline between the two-pressure transducers (P1 and P2) were found not to influence the injected mass calculations.
- In the current pipeline design, the pressure methods predicted mass injected values close to gravimetric measurements for all engine speeds up to 3500 rpm. Above simulated engine speeds higher than 3500 rpm, the mass calculated was significantly different from the gravimetric measurement. The reflected pressure waves from the preceding injection influenced the current injection, limiting the use of both pressure methods at higher engine speeds. This indicated that the TPTM could only be used where small pressure reflections are present.
- The OPTM and TPTM were compatible with different injector types and injection pressures.

While OPTM and TPTM can be implemented to calculate the mass injected for each injection, there are limits on its applicability at higher engine speeds where pressure reflections influence the subsequent injection, and careful pipeline design is required for accurate calculations. Overall, the OPTM has a smaller standard deviation in the results, while the TPTM is generally more robust to small reflections near the injections. With the current coiled pipeline, the pressure methods can only be implemented for injection measurements on injectors for engine speeds below 3500 rpm (pipeline design dependent); above this engine speed, the pressure reflections impact both the OPTM and TPTM.

8.2.3 Transmission line modelling

The TLM technique was used to develop a fuel pipeline model based on the experimental setup. TLM simulated pressure data reasonably matched the experimental data after EOI until the end

of the first pressure reflection due to the forced injection input condition at the injector end. It was observed that the low-frequency pressure reflections decayed faster than the higher frequencies. The lower frequency pressure reflections were observed to impact the consequent injection in experiments, and this lack of matching only enables the use of the model to 2500 rpm; however, even in this case, the information on the pressure reflections after the first reflections cannot be used to predict the pipeline's physical characteristics.

Both OPTM and TPTM could be applied to the simulated engine speed data up to 2500 rpm with the forced injection approximation, showing the TLM application's potential for fuel pipeline simulation. In the pipeline model, a fixed speed of sound near the fluid speed of sound could be used even if there are pressure fluctuations in the pipeline.

In the pipeline model, the fitting and T-junction parameters directly influence the pressure reflections observed. These parameters were used in a multi-variable optimisation to improve the model. The optimisation provided a closer match to the reflected wave for the first reflection, but the lower frequency wave reflections continued to decay faster than experimental data.

While the pipeline model derived from TLM could provide a starting point for pressure wave reflection predictions, in its current form, further experiments and characterisation of components would be required to improve the simulation results' accuracy of pressure reflections after the first reflection. A closer examination of each component pressure data is required to improve accuracy and the use of this model for fuel pipeline simulation.

8.2.4 On-engine testing

Pressure measurement data was taken from the on-engine deployment of the pressure transducer set up on an engine. The experiments were conducted in the engine under a motored condition (no spark ignition in the cycle) for the three injection durations (exact durations as the spray rig experiments) tested on the spray rig at five different engine speeds. The OPTM and TPTM were

applied to the pressure data collected, with the injected mass calculation done offline (after data collection). Both pressure methods gave similar averaged values of mass injected across the engine speeds tested for the three injection durations, confirming no adverse effects on the pressure methods from the engine vibrations.

8.3 Future work

8.3.1 Coriolis flowmeter

While the Coriolis meter shows the potential to be used in GDI injection mass measurement applications, improvements would be required to enable injected mass calculation and injection rate shape measurement using this method. This method can be improved with CFMs with an increased frequency of oscillation (order of kHz). This will enable a broader range of injection frequency and reduce the injection stretch in time that has been observed in the experiments. Further work is required to understand the impact of the instantaneous phase if the CFMs oscillation period is in the range of injection durations as a correction method might still be required to ascertain mass injected per injection.

With current CFMs needing to be isolated from external vibrations for injection detection, the higher frequency CFMs will need to be studied further to understand the consequences of engine frequency vibrations on the phase difference measurement. Tests with an imbalanced mass motor are required to study the impact of vibrations on mass flow rate measurement before including the CFM setup onto an engine. This will be important for the on-engine implementation of CFMs for injected mass measurement, as there will be engine vibrations.

8.3.2 Pressure methods

The effect of pressure reflections on the injection pressure waves needs to be understood to successfully implement the pressure method on the full range of engine speeds. Further experiments are required to characterise the pressure reflections observed at simulated engine speeds higher than 3000 rpm; this was also dependent on the pipeline design used. The effects

of pipeline reflections lead to a breakdown of both the OPTM and TPTM at higher engine speeds. This data can then be used to improve the OPTM and TPTM for higher engine speed implementation. Further improvements in pipeline design can be explored to improve the reflection response at higher engine speeds.

8.3.3 Transmission line modelling

Further experiments are required to characterise the junctions (fittings) and other components used in the spray rig, such as the injector, to improve the model's resistance parameters and implementation. The experiments' data will enable improvements in the implementation of the current pipeline model to better the response of pressure reflections after the first reflection and match the experimental data closer. This improved TLM pipeline model could be used to predict pressure reflections accurately in current pipeline designs to improve the OPTM and TPTM implementation and provide valuable information on new designs of fuel pipelines.

8.3.4 On-engine implementation

Tests are first required to correct the injection trigger signals in the BNC, so the fuel is injected at the correct cycle location in the engine cycle. Then experiments are required to get further data at different injection durations on the engine. The injected mass calculations from the pressure methods must be validated using a secondary device to calculate the fuel intake such as a gravimetric measurement, CFM or by comparing it with the average fuel consumption calculation done using the exhaust lambda sensor and the volumetric air-flow meter at intake. As part of this validation, combustion tests would need to be completed for comparing the mass injected calculation from the OPTM and TPTM to the engine consumption.

Online implementation of pressure methods will be required for real-time fuel measurement and correction. This will require measurements of the power output, lambda sensor and the mass injected, and these will then be used to develop algorithms for fuel correction to improve

fuel efficiency. Online fuel monitoring using pressure methods can also improve understanding of the impact and mechanics of deposit formation on GDI injectors.

8.4 Publications related to this work

1. F. Leach, M. Davy, M. Henry, M. Malladi, M. Tombs, F. Zhou, M. Gold, R. Pearson, "Fast NGC: A New On-Line Technique for Fuel Flow Measurement," *SAE Tech. Pap. Ser.*, no. 2019-01–0062, 2019.
2. M. Henry, F. Zhou, M. Tombs, F. Leach, M. Davy, and M. Malladi, "Prism Signal Processing of Coriolis meter data for gasoline fuel injection monitoring," *Flow Meas. Instrum.*, vol. 70, 2019.

9 References

[1] BP, “Energy Outlook 2020 edition,” 2020. [Online]. Available: https://www.bp.com/content/dam/bp/business-sites/en/global/corporate/pdfs/energy-economics/energy-outlook/bp-energy-outlook-2020.pdf. [Accessed: 22-Jul-2021].

[2] S. Petit, “World Vehicle Population Rose 4.6% in 2016 | content from WardsAuto,” *WardsAuto*, 2017. [Online]. Available: http://subscribers.wardsintelligence.com/analysis/world-vehicle-population-rose-46-2016. [Accessed: 05-Nov-2018].

[3] “Cars (VEH02) - GOV.UK.” [Online]. Available: https://www.gov.uk/government/statistical-data-sets/veh02-licensed-cars. [Accessed: 22-Jul-2021].

[4] G. Kalghatgi, “Is it really the end of internal combustion engines and petroleum in transport?,” *Appl. Energy*, vol. 225, Sep. 2018.

[5] R. D. Reitz *et al.*, “IJER editorial: The future of the internal combustion engine:,” *https://doi.org/10.1177/1468087419877990*, vol. 21, no. 1, Sep. 2019.

[6] Z. Wang, X. Pan, W. Zhang, Y. Zhao, H. Li, and P. Liu, “The Development Trend of Internal Combustion Engine,” *J. Phys. Conf. Ser.*, vol. 1626, no. 1, 2020.

[7] “Emissions in the automotive sector - European Commission.” [Online]. Available: https://ec.europa.eu/growth/sectors/automotive/environment-protection/emissions_en. [Accessed: 23-Jul-2018].

[8] “Regulation (EC) No 443/2009 of the European Parliament and of the Council of 23 April 2009 setting emission performance standards for new passenger cars as part of the Community’s integrated approach to reduce CO 2 emissions from light-duty vehicles (Text with EEA relevance) - EU Law and Publication.” [Online]. Available: https://publications.europa.eu/en/publication-detail/-/publication/29f45c63-cd73-4b00-ab14-87a02a7a1b97/language-en. [Accessed: 11-Aug-2018].

[9] “How will the petrol and diesel car ban work? - BBC News.” [Online]. Available: https://www.bbc.co.uk/news/uk-40726868. [Accessed: 05-Jun-2021].

[10] H. Government, “The Ten Point Plan for a Green Industrial Revolution,” 2020. [Online]. Available: https://assets.publishing.service.gov.uk/government/uploads/system/uploads/attachment_data/file/936567/10_POINT_PLAN_BOOKLET.pdf. [Accessed: 23-Jul-2021].

[11] Z. Lee, T. Kim, S. Park, and S. Park, “Review on spray, combustion, and emission characteristics of recent developed direct-injection spark ignition (DISI) engine system with multi-hole type injector,” *Fuel*, vol. 259. Elsevier Ltd, 01-Jan-2020.

[12] S. Shuai, X. Ma, Y. Li, Y. Qi, and H. Xu, “Recent Progress in Automotive Gasoline Direct Injection Engine Technology,” *Automot. Innov.*, vol. 1, no. 2, Apr. 2018.

[13] A. Ferrari, C. Novara, E. Paolucci, O. Vento, M. Violante, and T. Zhang, “Design and rapid prototyping of a closed-loop control strategy of the injected mass for the reduction of CO2, combustion noise and pollutant emissions in diesel engines,” *Appl. Energy*, vol. 232, 2018.

[14] L. Hentschel, W. Demmelbauer-Ebner, J. Theobald, W. Wendt, M. Thiele, and H.

Blume, “The New 1 . 0 l TSI with 85 kW and Petrol Particulate Filter – Clean , Efficient Performance for the Up ! GTI,” in *26th Aachen Colloquium Automobile and Engine Technology*, 2017.

[15] R. Stone, *Introduction to internal combustion engines*. Palgrave Macmillan, 2012.

[16] H. Bauer, *Gasoline-Engine Management*, 2nd ed., c. Plochingen : Bury St. Edmunds: Wiley, 2004.

[17] F. Zhao, M.-C. Lai, and D. L. Harrington, “Automotive spark-ignited direct-injection gasoline engines,” *Prog. Energy Combust. Sci.*, vol. 25, 1999.

[18] S. P. Chincholkar and J. G. Suryawanshi, “Gasoline Direct Injection: An Efficient Technology,” in *5th International Conference on Advances in Energy Research*, 2016, vol. 90.

[19] M. Costa, U. Sorge, S. Merola, A. Irimescu, M. La Villetta, and V. Rocco, “Split injection in a homogeneous stratified gasoline direct injection engine for high combustion efficiency and low pollutants emission,” *Energy*, vol. 117, pp. 405–415, 2016.

[20] M. Costa, U. Sorge, and L. Allocca, “Increasing energy efficiency of a gasoline direct injection engine through optimal synchronization of single or double injection strategies,” *Energy Convers. Manag.*, vol. 60, 2012.

[21] U. Spicher, M. Magar, and J. Hadler, “High Pressure Gasoline Direct Injection in Spark Ignition Engines - Efficiency Optimization through Detailed Process Analyses,” *SAE Int. J. Engines*, no. 2016-01–2244, 2016.

[22] R. H. Muñoz, Z. Han, B. a Vanderwege, and J. Yi, “Effect of Compression Ratio on Stratified-Charge Direct- Injection Gasoline Combustion Reprinted From : SI Combustion and Direct Injection SI Engine Technology,” *SAE Tech. Pap.*, no. 2005-01–0100, 2005.

[23] M. B. Çelik and B. Özdalyan, “Gasoline Direct Injection,” in *Fuel Injection*, D. Siano, Ed. Sciyo Published, 2010.

[24] S. S. Smith and W. Imoehl, “Measurement and Control of Fuel Injector Deposits in Direct Injection Gasoline Vehicles,” *SAE Tech. Pap.*, no. 2013-01–2616, 2013.

[25] H. Xu, C. Wang, X. Ma, A. K. Sarangi, A. Weall, and J. Krueger-Venus, “Fuel injector deposits in direct-injection spark-ignition engines,” *Prog. Energy Combust. Sci.*, vol. 50, 2015.

[26] “Gasoline direct injection.” [Online]. Available: https://www.bosch-mobility-solutions.com/en/products-and-services/passenger-cars-and-light-commercial-vehicles/powertrain-systems/gasoline-direct-injection/. [Accessed: 08-Nov-2018].

[27] J. Song, Z. Lee, J. Song, and S. Park, “Effects of injection strategy and coolant temperature on hydrocarbon and particulate emissions from a gasoline direct injection engine with high pressure injection up to 50 MPa,” *Energy*, vol. 164, Dec. 2018.

[28] “GDi: The future of the internal combustion engine | Delphi Auto Parts.” [Online]. Available: https://www.delphiautoparts.com/usa/en-US/article/gdi-future-internal-combustion-engine. [Accessed: 14-Jun-2021].

[29] B. Lehnert, C. Conrad, and M. Wensing, “GDI Sprays with up to 200 MPa Fuel Pressure and Comparison of Diesel-like and Gasoline-Like Injector Designs,” *SAE Tech. Pap.*,

2020.

[30] G. Hoffmann, B. Befrui, A. Berndorfer, W. F. Piock, and D. L. Varble, “Fuel System Pressure Increase for Enhanced Performance of GDi Multi-Hole Injection Systems,” *SAE Int. J. Engines*, vol. 7, no. 1, 2014.

[31] H. Husted, T. D. Spegar, and J. Spakowski, “The Effects of GDi Fuel Pressure on Fuel Economy,” *SAE Tech. Pap.*, no. 2014-01–1438, 2014.

[32] A. Nauwerck, J. Pfeil, A. Velji, U. Spicher, and B. Richter, “A Basic Experimental Study of Gasoline Direct Injection at Significantly High Injection Pressures Reprinted From : SI Combustion and Direct Injection SI Engine Technology,” *SAE Tech. Pap.*, no. 2005-01–0098, 2005.

[33] J. Gueit and J. Obiols, “Injector Fouling in Direct Injection Spark Ignition Engines - A New Test Procedure for the Evaluation of Gasoline Additives,” *SAE Tech. Pap.*, no. 2017-01–2294, 2017.

[34] D. Neacsu, F. Ivan, and M. Niculae, “About methods to reduce emissions of turbo charged engine gasoline direct injection,” *IOP Conf. Ser. Mater. Sci. Eng.*, vol. 227, no. 1, 2017.

[35] Z. Ye and L. L, “Control options for exhaust gas after treatment and fuel economy of GDI engine systems,” in *42nd IEEE International Conference on Decision and Control*, 2003, vol. 2.

[36] S. Henkel *et al.*, “Injector Fouling and Its Impact on Engine Emissions and Spray Characteristics in Gasoline Direct Injection Engines,” *SAE Int. J. Fuels Lubr.*, vol. 10, no. 2, 2017.

[37] C. Jiang *et al.*, “Effect of fuel injector deposit on spray characteristics, gaseous emissions and particulate matter in a gasoline direct injection engine,” *Appl. Energy*, 2017.

[38] A. Joedicke, J. Krueger-Venus, P. Bohr, R. Cracknell, and D. Doyle, “Understanding the Effect of DISI Injector Deposits on Vehicle Performance,” *SAE Tech. Pap.*, no. 2012-01–0391, 2012.

[39] B. Wang, T. Badawy, Y. Jiang, H. Xu, A. Ghafourian, and X. Zhang, “Investigation of deposit effect on multi-hole injector spray characteristics and air/fuel mixing process,” *Fuel*, vol. 191, 2017.

[40] K. Dearn *et al.*, “An Investigation into the Characteristics of DISI Injector Deposits Using Advanced Analytical Methods,” *SAE Int. J. Fuels Lubr.*, vol. 7, no. 3, pp. 771–782, 2014.

[41] A. A. Aradi, B. Imoehl, N. L. Avery, P. P. Wells, and R. W. Grosser, “The Effect of Fuel Composition and Engine Operating Parameters on Injector Deposits in a High-Pressure Direct Injection Gasoline (DIG) Research Engine,” *SAE Tech. Pap.*, no. 1999-01–3690, 1999.

[42] G. T. Kalghatgi, *Fuel/engine interactions*. Warrendale, Pennsylvania: SAE International, 2014.

[43] B. Wang, T. Badawy, P. Hutchins, P. Tu, H. Xu, and X. Zhang, “Numerical Investigation of the Deposit Effect on GDI Injector Nozzle Flow,” *Energy Procedia*, vol. 105, 2017.

[44] R. C. Baker, *Flow Measurement Handbook : Industrial Designs, Operating Principles, Performance, and Applications*. Cambridge: Cambridge University Press, 2000.

[45] A. A. H. Pá Dua, J. M. N. A. Fareleira, J. C. G. Calado, and W. A. Wakeham, "Density and Viscosity Measurements of 2,2,4-Trimethylpentane (Isooctane) from 198 K to 348 K and up to 100 MPa," 1996.

[46] H. W. Ebner and K. Köck, "New Fuel Mass Flow Meter – A Modern and Reliable Approach to Continuous and Accurate Fuel Consumption Measurement," *SAE Tech. Pap.*, no. 2000-01–1330, 2000.

[47] J. Deng, B. Maass, R. Stobart, E. Winward, and Z. Yang, "Accurate and Continuous Fuel Flow Rate Measurement Prediction for Real Time Application," *SAE Int. J. Engines*, vol. 4, no. 1, 2011.

[48] N. Papaioannou, "Thermal investigations on a high-speed direct injection diesel engine - DPhil Thesis," University of Oxford, Oxford, 2018.

[49] H. Fonseca, C. Ferreira, and T. Fernandes, "New Methodologies to Measure in Real Time Fuel Consumption of Internal Combustion Engines," in *15th International Conference on Experimental Mechanics*, 2012.

[50] M. Marcic, "Sensor for Injection Rate Measurements," *Sensors*, vol. 6, no. 10, 2006.

[51] W. Bosch, "The Fuel Rate Indicator: A New Measuring Instrument For Display of the Characteristics of Individual Injection," *SAE Tech. Pap.*, no. 660749, 1966.

[52] A. Takamura, S. Fukushima, Y. Omori, and T. Kamimoto, "Development of a New Measurement Tool for Fuel Injection Rate in Diesel Engines," *SAE Tech. Pap.*, no. 890317, 1989.

[53] S. Matsuoka, K. Yokotat, and T. Kamimoto, "The Measurement of Injection Rate," in *Proceedings of the Institution of Mechanical Engineers*, 1966, vol. 184, no. 2.

[54] G. Peng, H. Xu, X. Wang, and Y. Shen, "A new measurement of the fuel injection rate of diesel engine fuel pump based on transmission line dynamics," *Fluid power*, vol. 1993, no. 2, 1993.

[55] M. Marčič, "New diesel injection nozzle flow measuring device," *Cit. Rev. Sci. Instruments*, vol. 71, no. 1876, 2000.

[56] "Loccioni Mobility Mexus | Loccioni Mobility." [Online]. Available: http://mobility.loccioni.com/instruments/mexus/mexus-dld-gld/?lang=en. [Accessed: 08-Jul-2018].

[57] G. R. Bower and D. E. Foster, "A Comparison of the Bosch and Zuech Rate of Injection Meters," *SAE Tech. Pap.*, no. 910724, 1991.

[58] A. Ferrari and T. Zhang, "Benchmark between Bosch and Zeuch method–based flowmeters for the measurement of the fuel injection rate," *Int. J. Engine Res.*, Mar. 2019.

[59] F. Payri, J. M. Luján, C. Guardiola, and G. Rizzoni, "Injection diagnosis through common-rail pressure measurement," *Proc. Inst. Mech. Eng. Part D J. Automob. Eng.*, vol. 220, no. 3, 2006.

[60] A. Ferrari and F. Paolicelli, "An indirect method for the real-time evaluation of the fuel mass injected in small injections in Common Rail diesel engines," *Fuel*, vol. 191, 2017.

[61] A. Ferrari and P. Pizzo, "Optimization of an Algorithm for the Measurement of Unsteady Flow-Rates in High-Pressure Pipelines and Application of a Newly Designed Flowmeter to Volumetric Pump Analysis," *J. Eng. Gas Turbines Power*, vol. 138, no. 3, Oct. 2015.

[62] A. E. Catania and A. Ferrari, “Development and assessment of a new operating principle for the measurement of unsteady flow rates in high-pressure pipelines,” *Flow Meas. Instrum.*, vol. 20, 2009.

[63] B. S. Massey and A. J. Ward-Smith, “Mechanics of fluids.” Spon Press, Abingdon, Oxon ; New York, N.Y., 2012.

[64] “Stress for Thick Walled Cylinders using Lamé’s Equations – My DataBook.” [Online]. Available: http://www.mydatabook.org/solid-mechanics/stress-for-thick-walled-cylinders-and-spheres-using-lames-equations/. [Accessed: 19-Nov-2019].

[65] “Darcy-Weisbach Pressure and Major Head Loss Equation.” [Online]. Available: https://www.engineeringtoolbox.com/darcy-weisbach-equation-d_646.html. [Accessed: 22-Nov-2021].

[66] “Gustave-Gaspard Coriolis | French physicist | Britannica.com.” [Online]. Available: https://www.britannica.com/biography/Gustave-Gaspard-Coriolis. [Accessed: 13-Feb-2018].

[67] R. C. Baker, “Coriolis flowmeters: industrial practice and published information,” *Flow Meas. Instrum.*, vol. 5, no. 4, 1994.

[68] T. Wang and R. Baker, “Coriolis flowmeters: a review of developments over the past 20 years, and an assessment of the state of the art and likely future directions,” *Flow Meas. Instrum.*, vol. 40, Dec. 2014.

[69] J. Hemp, “The weight vector theory of Coriolis mass flowmeters,” *Flow Meas. Instrum.*, vol. 5, no. 4, 1994.

[70] B. R. Binulal, A. Rajan, and J. Kochupillai, “Dynamic analysis of Coriolis flow meter using Timoshenko beam element,” *Flow Meas. Instrum.*, vol. 47, Mar. 2016.

[71] R. Cheesewright, C. Clark, and D. Bisset, “The identification of external factors which influence the calibration of Coriolis massflow meters,” *Flow Meas. Instrum.*, vol. 11, 2000.

[72] A. Belhadj, R. Cheesewright, and C. Clark, “The simulation Of Coriolis meter response to pulsating flow using a general purpose F.E. code,” *J. Fluids Struct.*, vol. 14, 2000.

[73] M. Li and M. Henry, “Complex bandpass filtering for Coriolis mass flow meter signal processing,” in *IECON Proceedings Industrial Electronics Conference*, 2016, no. 2.

[74] L. van de Ridder, W. B. J. Hakvoort, D. M. Brouwer, J. van Dijk, J. C. Lötters, and A. de Boer, “Coriolis mass-flow meter with integrated multi-DOF active vibration isolation,” *Mechatronics*, vol. 36, pp. 167–179, Jun. 2016.

[75] F. Leach, S. Karout, F. Zhou, M. Tombs, M. Davy, and M. Henry, “Fast Coriolis mass flow metering for monitoring diesel fuel injection,” *Flow Meas. Instrum.*, vol. 58, no. September, Dec. 2017.

[76] F. Leach, M. Davy, M. Henry, M. Tombs, and F. Zhou, “A new method for measuring fuel flow in an individual injection in real time,” *SAE Tech. Pap.*, no. 2018-01–0285, 2018.

[77] “Signal Processing 101 | IEEE Signal Processing Society.” [Online]. Available: https://signalprocessingsociety.org/our-story/signal-processing-101. [Accessed: 13-Mar-2018].

[78] M. Li and M. Henry, “Signal processing methods for Coriolis Mass Flow Metering in

two-phase flow conditions," in *Proceedings of the IEEE International Conference on Industrial Technology*, 2016, vol. 2016.

[79] M. P. Henry, "Ultra narrowband filtering with Prism signal processing : design and simulation," in *IEEE IECON 2018*, 2018.

[80] M. Henry *et al.*, "The Prism – Efficient signal processing for IoT applications," *IEEE Ind. Electron. Mag.*, vol. 11, no. 4, 2017.

[81] M. Henry and V. V. Sinitsin, "Prism signal processing for machine condition monitoring II: Design and simulation," in *Proceedings - 2018 IEEE Industrial Cyber-Physical Systems, ICPS 2018*, 2018.

[82] M. Henry, F. Zhou, M. Tombs, F. Leach, M. Davy, and M. Malladi, "Prism Signal Processing of Coriolis meter data for gasoline fuel injection monitoring," *Flow Meas. Instrum.*, vol. 70, Dec. 2019.

[83] M. Henry, O. Y. Bushuev, and O. L. Ibryaeva, "Prism signal processing for sensor condition monitoring," *IEEE Int. Symp. Ind. Electron.*, Jun. 2017.

[84] J. Camm, "Mixture Preparation and Injection Strategy in Direct Injection Spark Ignition Engines - DPhil Thesis," University of Oxford, 2016.

[85] "HEYPAC pump brochure." [Online]. Available: http://www.heypac.com/docs/brochures/EnglishBrochure.pdf. [Accessed: 27-Aug-2020].

[86] "K2R PUMP FINDER." [Online]. Available: https://www.heypac.com/k2r-pump-finder. [Accessed: 14-Aug-2021].

[87] M. Hafizul *et al.*, "Effect of Injection Pressure, Injection Duration, and Injection Frequency on Direct Injector's Mass Flow Rate for Compressed Natural Gas Fuel."

[88] R. Kowsari, "Effects of Fuel Ethanol Content and Injector Temperature on the Spray Characteristics of Gasoline Direct-Injection Atomizers - PhD Thesis," University of British Columbia, 2006.

[89] "Rheonik Coriolis Mass Flow Meters." [Online]. Available: http://www.panametria.cz/produkty_pdf/RHMExx_brochure.pdf. [Accessed: 13-Feb-2018].

[90] "Rheonik Coriolis Flowmeters." [Online]. Available: https://www.rheonik.com/wp-content/uploads/pdf/Rheonik-Coriolis-Brochure_A4.pdf. [Accessed: 13-Feb-2018].

[91] "H-30 3100 Series and 3200 Heavy Duty Series Compact OEM Pressure Transmitters."

[92] "Piezoresistive high pressure sensor for the injection pressure application- 4067E." [Online]. Available: https://www.kistler.com/en/product/type-4067e/. [Accessed: 29-Jan-2021].

[93] "Piezoelectric Theory and Applications," 2000.

[94] "High temperature pressure sensor for temperatures up to 200 °C."

[95] "Current probe 60 A BNC connector." [Online]. Available: https://www.picotech.com/accessories/bnc-current-probes/60-a-current-probe-bnc. [Accessed: 12-Mar-2021].

[96] "USB-6211 Specifications." [Online]. Available:

http://www.ni.com/pdf/manuals/375195d.pdf. [Accessed: 13-Jul-2018].

[97] "NI DIDS-2100 Series User Manual | © National Instruments | 1 NI Direct Injector Driver System User Guide," 2016.

[98] "Zynq-7000 SoC." [Online]. Available: https://www.xilinx.com/products/silicon-devices/soc/zynq-7000.html#productTable. [Accessed: 17-Jul-2018].

[99] M. Sandford, G. Page, and P. Crawford, "The all new AJV8," *SAE Tech. Pap.*, no. 2009-01–1060, 2009.

[100] "DynPro2 | Taylor Dynamometer." [Online]. Available: https://www.taylordyno.com/products/instrumentation/dynpro2/. [Accessed: 26-Nov-2021].

[101] "Multi-trigger Digital Delay Generator | Berkeley Nucleonics." [Online]. Available: https://www.berkeleynucleonics.com/model-725-multi-trigger-digital-delay-generator. [Accessed: 30-Nov-2021].

[102] "AVL X-ion™." [Online]. Available: https://www.avl.com/-/avl-x-iontm?redirect=https%3A%2F%2Fwww.avl.com%3A443%2Fsearch%3Fp_p_id%3D3%26p_p_lifecycle%3D0%26p_p_state%3Dnormal%26p_p_mode%3Dview%26p_p_col_id%3Dcolumn-1%26p_p_col_count%3D1%26_3_search%3D%26_3_keywords%3Dx-ion%26_3_groupId%3D101. [Accessed: 26-Nov-2021].

[103] "IndiCom Indicating Software - IndiCom Indicating Software - Content - avl.com." [Online]. Available: https://www.avl.com/-/indicom-indicating-software. [Accessed: 30-Nov-2021].

[104] "2,2,4-Trimethylpentane | C8H18 - PubChem." [Online]. Available: https://pubchem.ncbi.nlm.nih.gov/compound/2_2_4-Trimethylpentane. [Accessed: 14-May-2020].

[105] "Undecane | C11H24 - PubChem." [Online]. Available: https://pubchem.ncbi.nlm.nih.gov/compound/Undecane. [Accessed: 14-May-2020].

[106] BP, "Material Safety Data Sheet: Gasoline." [Online]. Available: https://www.bp.com/content/dam/bp-country/en_au/products-services/fuels/regular-fuels/MSDS Link 95.pdf. [Accessed: 11-Jun-2018].

[107] Barrettine, "Material Safety Data Sheet: White Spirit." [Online]. Available: https://www.barrettinepro.co.uk/uploads/assets/Documents/MSDS/White Spirit.pdf. [Accessed: 09-Apr-2018].

[108] P. A. Giuliano Albo, S. Lago, R. Romeo, and S. Lorefice, "High pressure density and speed-of-sound measurements in n-undecane and evidence of the effects of near-field diffraction," *J. Chem. Thermodyn.*, vol. 58, 2013.

[109] F. Plantier and J. L. Daridon, "Speed of Sound of 2-Methylpentane, 2,3-Dimethylpentane, and 2,2,4-Trimethylpentane from (293.15 to 373.15) K and up to 150 MPa," 2005.

[110] M. P. Henry, "PRISM signal processing: a recursive fir technique applied to the efficient tracking of resonant sensor systems," in *3rd International conference on microfluidic handling systems*, no. 3.

[111] J. A. Fox, *Hydraulic Analysis of Unsteady Flow in Pipe Networks*. London: Macmillan

Education UK, 1977.

[112] E. B. Wylie and V. L. Streeter, *Fluid transients*. McGraw-hill, 1978.

[113] L. Yang and T. Moan, “Bond graph representations of hydraulic pipelines using normal modes with dissipative friction.”

[114] S. M. Beck, H. Haider, and R. F. Boucher, “Transmission line modelling of simulated drill strings undergoing water-hammer,” *Proc. Inst. Mech. Eng. Part C J. Mech. Eng. Sci.*, vol. 209, no. 6, 1995.

[115] D. M. Auslander, “D. M. Analysis of networks of wavelike transmission elements,” Massachusetts Institute of Technology, Cambridge, Massachusetts, 1966.

[116] M. F. Ghazali, “Leak detection using instantaneous frequency analysis - PhD Thesis,” University of Sheffield, Sheffield, 2012.

[117] C. Christopoulos, *The transmission-line modeling method : TLM*. New York : Oxford: Institute of Electrical and Electronic Engineers ; Oxford University Press, 1995.

[118] R. F. Boucher and E. E. Kitsios, “Simulation of fluid network dynamics by transmission line modelling,” *Proc. Inst. Mech. Eng. Part C J. Mech. Eng. Sci.*, vol. 200, no. 1, 1986.

[119] E. E. Kitsios and R. F. Boucher, “Transmission Line Modelling of a Hydraulic Position Control System,” *Proc. Inst. Mech. Eng. Part B Manag. Eng. Manuf.*, vol. 200, no. 4, pp. 229–236, Nov. 1986.

[120] “Undecane.” [Online]. Available: https://pubchem.ncbi.nlm.nih.gov/compound/Undecane. [Accessed: 11-Oct-2019].

[121] “Roughness & Surface Coefficients.” [Online]. Available: https://www.engineeringtoolbox.com/surface-roughness-ventilation-ducts-d_209.html. [Accessed: 05-Dec-2019].

[122] “Colebrook Equation.” [Online]. Available: https://www.engineeringtoolbox.com/colebrook-equation-d_1031.html. [Accessed: 22-Nov-2021].

[123] P. Mishra and S. N. Gupta, “Momentum Transfer in Curved Pipes. 1. Newtonian Fluids,” *Ind. Eng. Chem. Process Des. Dev.*, vol. 18, no. 1, Jan. 2002.

10 Appendices

10.1 Pipeline model using TLM

The code for the pipeline model for setup 6 is provided below.

```
%%%%%%%%%%%%%%%%%%%%%%%%%%%%%%%%%%%%%%%%%%%%%%%%%%%%%%%%%%%%%%%%%%%%%%%%%%%%%%%
% TLM Pressure Method - Maruthi Malladi
% Version 3.3
% 15/02/2021
% Method based on Beck et al.
% Apply the TLM method to pipeline
% Setup 6 with bent pipe
% Slope in injection
% Scattering matrix for T-junction (resistance)
% Includes pressure method caclulations
%%%%%%%%%%%%%%%%%%%%%%%%%%%%%%%%%%%%%%%%%%%%%%%%%%%%%%%%%%%%%%%%%%%%%%%%%%%%%%%

clear all
close all

% General parameter setup

d_pipe = 4e-3;                  % diameter of pipe (m)
A_pipe = pi*d_pipe*d_pipe*0.25; % area of pipe (m^2)
d_fit = 4.8e-3;                 % diameter of fitting (m)
A_fit = pi*d_fit*d_fit*0.25;    % area of fitting (m^2)

sen_dis = 0.2;                  % distance between pressure transducer (m)
c_fluid = 1400;                 % speed of sound - Undecane (m/s)
l_segment = 10e-3;              % length of pipeline segment (m)
T = l_segment/c_fluid;          % time step (s)
Freq= 1/T;                      % frequency of the model (Hz)
steps = 2.2*Freq;               % number of steps of the model
t= 1*T:1*T:2.2;                 % time steps vector (s)

inj_dur = 2e-3;                 % injection duration (s)
inj_per = 0.2;                  % injection period (s)

P_start = 153e5;                % Fuel pressure (bar)
P_drop = 0.1*P_start;           % Pressure drop during injection (bar)

Y_pipe = A_pipe/c_fluid;        % Pipe admittance (m s)
Y_fit = A_fit/c_fluid;          % Fitting admittance (m s)

segments = 42;                  % number of segments in the model

wave_speed = zeros(segments*2,steps); % u,v waves steup
p_chamber = zeros(2,steps);           % pressure at pressure transducers

S = zeros(segments*2,segments*2);     % scattering matrix
F = zeros(segments*2,1);              % forcing vector
P = zeros(segments*2,steps);          % pressure input matrix
```

```
% Pressure inputs setup
P_inj = zeros(1,(inj_dur+0.2e-3)*Freq);     % Pressure injector
% Pressure drop at SOI
for k = 1:0.2e-3*Freq
    P_inj(1,k) = P_start - P_drop*(k/28);
end
P_inj(1,29:inj_dur*Freq) =P_start-P_drop;   % Pressure during injection
% Pressure rise at EOI
for k = 1:0.2e-3*Freq
    P_inj(1,k+inj_dur*Freq) = P_start-P_drop + (P_drop+0.5e5)*(k/28);
end

P(1,:) =P_start;                                        % inlet side
P((segments)*2,:)=P_start;                              % injection side
injections = zeros(1,round(10*(inj_dur+0.2e-3)*Freq)); % injection time

% Injection setup into pressure input matrix
for i = 1:10
    P((segments)*2,28000+1501+(inj_per*Freq)*(i-1):28000+1500+((inj_dur+0.2e-
3)*Freq)+(inj_per*Freq)*(i-1)) = P_inj;
    injections(1,(inj_dur+0.2e-3)*Freq*(i-1)+1:(inj_dur+0.2e-
3)*Freq*(i))=(28000+1501+(inj_per*Freq)*(i-1):28000+1500+((inj_dur+0.2e-
3)*Freq)+(inj_per*Freq)*(i-1));
end

% Setup of resistance parameters and scattering matrix
% Resistance of each pipe type
R_input = 5e04;     % Input
R_output = 5e04;    % Output
R_fit = 3e06;       % Fitting
R_tjun_s = 5e06;    % T-junction straight
R_tjun_t = 10e06;   % T-junction perpendicular
R_valve = 10e06;    % Valve
R_pipe = 0;         % Pipeline
R_coil = 0;         % Coil
R_bend = 0;         % Bend
R_elbow = 5e05;     % Elobow
R_end = 1e05;       % End

% T-junction
K_tt = Y_fit/(1+(R_tjun_t)*Y_fit);
K_ts = Y_fit/(1+(R_tjun_s)*Y_fit);
% scattering elements
s_ss = (2*K_ts*K_ts)/(sqrt(Y_fit*Y_fit)*(K_ts+K_ts+K_tt));
s_sr = K_ts*(2*K_ts+((R_tjun_s)*Y_fit-1)*(K_ts+K_ts+K_tt))/(Y_fit*(K_ts+K_ts+K_tt));
s_tt = (2*K_ts*K_tt)/(sqrt(Y_fit*Y_fit)*(K_ts+K_ts+K_tt));
s_tr = K_tt*(2*K_tt+((R_tjun_t)*Y_fit-1)*(K_ts+K_ts+K_tt))/(Y_fit*(K_ts+K_ts+K_tt));
T_str = s_ss;       % T-junction straight transmission
T_tri = s_tt;       % T-junction perpendicular transmission
T_ref = s_sr;       % T-junction straight reflection
T_t_prop = s_tt;    % T-junction perpendicular transmission
T_t_ref = s_tr;     % T-junction perpendicular reflection

% forcing element at input and output
F(1,1) = sqrt(2*Y_fit)/(R_input*Y_fit+1);
F((segments)*2,1) = sqrt(2*Y_pipe)/(R_input*Y_fit+1);

% setup the scattering matrix
S((segments)*2,(segments)*2-1) = (R_output*Y_pipe-1)/(R_output*Y_pipe+1); % output
S(1,2) = (R_input*Y_fit-1)/(R_input*Y_fit+1); % input
```

```
%elements from fitting
K_p = Y_pipe/(1+R_fit*Y_pipe);
K_f = Y_fit/(1+R_fit*Y_fit);

s_pp = K_p*(2*K_p+(R_fit*Y_pipe-1)*(K_p+K_f))/(Y_pipe*(K_p+K_f)); % pipe reflection
s_pf = (2*K_p*K_f)/(sqrt(Y_pipe*Y_fit)*(K_p+K_f)); % pipe fitting transmission
s_ff = K_f*(2*K_f+(R_fit*Y_fit-1)*(K_p+K_f))/(Y_fit*(K_p+K_f)); %fitting reflection

% ftting to pipeline
n_fit = [1,4,7,10,13,16];

for k_fit = 1:length(n_fit);
    k = n_fit(k_fit);
    S(2*k,2*k-1) = s_ff;
    S(2*k,2*k+2) = s_pf;
    S(2*k+1,2*k-1) = s_pf;
    S(2*k+1,2*k+2) = s_pp;
end

% pipeline to fitting

n_fit_2 = [2,5,8,11,14];

for k_fit = 1:length(n_fit_2);
    k_in = n_fit_2(k_fit);
    S(2*k_in,2*k_in-1) = s_pp;
    S(2*k_in,2*k_in+2) = s_pf;
    S(2*k_in+1,2*k_in-1) = s_pf;
    S(2*k_in+1,2*k_in+2) = s_ff;
end

% blocked end
S(6*2,6*2-1) =1+ Y_fit*R_end/(Y_fit*R_end+1);
S(15*2,15*2-1) =1+ Y_fit*R_end/(Y_fit*R_end+1);

% elbow
K_e = Y_fit/(1+R_elbow*Y_fit);
s_e_11 = K_e*(2*K_e+(R_elbow*Y_fit-1)*(K_e+K_e))/(Y_fit*(K_e+K_e)); %elbow has the same return
wave coeff in both directions
s_e_12 = (2*K_e*K_e)/(sqrt(Y_fit*Y_fit)*(K_e+K_e));

S(2*9,2*9-1) = s_e_11;
S(2*9,2*9+2) = s_e_12;
S(2*9+1,2*9-1) = s_e_12;
S(2*9+1,2*9+2) = s_e_11;

% T-junction
T_jun = [3 4 7;12 13 16];
for k_fit = 1:size(T_jun,1);
    S((T_jun(k_fit,1))*2,(T_jun(k_fit,2))*2)= T_tri;
    S((T_jun(k_fit,1))*2,(T_jun(k_fit,3))*2)= T_str;
    S((T_jun(k_fit,1))*2,(T_jun(k_fit,1))*2-1)= T_ref;
    S((T_jun(k_fit,2))*2-1,(T_jun(k_fit,1))*2-1)= T_t_prop;
    S((T_jun(k_fit,2))*2-1,(T_jun(k_fit,3))*2)= T_t_prop;
    S((T_jun(k_fit,2))*2-1,(T_jun(k_fit,2))*2)= T_t_ref;
    S((T_jun(k_fit,3))*2-1,(T_jun(k_fit,1))*2-1)= T_str;
    S((T_jun(k_fit,3))*2-1,(T_jun(k_fit,2))*2)= T_tri;
    S((T_jun(k_fit,3))*2-1,(T_jun(k_fit,3))*2)= T_ref;
end
```

```
%bends
K_b = Y_pipe/(1+R_bend*Y_pipe);
s_b_11 = K_b*(2*K_b+(R_bend*Y_pipe-1)*(K_b+K_b))/(Y_pipe*(K_b+K_b)); %bend has the same return
wave coeff in both directions
s_b_12 = (2*K_b*K_b)/(sqrt(Y_pipe*Y_pipe)*(K_b+K_b));

n_fit_4 = [17:36,38,39]; % bend joinings
for k_fit = 1:length(n_fit_4);
    k = n_fit_4(k_fit);
    S(2*k,2*k-1) = s_b_11;
    S(2*k,2*k+2) = s_b_12;
    S(2*k+1,2*k-1) = s_b_12;
    S(2*k+1,2*k+2) = s_b_11;
end

n_fit_3 = [37,40,41]; % pipe joinings for pressure transducers and injector
for k_fit = 1:length(n_fit_3);
    k = n_fit_3(k_fit);
    S(2*k,2*k-1) = 0;
    S(2*k,2*k+2) = 1;
    S(2*k+1,2*k-1) = 1;
    S(2*k+1,2*k+2) = 0;
end

% Run pipeline model

% waves initailisation
wave_speed(2:end,1) = sqrt(Y_pipe/2)*150e5;
wave_speed(:,1) = S*wave_speed(:,1) + F.*P(:,1); % at first time step
for k = 2:300
    wave_speed(:,k) = S*wave_speed(:,1) + F.*P(:,1);
end

% run wave calculations
for k = 301:steps
    if true(find(k == injections))
        F((segments)*2,1) = sqrt(2*Y_pipe)/(R_input*Y_fit+1);
        S((segments)*2,(segments)*2-1) = (R_output*Y_pipe-1)/(R_output*Y_pipe+1);
    else
        F((segments)*2,1) = 0;
        S(segments*2,segments*2-1) =1+ Y_pipe*R_output/(Y_pipe*R_output+1);
    end
    wave_speed(:,k) = S*[wave_speed(1:2,k-1); wave_speed(3:4,k-30); wave_speed(5:6,k-1);
wave_speed(7:8,k-1); wave_speed(9:10,k-1); wave_speed(11:12,k-1); wave_speed(13:14,k-1);
wave_speed(15:16,k-10); wave_speed(17:18,k-1); wave_speed(19:20,k-1);
        wave_speed(21:22,k-10); wave_speed(23:24,k-1); wave_speed(25:26,k-1);
wave_speed(27:28,k-5); wave_speed(29:30,k-1); wave_speed(31:32,k-1); wave_speed(33:34,k-30);
wave_speed(35:36,k-10); wave_speed(37:38,k-10); wave_speed(39:40,k-10);
        wave_speed(41:42,k-10); wave_speed(43:44,k-10); wave_speed(45:46,k-10);
wave_speed(47:48,k-10); wave_speed(49:50,k-10); wave_speed(51:52,k-10); wave_speed(53:54,k-
10); wave_speed(55:56,k-10); wave_speed(57:58,k-10); wave_speed(59:60,k-10);
        wave_speed(61:62,k-10); wave_speed(63:64,k-10); wave_speed(65:66,k-10);
wave_speed(67:68,k-10); wave_speed(69:70,k-10); wave_speed(71:72,k-10); wave_speed(73:74,k-5);
wave_speed(75:76,k-5); wave_speed(77:78,k-10); wave_speed(79:80,k-5);
        wave_speed(81:82,k-5);wave_speed(83:84,k-5)] + F.*P(:,k);
    p_chamber(1,k) = sqrt(1/(2*Y_pipe))*(wave_speed(41*2-1,k)+wave_speed(41*2,k-10))/1e5;
    p_chamber(2,k) = sqrt(1/(2*Y_pipe))*(wave_speed(39*2-1,k)+wave_speed(39*2,k-20))/1e5;
end
```

```
% Pressure methods
P1_inj = zeros(10,inj_per*Freq); % injection traces
P2_inj = zeros(10,inj_per*Freq);
for i =1:10;
    P1_inj(i,:) = p_chamber(1,28001+(inj_per*Freq)*(i-1):28000+(inj_per*Freq)*(i))*1e5;
    P2_inj(i,:) = p_chamber(2,28001+(inj_per*Freq)*(i-1):28000+(inj_per*Freq)*(i))*1e5;
end
t_method = T:T:inj_per;

% OPTM and TPTM
figure
hold on
for i = 1:10;
    p_1= P1_inj(i,:);
    p_2= P2_inj(i,:);
    delta_p2 = p_2 - p_1;
    diff_p2 = (delta_p2(:));
    p_1_mean = mean(p_1(1361:1500));

    SOI(i,1) = 1501+15;
    EOI(i,1) = 1500+15+(inj_dur+0.2e-3)*Freq;
    Inj_dur(i,:) = [SOI(i,1),EOI(i,1)];
    %OPTM
    d_p_1 = (p_1)-(p_1_mean);
    G_inj_small_tr = -A_pipe*(d_p_1/(c_fluid));
    plot(t_method,G_inj_small_tr,'b-');
    m_inj_tr(i) = trapz(t_method(SOI(i,1):EOI(i,1)), G_inj_small_tr(SOI(i,1):EOI(i,1)));
    plot(t_method(Inj_dur(i,:)),G_inj_small_tr(Inj_dur(i,:)),'rv');
    %TPTM
    avg_val = mean(delta_p2)*t_method(:);
    G_inj_large = A_pipe/sen_dis*cumtrapz(t_method(:),diff_p2) - A_pipe/sen_dis*avg_val;
    m_inj_large(i) = trapz(t_method(SOI(i,1):EOI(i,1)), G_inj_large(SOI(i,1):EOI(i,1)));
    plot(t_method,G_inj_large,'k-');
    plot(t_method(Inj_dur(1,:)),G_inj_large(Inj_dur(1,:)),'ro')
end

Mass_inj.TLM_mean = mean(m_inj_tr);
Mass_inj.TLM_std = std(m_inj_tr);
Mass_inj.TLM_large_mean = mean(m_inj_large);
Mass_inj.TLM_large_std = std(m_inj_large);
xlabel('Time (ms)')
ylabel('Mass flow rate (g/s)')
legend('OPTM','OPTM SOI & EOI','TPTM','TPTM SOI & EOI');
xlim([0.01 0.03])
```